Tuning the Properties of Quantum Nanocrystals and Magnetic Nanoparticles using Spherical Ligands: Carboranes and Metallacarboranes

Arpita Saha

Universitat Autònoma de Barcelona

Tuning the Properties of Quantum Nanocrystals and Magnetic Nanoparticles using Spherical Ligands: Carboranes and Metallacarboranes

Arpita Saha

Doctoral Thesis
(Programa de Doctorat en Quimica)

Supervisor: Prof. Francesc Teixidor i Bombardo
Supervisor: Prof. Clara Viñas i Teixidor
Tutor: Prof. Joan Ortuño Suades

Departament de Quimica
Facultat de Ciences

2019

ICMAB INSTITUT DE CIÈNCIA DE MATERIALS DE BARCELONA
EXCELENCIA SEVERO OCHOA
CSIC CONSEJO SUPERIOR DE INVESTIGACIONES CIENTÍFICAS

Memòria presentada per aspirar al Grau de Doctor per

Arpita Saha

Vist i plau

Prof. Francesc Teixidor i Bombardo (Supervisor)

Prof. Clara Viñas i Teixidor (Supervisor)

Prof. Joan Suades Ortuño (Tutor)

Bellaterra, 11th July, 2019

MINISTERIO
DE CIENCIA, INNOVACIÓN
Y UNIVERSIDADES

ICMAB
INSTITUT DE CIÈNCIA DE MATERIALS DE BARCELONA

CSIC

Le Professor Francesc Teixidor i Bombardo y La Professora Clara Viñas i Teixidor, Profesores d'Investigació del *Consejo Superior de Investigaciones Científicas* a l'*Institut* de *Ciència de Materials de Barcelona*

CERTIFICA

Que n' ARPITA SAHA, llicenciada en Química, ha realizat sota la seva dirección el treball que porta per titol "*Tuning the properties of Quantum Nanocrystals and Magnetic Nanoparticles using Spherical Ligands: Carboranes and Metallacarboranes*" que queda recollit en aquesta memoria per optar al titol de Doctor per la Universitat Autònoma de Barcelona.

I, perquè aixi consti i tingui els efectes corresponents, signa aquest certificat a Bellaterra, a 11 de Julio del 2019.

Prof. Francesc Teixidor
ICMAB-CSIC

Prof. Clara Viñas
ICMAB-CSIC

http://icmab.es

Campus de la Universitat Autònoma de Barcelona
08193 Bellaterra, Catalunya, Espanya
Telf.: +34 935 801 853
Fax.: +34 935 805 729

http://icmab.es

Campus de la Universitat Autònoma de Barcelona
08193 Bellaterra, Catalunya, Espanya
Telf.: +34 935 801 853
Fax.: +34 935 805 729

Aquest treball de recerca ha estat finançat per la Comisión Interministerial de Ciencia y Tecnología, CICYT, mitjançant els projectes CTQ2013-44670-R i CTQ2016-75150-R; per la Generalitat de Catalunya amb el projecte 2014/SGR/149 i els projectes concedit per Unió Europea H2020-NMBP-13-2017 y KARDIATOOL (Grant No-768686). Agraïr la beca de Formació de Personal Universitari (FI, ref.: 2016FI_B 00214) concedida pel Generalitat de Catalunya, durant el període maig del 2016 al abril del 2019.

Aquest treball d'investigació, amb data de defensa del 12 de Setembre de 2019, té com a membres del tribunal a:

- President: Prof. Joan Bausells Roigé, Professor d'Investigació, NEMS i grup de nanofabricació, Institut de Microelectrònica de Barcelona, CSIC.

- Secretari: Prof. Miquel Solà i Puig, Catedràtic d'Universitat, Institut de Química Computacional i Catàlisi, Universitat de Girona.

- Vocal: Prof. Abdelhamid Elaissari, Director d'Investigació, Laboratori d'Automatització, Enginyeria de Processos i Enginyeria Farmacèutica, Claude Bernard University Lyon1, Lyon, França.

Com a membres suplents:

- Suplent 1: Dra. Rosario Núñez Aguilera, Investigador Ciéntific del CSIC, Institut de Ciència de Materials de Barcelona (ICMAB-CSIC).

- Suplent 2: Dr. Jordi Poater, ICREA Research Professor, Departament de Química Inorgànica i Orgànica, Universitat de Barcelona.

Acknowledgements

This Ph.D. thesis has been an incredible chapter in the journey of my life. As I finish this chapter of my life, there are many people I would like to thank as without their continued support and presence, finishing this thesis would not have been possible.

At first, I would like to thank my supervisor, Prof. Francesc Teixidor for believing in my potential and accepting me in his group as a Ph.D. graduate. It has been my great pleasure to share, discuss and exchange ideas with him not just related to science but on other topics and learn new things. His constant guidance, support, enthusiasm and scientific advice has been a great stimulator throughout these past few years for me to achieve the results. Also, I would like to show my deepest gratitude to my co-supervisor, Prof. Clara Vinas for accepting to be my supervisor for the FI grant and allow me to work with her. It has been an enjoyable ride for me to work with you and participate in discussions with you regarding science. It has always left me more enlightened. Thank you to both of you for being there in the last few years at every step of this process and help me to reach the finish line.

I would also like to extend my gratitude to Dr. Rosario Nunez, Dr. Marisa Romero and Dr. Jose Giner. Thank you, Rosario for the very warm welcome on my first day in the institute and for the numerous excursions and lunches that you organized during these years for the group. Your initiative to organize workshops and conferences in ICMAB and encouraging us to participate in them has always been a big motivation.

Thank you to Prof. Xavier Obradors, Director of ICMAB for accepting me to be a part of this institution, thanks to Sonia and Pietat for all the help in making my contract and answering my numerous questions regarding the work permit and other bureaucratic issues. Thanks to Anna Fernandez, Maria Rivera, Antoni Miquel from the administration with all the help during this time. A big thanks to Anna May for being the most enthusiastic person in the institute and organizing the many events in the institute and informing us all about them and helping us to participate in these events within the institute and outside. Thank you to Prof. Joan Ortuna Suades from UAB for accepting to be my

tutor. Also, I would like thank Elena Jimenez for the constant help she provided during the entire Ph.D. tenure. It would have been very difficult to finish the thesis without your support.

My regards and gratitude to Prof. Abdelhamid Errachid from ISA, Lyon for all the help with the KARDIATOOL project and allowing me to be a part of it.
Also, I would like to thank Dr. Anna Rosell, Alba Grayston, Joan X. Comella, Anna Morancho and Koen Galenkamp from the Vall d'Hebron research institute for letting me be a part of the collaboration on the nano-hybrid study in biological systems. Also, thank you to Diego Alberti, Simonetta Geninatti and Nicoletta Protti from Italy for helping me.

All the characterization done in this thesis has been due to the cumulative effort of all the technicians who have been superlative in their effort and support. Thank you Judit, for the many TEM images that you took and for always accommodating me in your schedule even at short notice. Thank you to Jose Amable for teaching me the soft lab characterization techniques and allowing me to use the instruments. Further I would like to acknowledge Bernat Bozzo for the magnetic SQUID studies, Ana Esther for SEM and EDX studies, Neus Roma for helping me with the clean room facilities and Vega Lloveras for teaching me the IR, UV and Optical microscope.

I appreciate the help I received from the other technicians from ICN2 especially Belen Ballesteros for having the patience to deal with my samples and analysing them. Thanks to Marcos Rosado for always being so active in helping me out with the HRSEM and XHRSEM. Thanks to Francisco Bellare for the help with the ITO coated Glass slides and helping to cut them in necessary size and shapes. Thanks to Gillaume Sauthier for the XPS results.

Other than ICN2, I would like to extend my appreciation for the members of the microscopy department in UAB for helping me to learn the HRTEM and HRSEM instruments. Thanks a lot, to Emma Rossinyol for taking the initiative to teach me how to analyze the samples using the electron microscopy. Thanks to Marti and Pau for being there whenever I needed help with the microscopes. My gratitude to Nuria Barba and Helen in the confocal microscopy for teaching me how to use the device and the software for analysing my samples and helping me to study my samples.

I extend my thanks to the luminescence department of the UAB, especially to Bartolomeu Salvatore for the luminescence studies and also the members of chemical analysis department and mass spectrometry department.

A big thank you to Jordi Cortes and the group members past and present for making my stay here a pleasant and entertaining one. Firstly, I am so thankful to Elena, my good friend, for being there with me during my initial days and helping me out with everything both personally and professionally. I could never thank you enough for all the times that you have been there for me in so many ways. To all the past Ph.D. students and now the doctors, Victor, Justo, Adnana, Ivy, Ines and Mahdi for being there. A special thanks to Ines for being my coffee partner and for all the long discussions and talk we had. A hearty thanks to Isabel, for all the time helping with the translations and other things, thanks to Bego, Flavia, Joan, Isabel Guerrero, Lei, Albert, Zsolt, Miquel, Pol and the new ones Sohini and Zhen Li. Also, my thanks to Raquel for being a good friend and for all the help with the electroluminescence studies in UB and to Juan too for helping us to analyse the samples whenever we needed.

A special mention to Abhishek Saini (Devil ψ), the next doctor and my closest and most trusted person for making my life easy here. It is so nice to have someone you know from before and to be able to share things. Words would not be enough to express my gratitude towards you for being there all these years at every step, in order for me to complete this. You have been a great support in good times and bad, at both home and in the lab.

Finally, I would like to thank my family, my parents for supporting me and my brother who has been always very encouraging. It would not have been possible without you to be who I am today.

Hopefully I have not missed anyone but you all know that this would not have been possible if even one of you did not play your part the way you have. Thank you to all of you for helping me make this journey a success.

Organització del Manuscrit

D'acord amb la normativa vigent i prèvia acceptació de la Comissió de Doctorat de la Universitat Autònoma de Barcelona, aquesta memòria es presenta com a compendi de publicacions, presentats i acceptats per la Comissió de Doctorat en Química de la UAB, el 3rd de Juny de 2019. Els treballs inclosos en aquesta memòria són els següents:

- Biomimetic Inspired Core-Canopy Quantum Dots: Ions Trapped in Voids Induce Kinetic Fluorescence Switching, Arpita Saha, Elena Oleshkevich, Clara Vinas and Francesc Teixidor, *Advanced Materials*, **2017**, *29*, 1704238.
  DOI: 10.1002/adma.201704238.

- The Next Stage in Colloidal Synthesis of Aqueous CdSe QDs: High Throughput and Intense Emissive Properties, Arpita Saha, Abhishek Saini, Clara Vinas and Francesc Teixidor, *ChemNanoMat,* **2019,** *5.*
  DOI: 10.1002/cnma.201900247.

- Combining Magnetic Nanoparticles and Icosahedral Boron Clusters in Biocompatible Inorganic Nanohybrids For Cancer Therapy, Elena Oleshkevich, Anna Morancho, Arpita Saha, Koen M. O. Galenkamp, Alba Grayston, Simonetta Geninatti Crich, Diego Alberti, Nicoletta Protti, Joan X. Comella, Francesc Teixidor, Anna Rosell and Clara Vinas *Nanomedicine : Nanotechnology, Biology and Medicine*, **2019**, 20, 101986.
  DOI: 10.1016/j.nano.2019.03.008

Abbreviations

QDs	Quantum Dots
CdSe	Cadmium Selenide
CdTe	Cadmium Telluride
QY	Quantum Yield
MAA	Mercaptoacetic acid
3-MPA	Mercaptopropionic acid
AIE	Aggregation Induced Emission
ACQ	Aggregation Caused Quenching
TGA	Thioglycolic acid
C_{60}	Fullerene (Bucky ball)
$C_{20}H_{20}$	Dodecahedrane
CarbSH	*ortho*-mercaptocarborane
Au NPs	Gold nanoparticles
BNCT	Boron neutron capture therapy
TGA	Thermal gravimetric analysis
CSD	Cambridge Structural Database
3-D	Three dimensional
m-carboranyl	*meta*-carboranyl
Li[CarbS]	Lithium salt of carboranyl thiol
Na[CarbS]	Sodium salt of carboranyl thiol
Na_2SeSO_3	Sodium selenosulphite
PL	Photoluminescence
CarbPhos	carboranyl phosphinate
KFS	Kinetic Fluorescence Switching
UV-vis	Ultaviolet-visible spectroscopy
EDX	Energy dispersive X-ray
TEM	Transmission electron microscope
SEM	Scanning electron microscope
IR	Infra-red spectroscopy
DLS	Dynamic Light Scattering
EA	Elemental Analysis
SAED	Selected area electron diffraction
2-D	Two dimensional
PhenPhos	Phenyl Phosphinate
$[N(But)_4Me_0]^+$	Terabutylammonium
$[N(Caprylyl)_3Me_1]^+$	Tricaprylylmethylammonium
$[N(Octadecyl)_2Me_2]^+$	Dimethylsioctadecylammonium
$[N(Cetyl)Me_3]^+$	Cetyltrimethylammonium
QNCs	Quantum nanocrystals
QRs	Quantum rings
QRods	Quantum Rods

PVA	Polyvinyl alcohol
PDMS	Polydimethyl siloxane
NCs	Nanocomposites
HRSEM	High resolution TEM
HRSEM	High resolution SEM
XHRSEM	Extreme high-resolution SEM
EL	Electroluminescence
SPIONs	Superparamagentic Iron Oxide Nanoparticles
TB	Blocking temperature
NPs	Nanoparticles
MNPs	Magnetic nanoparticles
1-MNPs	Magnetic nanoparticles coated with m-carboranyl phosphinate
$Ø_{TEM}$	Size measured by TEM
XPS	X-ray photoelectron spectroscopy
SQUID	Superconductive quantum interference device
ZFC	Zero field cooling
FC	Field cooling
M_R	Remnant magnetization
H_c	Coercivity
PBS	Phosphate buffer saline solution
DMEM	Eagle's minimal essential medium
EGM-2	Endothelial cell growth medium 2
RPMI	Roswell Park Memorial Institute culture media
EFTEM	Energy filtered TEM
ICP-MS	Inductive coupled plasma-mass spectroscopy
EELS	Electron energy loss spectroscopy
MRI	Magnetic resonance imaging
hCMEC/D3	Brain endothelial cells
A172	Glioblastoma cells
CNTs	Carbon nanotubes
MWCNTs	Multiwalled carbon nanotubes
SWCNTs	Single walled carbon nanotubes
MNCs	Magnetic nanocomposites
H[COSAN]	Cobltabis (dicarbollide)
Mcb	Metallacarborane
STEM	Scanning transmission electron microscopy
M_S	Saturated magnetization

APMS	3-(2-aminoethylamino) propylmethyl dimethoxy silane
TMAH	Tetramethyl ammonium hydroxide
TEOS	Tetra ethyl ortho silicate
PTFE	Poly tetrafluororethelene
HOMO	Highest occupied molecular orbital
LUMO	Lowest unoccupied molecular orbital

Summary of the Thesis

The research presented in this thesis has been summarized as a compendium of articles published and to be published in the future. There are five chapters dealing with the results and discussions. The results and discussions are preceded by a general introduction and objectives. The summary of each chaper of the results is given below.

- The 1st chapter deals with aqueous quantum dots (QDs) capped with *meta*-carboranyl phosphinate which gives us a brand new architecture of QDs named as core-canopy QDs. This is the first time spherical ligands have been experimentally used to cap QDs. Due to this architecture, we obtained a new luminescence property in these QDs, called the kinetic fluorescence switching (KFS) which has never been reported before. It is not similar to aggregation induced emission (AIE) nor aggregation caused quenching (ACQ), but it is a new phenomenon in which the luminescence fades with time but upon application of kinetic energy regains the full intensity of emission. These core-canopy QDs are compared with other QDs and characterized.
- The next chapter deals with synthesis of QDs in water using a new set up developed by us. It produces QDs with high PL, QY and longer lifetime of emission in water medium. The set up used is different to the reflux based method used to synthesize QDs in water at 100^{o}C. Here we used a cork insulated sand bath, with ace pressure tubes of glass. The QDs are generated in these pressure tubes at 150^{o}C under autogeneous pressure produced by the tubes. They have been compared to the traditional water based QDs and charaterized. These QDs combine the advanatge of high QY and different luminescence colours of organometallic synthesized QDs and the easy and cheap production of a water based synthesis.
- The next chapter deals with quantum nanocrystals (QNCs) being synthesized in water for the first time. No other QNC has been synthesized in a completely water

medium other than QD. We have demonstrated an easy synthetic route and setup design using which quantum rods (Qrods) and quantum rings (QRs) can be easily synthesized in a water medium. This is the first time that this has been experimentally synthesized and studied. These QNCs could be easily stored in powdered form, remain suspended in various solvents for more than 18 months, without degradation in their colloidal stability or luminescence properties. Moreover, they can be used to form nancomposites using polymers. These polymeric films containing the QNCs showed luminescence which lasted over a year and could also show electroluminescence, hence making them viable for QLED applications in the future.

- The 4th chapter of the results and discussions deals with magnetic nanoparticles (MNPs) coated with *meta*-carboranyl phosphinate. These give rise to new nano-hybrids which can be used for biological application of boron neutron capture therapy (BNCT). These nanohybrids have been synthesized, characterized and used in biological applications. Their magnetic properties and stability has been studied after autoclave sterilization, further their colloidal stability in different biological culture mediums has also been studied. Then their cellular uptake has been studied and quantified. The uptake of the MNPs by the glioblastoma tumor cells has been visualized and also studied in vivo for BNCT applications.
- Finally, the last chapter deals with the synthesis of MNPs using colloidal co-precipitation method and coating with inorganic silica shell. These coated MNPs are further functionalzied with amino and carboxylic groups for them to be attached with antibodies in the future for biosensing applications. MWCNTs are also used in conjugation with these MNPs to generate magnetic nanocomposites (MNCs). Both the MNPs and MNCs are used to generate for the first time a non-bonded complex with H[COSAN]. H[COSAN] being a redox specie can be used to manipulate the HOMO-LUMO levels, thus enabling these MNPs and MNCs as effective sensing layer materials. They have been thoroughly characterized.

Table of Contents

1. Introduction
   1.1. Aqueous vs Organometallic vs our method
   1.2. Commonly used ligands and synthetic routes
2. Ace pressure tube synthesis
   2.1. Understanding the synthesis
3. Characterizations
   3.1. TEM, DLS and size
   3.2. Fluorescence studies
   3.3. Chemical composition studies
   3.4. Zeta potential studies
4. Comparisons
   4.1. Comparison with usual water based QDs
5. Conclusions
6. References

3.1.3. Quantum Rods and Rings in water

1. Introduction
   1.1. Quantum Rods
   1.2. Quantum Rings
2. Synthesis
   2.1. Synthesis of Quantum Rods
   2.2. Synthesis of Quantum Rings
   2.3. Synthesis of Polymeric films
3. Characterizations of QNCs in Solution
   3.1. TEM study and size
   3.2. Composition study
   3.3. Fluorescence study
   3.4. Zeta potential study
4. Characterizations of QNCs in Films
   4.1. HRTEM and HRSEM studies
   4.2. Composition study
   4.3. Photoluminescence study
   4.4. Electroluminescence study
   4.5. Thickness of the films
5. Conclusions
6. References

3.2.1. Nano-hybrids for Cancer Therapy

1. Introduction
   1.1. Magnetic nanoparticles (MNPs)
   1.2. Commonly used Coatings and Ligands
   1.3. Common synthesis routes for MNPs
   1.4. MNPs in biological studies and BNCT
2. New 1-MNPs
   2.1. Synthesis of the 1-MNPs
3. Characterizations

3.1. TEM and size
3.2. Chemical composition studies
3.3. Hysteresis study
4. Colloidal stability study
5. Biological studies
5.1. Cellular Uptake Studies
5.2. Magnetic Resonance Imaging (MRI)
5.3. BNCT Study
5.4. Toxicity studies (in vitro and in vivo)
6. Conclusions
7. References

3.2.2. Magnetic Nanoparticles and Nanocomposites with H[COSAN]

1. Introduction
1.1. MNPs with SiO_2 coating
1.2. Cobaltabis(dicarbollide): H[COSAN]
1.3. Carbon nanotubes (CNT)
2. Synthesis of MNPs
2.1. 2.1. Fe_3O_4@SiO_2 (Small and Large)
2.2. Amine and Carboxylic functionalized MNPs
2.3. H[COSAN] attached MNPs
3. Characterizations
3.1. TEM, STEM and SEM studies and Size
3.2. Chemical Composition Studies
3.3. UV-vis studies and Zeta-Potential
3.4. Elemental mapping
3.5. Magnetic Hysteresis Study
4. Synthesis of Nanocomposites
4.1. Nanocomposite of CNT with functionalized MNPs
4.2. H[COSAN] attached nanocomposite
5. Characterizations
5.1. TEM, STEM and SEM studies
5.2. Chemical Composition Studies
5.3. UV-vis studies and Zeta Potential
5.4. Elemental mapping
5.5. Magnetic Hysteresis Study
6. Colloidal Stability Studies
6.1. Stability with different Surfactants
7. Conclusions
8. References

4. Conclusions

5. Annex I

1. Introduction

A brief introduction to the carboranes, metallacarboranes is written in this part. Also, nanoparticles have been introduced along with the two different types of nanoparticles in specific (semiconductor and magnetic nanoparticles) which have been particularly used in this thesis. The nanoscience of semiconductors and magnetism has also been described here in order to understand the work discussed in the results and discussion section.

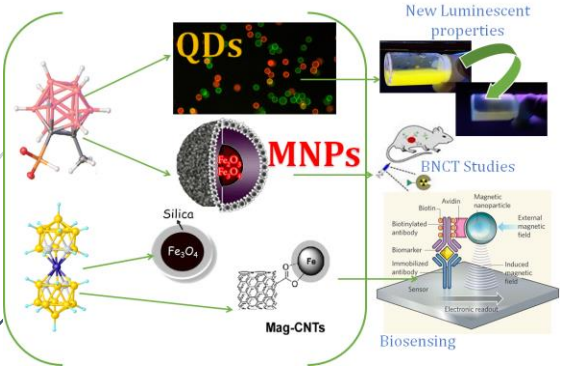

Arpita Saha
ICMAB-CSIC (UAB)

Contents

1. Boron: Historic Overview

Boron dates long back to history and it has been used over the ages for over a long period of time. Its usage dates back to over 6000 years ago and ever since it has been found, people have realized boron to be a ubiquitous element which can be found in rocks, soil and water. Historical source suggest that Babylonians used the Borax over 4000 years ago by importing it from the Far East to use it as a flux for gold.[1] Egyptians have also been attributed for the use of boron for mummifying, medicinal purposes and metallurgical applications.

In the year 1808, the French chemists Gay Lussac and L. J. Thenard and also the English Sir Humphry Davy obtained the elemental Boron though none of them recognized it as a new element. It was only in 1824 that Jöns Jacob Berzelius acknowledged it as a new element. The varied chemistry and importance of boron is mainly dominated by the fact that borates can form trigonal and also tetrahedral bonding patterns and can also form complexes with organic functional groups which are of much biological importance. In the year of 1912 after various investigations and analysis German chemist Alfred Stock synthesized the first hydrogen and boron-based compounds that are Boranes. Later on, in the sixties, the first carboranes were explained which were polyhedral clusters of boron and also incorporated carbon atoms in their structure. [2-4] Boranes remained primarily of academic interest until World War II. After that, the study of the boranes and carboranes has become one of the most rapidly increasing areas of inorganic research. William N Lipscomb received the Nobel Prize in the year 1976 for Chemistry for his studies on the structure of boranes illuminating the problems of chemical bonding. [5] He also demonstrated that polyhedral boron clusters could be described as species with occupied orbitals and multicentric bonds in different resonant forms. [6] In this way boranes were no longer considered electron deficient and were soon termed as superatomics. [7-8] More recently,

they have been demonstrated by Teixidor, Sola and Co. that they are simply aromatic, obeying the Huckel's rule. [9,10] Herbert Charles Brown also received the Nobel Prize in Chemistry in the year 1979 for discovering the great reducing effect of BH units over unsaturated organic compounds. [11] As a result of this nowadays boron hydrides have an important influence on the organic syntheses. [12-14]

1.1. Carboranes

In recent years it has been considered that the boron cluster chemistry acts like a bridge between organic, inorganic and organometallic chemistry with vivid influences in the fields of theoretical chemistry, medicines and polymers. It has been established by Teixidor, Sola and Co. a link between the hydrocarbon and borohydride chemistries by showing that hydrocarbons and borohydrides have a common root regulated by the number of valence electrons in a confined space. They have also established further by applying the electronic confined space analogy (ECSA) method to bridge fundamental aromatic hydrocarbons and the analogous closo BH clusters.[9,15] Boranes are boron clusters which are either anionic or neutral in nature. They are formed by triangular faced polyhedra which contains at each vertex a B-H unit. These vertices when substituted by heteroatoms give rise to the family of heteroboranes. Amongst these heteroboranes, carboranes also known as carbaboranes are the most studied ones, having at least one atom of boron being replaced by an atom of carbon.

The empiric formula of these compounds is:
[CnBmHn+m+p] x-= [(CH) n (BH) mHp] x
Where n – number of C atoms within the vertices of the cluster
m – Number of B atoms within the cluster and
p – Number of bridging H (bridge H)

The clusters of boranes and carboranes are consistent with some electronic requirements which were studied in detail

by Wade, and are famously known as the Wade rules. [16 -19] Using these rules one can determine a tridimensional structure starting from the number of occupied vertices and also on the number of electron pairs required to form the cluster skeleton. If we consider n to be the number of polyhedral vertices and if the number of electron pairs maintaining the cluster together is n+1, then the compound has a closo structure, if this becomes n+2 then the compounds are nido whereas if it is n+3 the compounds become arachno. One vertex made up by a B-H unit gives two electrons to the cluster from the boron atom and in the same way if one vertex consists of a C-H unit the carbon will give three electrons to the cluster. Respectively the bridge hydrogen would only give one electron. Different classes of carboranes are listed below.

- *Closo Boranes-* (from Greek Clovos, a Cage). They have complete, closed polyhedral clusters of n boron atoms; they need 2n+2 electrons to maintain the cohesion of the cluster.

- *Nido Boranes-* (from Latin nidus, a Nest). They have non closed structures obtained from the loss of one vertex of the corresponding closo cluster; they require 2n+4 electrons to maintain the cohesion of the cluster.

- *Arachno Boranes-* (from Greek Arachne, a Spider´s web). They have even more open clusters, obtained from the loss of two vertices of the corresponding closo cluster. They require 2n+6 electrons to maintain the cohesion of the cluster.

- *Hypo Boranes-* (from Greek, hyphe, a Net). They have the most open clusters, obtained from the loss of three vertices of the corresponding closo cluster; they require 2n+8 electrons to maintain the cohesion of the cluster.

- *Conjuncto Boranes-* (from Latin conjuncto, Join together). They have structures formed by linking two (or more) of the preceding types of cluster.

ortho-, meta- and para-Carborane: The most known group amongst all the carboranes is the group of the icosahedric clusters which possesses two carbon atoms, named dicarba-closo-dodecarboranes which has the empirical formula of $C_2B_{10}H_{12}$. Among these the 1, 2-dicarba-closo-dodecarborane and 1,7-dicarba-closo-dodecarborane are known as the *ortho*-carborane and *meta*-carborane respectively. *Ortho*-carborane has the two carbon atoms in the adjacent positions while in the meta-isomer two carbon atom are separated by one boron.). Upon heating at 420°C, the *ortho*-carborane rearranges to the *meta*-isomer. Upon further heating, one obtains *para*-carborane. *Ortho*- and *meta*-isomeric forms have been used in this doctoral thesis.

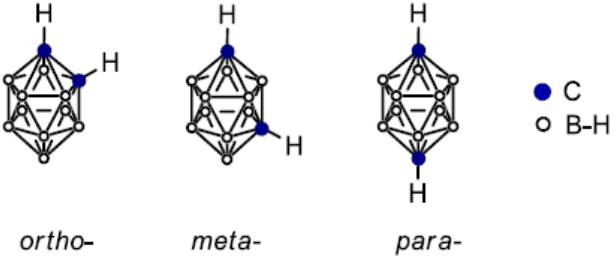

Figure 1: The three isomers of icosahedral dicarba-closo-dodecarboranes ($C_2B_{10}H_{12}$)

Chemical Reactivity of Carboranes: Although *ortho*- and *meta*-carborane clusters are remarkably stable, in certain reaction conditions they exhibit high synthetic reactivity. From an electrophilic substitution point of view, at the C_c-H vertices (C_c: carbon atom belonging to carborane cluster), both isomers display similar chemical reactivity. In both carborane isomers, the hydrogen atoms of the C_c-H units are more acidic than the ones at B-H vertices, due to more electronegative character of carbon with respect to boron (2.5 and 2.0 respectively, according to Pauling scale). Thus, hydrogen atoms attached to carbon can be considered as acidic while those bonded to boron as hydride. The acidity

of the C_c-H vertices decreases in the order of *ortho*-, *meta*- and *para*-carborane. In the same order, its vulnerability to get deprotonated decreases too.

This relatively acidic character of C_c-H units allows their deprotonation by strong alkali and alkaline earth metal bases, like for example *n*-butyllithium or Grignard reagents. The generated negative charge on the carbon atom of the cluster, C_c, attracts electrophilic reagents, opening the way to the introduction of functional groups at the C_c position of the cluster.

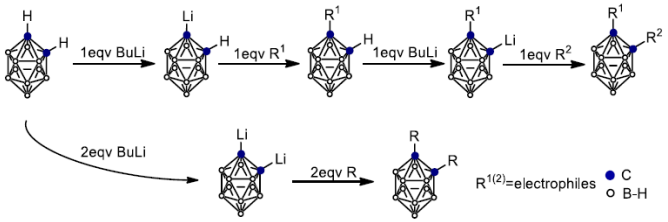

Figure 2: Deprotonation reaction of C_c-H units followed by substitution with electrophilic agents.[20]

Figure 2 shows the two possible pathways for substitutions at one or both of the Cc atoms. After di-lithiation of the carborane cluster it is possible to introduce simultaneously twice the same substituent, which leads to symmetrically substituted carborane. The other pathway (top) demonstrates mono-substitution of the carborane cluster or the unsymmetrical di-substitution. The synthesis of mono-substituted carborane derivatives is more complicated compared to di-substituted. The reason is the disproportionation of Li[1,2-$C_2B_{10}H_{11}$] into Li2[1,2-$C_2B_{10}H_{10}$] and 1,2-$C_2B_{10}H_{12}$ how it was found for *ortho*-carborane.[21] Several approaches have been developed to overcome this problem. Among them is using the way of protection/deprotection methodologies with dimethoxyethane as the solvent or by doing the reaction at

high dilution. [22-24] Perhaps more simple method is carrying the mono-substitution reactions in ethereal solvents at low temperature and specific carborane concentration. It was suggested that depending on type of electrophile it is possible to find combination of conditions (ethereal solvent, temperature, carborane concentration) that facilitate the largest degree of mono-substitution. [25] By using the substitution process, thiol groups and phosphinic groups have been added to the carbons of the carborane cluster helping to obtain carboranyl phosphinic acids[26] and mercaptocarboranes.[22] These ligands have been used in this doctoral thesis to cap quantum dots and have enabled us to obtain new luminescence properties in them. They have helped us to design a new architecture for quantum dots called Core-Canopy QDs. They are individually discussed in the related chapters.

1.2. Metallacarboranes

The *closo ortho*-$C_2B_{10}H_{12}$ goes to partial deboronation under nucleophilic conditions reaction. The nucleophilic attack is produced selectively over one of the boron atoms that are directly bonded to the cluster carbons, because these boron atoms, either B(3) or B(6), are the ones most electronically impoverished (Figure 3). The partial deboronation reaction leads to the anionic *nido* cluster [7,8-*nido*-$C_2B_9H_{12}$]-. This species has formally lost one B^+ fragment with respect to its *closo* precursor, allowing the formation of a cluster bearing one open pentagonal face, C_2B_3, where its remaining hydrogen is still present; this resultant *nido* cluster is a monoanionic species, as presented in Figure 3. X-ray diffraction studies show that this H_{bridge} is more bonded to B(10) than to B(9) or B(11) and that it maintains itself equidistant to these last two.[27-28] In the [7,8-*nido*-$C_2B_9H_{11}]^{2-}$ ion, the metal may be considered to be η^5-bonded to the open C_2B_3 pentagonal face of an icosahedral fragment, as in the case of the formation of ferrocene from $C_5H_5^-$. In so doing the metal simultaneously completes two icosahedra.

In 1965 the first metallacarboranes, [3,3-Fe(1,2-$C_2B_9H_{11})_2]^{n-}$ (n = 1, 2), were reported. [29] Recently, it has been reported by C. Vinas and Co. a green, quick synthetic method with high throughput.[30] It requires no solvent and this finding shall facilitate the research on these species.

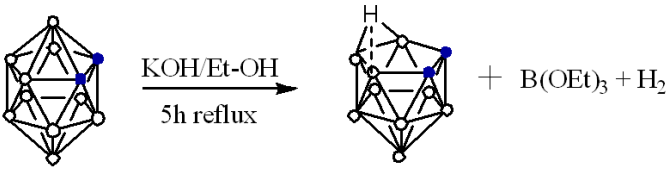

Figure 3: *ortho*-carborane partial deboronation reaction

The cobaltabis(dicarbollide) [3,3'-Co(1,2-$C_2B_9H_{11})_2$, was synthesized in 1965 (Figure 4).[31] This anion has a great chemical stability, high molecular volume, low nucleophilic character and low charge density because the negative charge is distributed between 45 atoms.16 This has been used in this doctoral thesis to form complexes with magnetic nanoparticles and magnetic nanocomposites. When the metal is replaced with iron instead of cobalt it is called ferrabis(dicarbollide).

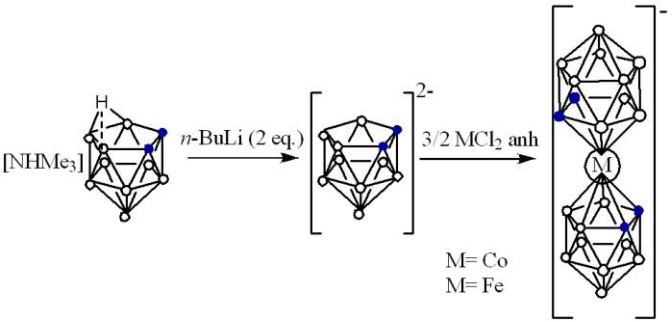

Figure 4: General Synthesis of Metallacarboranes. When the metal is Cobalt then it is called Cobaltabis(dicarbollide) and when it is Iron then it is called Ferrabis(dicarbollide).

The derivative chemistry of the cobaltabis(dicarbollide) remains very much unexplored.[32-33] Teixidor and Olid have done a comprehensive revision on the methods to produce the B-C, B-P, B-N and B-S bonds of the boron clusters. [34]

The fundamental reason is the lack of a comprehensive synthetic strategy leading to these derivatives. As for the $C_2B_{10}H_{12}$ carborane compounds, substitutions may occur on [3,3' Co(1,2-$C_2B_9H_{11})_2$]$^-$, either on carbon or on boron. Further structural details of cobaltabis(dicarbollide) has been given in the chapter 5 of the thesis, which deals with it forming a complex in magnetic nanoparticles and nanocomposites.

1.3. Applications

The currently claimed applications for boron clusters compounds are based either on the unique properties of the molecules or on specific properties of the basic element itself such as: the extreme acidity of acids conjugated to the polyhedral ions combined with a unique hydrophobicity of these anions, the exceptional stability of the polyhedral species due to their aromaticity and the unexpected ability to nearly all open-cage clusters to form sandwich metallic complexes. Some of the applications of the boron clusters are listed below.

- *Radionuclides Extraction*

Boron clusters can be successfully applied in the selective extraction of nuclear residues like radionuclides. The sandwich-type anion, [3,3'-Co($C_2B_9H_{11})_2$]$^-$, shows high stability in an acidic medium, in which the radioactive cations that are to be extracted is found. This was the first compound to be used with such purposes. [35-42] Moreover the high solubility of this anion in organic solvents makes it easily extractible from aqueous phases. Also, it has high chemical and thermal stability as well as resistance to radiation. All these factors make the cobaltbis(dicarbollide) anion as an ideal extracting agent for metallic ions, found in residual waters.

- *Homogeneous Catalysis*

Ruthenium and Rhodium based carboranes have been widely used in homogeneous catalysis in a variety of

reactions, such as terminal[43-47] and internal[48] alkenes' hydrogenation[49,50],hydrosililation[51-56], cyclopropanation[57-60] and Kharash CCl_4 addition reactions to olefins.[61]

- *Smart Materials*

In conducting organic polymers also boron clusters can be used as doping agents due to their low charge density, which improves the stability and in particular, their resistance to over oxidation.[62, 63]

- *Medicine*

The special feature of the Boranes and Carboranes is their biocompatibility.[64] These are mostly artificially synthesized compounds and therefore neither are recognized nor metabolized by the living organisms and hence displaying very low toxicity. Moreover, some iron based metallacarboranes having $[MeC_3B_7H_9]^-$ units have shown cytotoxic properties on different tumour cell lines.[65] Also some recent studies have proven that some cobaltabis(dicarbollide) derivatives can act as potent specific inhibitors of protease HIV-1. [66]

- *Boron Neutron Capture Therapy (BNCT):* Neutron Capture Therapy (NCT) is a bimodal therapy that utilizes a neutron source to generate an internal destroying radiation in tumour cells that leads to their death. As opposed to conventional radiation therapy using X rays or ɣ rays where an external radiation source is required, a big advantage of NCT is that the surrounding healthy tissue is not exposed to the radiation that can be a big issue in treatment of tumours in deep parts of the body. Thus, NCT requires the use of an isotope with high neutron capture cross section. The "organic" elements such as C, H, O, N have very low neutron capture cross section (< 2 barn). In contrast, isotopes of other elements such as boron and gadolinium, ^{10}B and ^{157}Gd, are good at absorbing neutrons (capture cross section for ^{10}B is 3840 barn, for ^{157}Gd- 25400 barn). Also, ^{10}B isotope was an attractive element due to its high natural

abundance of 20%. ^{157}Gd isotope also has a natural abundance of 15.7% that can be effective to capture neutrons. Up to now GdNCT has never been used clinically (i.e., in humans), the reason being the toxicity concern of gadolinium. On the other hand, over 900 patients have already undergone Boron Neutron Capture Therapy (BNCT), worldwide and effects of BNCT on malignant tumours and healthy surrounding tissue seemed to be established. [67]

The history of BNCT started in 1932 since the discovery of the neutron by Chadwick,[68] followed by Locher´s proposal to use neutron capture reactions in cancer treatment.[69] BNCT technique consists of two steps: the selective delivery of ^{10}B-containing agents to tumour cells followed by their irradiation with low-energy neutrons, which results into the prompt nuclear reaction. The predominant products of this reaction are ^{7}Li nuclei and high linear energy transfer (LET) α particles. LET particles are lethal but their effect is concentrated mostly inside of host cells due to their short path length in tissues (4.5-10μm).

a.

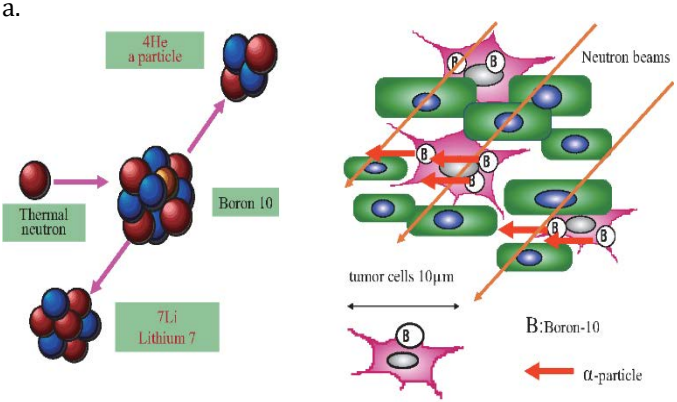

b.

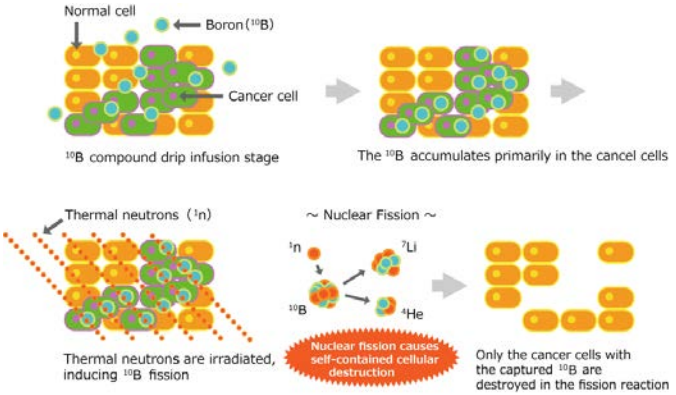

Figure 5: (a)The schematic representation of BNCT in glioblastoma cells [70]. (b) Only the cancer cells are destroyed in BNCT. One of the constituents of natural boron, known as boron-10 (or ^{10}B), is irradiated with low-energy thermal neutrons, yielding high linear energy transfer alpha particles and recoiling lithium-7 (or ^{7}Li) nuclei. These biochemical interactions are known as nuclear capture and fission reactions. Tumour cells absorb much more ^{10}B boron than normal cells. For example, malignant brain cells may take in seven times as much ^{10}B as normal cells. As a result, the fission reaction process destroys only cancer cells. [ref]

Research in the area of development of boron-containing delivery agents for BNCT started ~60 years ago with the investigation of a large number of boron compounds, that were regarded as "first-generation" agents for BNCT.[71] The most important requirements for a BNCT delivery agent are: i) low toxicity, ii) water solubility, iii) good tumour-cell selectivity, with a tumour: normal tissue and tumour: blood ratios higher than 3, iv) be deliverable at around 20 μg ^{10}B/g (tumour tissue), v) persistence in tumour cells during the course of neutron irradiation, vi) capacity to penetrate biological barriers such as the blood-brain barrier (BBB).
So far, clinically for the treatment of patients with malignant brain tumours and malignant melanoma has been used two main boron delivery agents: sodium borocaptate, $Na_2B_{12}H_{11}SH$ (BSH), and boronophenylalanine (BPA) which formulas are displayed in the Figure 6.

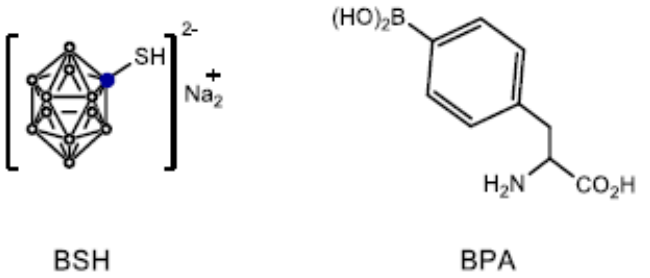

BSH BPA

Figure 6: The chemical structure of the boron compounds used in BNCT clinical trials.

During the last 20 years a big number of boron delivery agents have appeared using different approaches. Among them are derivatives of biological molecules (amino acids, nucleic acids, peptides, DNA-binding molecules), porphyrin derivatives, nano-vehicles (liposomes), dendrimers. Also, other delivery systems such as nanoparticles are currently under research. Hosmane et al. attempted to use magnetic nanoparticles for boron delivery into tumour cells.[72] BNCT has been explored with the magnetic nanoparticles coated with m-carboranyl phosphinic acid (1-MNPs) in this doctoral thesis and is dealt with it in chapter 4. These new nano-hybrids have been tested for BNCT for cancer therapy.

2. Nanoparticles

The Nanoparticles (NPs) are tiny particles which have their dimensions within the nanoscale range. The general definition for nanoscale range is from 1-1000nm, but for NPs or nanomaterials (NMs), this is usually considered to be from 1-100nm. The nanoparticles are characterized into various classes depending on their properties, shape and composition etc. [73] The huge interest related to them has arisen due to the unique properties represented by these materials in lieu of the small dimensions. The properties shown by these particles vary greatly than showed by the

same materials in their bulk counterparts owing to the greater surface to volume ratio that they possess. NPs have different shapes like spheres, rods, tetra-pods, wires, belts, rings disks etc. which helps in achieving further interesting results in their properties. Depending on the overall shape these materials can be 0D, 1D, 2D or 3D. This classification is highly dependent on the electron movement along the dimensions in the NMs. [74] For example, electrons in 0D NMs are entrapped in a dimensionless space whereas as 1D NMs have electrons that can move along the *x*-axis, which is less than 100 nm. Likewise, 2D and 3D NMs have electron movement along the *x*–*y*-axis, and *x*, *y*, *z*-axis respectively. The importance of these materials were realized when researchers found that their size can influence the physiochemical properties of a substance e.g. the optical properties. The various categories of NPs or NMs are listed below:

- *Carbon Based Nanomaterials:* These are NMs which contain carbon in them and can be found in different shapes like in forms of tubes, spheres or ellipsoids etc. The most common ones are Carbon nanotubes (CNTs), Graphene sheets (Gr), Carbon nanofibers, Carbon onions and Fullerenes (C_{60}).
- *Inorganic Nanoparticles:* The inorganic NPs are the ones which usually consist of metal, metal oxides, semiconductors or ceramic based particles within the nanoscale.
- *Organic based Nanoparticles:* These NPs are made mostly from organic matter. They are usually the dendrimers, liposomes, micelles or polymeric NPs.
- *Composite Nanomaterials:* Composite NMs are multiphase NPs and NMs with one phase in the nanoscale dimension that can either combine NPs with other NPs or NPs combined with larger or with bulk-type materials (e.g., hybrid nanofibers) or more complicated structures, such as a metal-organic frameworks (MOFs). The composites may be any combinations of carbon-based, metal-based, or organic-based NMs with any form of metal, ceramic, or polymer bulk materials. [75]

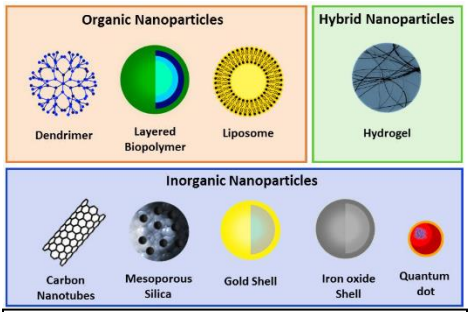

Figure 7: Different kinds of nanoparticles

Out of all the types of NPs and NMs mentioned above, the focus in this thesis has been mostly on semiconductor NPs which show unique optical properties in nano-dimension, metal oxide particles of Iron oxide which show superparamagnetic properties in nano scale. Also, CNTs which are carbon-based NPs, have been used in forming magnetic nanocomposites and semiconductor NPs have also been used with polymers to form nanocomposite films in this doctoral thesis. The science of nanoscale semiconductor materials, semiconductor NPs, science of nanoscale magnetic materials, magnetic NPs and CNTs are discussed in the next sections.

3. Nanoscience of Semiconductors

Semiconductors (SCs) are materials which have a band gap consisting of the valence band and the conduction band. The SCs are usually belonging to the II-VI or III-V group in the periodic table. They show drastic change in their chemical and physical properties when their size is reduced. To understand this change in their properties in nano-dimension we need a brief overview of the physics of semiconductors.

Physics of Semiconductors: Electrons are confined to a number of bands of energy, and forbidden from other regions. The term "band gap" refers to the energy difference

between the top of the valence band and the bottom of the conduction band; electrons are able to jump from one band to another. In order for an electron to jump from a valence band to a conduction band, it requires a specific amount of energy for the transition. The required energy differs with different materials. The conductivity of intrinsic semiconductors is strongly dependent on this band gap. The only available carriers for conduction are the electrons which have to have enough thermal energy to be excited across the band gap in order to make the SCs conductive. The band gap is formed due to atomic orbitals which are discrete set of energy levels. When several atoms are brought together to form a molecule, their atomic orbitals split. Similarly, when a greater number of atoms like the order of 10^{20} or more are brought together to form a solid, the number of atomic orbitals become increasingly large and therefore the energy levels do not remain discrete but become continuous as the difference in the energies between them become smaller. However, some intervals of energy contain no orbitals, no matter how many atoms are aggregated, forming *band gaps*. This is the bulk state of the SCs, in which the energy levels of the band gap are a continuum. This changes when the size of the SCs start to decrease. It is described below:

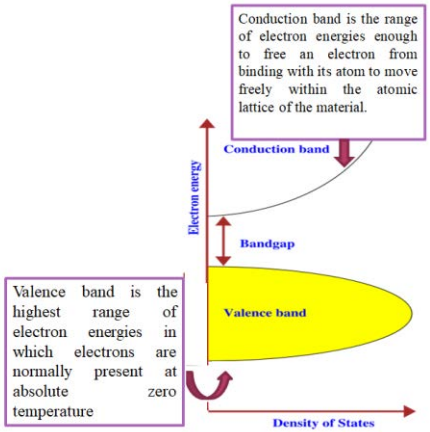

Figure 8: Valence and Conduction band in Semiconductors.

✓ If the size of a semiconductor crystal becomes small enough that it approaches the size of the material's Exciton Bohr Radius, the electron energy levels can no longer be treated as continuous but treated as discrete, namely there is a small and finite separation between energy levels.

✓ This situation of discrete energy levels is called ***quantum confinement***. [76]

✓ **Bohr radius:** It is a physical constant which states that the most probable distance between the proton and electron in a hydrogen atom in its ground state. [77]

✓ **Exciton:** A bound state of an electron and hole which are attracted to each other by the electrostatic coulomb force: Electron-hole pair. An exciton can form when a photon is absorbed by a semiconductor. This excites an electron from the valence band into the conduction band, thus leaving a hole in valence band. This hole and the electron bound pair forms the exciton.

If the semiconductor particle size approaches the Bohr Exciton radius and is either close to it, equal to it or less than it then the quantum confinement effect is shown by these semiconductor NPs. Weak quantum confinement effect is shown by the semiconductor NPs when their size is farther from the Bohr Exciton radius value. The farther it is from the Bohr Exciton radius the lesser is the quantum confinement effect. On the contrary the closer the size of the particle is to the Bohr exciton radius, the stronger the effectt of the quantum confinement. [78] The Bohr Exciton radius of the CdSe is 5.4nm, hence the size of CdSe NPs equal to this value or lesser than this (for example 1-2nm) show strong quantum confinement effects. This is why it is extremely important to control the size of the semiconductor NPs.

On understanding this underlying concepts, one can understand why semiconductor nanoparticles are so

unique and have captivated researchers for the last two decades.

3.1. Semiconductor Nanoparticles

The semiconductor NPs are semiconductor materials having dimensions in the nano scale. As we have already familiarised about the nanoscience of semiconductor materials, the semiconductors which have a size range which falls within the quantum confinement region show quantum effect. These particles or materials are called quantum dots (QDs), quantum rods (QRods) or quantum rings (QRs) depending on their geometry. Each of them has at least 1-dimension in the quantum regime in order to show the quantum confinement effect in them. The most studied among these is QDs which are confined on all 3 dimensions and allow us to study 0D quantum structures. After them QRods are the second most studied and allow us to study 1D quantum structures as they are confined in only two direction which is their cross section. The least studied among them are the QRs as they are difficult to synthesize. The quantum confinement effect allows these particles to have a tuneable bandgap and in essence tuneable emission properties. This is because the electron in the valence band is excited by the absorption of a photon, and it goes to the conduction band forming a hole. Then it relaxes back to combine with the hole, and this recombination can be radiative that is by emitting a photon (light energy) or non-radiative recombination in which the energy of the electron is converted to a phonon or thermal energy due to lattice vibrations. [79] Therefore, when the size of the band gap changes, the energy to be emitted changes and hence the emission colour changes. Hence, according to the size of QDs, the band gap energy is altered and hence we have – ***a tunable bandgap!*** This is possible as long as the size of the dot is close to or below the Exciton Bohr Radius, as the size increases the band gap decreases and vice versa.

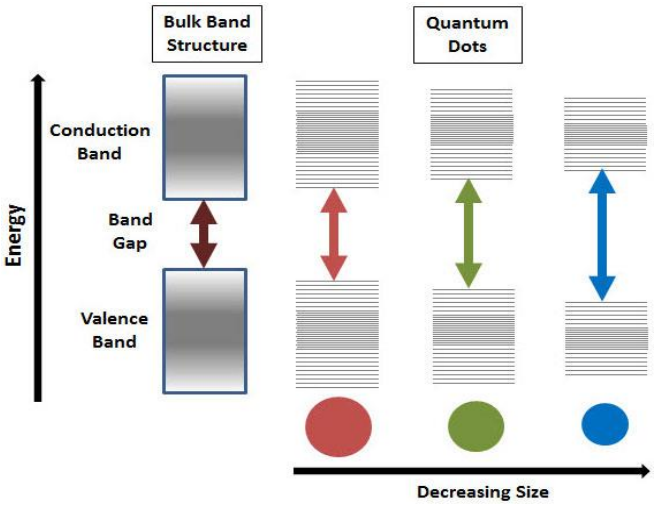

Figure 9: Tuneable band gap of the semiconductor nanoparticles when the size is closer or below the Bohr exciton radius. [80]

The size of the bandgap is controlled simply by adjusting the size of the dot. Because the emission frequency of a dot is dependent on the bandgap, it is therefore possible to control the output wavelength of a dot or by that matter of a QRod or QR. Smaller the dot, they fluoresce more in the blue region while larger the dot, they fluoresce in the red region. The most common QDs are CdS, CdSe, ZnS, ZnSe, PbS, PbTe, CdTe in the group of II-VI while for the group III-V, they are GaP, GaAs, GaSb, InP, InAs, InSb, AlSb etc. They usually consist of a core which is the primary

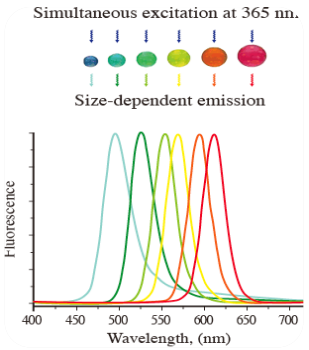

Figure 10: Colour of emission dependant on the size of the QDs [81]

semiconductor material, then a shell which can either be capping ligands or another semiconductor layer. They can be synthesized chemically in colloidal form or by physical methods. [82-84] In colloidal synthesis they can be either done in an aqueous medium or in an organic medium. In this doctoral thesis the choice of semiconductor material has been CdSe and the medium of synthesis is aqueous. More detailed information about the advantage of this synthesis route, ligands used and about CdSe is described in the chapter 1. The introduction to QD, QRod, QRs are dealt with in their respective chapters. The emphasis is laid mostly on the optical properties of these quantum nanocrystals (QNCs) over here as it has been most extensively studied in this thesis. Other properties like conductivity of these QNCs are not dealt with in this doctoral thesis.

3.2. Applications

The applications of Quantum Nanocrystals (QNCs) are many. Out of which few are listed here: Optoelectronic sensors and Chemosensing, Photovoltaic devices, Catalytic activities, Hydrogen production, Bioimaging and targeted drug delivery, Quantum light emitting diodes (QLEDs), Thin film transistors, QD Lasers, Nanoelectronics etc. [85] The research in this field is still going on to obtain more and more applications by manipulating the various aspects of these QNCs.

4. Nanoscience of Magnetism

Magnetism is a physical phenomenon which is mediated by magnetic fields. The base of magnetism lies in two important characteristics of electrons, they are the orbital movement of the electron around the atomic nucleus and the movement of the electron spin around its axis. The association of orbital and

spin magnetic moments together makes an electron to behave like a tiny magnet. Magnetization is the sum of all magnetic moments (m) of the atoms in a material per unit volume (V), M= m/V (emu/cm^3). Though for practical reasons, magnetization (M) is often referred in unit mass and expressed as emu/g.

Materials respond differently to the external magnetic field and they are categorised based on their responses into diamagnetic, paramagnetic, ferromagnetic, antiferromagnetic and ferrimagnetic materials. [86-88] Out of these materials, diamagnets are repelled by a magnetic field while paramagnets are weakly attracted by them. On the other hand, ferromagnets have a strong net magnetization when in presence of an external magnetic field and also retains partial magnetisation when the magnetic field is removed as opposed to paramagnets.

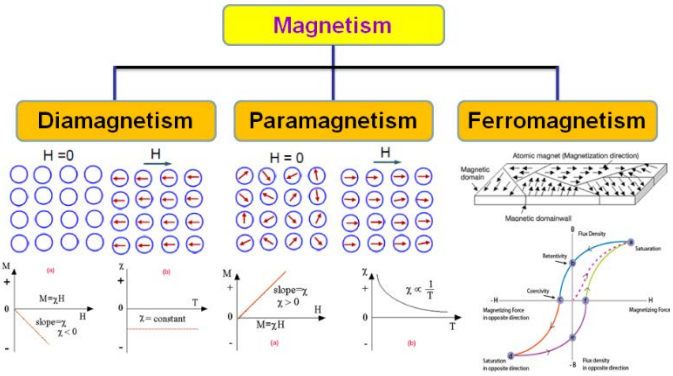

Figure 11: It shows the diamagnetism, paramagnetism and ferromagnetism. Ferromagnetic materials have a hysteresis cycle when applied with a magnetic field as they retain the magnetic property even when the applied magnetic field is removed.

Antiferromagnets show zero magnetization in the presence of a magnetic field due to opposing magnetic moments of atoms, similarly, ferrimagnets have opposing moments too but, in their case, the opposing moments are unequal and they possess some magnetization. Ferromagnetic materials have several domains but when the size reduces below a critical value, then the materials compose of a single domain and this exposes the size dependence properties of ferromagnetic materials. For single domain ferromagnetic materials, their magnetic energy is comparable to their thermal energy. Thus, when the size of the particles reduces below the size of single domain, their thermal energies overcome their magnetic energy and hence the magnetization vector of single domain particles can be reversed spontaneously. This makes the particles superparamagnetic. [86]

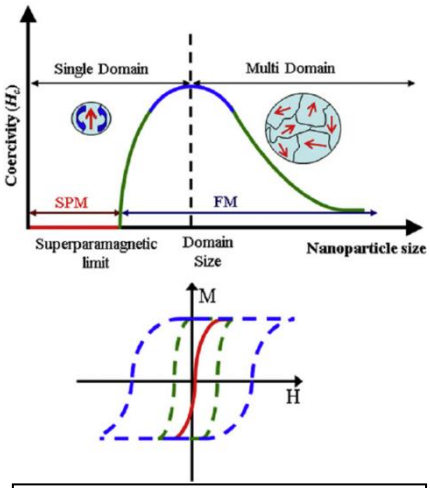

Figure 12: Size dependence of domains. Beyond a certain critical size, the domains in the ferromagnetic material becomes one, thus nanoparticles have single domains.

Nano scale magnets which have at least one dimension in nano range possess this super-paramagnetism. The size dependant magnetic properties like super-paramagnetism, remanence enhancement, exchange averaging of anisotropy and giant magnetoresistance all come to fore when the size drops to nanoscale. [89-90] Temperature plays

a major role in superparamagnetism of nanoparticles, as below a certain temperature the particles lose their superparamagnetic properties. This temperature is characterized as the Blocking Temperature (T_B). Above the blocking temperature they become paramagnetic in nature. [91] Normally, ferromagnetic materials have a hysteresis loop which graphs the response of these particles under the influence of magnetic field. It has two distinct parameters, The remanence (M_R) and coercivity (H_c). These parameters no longer exist when the particles become superparamagnetic as they do not have the hysteresis loop anymore. This size dependency of magnetism opens up a new avenue for research. The changed magnetic properties at nanoscale dimension has garnered a lot of attention for the past two decades in every field of research as these materials carry nanoparticles which exhibit superpramagnetism. A chief characteristic of the superparamagnetism is that it operates at the nanoscale and it arises due to spin-based momentum of the unpaired electrons present in a material. To add to this, superparamgnetism is characterized by the presence of single magnetic domains in the material concerned, i.e. the magnetization induced in a material is same throughout across a material in the presence of an external magnetic field. [90] Among all nanoscale magnetic materials, magnetite nanoparticles (Fe_3O_4 NPs) grab special attention at the

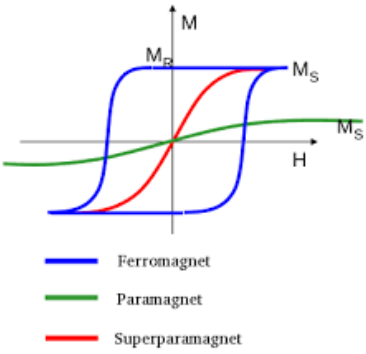

Figure 13: Hysteresis curves of ferromagnets, paramagnets and superparamagnets.

behest of their enhanced magnetic property among all other naturally occurring magnetic materials. They are used in this doctoral thesis to form nano hybrids for cancer therapy which is discussed in chapter 4. Chapter 5 deals with magnetite nanoparticles being functionalized using different moieties, forming composites with CNTs and also a new complex with H[Cosan] or cobaltabis(dicarbollide).

4.1. Magnetic Nanoparticles

Magnetite (Fe_3O_4 NPs), Maghemite (ɣ-Fe_2O_3) and Hematite (α-Fe_2O_3) are the most common magnetic materials which are extensively studied in nano-dimension. They are often referred to as SPIONs (Super Paramagnetic Iron Oxide Nanoparticles) as they show superparamagnetic properties due to their size. Though they have been used in a variegated field, their usage has been lemmatized due to their tendency to get oxidized and also get agglomerated. In order to overcome this, these MNPs are usually coated with a layer of material thus giving us a core shell structure of MNPs. This shell not only helps in stabilizing the MNPs by reducing their oxidation, but also, they provide for a platform for further functionalization of the MNPs. [92-93] The most commonly used shells are of metal oxides, inorganic materials and polymers of different types. [94-96] They are also used with graphene and carbon nanotubes (CNTs) to form nanocomposites which are used in applications like sensing. These nanocomposites help in attaining hybrid materials having superior properties owing to the superparamagnetic abilities of the MNPs coupled with high conductivity, thermal and mechanical properties of graphene or CNTs. These MNPs can also be further doped with other metals which can enhance their properties, thus improving their performance for the applications. But there are a few problems too when these particles are coated with various shell layers or made into nanocomposites. Sometimes, owing to the presence of too much modification of the magnetic core by the protective layers, the magnetic

properties of the core reduces and it does not remain as efficient as it should be. This is why there has been substantial focus towards developing synthetic routes to synthesize MNPs of different sizes, composition and morphology and to stabilize these particles in varying conditions for their successful applications in multiple fields. Commonly used MNPs are usually within the dimension of 5-20nm as magnetite and maghemite usually have single domains within this size range, but the size requirement does considerably depend upon the applications for which they have to be used. Recent studies on larger nanoparticles in the form of magnetic nanorods or larger spherical ones have garnered quite an interest for their larger magnetization properties. The magnetic nanorods are of special interest as they have one larger dimension while the other two dimensions are in the nano-range. [97-98] They preserve the properties of the superparamagnetism coupling the need of larger magnetic materials for certain applications like for enhanced data storage or plasmonics. More detailed description about the synthetic routes used for MNPs, the coatings done on their core and their use in biological applications are described in chapter 4. A few of the common applications are listed in the next section.

4.2. Applications

There are many applications of the magnetic nanoparticles but few are mentioned here. The most important ones are its use in biomedical field of drug delivery, magnetic resonance imaging, also used immensely in biosensing, catalysis, memory storage devices, energy storage and capacitance or for environmental purposes like waste water cleaning etc. [99-105]

5. Carbon Nanotubes (CNTs)

CNTs, also called buckytubes, are cylindrical carbon molecules with unique properties that make them potentially useful in a wide variety of applications. CNTs exhibit extraordinary strength as well as unique electrical, mechanical and thermal properties. CNTs are the members of the fullerene family, which was discovered by Kroto et al. [106] in 1985. Buckyballs are spherical fullerenes, whereas CNTs are cylindrical, with at least one end typically capped with a hemisphere with the buckyball structure. The name CNT derives from the size, as the diameter of a nanotube is on the order of a few nanometers. Iijima [107] first synthesized multi-walled carbon nanotubes (MWNTs) in 1991 using a simple arc-evaporation method. However, CNTs were discovered long before researchers even imagined that carbon may exist in such a diverse allotropic form. In 1952, Radushkevich and Lukyanovich [108] reported the discovery of "worm-like" carbon formations. These were observed during their study of the soot formed by the decomposition of carbon monoxide (CO) on iron particles at 600°C. Though this was reported but it went unnoticed due to lack of information in the field of nanoscience at that time. The formation of CNTs can be explained by rolling up of graphene sheets. Ideally, it is enough to consider a perfect graphene sheet (graphene is a polyaromatic monoatomic layer consisting of sp^2-hybridized carbon atoms arranged in hexagons; genuine graphite consists of layers of this graphene) and to roll it into a cylinder, making sure that the hexagonal rings placed in contact join coherently. Then the tips of the tube are sealed by two caps, each cap being a hemi-fullerene of the appropriate diameter It is shown in the Figure 14.

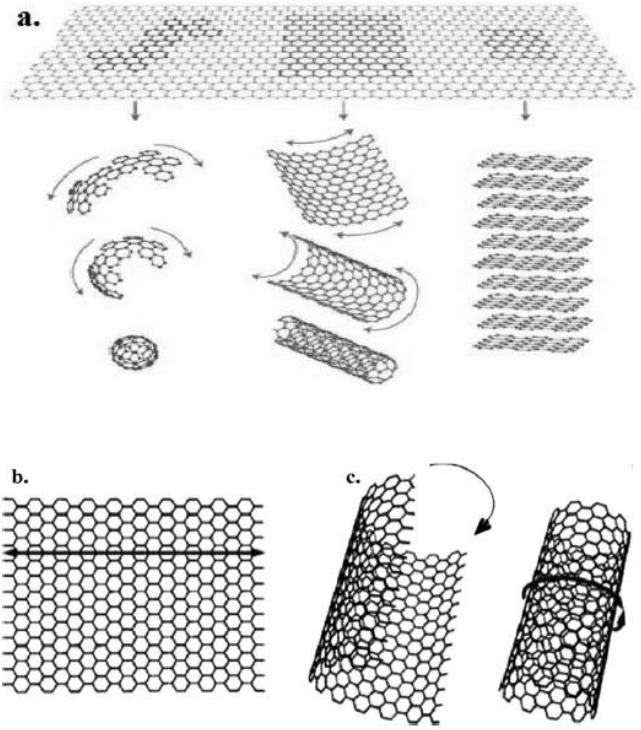

Figure 14: (a) Formation of Graphene derivatives, (b) Graphene sheet (c) Graphene sheet rolled into CNT. [ref]

Structure of CNTs: CNTs, also known as tubular fullerenes, are cylindrical graphene sheets of sp2-bonded carbon atoms. In CNTs the graphene sheet is rolled upon itself to form different allotropes of carbon, including graphite, fullerenes and CNTs. [109]

Different types of CNTs: CNTs can be divided into three categories on the basis of the number of tubes present in the CNTs. They are as follows:

- Single Walled CNTs (SWCNTs): Single-walled CNTs (SWCNTs) are made of a single graphene sheet rolled upon itself with a diameter of 1–2 nm. The length can vary depending on the preparation methods.
- Double Walled CNTs (DWCNTs): These nanotubes are made of two concentric carbon nanotubes in which the outer tube encloses the inner tube.
- Multi Walled CNTs (MWCNTs): MWNTs consist of multiple layers of graphene rolled upon itself with diameters ranging from 2 to 50 nm depending on the number of graphene tubes. These tubes have an approximate inter-layer distance of 0.34 nm. [110]

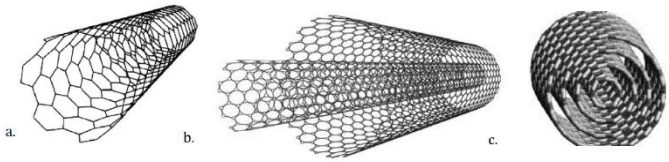

Figure 15: (a) SWCNT [111], (b) DWCNT [112] and (c) MWCNT. [113]

Common methods to synthesize CNTs are:

- Arc-Discharge method
- Laser Ablation
- Chemical Vapor Deposition
- Vapor Phase Growth
- Flame Synthesis method
- Nebulized Spray Pyrolysis Method

The CNTs after being synthesized can be functionalized either by non-covalent functionalization or by covalent functionalization.

Non-covalent functionalization: This type of functionalization is based on Van der Waal's forces. Beside these forces, hydrophobic or Pi-Pi interactions have also been reported. Non-covalent functionalization is important

and interesting because it does not damage or modify the CNTs structure to a great extent. It can be done by surfactant or polymer wrapping

Covalent Functionalization: In this type of functionalization, the desired groups are attached onto the sidewall or tips of the CNTs permanently in an irreversible manner. Various chemical groups such as carboxylic, p-aminobenzoic acid, fluorine, added dichloro-carbon groups are attached to the surface or at the ends of the CNTs. [114-117] The advantages of chemical functionalization are that it can be attached covalently with polymeric materials and dispersed well in different solvents. The main disadvantage of the chemical function is the production of defects on CNTs.

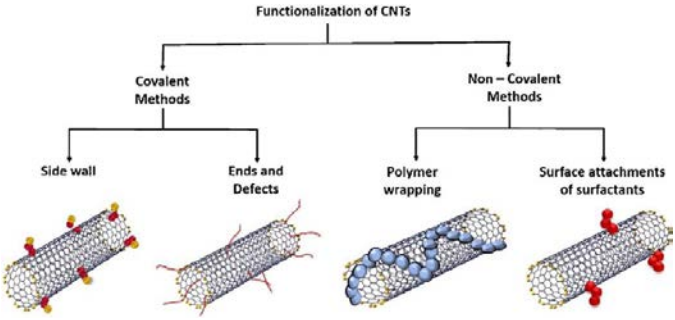

Figure 16: Types of functionalization of CNTs. [118]

In this doctoral thesis MWCNTs have been used to form composite with MNPs. Also, the type of functionalization done on the MWCNTs is covalent functionalization, by acid treatment COOH groups were generated to anchor the MNPs on them. The CNTs can be used for many applications which are given below in the next section. In this doctoral thesis the composites were made to be used in sensing applications by combining the conductivity of MWCNTs along with the magnetic properties of the MNPs.

5.1. Applications

CNTs are the most rapidly growing nanomaterials in the field of nanotechnology due to their various applications. Many investigators and researchers have dedicated much effort to the creation of novel properties and to expanding the number of novel applications in diverse fields, from materials science, medicine, electronics and energy storage, with many studies focusing on nanotechnology and the use of CNTs as fillers. [119] More attractive applications of CNTs can be achieved through the use of CNTs for applications that require conductivity and a high absorption capacity and for the creation of high-strength composites, fuel cells, energy conversion devices, field-emission devices, hydrogen storage devices, and semiconductor devices.[120-121] Wastewater treatment by CNTs is also a rapidly growing field for those who are interested in adsorption studies. [122] The major problem associated with CNTs is their high cost and non-renewable characteristic. At present, special efforts are in progress to develop certain preparation methods for CNTs which minimize their cost. The applications in gist are shown in the Figure 17.

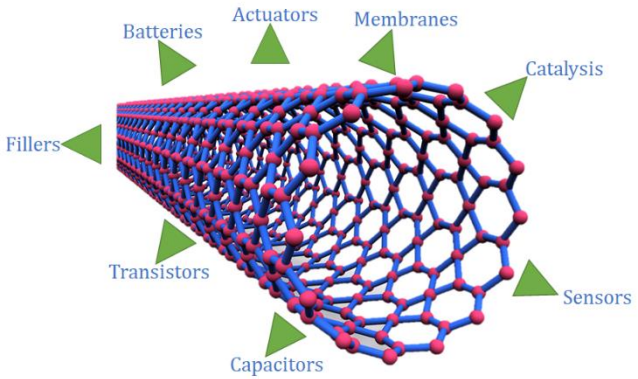

Figure 17: Some of the applications of CNTs.

6. References

1. W. G. Woods, *Environmental Health Perspectives*, **1994,** *102, 5.*
2. I. Shapiro, C. D. Good, R. E. Williams, *J. Am. Chem. Soc.,* **1962**, *84*, 3837.
3. R. N. Grimes, *Carboranes*, Academic Press New York, **1974**.
4. T. Onak, E. L Muetterties, Ed., Academic Press New York, **1973**, 349.
5. http://www.nobelprize.org/nobel_prizes/chemistry/laureates/1976/
6. N. W. Lipscomb, *Boron Hydrides*, Benjamin, New York, **1963**.
7. R. Hoffmann, W. N. Lipscomb, *J. Chem. Phys*., **1962**, *36*, 3489
8. Z. F. Chen, R. B. King, *Chem. Rev*.,**2005**, *105*, 3613.
9. J. Poater, M. Solà, C. Viñas and F. Teixidor, *Angew. Chemie - Int. Ed.*, **2014**, *53*, 12191.
10. J. Poater, M. Solà, C. Viñas and F. Teixidor, *Chem. - A Eur. J.*, **2016**, *22*, 7437.
11. H. C. Brown, *Science*, **1980**, *210*, 485.
12. H. C. Brown, H. I. Schlesinger, A. B. J. Burg, *J. Am. Chem. Soc*., **1939**, *61*, 673.
13. H. I. Schlesinger, H. C. Brown, H. R. Hoekstra, L. R. Rapp, *J. Am. Chem. Soc*., **1953**, *75*, 199.
14. K. P. C. Vollhardt, *Organic Chemistry*, W. H. Freeman and Co., New York, **1987**.
15. J. Poater, M. Solà, C. Vinas, F. Teixidor, *Chem. Eur. J*. **2013**, *19*, 4169.
16. R. N. Grimes, *Carbaboranes*, Academic Press New York, **1971**.
17. S. Papetti, T. L. Heying, *J. Am.Chem. Soc.,***1964**, *86*, 2295.
18. R. W. Rudolph, *Acc. Chem. Res*., **1976**, *9*, 446.
19. R. E. Williams, *Inorg. Chem.,* **1971**, *10*, 210.
20. Image reference
21. Elena Oleshkevich, PhD thesis, 2017.
22. R. N. Grimes, *Carboranes 2nd Edition*, Academic Press: Burlington, MA; Burlington, MA, **2011**.
23. F. A.Gomez, M. F. Hawthorne, *J. Org. Chem.* **1992**, *57, 1384*.
24. C. Vinas,et al., *J. Inorg. Chem.* **1995**, *34, 3844*.
25. J. F. Valliant, et al., *J. Coord. Chem. Rev.* **2002**, *232, 173*.
26. A. R. Popescu, et al., *Chem. - A Eur. J.* **2012**, *18*, *3174*.
27. E. Oleshkevich, et al,, Chem. Eur. J,, **2016,** *22, 3665*.
28. J. Buchanan, et al., *Dalton Trans*., **1990**, *677*.
29. X. L. R. Fontaine, et al., *Dalton Trans*., **1990**, *681*.
30. I. Bennour, et. al., *Green Chemistry,* **2019,** *21,* 1925.
31. M. F. Hawthorne, D. C. Young, P. A. Wegner, *J. Am. Chem. Soc.*, **1965**, *87*, *1818*.
32. I. B. Sivaev, V. I. Bregadze, *Collect. Czech. Chem. Commun.*, **1999**, *64*, *783*.
33. E. J. Juárez-Pérez, et al., *Eur. J. Inorg. Chem*., **2010**, *2385*.
34. D. Olid, et. al., *Chem. Soc. Rev.,* **2013,** *42,* 3318.
35. R. M. Chamberlin, et al., *Inorg. Chem*., **1997**, *36, 809*.
36. I. Rojo, et al., *Chem. Eur. J*., **2004**, *10*, *5376*.
37. E. J. Juárez-Pérez, et al., *Chem. Eur. J*., **2008**, *14*, *4924.*
38. E. J. Juárez-Pérez, et al., *J. Organomet. Chem*., **2009**, *694*, *1764*.

39. J. Plesek, et. al., *Collect. Czech. Chem. Commun.* **1984**, *49*, 2776.
40. J. Plesek, et. al., *Polyhedron,* **2002,** *21,* 975.
41. B. Gruner, et. al., *J. Organoet. Chem.,* **2009,** *694,* 1678.
42. C. Viñas, et al., *J. Organoet. Chem.,* **1999,** *1-2,* 188.
43. C. Viñas, et al., *Inorg. Chem.,***1997**, *36, 2482*.
44. C. Viñas, et al., *Chem. Commun*., **1998**, *191.*
45. C. Viñas, et al., *Inorg. Chem.*, **1998**, *37, 3640*.
46. C. Viñas, et al., *Dalton Trans.,* **1998**, *2849*.
47. C. Viñas, et al., *Inorg. Chem*., **1997**, *36, 2988.*
48. J. N. Francis, M. F. Hawthorne*, Inorg. Chem*., **1971**, *10, 594.*
49. F. Teixidor, et. al., *Angew. Chemie-Int. Ed.,* **1996,** *35*, 2251.
50. F. Teixidor, et. al., *J. Am. Chem. Soc.*, **2005,** *127,* 10158.
51. J. Plešek, et al., *Collect. Czech. Chem. Commun.,* **1976**, *41, 3509*.
52. Z. Janousek, et al., *Collect. Czech. Chem. Commun.,* **1981,** *46, 2818*.
53. I. Rojo, et al., *Chem. Eur. J.*, **2003,** *9, 4311*.
54. P. González-Cardoso, et al., *Chem. Eur. J.*, **2010**, *16, 6660*.
55. P. Farras, D. Olid, C. Viñas, F. Teixidor, *Eur. J. Inorg. Chem*., **2011**, *2525*.
56. D. Olid, C. Viñas, F. Teixidor, *Chem. Eur. J*., **2012,** *18, 12936*.
57. P. K. Hurlburt, et al., *Inorg. Chem*., **1995**, *34, 5215*.
58. L. Matel, et al., *Radiochem. Radioanal. Lett.*, **1978**, *35, 241*.
59. T. E. Paxson, et al., *J. Am. Chem. Soc.,* **1972**, *94, 4882*
60. J. C. Fanning, et al., *Polyhedron,* **1995,** *14, 2893.*
61. L. Matel, et al., *Polyhedron*, **1982**, *1, 511*.
62. R. Nunez, et. al., *Chem Soc. Rev.,* **2016,** *45,* 5147.
63. R. Nunez, et. al., *Chem Rev.,* **2016,** *116,* 14307.
64. I. Rojo, et al., *J. Am. Chem. Soc*., **2003**, *125, 14720*.
65. J. Plešek, et al., *Collect. Czech. Chem. Commun*., **1997**, *62, 47*.
66. P. Selucky, et al., *J. Radioanal. Nucl. Chem.,* **1991**, *149, 131*.
67. K. Nedunchezhian, et. al., *J Clin Diagn Res.,* **2016,** *10,* ZE01.
68. J. Chadwick, R. Proc. *Soc. London A Math. Phys. Eng. Sci.* **1932**, *136, 830*.
69. G.L. Locher. *Am J Roentgenol Radium Ther.* **1936**, *36, 1.*
70. T. Kagechi, et. al., *JMI,* **2014,** *61*, DOI:10.2152/jmi.61.254.
71. M. F. Hawthorne, Maderna, A. 1999.
72. Y. Zhu, et al., *J. Nanomater*. **2010**, *2010, 1*.
73. United Nations ;Questions About Nanotechnology, **2012**.
74. V.V Pokropivny, V.V. Skorokhod, *Mater Sci Eng, C.* **2007**, *27, 990.*
75. J. Jeevanadam et al., *Beilstein J Nanotechnol.* **2018**, *9, 1050.*
76. A. D. Yoffe, *Adv. Phys.,* **1993**, *42, 173.*
77. A. D. Yoffe, *Adv. Phys.,* **2001**, *50, 1.*
78. V. I. Klimov, *J. Phys. Chem. B,* **2006**, *110, 16827.*
79. A. Issac, C. von Borczyskowski, F. Cichos, *Phys. Rev. B.* **2005**, *71, 161302.*
80. Sigma Aldrich.
81. Sigma Aldrich.
82. E. Kucur, et al., *J. Phys. Chem. B,* **2005**, *109, 20355.*
83. V. L. Colvin, A. N.Goldstein, A. P. Alivisatos, *J. Am. Chem. Soc.* **1992**, *114, 5221.*
84. B. O. Dabbousi, et al., *Chem. Mater.,* **1994,** *6, 216.*
85. D. Bera, et al., *Materials,* **2010**, *3, 2260.*
86. J. Frenkel, J. Dorfman, *Nature,* **1930**, *126, 274.*

87. C. Kittel*, Phys. Rev.,* **1946**, *70, 965.*
88. S. Mørup, M. F. Hansen, C. Frandsen, *Comprehensive Nanoscience and Technology,* **2011** , Elsevier.
89. P. Weiss, *Comptes Rendus*, **1906,** *143, 1136*.
90. L. Néel*, Ann. Géophys*, **1949**, *5,99*.
91. G. F. Goya, M. P. Morales. *Journal of Metastable and Nanocrystalline Materials*, **2004**, *20, 673*.
92. S. Santra, et al., *Langmuir,* **2001,** *17*, 2900.
93. H. Yang, *Anal. Chem.*, **2004**, *76, 1316*.
94. P. Nicolás, et al., *Acta Biomat.* **2013** *9, 4754.*
95. W. Wu, Q. G. He, C.Z. Jiang, *Nano. Research Lett.,* **2008**, *3, 397.*
96. M. Okuda, et al., *Nanotechnology,* **2012**, *23, 415601*.
97. L. Bao, et. al., *J. Mater. Chem.,* **2012,** *22,* 7117.
98. S. J. Park, et. al., *J. Am. Chem. Soc.,* **2000,** *122,* 8581.
99. M. F. Casula, et al., C. *Chem. Mater.* **2010**, *22*, 1739.
100. N. Lee, T. Hyeon, *Chem. Soc. Rev.* **2012**, *41,* 2575.
101. D. Ling, T. Hyeon, *Small* **2013**, *9* , 1450.
102. D. Yoo, J.H. Lee, T. H. Shin, J. Cheon, *Acc. Chem. Res.* **2011**, *44* , 863.
103. Y. Jun, J. Lee, J. Cheon, *Angew. Chemie Int. Ed.* **2008**, *47* 5122.
104. M. Mahmoudi, et al., *ACS Chem. Neurosci.* **2011**, *2*, 118.
105. D. E. Sosnovik, M. Nahrendorf, R. Weissleder, *Circulation* **2007**, *115*, 2076.
106. H.W. Kroto et al., *Nature*, **1985**, *318, 162*.
107. S. Iijima*, Nature*, **1991** ,*354, 56*.
108. L.V. Radushkevich, V.M. Lukyanovich, *Zurn Fisic Chim***, 1952,** *26, 88*.
109. S. Iijima, T. Ichihashi, *Nature*, **1993,** *363, 603*.
110. P.M. Ajayan PM. Bulk metal and ceramics nanocomposites., eds. Nanocomposite Science and Technology, Wiley-VCH Verlag GmbH & Co., 1, **2004**.
111. E. Saether, S.J.V Frankland, R. B. Pipes, *Compos Sci Technol*, **2003**, *63, 1543*.
112. T. Pichler, *Nature Mater,* **2007**, *6, 332*.
113. M. S. Dresselhaus, et al., *Mater Sci Engg: C*, **2003,** *23, 129*.
114. J. H. Kim, B. G. Min, *Carbon Lett.,* **2010** ,*11, 298.*
115. K. Saeed, *J Chem Soc Pak*, **2010**, *32, 561.*
116. H.C. Wu et al., *J. Mater Chem*, **2010**, *20, 1036*.
117. M.C. Hersam, *Nat Nanotechnol*, **2008,** *3, 387*.
118. Reference to be added
119. Helland A, Wick P, Koehler A, Schmid K, Som C. Reviewing the environmental and human health knowledge base of carbon nanotubes. Environ Health Perspect, **115**, 1125 (2007).
120. R. H. Baughman, A.A. Zakhidov, W. A. de Heer. *Science,* **2002**, *297, 787*.
121. A. Cao et al., *Chem Phys Lett*, **2001**, *342, 510*.
122. S. Kar, et al., *Int J Nucl Desalin*, **2008**, *3, 143.*

Objective of the Thesis

The objective of the thesis is given below:

- The initial motive and the objective of this thesis encompassed the idea of using spherical carborane ligands appended to quantum dots in water medium to test their viability as capping ligands.
- There had been no previous study on quantum dots with different shaped ligands other than long chains of carbon and we wanted to check hoe these can affect the properties of the quantum structures.
- Further we wanted to design a synthetic route for obtaining quantum dots in water at higher temperature and pressure without using autoclaves or long time of reaction and using the common reagents.
- The objective was not only to obtain quantum dots in water but also other quantum nanocrystals if possible, like quantum rods or quantum rings. These quantum nanocrystals have never been synthesized in a colloidal synthetic route in water and never been reported before, so we wanted to try to synthesize these unique morphologies in water and characterize their properties.
- Further we wanted to also use carboranyl ligands for not only with quantum dots but also with magnetic nanoparticles and see how they can be influenced. The objective was to successfully synthesize them and also test their viability in biological applications
- One of the other objectives was not only to cap the magnetic nanoparticles with carboranyl ligands but also with metallacarboranes like H[COSAN] as H[COSAN] is a redox specie and could help to tune the properties of these nanoparticles to be used in sensors. Magnetic nanocomposites with multiwalled carbon nanotubes were also envisioned to be studied and used to form a complex with H[COSAN] in order to have a highly conductive material.

Results and Discussions Part 1
(Quantum Nanocrystals)

3.1.1. Core-Canopy Quantum Dots

A brand-new architecture for QDs in water with spherical ligands being used. The new architecture leads to exciting new properties, one of which is observed in these QDs is Kinetic Fluorescence Switching (KFS), which is neither similar to aggregation induced emission (AIE) or aggregation caused quenching (ACQ).

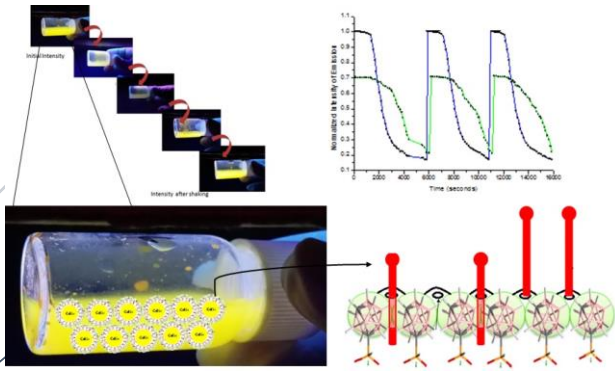

Arpita Saha
ICMAB-CSIC (UAB)

Contents

1. Introduction

Quantum Dots (QDs) are semi-conductor nanoparticles having dimensions in the range of 1-10nm [1], sometimes extending up-to 20nm. Due to their extremely small size, they have a vast range of properties which makes them extensively attractive for varied applications in the present-day scenario [2-13]. This is due to the quantum confinement effect as stated before in the general introduction of the QDs at the beginning of the thesis, which enables them to have a size tuneable bang-gap and in effect that of a size-tuneable emission [14]. QDs normally have a core capped with ligands which hinders their growth beyond the needed dimension in order for them to exhibit their unique properties. They are synthesized by physical methods or by chemical colloidal synthetic routes. In chemical synthetic routes, they are mostly made by high-temperature hot-injection organic method or the more environment-friendly water-based method [15]. The QDs are usually comprised of a core which is made up of either II-VI or III-V elements, then it has a shell which is usually another semiconductor of wide bandgap [16]. The second layer is used to passivate the surface deficiency and also to aid in improving the quantum yield (QY)[17]. The QDs require capping ligands to surround the core or the core/shell structure. This is because the capping ligands prevent the QDs to grow beyond a particular dimension [18]. This is modified by the quantity and type of the ligand along with the temperature of the reaction [19]. This is of utmost importance as all the properties of the QDs rely on their dimensions. We have concentrated ourselves with the aqueous synthetic route owing to its many advantages over the organometallic synthetic route. The most important necessity to obtain highly fluorescent water based QDs is for their application in bioimaging and other biological applications.

1.1. Aqueous QDs

Aqueous QDs are the ones which are directly synthesized using water as the solvent for the synthesis procedure. In this it follows a typical route where a Cd precursor (which is a water-soluble Cd metal salt) is dissolved in water along with the stabilising agent or capping agent. Then it is purged with N_2 gas before the chalcogen source of Se or Te is added to the solution mixture. In the aqueous synthesis, mild heating is used in the initial phase of the reaction process in order to obtain the particle growth. Very high temperatures are usually not used in the water-based synthesis opposed to the organic synthesis where reaction temperatures range from 200^{o}C to 350^{o}C [20,21]. In the aqueous method, the pH of the reaction is important and needs to be maintained. This has been shown by Li et. al that at lower pH of 8-8.2 the QY value of 60% for CdTe can be achieved while Rogach et. al have also shown that at a higher pH of 12, in order to achieve the matching QY value we need to tailor the amount of the Cd precursor and the capping agent in the reaction [22,23]. Usually, CdTe is more commonly synthesized in the aqueous form while CdSe is preferred in the hot injection synthetic route [24-30]. There are many advantages of QDs synthesized in water over the QDs synthesized in organometallic synthesis. The aqueous synthesis has gained huge prominence due to its production of biocompatible QDs in an environmental- friendly solvent along with the ease of obtaining the QDs in powdered form as opposed to the organic synthetic route [31]. The major drawbacks of the QDs synthesized in water is their photoluminescence properties are inferior to their organically synthesized counterparts and low QY. This is mainly attributed to the mild temperature conditions used during the synthesis of aqueous QDs [32]. There have been few reports in which QDs in water have been synthesized in slightly higher temperatures in autoclaves under pressure using the hydrothermal synthesis [33,34]. They improved the QDs in

water considerably in terms of their luminescence properties but these QDs have higher tendencies to aggregate than the ones made at milder conditions. The Table 1 below lists the advantages of aqueous method over the organometallic synthesis of QDs.

Advantages of Aqueous Synthesis	**Disadvantages of Aqueous Synthesis**
Can be easily used in medical applications without cumbersome ligand exchange process	Lower QY
Green solvent and environmentally friendly	Smaller range of colours (usually individual colours or yellow and orange emission)
Low Cost Process with high reproducibility	Less control over size
Safer reagents than the ones used in organometallic synthesis	Room temperature or Lower temperatures of 100°C used]
Easy isolation in powdered form and can be stored and re-dispersed on choice	Shorter lifetime with rapid decay in emissive properties
Better control of the surface charges by the choice of the stabilising agent	Poor crystallinity compared to the QDs synthesised in organometallic method
Has the potential to be carried out in vast scale for large quantity production of QDs	Sometimes the reactions are slower and longer taking up to days for the synthesis of QDs

Table 1: Advantages and disadvantages of aqueous synthesis of QDs [35]

The aqueous synthesis attracted us mostly due to its ease of production and the ease of its use in biological applications without further processing required [36]. Moreover, the choice of capping ligands produces different effects in the QDs produced in water. Thre are a number of parameters that help determine the aqueous synthesis of QDs. The parameters are listed below [37].

Reactant concentration: The molar ratio of the precursors of Cd:Se, Cd:S, Cd:Te along with their ratio with the stabilising agent plays a very important role in the quality of the resultant QDs. In certain cases, higher Cd with respect to Se or Te is present and this is necessary so as to be passivated by the thiol capping ligands and thus give broader PL peaks. While in other cases higher Se helps in obtaining sharper and better PL quality but the capping ligands changes in that case.

pH: In most cases a basic pH is used for the synthesis of the QDs in water. This is particularly because lower pH than 8 causes the QDs to aggregate and deterioration of the luminescence properties of the QDs. Usually the pH is kept between 8 to 12 for the synthesis of all Cd based QDs in water as pH is a key factor in influencing the growth rate of the QDs and the QY of the resultant QD.

Temperature of the reaction: The surface structure of the QDs depend on the temperature of the reaction mixture. Higher temperatures cause the surface defects to minimise due to faster growth rate but it also leads to aggregation of the QDs. In order to minimise aggregation and also the surface defects of the QDs, a compromise is achieved and slight temperatures are used at the start of the reaction or lower temperatures are used and longer reaction time.

Heating time: Heating time is directly proportional to the size of the QDs, longer heating time produces larger dots.

Stabilising agents: The choice of stabilising agents is of utmost importance while synthesising QDs in water. Most commonly thiols are used as they are effective in stabilising the dots and regulating the size. The choice of ligands helps in obtaining different advantages over the dots, like controlling the surface charges or their luminescence properties. This point is specially discussed in the next section.

1.2. Commonly Used Ligands

The ligands and the choice of ligand is very important as mentioned above for controlling the quality and the property of the QDs produced using the aqueous synthetic route. The commonly used ligands in water-based synthesis are thiols like mercaptoacetic acid (MAA), mercaptopropionic acid (3-MPA), mercaptosuccinic acid, thiolactic acid, 1-thioglycerol, 2-mercaptoethanol and 1-mercapto, 2-propanol. Out of these the most common are MAA and 3-MPA [38,39]. The thiols are mostly used for the cadmium chacogenide QDs as they are effective in size regulation and stabilisation of these QDs. Capping is mostly important as it further helps in reducing the toxicity of the QD core, make them water soluble and also helps in the luminescence of these QDs. Various phenomena like Aggregate Induced Emission (AIE)[40], Aggregation Caused Quenching (ACQ)[41] can be diminished or enhanced by the adequate choice of these ligands. We have discussed that commonly the thiols are used but in certain cases amines are also used in water based QDs. This is because amines help in manipulating the fluorescence of the QDs, longer chain lengths of the amines produced smaller QDs, thus in turn the fluorescence peak blue-shifted. But mostly straight carbon chains are used to cap the QDs in water. The length varies as longer chains give smaller dimension due to their more bulkiness as this prevents quick diffusion and so the particles grow slowly, while it is quite the opposite when the length of the chains is smaller [42]. For QDs that fluoresce in the red region, primary amines are the predominantly used capping agents for those as the QY for these colours is relatively low. Also, steric acid is a good capping agent for an orange or red fluorescing QD. Moreover, the capping ligands are sometimes chosen with mind to further conjugate the QDs with other moieties for further applicative purposes [43-46]. The Table 2 gives an idea of the dimension achieved for the different Cd based QDs using the different capping

agents[17, 23-27, 39,47-49]. The figures of the common capping ligands are shown in Figure 1.

QDs Type	QDs Size	Capping Ligands
CdTe	1.3-2.4nm approximately	2-mercaptoethanol, 3-MPA, 2-mercaptoethylamine (MA), L-cysteine, MAA,
CdTe	5 ± 0.5nm	Dithiol functionalised ionic liquid
CdTe	5.5 ± 0.5nm	3-MPA
CdSe	1.4 to 2.2nm	2-mercaptoethanol, 3-MPA
CdSe	2.2 to 3.2nm	MAA and thiolactic acid
CdS	1.3-3.9nm	1-thiogycerol, 3-MPA
CdS	3-5nm approximately	3-MPA, 1-thioglycerol

Table 2: List of the stabilising agents used and the size obtained for the common Cd QDs.

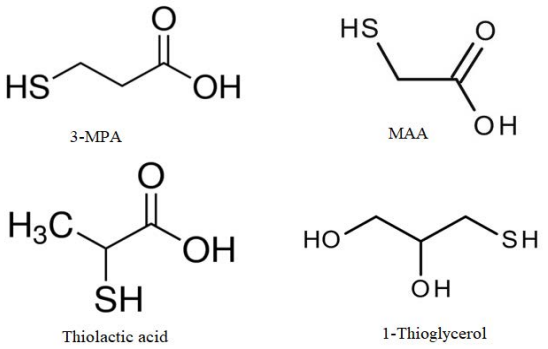

Figure 1: Commonly used capping ligands in water-based synthesis of Cd based QDs.

1.3. Spherical Ligand: m-Carboranyl Phosphinate

Spherical Ligands are those which are 3-D ligands having volume and a spherical structure. As mentioned before, since mostly straight chains of carbon have been used as capping ligands for QDs, the potential for the usage of spherical ligands had remained dormant for many years and thus no one realized what they could yield when combined with the QDs. This maybe attributed to the difficulty in the available carbon-based spherical molecules. The known ones are C_{60} and $C_{20}H_{20}$, while the solubility of the first one is an issue, the latter is very difficult to synthesize requiring many steps [50]. Thus, these molecules are never sought after to be used as ligands to nanoparticles or QDs in general.

Carboranes in this regard have certain advantages over their spherical carbon counterparts and can act as suitable spherical ligands for the QDs. The most studied boranes are icosahedral boranes, which can be visualized as spheres and their foremost examples are $[B_{12}H_{12}]^{2-}$, 1,2-$C_2B_{10}H_{12}$, 1,7-$C_2B_{10}H_{12}$ and 1,12-$C_2B_{10}H_{12}$. These are aromatic in nature [51-53] and are very stable species which are able to sustain high temperatures and harsh chemical conditions [54]. Detailed introduction for the borane species is given in the main introduction of the thesis but the difficulties faced by the carbon molecules are not found when producing boranes. For instance $[B_{12}H_{12}]^{2-}$ has been synthesized in a single step [55]. If these spheres are placed in a close packing, they generate openings, through which ions or solvent molecules can move and cannot be liberated easily, resembling cell membrane transport. This argumentation was used to explain that a gold nanoparticle capped with carboranyl thiol, 1-SH-1,2-*closo*-$C_2B_{10}H_{11}$, CarbSH, shuttles from an organic phase to an aqueous one by a redox process, using small ions, H^+, and $[BH_4]^-$ [56]. The example of Au nanoparticle being used in combination with mercaptocarborane

influenced us to think that they can be used effectively as spherical ligands for other nanoparticles like QDs and also a chance to study the ions' permeability through the peripheral layer of the QDs and their performance. Since mercaptocarborane was used for the Au nanoparticles and since thiols of carbon have also predominantly being used in combination with the QDs, our initial thought was to synthesize the QDs with them, but the solubility of mercaptocarborane in water is not that good. So, this turned our attention to the *meta*-carboranyl phosphinate.

Ortho-carboranyl thiol: Ortho-carborane, 1,2-closo $C_2B_{10}H_{12}$, nearly retains the perfect icosahedral geometry of the parent borane after substitution of two adjacent boron atoms with two carbons. It is highly stable both chemically and thermally like its derivatives. It has strong hydrophobicity and generates water-insoluble structures with limited bioavailability and hence is unsuitable for application in BNCT. *o*-carborane thiolate has salts of Li and Na which are considerably water soluble but require surfactant to make them further soluble in water. The synthesis procedure for *o*-carborane thiol is depicted in the following page (Figure 2)[57]

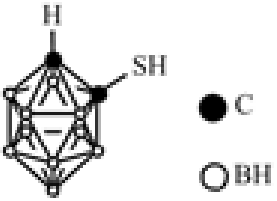

ortho-carboranylthiol

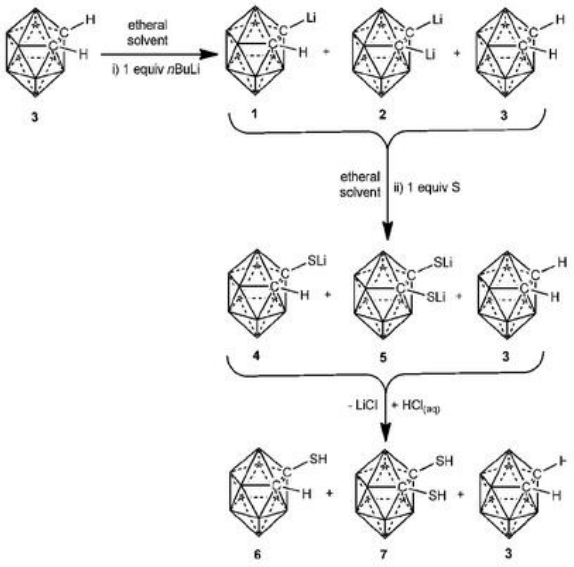

Figure 2: Synthesis procedure for *o*-carborane thiol.

meta-carboranyl phosphinates: These are new purely inorganic class of ligands. *ortho*-carboranylphosphinic acids were obtained for the first time at the end of '60s- beginning of '70s by L. I. Zakharkin, M. N. Zhubekova, A.V Kazantsev. At that time *ortho*-carborane phosphinic acid showed instability due to the weak character of Cc-P bond. In the literature there are a few examples of complexes with phosphinic acids due to its instability against oxidation (Figure 3). They are not stable and the phosphinic readily changes to phosphonic acid. However recent investigations found meta-carboranylphosphinic acid stable enough (TGA in Air and Argon atmosphere-stable till 300°C- Figure 4) and capable to produce complexes with transition metals.

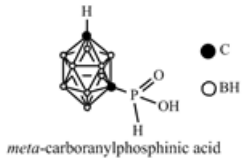

meta-carboranylphosphinic acid

There also remained a dearth of available reproducible synthesis and characterization for carboranylphosphinic acids and therefore they were not synthesized or used further. But this was recently synthesized using a reproducible method in our group and both the acidic form and the salt form of the ligand was synthesized [58].

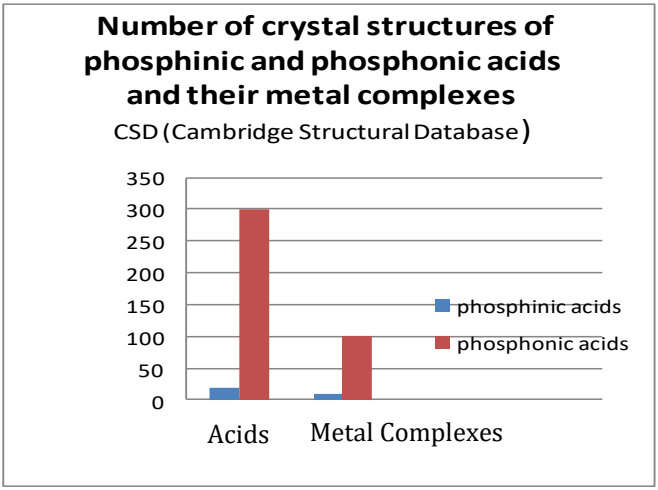

Figure 3: Number of crystal structure of phosphonic and phosphinic acids and their metal complexes

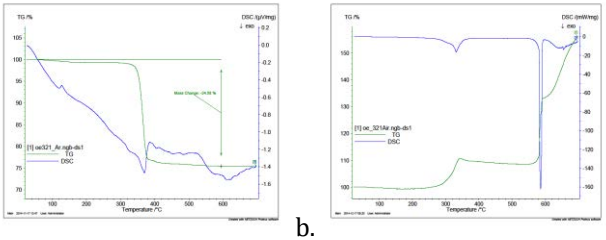

a. b.

Figure 4: TGA of m-carboranyl phosphinate (a) in argon and (b) in air.

The electron-withdrawal by the carboranyl carbon atoms, along with the space-filling efficiency and enhanced aromaticity of the cluster cage, renders the phosphorus

more difficult to oxidize. This enables carboranyl phosphinates to survive harsh oxidizing conditions, unlike the organic phosphinates. The synthetic procedure is depicted in the following Figure 5.

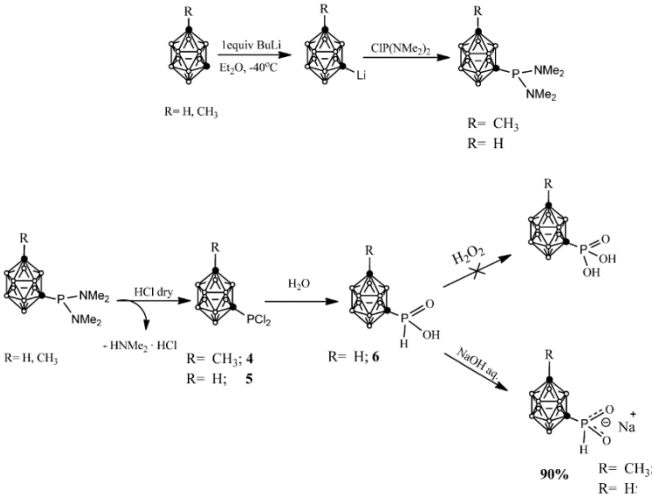

Figure 5: Synthesis procedure of m-carboranyl phosphinic acid and its sodium salt.

Thus, when it was synthesized and available, we decided to use it for the QDs. As per literature, we did not find any evidence of phosphinic acid being used as capping agent for QDs, phosphonic acids [58] have been used but not phosphinic acid. The major reasons for using it are listed below:

- Spherical shaped ligands
- Volume and 3-D ligand
- Very well soluble in water
- Chemically stable and robust
- Completely inorganic ligand
- Never used in combination with QDs before

2. Core-Canopy QDs

The core-canopy QDs are the new kind of QDs that we synthesized using a combination of CdSe core and spherical ligand of m-carboranyl phosphinate in a water-based synthesis [60]. In these new QDs, we have a standard CdSe core which has the spherical m-carboranyl ligand emanating out from the core of the CdSe. And acting as canopies covering the core. The sphere is connected to the core with pillars which are the stalks of the carborane ligand. The image below shows the core-canopy QD structure (Figure 6).

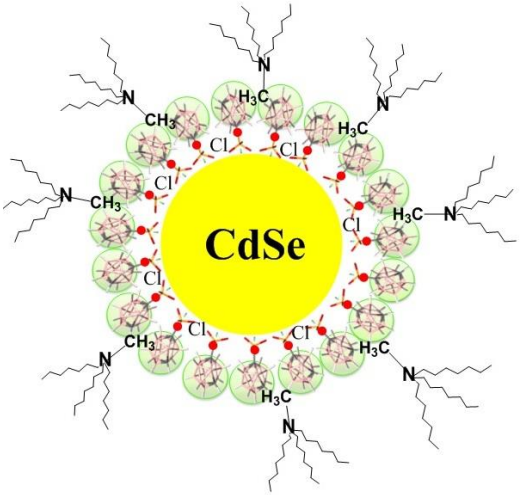

Figure 6: The core-canopy QD having the CdSe core and the m-carboranyl phosphinates are the canopies.

The synthesis of these core-canopy QDs introduced a brand-new architecture in the field of QDs. Though carboranes have been used before with QDs but none have been used to create such an architecture.

2.1. Concept of the architecture

The architecture is based on close packing of spheres on a sphere. When the close packing is done, there are voids which are left and these openings provide for channels through which ions can move. The spherical cage of the carborane acts the canopy while the stalk of the carborane acts as the pillar which joins the core of the CdSe QD with the ligand. The gaps formed due to the compact packing traps the ions which can move in and out of these openings and give rise to distinct properties. The properties are a complete consequence of the architecture forms using the new spherical ligands on a spherical core. The image below shows the spherical ligand in detail (Figure 7).

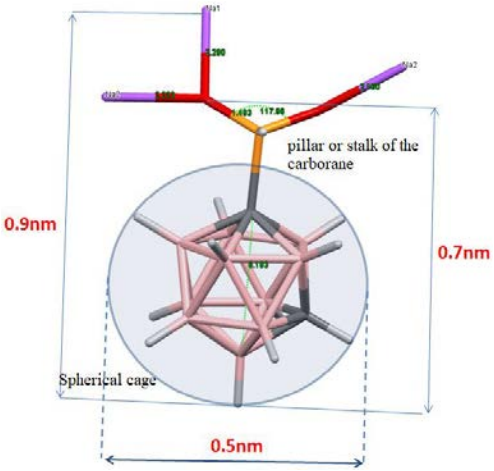

Figure 7: The figure of the m-carboranyl phosphinate ligand with the spherical cage and the pillar or stalk which joins it to the core do the QD.

The close packing of spherical carborane on spherical QD yielded the following structure as seen in the following image (Figure 8).

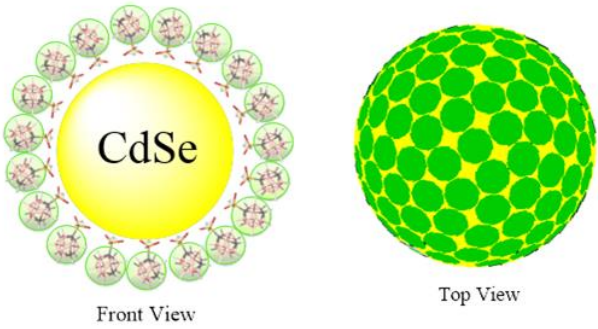

Figure 8: The compact close packing of the spherical ligand on the spherical core of the QD.

This architecture had openings which provided us with an opportunity to play with them. Trapping ions within them and preventing them from moving out would be interesting as it would help us see how the QDs behave when the ions are trapped and when the ions move out. For this we would need to convert the openings to gates by closing the voids partially using something and then opening them. This is also had an advantage from the synthetic point of view for the QDs. This is further discussed in the next section.

2.2. Synthesis of the QDs

Initial attempts were made to produce the Core-Canopy QDs with Li[1-S-1,2-*closo*-$C_2B_{10}H_{11}$], Li[CarbS], or Na[1-S-1,2-*closo*-$C_2B_{10}H_{11}$], Na[CarbS], however they were not soluble well in water, and when used with the cadmium and selenium precursors ($CdCl_2 \cdot 2.5H_2O$ and Na_2SeSO_3 [61]), different coloured colloids at different temperatures (25°C, 70°C, 90°C, 110°C) were formed that failed to produce photoluminescence (PL), either from the original aqueous solution, or when isolated and re-dispersed in ethanol or toluene (Figure 9). These results led us to use the water soluble *m*-carboranylphosphinate as mentioned earlier,

Na[1-OPH(O)-1,7-*closo*-$C_2B_{10}H_{11}$], Na[CarbOPH(O)], as an alternative to the water insoluble Li[CarbS] or Na[CarbS].

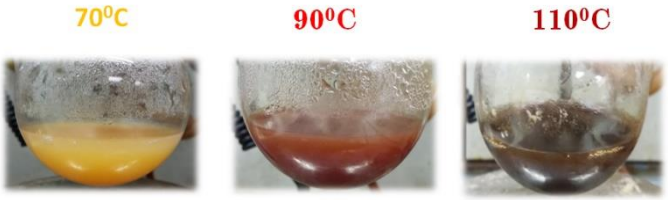

Figure 9: The differently coloured colloids obtained at different temperatures with Li[CarbS].

Early attempts to prepare CdSe@CarbOPH(O): The Cd precursor of $CdCl_2 \cdot 2.5H_2O$, and the capping agent Na[CarbOPH(O)] along with the Se precursor Na_2SeSO_3 were mixed in water at 25°C and it led immediately to a white colloid which turned yellow five minutes later. This dispersion showed yellow PL but it lasted only for 2 hours. No other phenomenon was observed. Initially only the capping ligand and the Cd precursor was mixed, then the Se precursor was added in one shot to the mixture and stirred at room temperature and no nitrogen purging was required.

Incorporation of the synergist cationic surfactant: The lifetime of luminescence was very short with the initial attempts of synthesizing the core-canopy QDs, so this led us to believe that it does need a second layer of capping for further stability. Moreover, 1-HOPH(O)-1,7-*closo*-$C_2B_{10}H_{11}$ is a strong acid (p*Ka*=1.32) and will expectedly produce the QD canopy that could host small anions in their voids and channels, so we thought of introducing cationic surfactants to compensate the negative charge of QDs and induce solubility and more stability. To find the right kind of cationic surfactant, four ammonium cationic surfactants each with a different number of methyl groups on the

nitrogen (from 0 to 3), and different number of carbon atoms were tested. They are as listed below:

- Tetrabutylammonium $[N(But)_4Me_0]^+$ (17 carbon atoms, 17C),
- Tricaprylylmethylammonium $[N(Caprylyl)_3Me_1]^+$(25C),
- Dimethyldioctadecylammonium $[N(Octadecyl)_2Me_2]^+$ (38C)
- Cetyltrimethylammonium $[N(Cetyl)Me_3]^+$ (19C).

The one that gave the best result was tricaprylylmethylammonium chloride $[N(Caprylyl)_3Me_1]Cl$, the one with only one methyl group on N. Not only it helped in providing better solubility and stability to the QDs, it gave rise to an unprecedented property. We observed that the QD suspension, which is highly emissive, quenches in 30-40 minutes but upon shaking (applying kinetic energy) recovers its emissive properties with maximum intensity. This phenomenon has not been observed before in anytime of QD. It is similar to the blinking of the QDs [62] but it was different as it required only mere kinetic energy to recover its original fluorescence. We named this property as Kinetic Fluorescence Switching (KFS). It will be explained in detail in the next section.

The ratio of reagents used was Cd:Se:$[CarbOPH(O)]^-$ 1.5:1:0.5. The proposed formulation of the generated QDs is $[CdSe@CarbOPH(O)]@Cl/[N(Caprylyl)_3Me_1]$, Cl^- being the anion trapped in between the QDs core and the carborane canopy. These $[CdSe@CarbOPH(O)]@Cl/[N(Caprylyl)_3Me_1]$ QDs show the KFS property that is repetitive for at least 6 months. The last measurement done on the QDs have shown a tendency of the fluorescence intensity increasing with the passage of time. The photographical and the schematic

representation of the synthetic procedure is shown below (Figure 10 and 11):

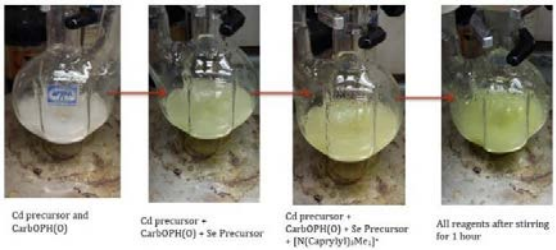

Figure 10: The photographical depiction of the synthetic procedure.

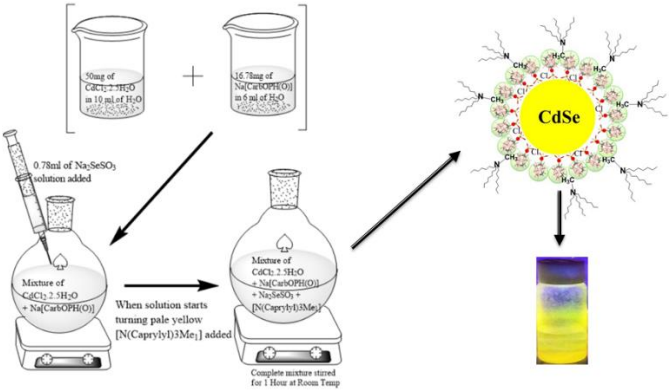

Figure 11: The schematic depiction of the synthetic procedure.

Revisiting the CdSe carboranylthiol synthesis: Noticing the KFS in [CdSe@CarbOPH(O)]@Cl/[N(Caprylyl)$_3$Me$_1$] QDs, and with the QD's architecture defined with the capping [CarbOPH(O)]$^-$, we considered that if the QDs architecture was paramount, the [CdSe@CarbSH]@Cl/[N(Caprylyl)$_3$Me$_1$] should also produce the KFS property. The same problem of solubility was faced for the synthesis with the [CdSe@CarbSH]@Cl/[N(Caprylyl)$_3$Me$_1$] as indicated before but we had a better understanding of the procedure with the incorporation of the surfactant, and despite not having the

best synthetic procedure yet in our hands, our results are very supportive of the compact sphere/pillar/ground architecture that is the basis for the Core-Canopy QDs concept. To obtain the mercapto carborane capped QD, [CdSe@CarbSH]@Cl/[N(Caprylyl)$_3$Me$_1$], we dispersed Na[CarbS] in a large excess of [N(Caprylyl)$_3$Me$_1$]Cl in water. This was mixed with the other reagents as it was done for [CdSe@CarbOPH(O)]@Cl/[N(Caprylyl)$_3$Me$_1$]. This led us to obtain [CdSe@CarbSH]@Cl/[N(Caprylyl)$_3$Me$_1$], however it lasted only for a week. This experiment supports the particular architecture, compact spheres packing/pillars/ground. Their unique ability to utilize space and leave openings coupled with the selective permeability produces a spectacular combination to produce this Kinetic Fluorescence Switching in CdSe Core-Canopy QDs. But their lifetime was drastically poor when compared to the other synthesized QD. Further work was done to improve the lifetime and it lasted for a month but not more than that. This is perhaps due to the lack of solubility of the mercapto salts of carborane.

3. Kinetic Fluorescence Switching (KFS)

The first property that we have obtained as a result of the new architecture designed for the QDs is Kinetic Fluorescence Switching (KFS). In KFS the QDs lose their fluorescence when aggregated but shine back with maximum intensity again after applying mild kinetic energy, in 30-40 minutes, fade again but upon shaking (applying kinetic energy) recover their emissive properties. This sequential process of luminescence, fading, back to luminescence, fading and so on, can be continuously run for

several months. This process is distinct to the blinking of the QDs as mentioned earlier. This property is not similar to the AIE or ACQ phenomena in QDs. It has been observed for the first time that the QDs can retain their original intensity of fluorescence after being applied with kinetic energy. Usually, on aggregation the QDs either have a quenching effect on their fluorescence or they have an enhancement in luminescence, but here on aggregation there is reduction in the intensity of the luminescence while again on de aggregation the intensity reverts back to its original value. This unique property of luminescence, fading and luminescence could be switched for numerous number of times without any deterioration of the sample quality. The property of KFS was observed for up-to 6 months after the preparation of the sample and within those 6 months there was a change in the emission colour of the QDs. Initially when synthesized the QDs emitted bright yellow colour, while after 5 months, the colour of emission changed from yellow to orange, which is well accounted as we see an increase in the size of the QDs. Although the emission colour changed, the property was still intact and it still showed the KFS. Below there is a pictographic representation of the KFS both of an initial sample (Figure 12) and a 5 month old sample (Figure 13).

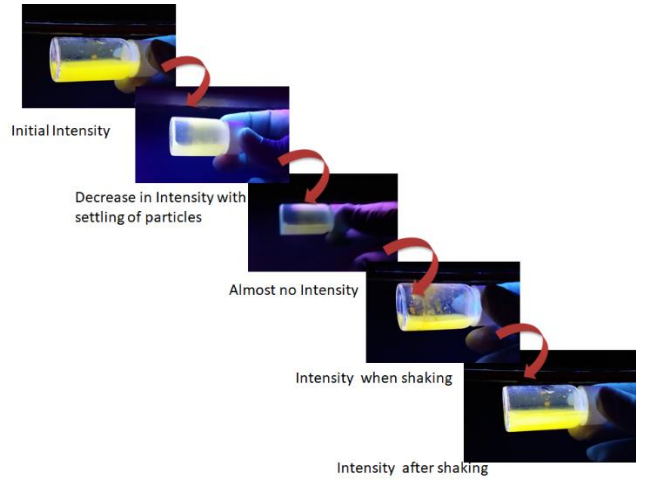

Figure 12: The photographic representation of KFS of an initial sample. QD suspension illuminated under UV lamp with 365nm wavelength.

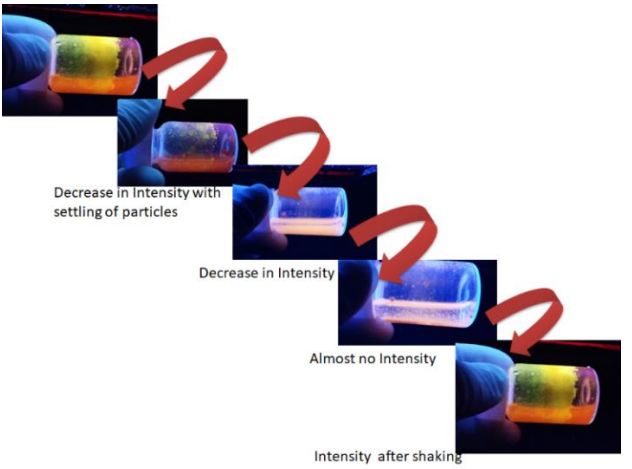

Figure 13: The photographic representation of KFS of an old sample. QD suspension illuminated under UV lamp with 365nm wavelength.

The intensity of emission increased with passage of time, until the QDs started to lose their emissive properties after

6 months and thus end up losing the KFS. The decline in the emissive properties is quite drastic after 6 months. Below the graphs show increase in intensity of the emission for four months (Figure 14).

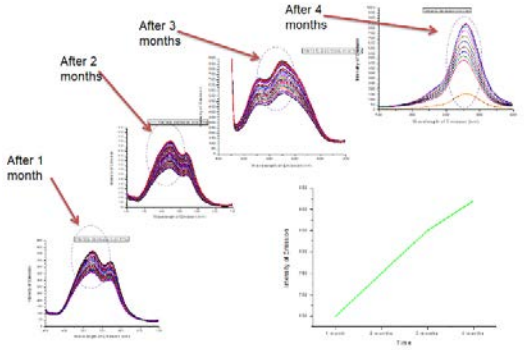

Figure 14: The increase in the intensity of emission shown with passage of time.

The graphical representation of the KFS is shown below. It also shows the KFS for an old and a new sample (Figure 15).

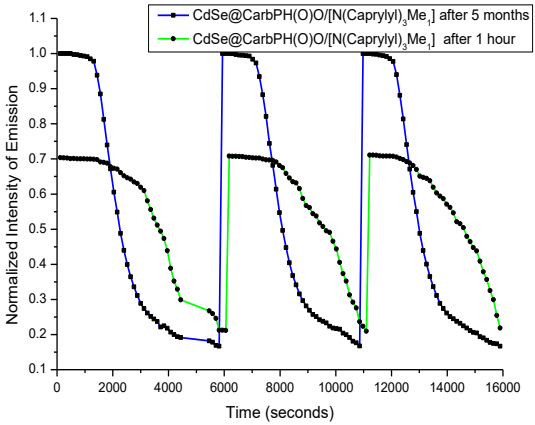

Figure 15: The graphical representation of KFS for an old sample and a new sample is shown above.

The KFS property shown by these QDs are a consequence of the architecture of the QD. The architecture and the synergy of the components used gives rise to this unprecedented property of KFS. This is further explained in the next section as to how we have achieved the KFS property by manipulating the architecture and the capping ligands along with the second capping layer.

3.1. Understanding KFS and the architecture

To understand the KFS better and the architecture we did a series of experiments and it led us to the conclusion that there needs to be a synergy between the cationic surfactant [N(Caprylyl)$_3$Me$_1$] and the spherical capping ligand CarbOPH(O). The experimental detail and the understanding of the synergist factor is as follows.

Synergy between the surfactant and the ligand: The strategies leading to the preparation of the QD [CdSe@CarbOPH(O)]@Cl/[N(Caprylyl)$_3$Me$_1$] indicated that a synergy between [CarbOPH(O)]$^-$ and the surfactant was required: [CarbOPH(O)]$^-$is necessary to produce the fluorescence while [N(Caprylyl)$_3$Me$_1$]$^+$ is needed for the stabilization of the QDs. To understand better the KFS property that is the sequential PL…/bright/fade/bright/fade/bright/fade/bright… of the [CdSe@CarbOPH(O)]@Cl/[N(Caprylyl)$_3$Me$_1$], we display in Figure 16 a set of images that contribute information about the fate of the nanoparticles upon the removal or due to the absence of some of the reagents. Not only is the KFS an unique occurrence in these [CdSe@CarbOPH(O)]@Cl/[N(Caprylyl)$_3$Me$_1$] but also the synergy of the carboranes with the cationic surfactant. This is the first time that such a synergy has been used to

synthesize QDs in water. These can be chosen to be surfactants that will prevent strong particle aggregation.

Our interpretation is that the KFS observed in the [CdSe@CarbOPH(O)]@Cl/[N(Caprylyl)$_3$Me$_1$] QDs is due to a medium strength binding of [CarbOPH(O)]$^-$ that requires extra available Na[CarbOPH(O)]$^-$ to cap and stabilize the surface. The experiments in Figure 16 are supportive of Equation (1).

$$CdSe@[CarbOPH(O)]^-_m/[Cl^-]_p/[N(Caprylyl)_3Me_1]^+_z \rightleftharpoons CdSe@[CarbOPH(O)]^-_{m-n}/[Cl^-]_{p-x}/\ [N(Caprylyl)_3Me_1]^+_{z-y} + n\ [CarbOPH(O)]^- + x\ [Cl^-] + y\ [N(Caprylyl)_3Me_1]^+$$

Equation 1: It shows the synergy between the cationic surfactant and capping ligand is necessary.

When the supernatant liquid from the initially synthesized QDs is removed and only fresh new distilled water is added, the equilibrium is shifted to the right. Electron trapping sites are then generated on the surface of the QDs producing quenching. When the cationic surfactant and its corresponding Cl$^-$ is added, some PL is observed because the equilibrium is shifted to the left. When **[**CarbOPH(O)**]**$^-$ is added the same occurs but it brightens more, that is the intensity of the emission observed is higher when compared to the intensity observed when only the cationic surfactant was added. This is because carboranylphosphinate is responsible for the brightening but it is neither sufficient for the stability of the QDs nor for the KFS. For this to occur, a combination of the cationic surfactant [N(Caprylyl)$_3$Me$_1$]$^+$, [Cl]$^-$ and [CarbOPH(O)]$^-$ is necessary. We interpret that the KFS property is derived from the architecture of the Core-Canopy QDs, in which chloride anions are trapped inside the channels thus originating a high load of trapped negative

charge that requires outer cations for charge neutralization. Because we did utilize cationic surfactants these prevented robust aggregation of the particles leading to the unprecedented feature Kinetic Fluorescence Switching (KFS), related neither to ACQ nor AIE.

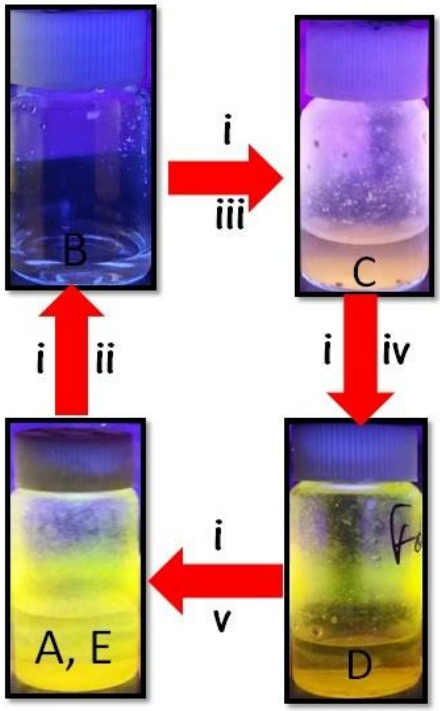

Figure 16: Starting from a just made sample of [CdSe@CarbOPH(O)]@Cl/[N(Caprylyl)$_3$Me$_1$] that incorporates the mother liquor (A), the following experiments were made i) the supernatant liquid was removed and ii) pure water was added. After shaking of the mixture no PL was observed, (B). Starting from B process i) is done, and iii) [N(Caprylyl)$_3$Me$_1$]$^+$ in solution is added; in this case the PL was improved but it was poor, due to too much precipitation, (C). Starting from C process i) is done, and iv) an aqueous solution of Na[CarbOPH(O)] is added, producing an enhanced PL in (D), but it lasted for only few hours. For the last experiment, starting from D, process i) is done, and v) an aqueous solution both of Na[CarbOPH(O)] and Cl[N(Caprylyl)$_3$Me$_1$] are added which regenerated the original properties (A) and (E).

The KFS observation came as a result of capping the CdSe QDs with $[CarbOPH(O)]^-$. If the close packing of spheres was not relevant, and noting that a rotating phenyl moiety occupies a comparable volume to a carboranyl group and that both phenylphosphinic and carboranylphosphinic acids have similar pKa values (1.77 and 1.32, respectively) it could be expected that the KFS phenomenon could be also observed with phenylphosphinic acid. But this was not the case. This is further explained in the section 5.

It has been already mentioned before that the four ammonium cationic surfactants gave different results in the terms of the KFS, the best performance has been produced by $[N(Caprylyl)_3Me_1]^+$ with one Me on the N, (the KFS and PL was observed for at least 6 months) then $[N(Octadecyl)_2Me_2]^+$, two Me near N, (did show one day PL), next was $[N(Cetyl)Me_3]^+$ (did show PL for a few hours) and the worst performing is $[N(But)_4Me_0]^+$ with no Me on the N (did not show any PL). Although the best performing in terms of KFS and PL are these with the highest number of C atoms in the molecule, it seems the number of methyl groups on the N in the surfactant is preeminent for the KFS. Keeping in synergy with the experimentations it can be interpreted that $[N(Caprylyl)_3Me_1]^+$ can fill the spheres' openings with its methyl preventing the Cl^- from leaking in a better way than the other surfactant cations. On observing the behavioural characteristics it is noted that the number of Me groups seems to be of paramount importance in the production of KFS rather than the number of C atoms in the alkylammonium surfactants which leads us to hypothesize that the surfactant, in this case $[N(Caprylyl)_3Me_1]^+$, is the plug that converts the openings on the canopy into gates. The hypothesis is represented in Figure 17. It shows that how the spherical ligand acts as the canopy over the core, thus producing channels, these channels trap the ions and

the opening of the channel is closed by the cationic surfactant using the single methyl group. When the opening is closed, that is the methyl group of the surfactant is plugged in, then we obtain the maximum intensity of the emission which is when the QDs are in dispersion. While when the QDs start to settle down, the methyl group of the surfactants plugs out of the opening created by the spherical ligand canopy and the synergy between the ligand and the surfactant is lost, as a result the intensity of emission is lost. This continuous movement of the surfactant through the openings, either closing it or opening it plays the most significant role in obtaining the emission intensity.

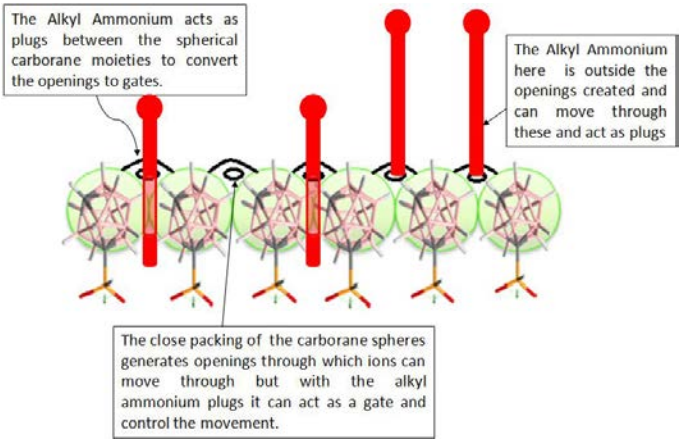

Figure 17: The pictographic model for the gates created by the core canopy quantum dots. The canopy created by the carborane spheres when closely packed generate openings which are converted to gates due to the presence of the alkyl ammoniums

The significance of the number of methyl groups is shown in the Figure 18. It shows how the increase in the number of methyl groups does not allow the other surfactants to close the openings, while it is easier to close it having a single methyl group.

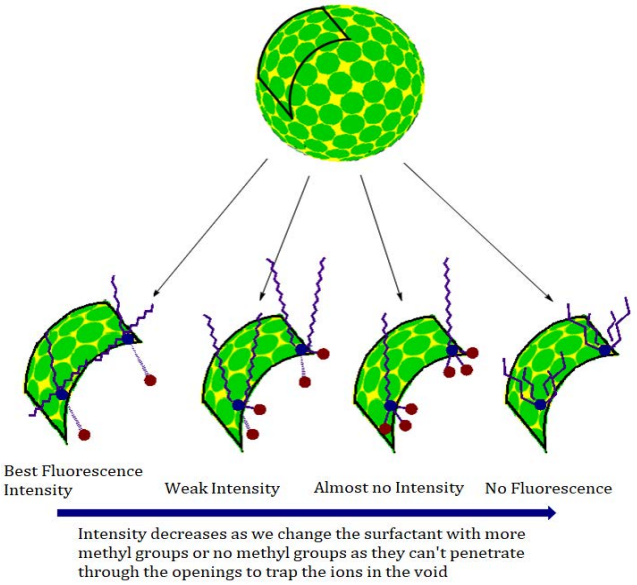

Figure 18: The different cationic surfactants used and the intensity of emission shown by them. It had a string dependence on the methyl groups of the surfactants used.

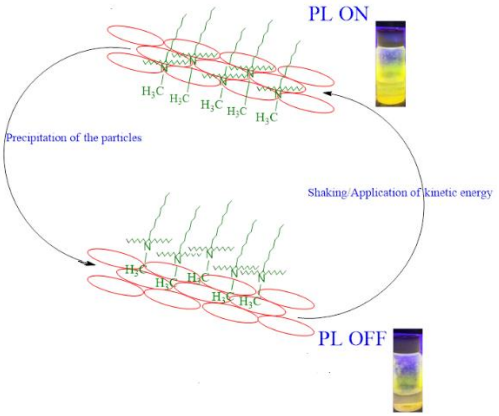

Figure 19: The KFS is a consequence of the architecture and the synergy between the surfactants and the spherical capping ligand.

4. Characterizations

This section deals with the characterizations of the QDs. They have been characterized using Fluorescence spectroscopy (excitation and emission spectra) and UV-vis for their luminescent properties, EDX (Energy dispersive X-ray), Chemical Analysis, IR (Infra-red spectroscopy) and Electron diffraction was done for their compositional studies. TEM (Transmission electron microscopy) and DLS (Dynamic Light Scattering) was done to measure their dimensions while Zeta potential was studied for their stability studies. The following sub-sections explain the characterizations done and the data obtained from them.

4.1. Fluorescence Studies

The fluorescence studies were done using Perkin Elmer LS45 fluorimeter and UV-vis spectrum was obtained using Cary-5000 UV-NIR Spectrometer.

UV-vis Study: The UV-Vis spectrum was obtained for the QDs. Obtaining was particularly challenging as the QDs in the water were a suspension and not a solution and they kept precipitating when not applied with kinetic energy. So, recording the spectrum for the UV was difficult. Also, to obtain the absorbance below 0.1 was difficult for these QDs. To obtain the spectrum that is shown in Figure 20, the QDs have been diluted further with a solution containing the cationic surfactant and the capping ligand. The values obtained is around 0.189 and the maximum absorbance peak is around 366nm. After the UV-vis studies were done, the excitation and the emission spectra were recorded.

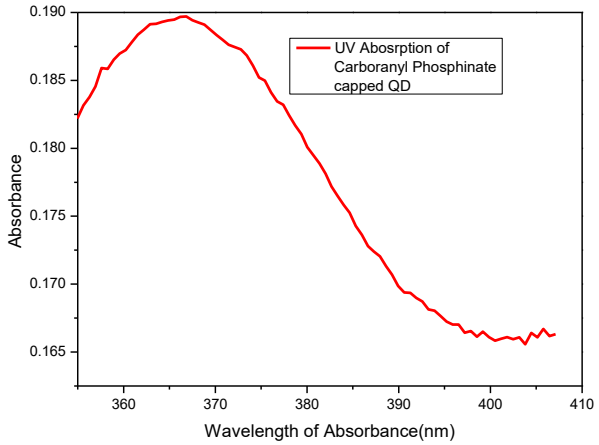

Figure 20: The UV-vis absorbance spectroscopy of the CdSe@CarbOPH(O)]@Cl/[N(Caprylyl)$_3$Me$_1$] QDs. It shows a maximum absorbance at 366nm.

Excitation and Emission Study: The excitation spectrum shows two peaks, one at 366nm and the other at the 400nm. The 366nm wavelength was chosen for the emissive studies. The excitation spectrum is shown below (Figure 21).

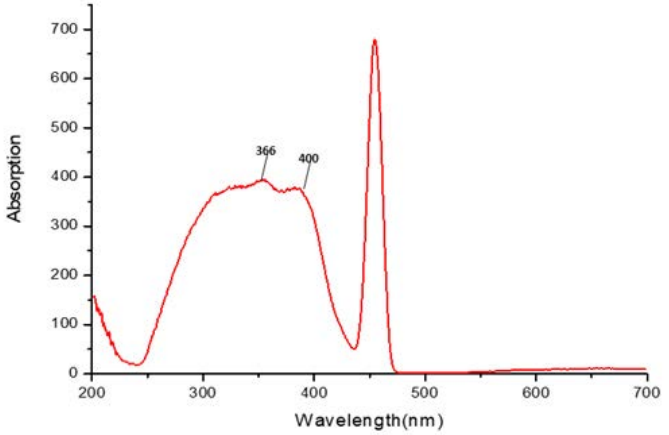

Figure 21: The excitation spectroscopy of the CdSe@CarbOPH(O)]@Cl/[N(Caprylyl)$_3$Me$_1$] QDs. It shows two peaks.

The emission spectra were recorded using 366nm wavelength as the excitation wavelength after the UV-vis spectroscopy, then the emission peak was used to obtain the excitation spectrum. The emission spectra were obtained for the samples with a time period. After recording the initial spectrum, every 4 minutes a new spectrum was recorded and every new emission spectrum of the sample had lesser intensity than the previous spectrum recorded. A total of 30 readings were taken over a period of 2 hours to obtain the emission spectrum for a particular sample. This was done for all the sample immediate after synthesis and then at the end of every month to quantify the KFS. The graphs for the emission are as follows.

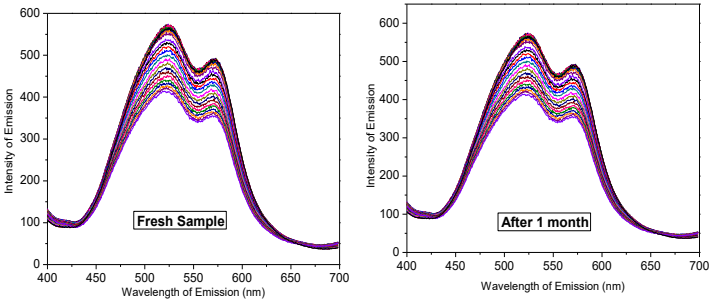

Figure 22: The emission spectroscopy of the CdSe@CarbOPH(O)]@Cl/[N(Caprylyl)$_3$Me$_1$] QDs. Left: fresh sample, right: 1-month old sample.

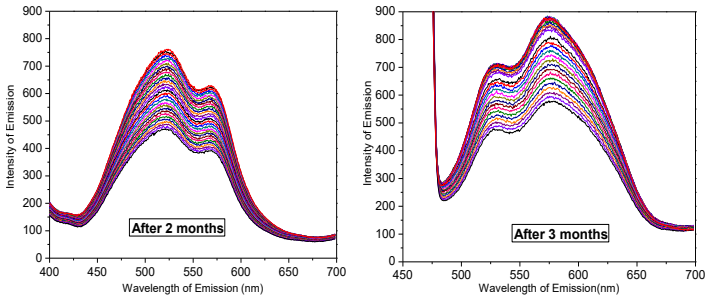

Figure 23: The emission spectroscopy of the CdSe@CarbOPH(O)] @Cl/[N(Caprylyl)$_3$Me$_1$] QDs. Left: 2 months old sample, right: 3 months old sample.

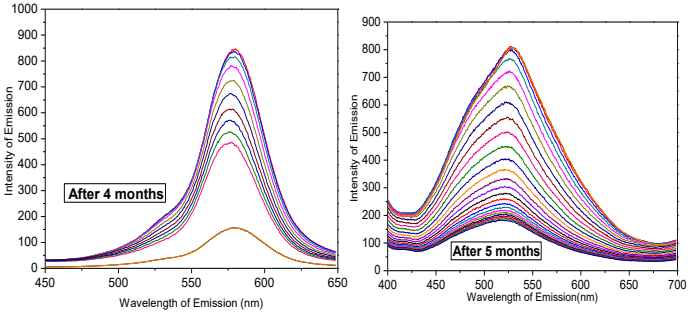

Figure 24: The emission spectroscopy of the CdSe@CarbOPH(O)]@Cl/[N(Caprylyl)$_3$Me$_1$] QDs. Left: 4 months old sample, right: 5 months old sample.

The initial samples show 2 emission peaks but as they age the peaks are shifted more towards the right and become a single peak. The initial presence of two peaks is due to the presence of two differently sized particles possibly. The smaller ones are more in number initially and dominate the luminescence colour and therefore the initial luminescence is yellow and the peak appears around 530nm. But as the QDs age the wavelength of emission red-shifts and is closer to 560nm. As the particles grow in size the emission colour also changes from yellow to orange and therefore there is a change in the emission wavelength. The second peak on the left disappears and there is a single peak remaining, which tells us that only QDs of a single size are present currently in the dispersion. This is also the reason probably for the increase in the intensity of emission as all the QDs are of a single size and they all emit the same colour, the intensity is not divided in different wavelengths as before and thus it increases with the passage of time. The change in the wavelength of emission is depicted below along with the change of emission from 2 peaks to 1 peak.

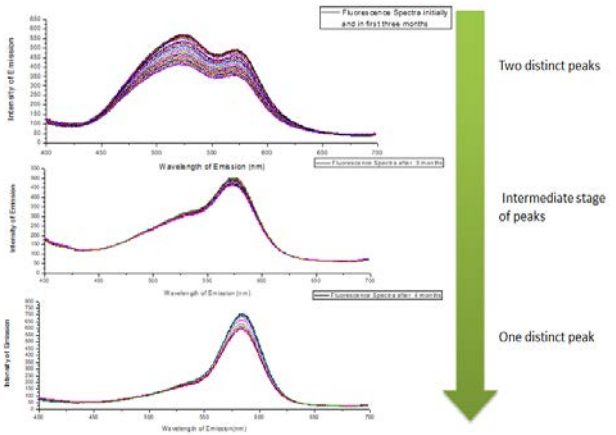

Figure 25: The change in the wavelength of emission of the CdSe@CarbOPH(O)] @Cl/[N(Caprylyl)$_3$Me$_1$] QDs. Initial samples have 2 peaks of emission due to two differently sized QDs but with time as the QDs grow in size and it becomes more uniform we obtain a single emission peak.

From the different emission graphs of the QDs, to represent the KFS we plotted the intensities of the emission over time. The 30 different maximums of emission spectra obtained periodically was plotted against time and 3 such cycles were done for an initial sample and the samples after every month. The initial samples showed lower intensity but had a wider plateau because they took more time to settle down and lose their intensity. The degradation against time was slower as the QDs due to their smaller size were better dispersed in the solvent. But with passage of time, the QDs grew in size and were considerably little less stable in the suspension and therefore they settled down quicker giving narrower plateaus, but they were of higher intensity. Interestingly though, when the area of these graphs was compared, it was seen that the area remained constant for a new and old sample, thereby proving that the number of photons is preserved.

3.1.1. Core-Canopy Quantum Dots

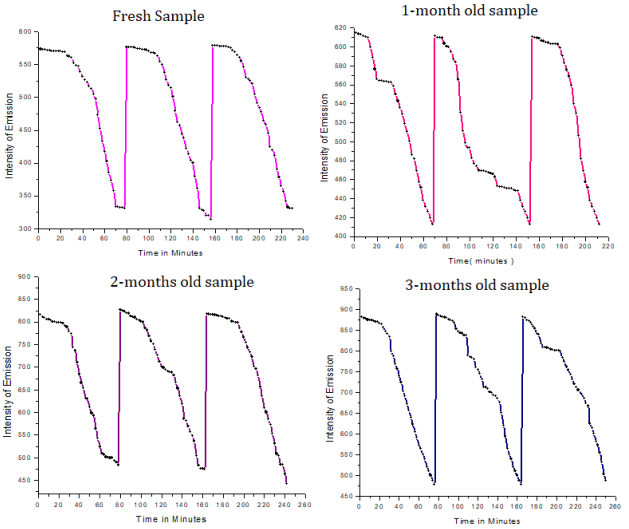

Figure 25: The graphical representation of KFS of the CdSe@CarbOPH(O)]@Cl/[N(Caprylyl)$_3$Me$_1$] QDs for the 1st 3 months.

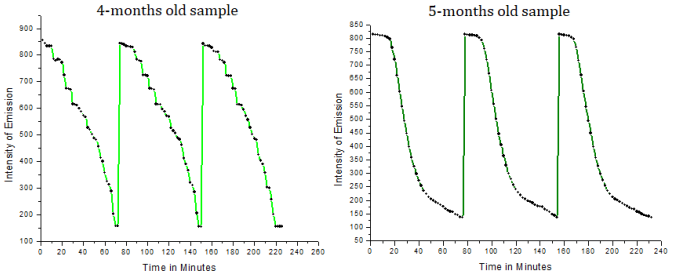

Figure 26: The graphical representation of KFS of the CdSe@CarbOPH(O)]@Cl/[N(Caprylyl)$_3$Me$_1$] QDs for the 4th and 5th months.

The graph shown after this shows us the difference in the plateaus of the initial and the older samples.

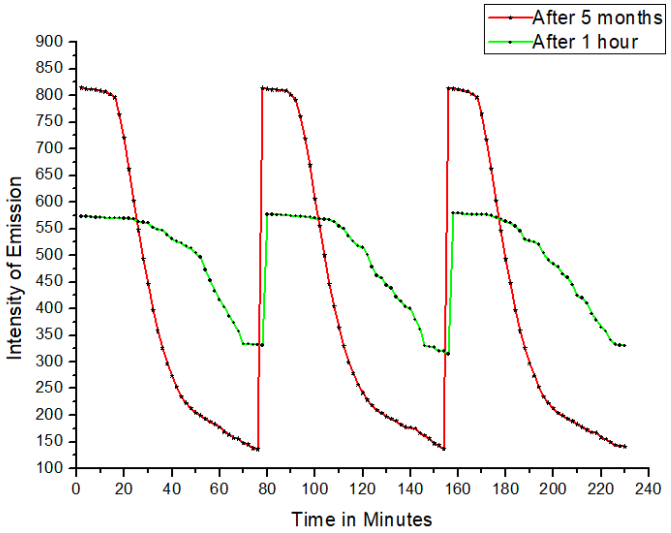

Figure 27: The graphical representation of KFS of the CdSe@CarbOPH(O)]@Cl/[N(Caprylyl)$_3$Me$_1$] QDs for the 1st and 5th months. The plateaus for the 1st month are broader than the 5th month one but the area remains constant so the number of photons is preserved.

4.2. TEM, DLS and Size

Transmission electron microscopy (TEM) studies were carried out using JEOL JEM 1210 at 120 kV. TEM samples were made by dropping a drop of carboranyl capped CdSe suspension onto the carbon coated copper grids. Dynamic Light Scattering (DLS) measurements were carried out in the Zetasizer Nano ZS (DLS light source used was He-Ne Laser, 633nm, Max 4mW, back scattering angle used was 173^o). ImageJ software was used for measuring the particles.

TEM Study: The TEM showed spherical QDs. The size from the TEM was estimated using the Gaussian graphs. A total of 250 QDs were manually measured and then the Gaussian size graphs were plotted and their mean size was obtained. It is shown in Figure 28 and 29.

3.1.1. Core-Canopy Quantum Dots

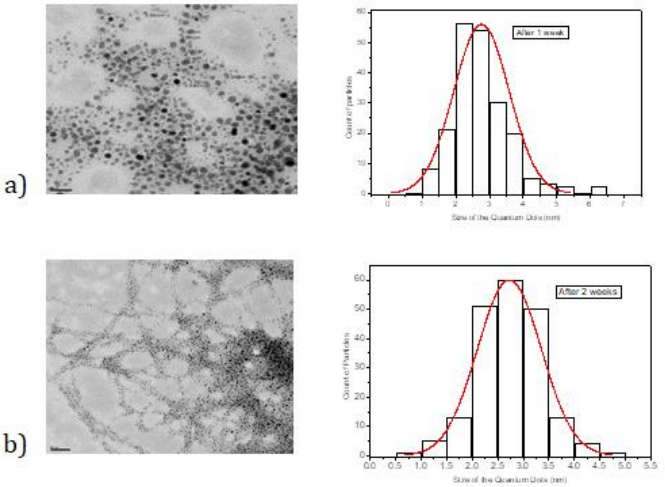

Figure 28: The TEM images and the gaussian size graphs of the CdSe@CarbOPH(O)]@Cl/[N(Caprylyl)$_3$Me$_1$] QDs after (a) 1 week, (b) after 2 weeks.

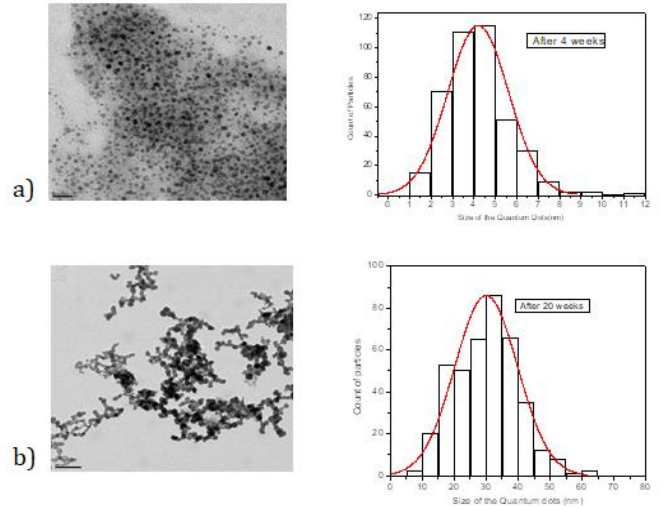

Figure 29: The TEM images and the gaussian size graphs of the CdSe@CarbOPH(O)]@Cl/[N(Caprylyl)$_3$Me$_1$] QDs after (a) 1 week, (b) after 2 weeks.

DLS Study: The size of the particles was also measured with DLS and it showed slight differences in size distribution for the first few weeks, though the major difference in size with respect to the TEM was in the sample which was nearly six months old. This is because the measurement in TEM is done by evaporating the solvent on the grid which causes the particles to aggregate, while the measurement of DLS is done while the particles are in suspension so they are not aggregated and therefore the dimensions of the QDs still fall within the quantum confinement values. The Figure 30 shows the DLS measurements vis Intensity and Volume both. After that there is a table which summarise the sizes obtained with both TEM and DLS.

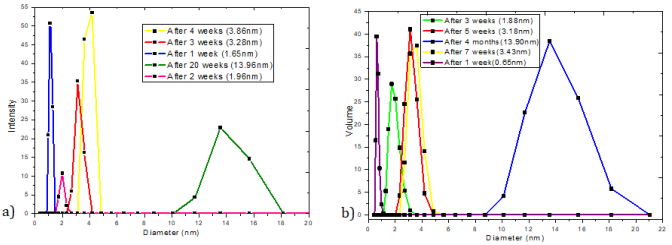

Figure 30: The DLS graphs of the CdSe@CarbOPH(O)]@Cl/[N(Caprylyl)$_3$Me$_1$] QDs after (a) Intensity measurement by DLS (b) Volume measurement by DLS.

QDs	QDs Size by TEM	QDs Size by DLS
1 week old QD	2.57nm	1.65nm
2 weeks old QD	3.94nm	1.96nm
3 weeks old QD	4.21nm	3.28nm
4 weeks old QD	4.9nm	3.86nm
20 weeks old QD	30.6nm	13.96nm

Table 3: The sizes by DLS and TEM for CdSe@CarbOPH(O)] @Cl/[N(Caprylyl)$_3$Me$_1$] QDs.

4.3. Chemical Composition Studies

Infrared Spectrum (IR) studies were done using the Perkin Elmer Spectrum One FT-IR machine. Energy Dispersive X-ray Spectroscopy (EDX) analysis was done using the QUANTA FEI 200 FEG-ESEM device and the sample was analyzed on the TEM grids. Organic Elemental Analysis was carried out in Flash EA 2000 CHNS, Thermo Fischer Scientific and EA 3010 EuroVector.

IR Study: The presence of both $[N(Caprylyl)_3Me_1]^+$ and $[CarbOPH(O)]^-$ in QDs is visible in IR spectrum through inspection of the B-H and C-H stretching bands in the old and as well as the new samples. The IR of the QDs are compared with the IR of the ligand and we can clearly see the B-H stretching at the same position for the ligand and the QD.

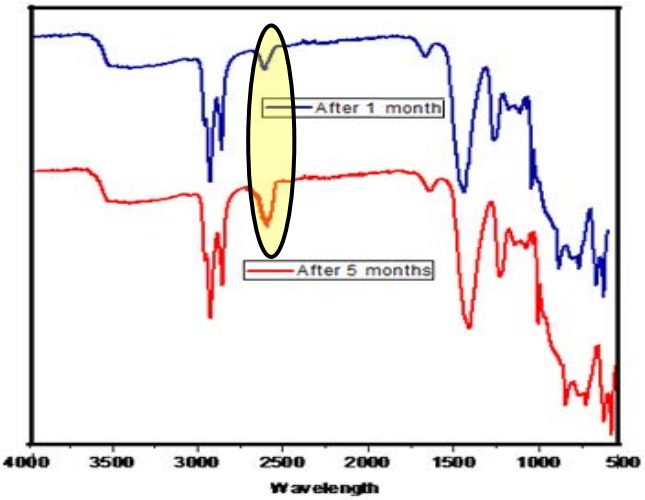

Figure 31: IR Spectrum of [CdSe@CarbOPH(O)] @Cl/$[N(Caprylyl)_3Me_1]$ after 1 month(blue) and after 5 months(red). It shows the B-H bond stretching from Carboranyl Phosphinate and the C-H bond stretching from the numerous C-H groups present in the Alkyl Ammonium.

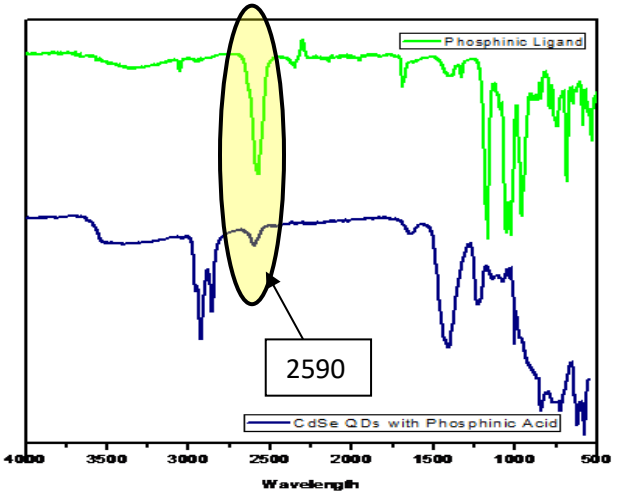

Figure 32: IR Spectrum of [CdSe@CarbOPH(O)] @Cl/[N(Caprylyl)$_3$Me$_1$] after 1 month(blue) and the Phosphinic ligand(green). The IR of the sample shows the B-H bond stretching from Carboranyl Phosphinate which corresponds to the B-H stretching from the ligand. The C-H bond stretching from the numerous C-H groups present in the Alkyl Ammonium is also seen in the sample.

EDX and Chemical Analysis: Common CdSe quantum dots have excess cadmium on the surface, thus they need anionic species to compensate the charge. This is also what happens with [CdSe@CarbOPH(O)] @Cl/[N(Caprylyl)$_3$Me$_1$] QDs. The EDX study of the heavy elements composition (Figure 33 and 34) along with the elemental analysis (EA, Table 4 and 5) indicates that a young sample, up to three months old, has a composition [Cd$_8$Se$_6$@(CarbOPH(O))$_4$]@[Cl]$_{2.5}$/[N(Caprylyl)$_3$Me$_1$]$_{2.5}$, whereas the one nearly six months old has the composition [Cd$_7$Se$_6$@(CarbOPH(O))$_4$]@[Cl]$_1$/[N(Caprylyl)$_3$Me$_1$]$_3$. The results of the EDX and EA match very well with these compositions. Basically the Se, [CarbOPH(O)]$^-$ and [N(Caprylyl)$_3$Me$_1$]$^+$, remain unaltered while there is a decrease in Cd that is probably lost as $CdCl_2$.

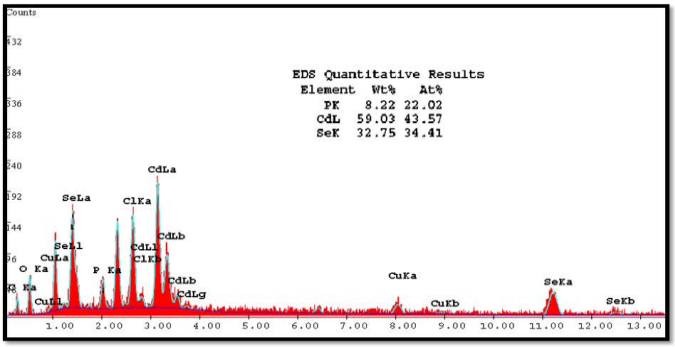

Figure 33: Energy dispersive X-ray (EDX) of the [CdSe@CarbOPH(O)]@Cl/[N(Caprylyl)$_3$Me$_1$] QD after 3 months. It shows the presence of Cadmium, Selenium and Phosphorus and their percentage of presence in the QD at that time. The formula obtained is [Cd$_8$Se$_6$@(CarbOPH(O))$_4$]@[Cl]$_{2.5}$/[N(Caprylyl)$_3$Me$_1$]$_{2.5}$

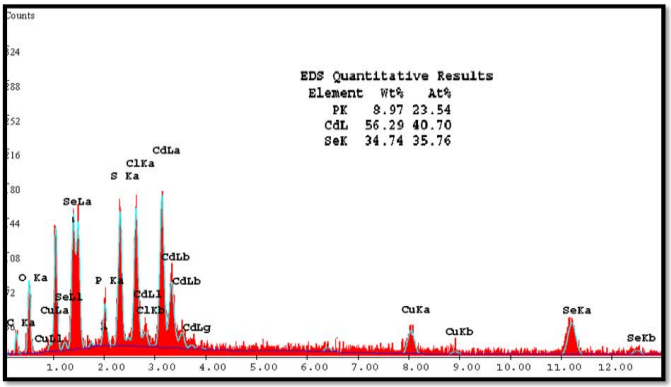

Figure 34: EDX of the [CdSe@CarbOPH(O)]@Cl/[N(Caprylyl)$_3$Me$_1$] QD after 5 months. It shows the presence of Cadmium, Selenium and Phosphorus and their percentage of presence in the QD at that time. The formula obtained is [Cd$_7$Se$_6$@(CarbOPH(O))$_4$]@[Cl]$_1$/[N(Caprylyl)$_3$Me$_1$]$_3$

Sample	% C	% N	% H
CdSe@CarbPH(O)O/[N(Caprylyl)$_3$Me$_1$] QDs (3 months old-Analysis1)	27.3 %	1.1%	5.5 %
CdSe@CarbPH(O)O/[N(Caprylyl)$_3$Me$_1$] QDs (3 months old-Analysis2)	25.34%	1.01 %	5.28 %
CdSe@CarbPH(O)O/[N(Caprylyl)$_3$Me$_1$] QDs (3 months old-Analysis Average)	26.32%	1.055 %	5.39 %

Table 4: The Elemental Chemical Analysis studies show the percentage of Carbon, Nitrogen and Hydrogen present in the sample. It corresponds with the estimated value obtained from the EDX studies of a sample 3 months old and the formula derived from it.

Sample	% C	% N	% H
CdSe@CarbPH(O)O/[N(Caprylyl)$_3$Me$_1$] QDs (6 months old-Analysis1)	28.62%	1.11%	5.72 %
CdSe@CarbPH(O)O/[N(Caprylyl)$_3$Me$_1$] QDs (6 months old-Analysis2)	30.5%	1.16 %	4.59 %
CdSe@CarbPH(O)O/[N(Caprylyl)$_3$Me$_1$] QDs (6 months old-Analysis Average)	29.56%	1.135 %	5.155 %

Table 5: The Elemental Chemical Analysis studies show the percentage of Carbon, Nitrogen and Hydrogen present in the sample. It corresponds with the estimated value obtained from the EDX studies of a sample 6 months old and the formula derived from it.

Electron Diffraction Studies: The electron diffraction studies were done for the core-canopy QDs. The diffraction patterns were quite amorphous for the samples and the rings were quite faint. They were analysed using Gatan and the (hkl) indices were studied for CdSe. It was determined that the QDs had the hexagonal wurtzite crystalline phase of CdSe. The patterns were studied on TEM copper grids. It was done

for both old and new samples and all the samples showed hexagonal phase of CdSe.

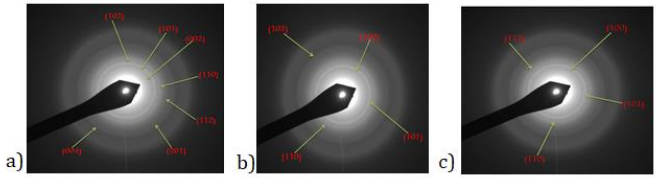

Figure 35: Electron Diffraction of the [CdSe@CarbOPH(O)]@Cl/[N(Caprylyl)$_3$Me$_1$] QDs after different time periods. All confirm the presence of CdSe in its hexagonal structure. (a) Electron Diffraction of [CdSe@CarbOPH(O)]@Cl/[N(Caprylyl)$_3$Me$_1$] QD after 1 month (b) Electron Diffraction of [CdSe@CarbOPH(O)]@Cl/[N(Caprylyl)$_3$Me$_1$] QD after 3 months (c) Electron Diffraction of [CdSe@CarbOPH(O)]@Cl/[N(Caprylyl)$_3$Me$_1$] QD after 5 months.

4.4. Zeta Potential Studies

Zeta Potential was measured using the Zetasizer Nano ZS. Zeta-Potential is a technique which helps us determine the stability of a colloidal system. Zeta-potential as defined is the potential difference between the slipping plane in the electronic double layer and the bulk potential. The values of zeta-potential when above $\pm$30 means that the particles are electrostatically stable. Although in colloidal system the stability of the particles is dependent on electrostatic and steric repulsion, zeta potential can still be considered as a good indication of the stability of the particles in the dispersing media. The Zeta Potential was measured of the samples and the value obtained was around -44mV on average over different time periods of time, thus indicating that the suspension is stable. It was measured for a new sample and the aging samples. It showed that while the particles remained in the suspension state, they were quite

stable. Zeta Potential was measured using the electrophoretic light scattering principle.

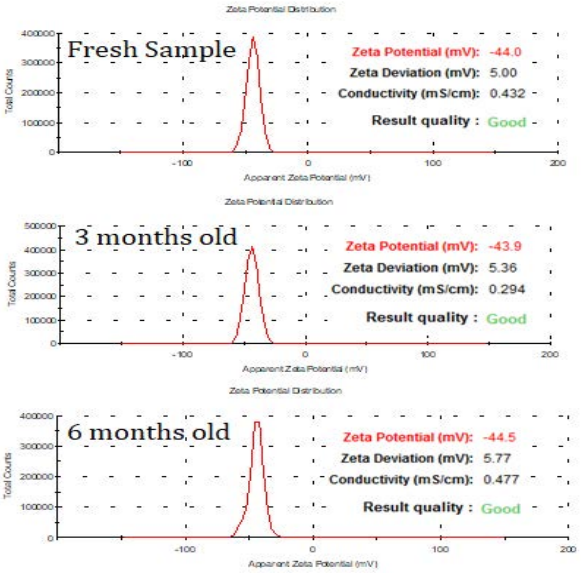

Figure 36: Zeta Potential values of the [CdSe@CarbOPH(O)]@Cl/[N(Caprylyl)$_3$Me$_1$] QDs after being freshly made, after 3 months and after 6 months.

5. Comparisons

The [CdSe@CarbOPH(O)]@Cl/[N(Caprylyl)$_3$Me$_1$] QDs were compared further with the QDs prepared with Phenyl phosphinate in order to see the relevance of the spherical ligands. The phenyl moiety is 2-D compared to the carborane cluster which is 3-D and it does not produce close packing like the carborane ligand yet having similar size. So we wanted to check how it fared with regard to the CarbPhos. Also, comparison was done with QDs synthesized with the usual capping of mercaptoacetic acid (MAA) in water.

5.1. Comparison with Phenyl Phosphinate

If the close packing of spheres was not relevant, then a rotating phenyl moiety occupying a comparable volume to a carboranyl group, and the fact that both Phenylphosphinic and Carboranylphosphinic have comparable pKa values (1.77 and 1.32, respectively) it could be expected that the KFS phenomenon could be also observed with phenylphosphinic acid. But this was not the case as has been stated before. The resulting CdSe QDs done with phenylphosphinic acid (CdSe@PhenPhos) precisely with the same ratio of reagents and temperature conditions did not show the KFS properties, although they were brightening for about one day after their synthesis but with much less intensity than the corresponding carboranyl ones. This experiment is reminiscent of the CdSe QDs with only CarbOPH(O)$^-$ in Figure 16 from C to D. The P:Cd:Se ratio obtained from EDX that is 2:12:7 is extremely enlightening for the CdSe@PhenPhos QD for which the load of phosphinic acid has dropped (*vs.* Cd) from ½ in [CarbOPH(O)]$^-$ QDs to 1/6 in the PhenylPhosphinic acid QDs. Further the 2:12:7 ratio in the CdSe@PhenPhos QDs produces an imbalance of charges, 24$^+$ for Cd and 16$^-$ for Se and phosphinic acid; this imbalance of positive charges along with the absence of voids in which to trap Cl$^-$ does not make the participation of cationic surfactants any easier from the perspective of the KFS as they would add even more positive charges. Moreover, the intensity of luminescence of the QDs with PhenPhos were quite low.

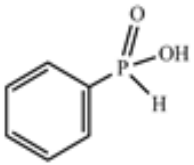

Phenylphosphinic acid

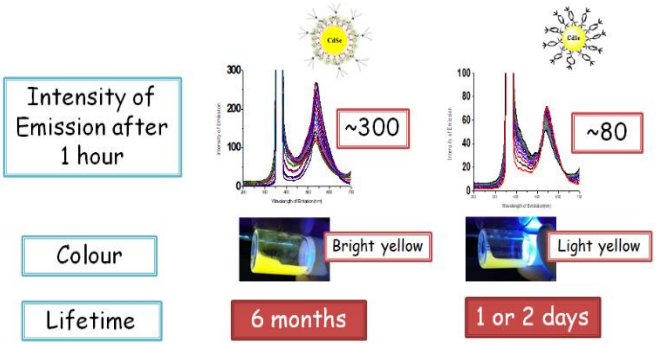

Figure 37: Comparison of the [CdSe@CarbOPH(O)]@Cl/[N(Caprylyl)$_3$Me$_1$] QDs with [CdSe@PhenPhos] @Cl/[N(Caprylyl)$_3$Me$_1$.

The comparison with the 2-D Phenyl moiety helps us to further consolidate that the spherical ligands are needed to obtain the KFS property and highly intense QDs.

5.2. Comparison with MercaptoAcetic Acid

The QDs synthesized in water with Mercaptoacetic Acid (MAA) or Mercaptopropionic Acid (3-MPA) do not show any such remarkable property as KFS. Not only that, the intensity obtained from the [CdSe@CarbOPH(O)]@Cl/[N(Caprylyl)$_3$Me$_1$] is also nearly 100 times more than the MAA capped CdSe with respect to the arbitrary units of the fluorometer. These core-canopy QDs have a much higher brightness and also do not require extra nitrogen purging and can be stored under normal conditions for up-to 6 months.

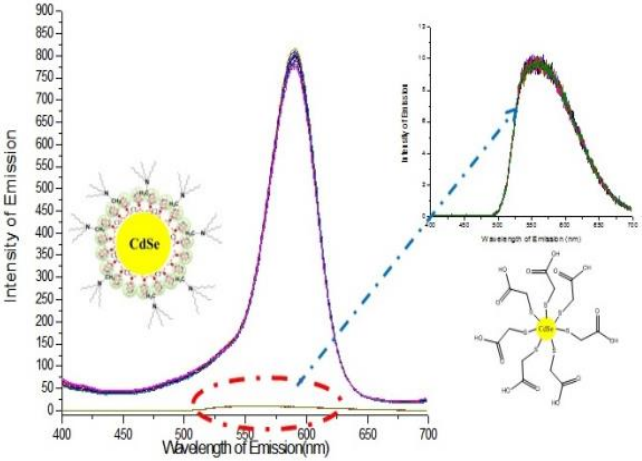

Figure 38: Comparison of the [CdSe@CarbOPH(O)]@Cl/[N(Caprylyl)$_3$Me$_1$] QDs with [CdSe@MAA]. The core-canopy QDs are 100 times more intense than the normal CdSe QDs produced in water.

6. Study with other anions

As established earlier that the KFS property was obtained due to the trapping of the Cl^- inside the voids created by CarbPhos and the synergy between the [N(Caprylyl)$_3$Me$_1$ and CarbPhos, we wanted to carry out a further study regarding the trapping of other anions in the voids. A total of 10 anions were used to test and see how they affect these QDs. The anions used are listed below:

SO_4^{2-}, SO_3^{2-}, NO_3^-, NO_2^-, CH_3COO^-, $Zn(CH_3COO)_2$, I^-, Br^-, ClO_4^- and ClO_3^-.

Out of all these anions, $Zn(CH_3COO)_2$ is a neutral complex. It was used to see how it affects the properties of the QDs. For these tests, [CdSe@CarbOPH(O)]@Cl/[N(Caprylyl)$_3$Me$_1$] was synthesized as it is, only during the initial step while

adding the Cd precursor along with CarbPhos, the salts of the respective anions were added three times the amount of the Cd precursor and stirred in water. After that Se precursor was added and then the surfactant was added and the fluorescence tests were done. This is still just a preliminary study and more work has to be done on this. But from the initial studies done so far, we have the following results. Out of all the cations, SO_4^{2-}, SO_3^{2-}, NO_3^-, NO_2^- show good fluorescence (yellow emission), for a couple of months and they also shift the fluorescence spectra towards the left, that is there is some blue shift in the spectra and they show mild green emission after a month. While CH_3COO^-, $Zn(CH_3COO)_2$ show good fluorescence too, but last only a month. $Zn(CH_3COO)_2$ trapped QDs have good intensity, which is comparable to almost the intensity of the original core-canopy QDs. I^-, Br^- trapped QDs show mild fluorescence emission and do not last more than a few hours. Finally, ClO_4^- and ClO_3^- trapped QDs show no fluorescence at all. The anions SO_4^{2-}, SO_3^{2-}, NO_3^-, NO_2^-, CH_3COO^- trapped QDs and the $Zn(CH_3COO)_2$ trapped QD, all showed KFS while they possessed their emissive properties. The table below summarizes the result obtained.

Anions Used	Fluorescence Results
SO_4^{2-}	It shows KFS for 2 months
SO_3^{2-}	It shows KFS for 2 months
NO_3^-	It shows KFS for 3 months
NO_2^-	It shows KFS for 3 months
CH_3COO^-	It shows KFS for 28 days
$Zn(CH_3COO)_2$	It shows KFS for 25 days
I^-	Mild fluorescence for few hours
Br^-	Mild fluorescence for few hours
ClO_4^-	Doesn't show fluorescence
ClO_3^-	Doesn't show fluorescence

Table 6: The different anions used for the study of trapping them in the voids of the core-canopy QDs in order to see changes in their properties.

The fluorescence emission spectrum given below shows the emission spectrum obtained from the different QDs having different anions trapped in their voids and how the various

spectra vary from the spectrum of the original core-canopy QD.

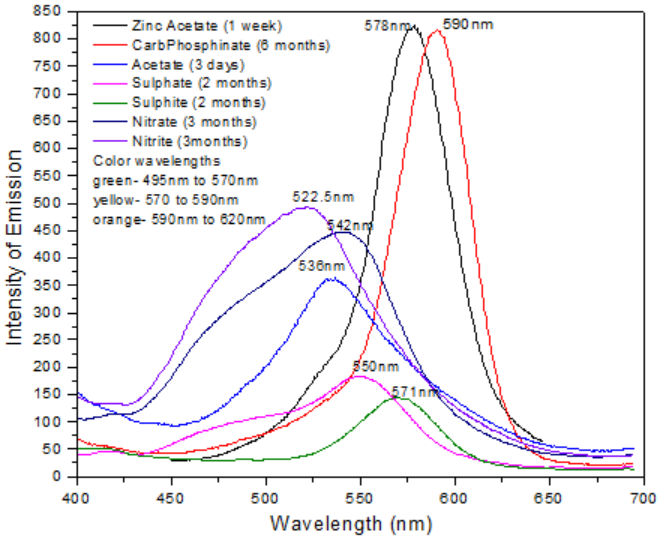

Figure 39: The emission spectra of the different anions used for the study of trapping them in the voids of the core-canopy QDs in order to see changes in their emissive properties.

None of these QDs could maintain the lifetime of the initial core-canopy QDs. All of them need to be further studied and analysed chemically in the future to truly understand how to obtain further changes in the properties of these core-canopy QDs and also how to obtain newer properties in them.

7. Conclusions

By combining CdSe QDs with hollow spheres (carboranylphosphinate ligands) in the particular architecture compact spheres packing/pillars/ground, and tricaprylylmethylammonium to compensate the excess of negative charges, partly created by the trapped Cl^- in generated channels, a synergism is created that produces the unprecedented Kinetic Fluorescence Switching (KFS). The physical observation is that the material shines brightly then loses its brightness; by the mild application of kinetic energy it shines back to the maximum power, and this process continues for an extended period of time, up to half a year at least. The phenomenon is basically structural due to a particular architecture. The spherical carboranyl entities are arranged either in a square or hexagonal close packing to produce maximum coverage of the CdSe surface leaving openings and generating voids/channels that trap anions, in this case Cl^-, that increase the negative charge of the core-canopy QDs. Through the openings the methyl groups from alkylammonium surfactants can be appended. The surfactant, in this case $[N(Caprylyl)_3Me_1]^+$, is the plug that converts the openings into gates.

The KFS property is the result of a core canopy QDs architecture and the adequate choice of the targeted property ingredients, in this case Cl^- and cationic surfactants. We are working on discovering new properties by keeping the same architecture and choosing the addressed property new components. This work has been published in Advanced Materials. [63]

8. References

[1] R. C. Ashoori, *Nature.* **1996,** *379*, 413.

[2] J. Y. Kim, O. Voznyy, D. Zhitomirsky, E. H. Sargent, *Adv. Mater.* **2013,** *25*, 4986.

[3] J. Wang, I. Mora-Sero, Z. Pan, K. Zhao, et al., *J. Am. Chem. Soc.* **2013,** *135,* 15913.

[4] Y. Yang, Y. Zheng, W. Cao, A. Titov, et al., *Nat. Photon.* **2015,** *9,* 259.

[5] W. K. Bae, J. Lim, D. Lee, M. Park, et al., *Adv. Mater.* **2014,** *26,* 6387.

[6] Y. C. Chen, C. Y. Huang, H. C. Yu, Y. K. Su, *J. Appl. Phys.* **2012,** *112,* 034518.

[7] K. K. Haldar, G. Sinha, J. Lahtinen, A. Patra, *ACS Appl. Mater. Interf.* **2012,** *4,* 6266.

[8] Y. Wang, R. Hu, G. Lin, I. Roy, K. T. Yong, *Appl. Mater. Interf.* **2013,** *5,* 2786.

[9] Y. Y. Liu, J. Stehlik, C. Eichler, et al., *Science.* **2015,** *347,* 285.

[10] P. Wu, X. P. Yan, *Chem. Soc. Rev.* **2013,** *42,* 5489.

[11] V. Kannan, H. S. Kim, H. C. Park, *Phys. Lett. A.* **2016,** *380,* 3743.

[12] D. R. Larson, W. R. Zipfel, R. M. Williams, et al., *Science.* **2003,** *300,* 1434.

[13] a) C. R. Kagan, E. Lifshitz, E. H. Sargent, D. V. Talapin, *Science.* **2016,** *353,* 6302; b) M. A. Boles, D. Ling, T. Hyeon, D. V. Talapin, *Nat. Mat.* **2016,** *15,* 141.

[14] S. J. Lim, M.U. Zahid, P. Le, et al., *Nat. Commun.* **2015,** *6,* 8210.

[15] V. Lesnyak, N. Gaponik, A. Eychmuller, *Chem. Soc. Rev.* **2013,** *42,* 2905.

[16] X. Michalet, F. F. Pinaud, L. A. Bentolila, et al., *Science*, **2005,** *307*, 538.

[17] S. Jin, Y. Hu, Z. Gu, L. Liu, H. C. Wu, *J. Nanomater*., **2011,** *2011*, 1.

[18] N. A. Bakar, A. A. Umar, T. H. T. Aziz, et al., (Eds.): *Semiconductor Electronics, 2008 ICSE*, 2008 IEEE Int. Conf., **2008.**

[19] D. Zhao, Z. He, W. H. Chan, M. M. F. Choi, *J. Phys. Chem. C*, **2008,** *113*, 1293.

[20] C. R. Bullen, P. Mulvaney, *Nano Lett.,* **2004,** *4,* 2303.

[21] W. W. Yu, X. Peng, *Angew. Chem. Int. Ed.,* **2002,** *41,* 2368.

[22] L. Li, H. Qian, N. Fang, J. Ren, *J. Lumin.,* **2006,** *116,* 59.

[23] A. L. Rogach, A. Kornowski, M. Gao et al., *J. Phys. Chem. B*, **1999,** *103,* 3065.

[24] L. Qu, Z. A. Peng, X. Peng, *Nano Lett.,* **2001,** *1,* 333.

[25] N. Gaponik, D. V. Talapin, A. L. Rogach, et al., *J. Phys. Chem. B*, **2002**, *106*, 7177.

[26] A. L. Rogach, L. Katsikas, A. Kornowski, D. Su, et al., *Berichte der Bunsengesellschaft für physikalische Chemie*, **1996,** *100*, 1772.

[27] J. Weng, X. Song, L. Li, et al., *Talanta,* **2006,** *70*, 397.

[28] B. O. Dabbousi, J. Rodriguez-Viejo, F. V. Mikulec, et al, *J. Phys. Chem. B,* **1997**, *101,* 9463.

[29] D. V. Talapin, A. L. Rogach, A. Kornowski, M. Haase, H. Weller, *Nano Lett.*, **2001**, *1,* 207.

[30] D. V. Talapin, A. L. Rogach, E. V. Shevchenko, et al., *J. Am. Chem. Soc.*, **2002**, *124*, 5782.

[31] S. M. Farkhani, A. Valizadeh, *IET Nanobiotechnology,* **2014**, *8,* 59-76.

[32] Y. Wang, H. Yang, Z. Xia, Z. Tong, L. Zhou, *Bull.Korean Chem. Soc.* **2011**, *32*, 2316.

[33] R. M. Hodlur, M. K. Rabinal, *Chem. Eng. J.* **2014**, *244*, 82.

[34] Y. Yan, X. Liu, C. Ma, Y. Yan, G. Yao, Y. Tang, P. Huo, W. Shi, *Ind. Eng. Chem. Res.* **2013**, *52*, 15015.

[35] S. M. Farkhani, A. Valizadeh, *IET Nanobiotechnology,* **2014**, *8,* 59.

[36] Y. Zhang, A. Clapp, *Sensors*, **2011**, *11,* 11036.

[37] D. Zhao, Z. He, W. H. Chan, M. M. F. Choi, *J. Phys. Chem. C*, **2008,** *113*, 1293.

[38] A. Eychmüller, A. L. Rogach, *Pure Appl. Chem.,* **2000**, *72*, 179.

[39] T. Vossmeyer, L. Katsikas, M. Giersig, et al, J. *Phys. Chem.*, **1994**, *98*, 7665.

[40] Y. N. Hong, J. W. Y. Lam, B. Z. Tang, *Chem. Soc. Rev.* **2011,** *40,* 5361.

[41] M. Noha, T. Kima, H. Leea, C. Kimb, S. Jooc, K. Leea, *Colloids Surf., A: Physicochem. Eng. Aspects.* **2010,** *359,* 39.

[42] H. Mattoussi, J. M. Mauro, E. R. Goldman, et al., *J. Am. Chem. Soc.*, **2000**, *122*, 12142.

[43] T. J. Deerinck, *Toxicol. Pathol.,* **2008**, *36*, 112.

[44] Z. J. Zhu, Y. C. Yeh, R. Tang, R., et al., *Nat. Chem*., **2011**, *3*, 963.

[45] Q. F. Ma, J. Y. Chen, P. N. Wang, et al., *J. Lumin.*, **2011**, *131*, 2267.

[46] V. W. Manner, A. Y. Koposov, P. Szymanski, et al., *ACS Nano*, **2012**, *6,* 2371.

[47] Y. C. Cao, J. Wang, *J. Am. Chem. Soc.*, **2004**, *126*, 14336.

[48] A. L. Rogach, T. Franzl, T. A. Klar, et al., *J. Phys. Chem. C*, **2007**, *111*, 14628

[49] S. Y. Choi, J. P. Shim, D.S. Kim, et al., *J. Nanomater*., **2012**, *2012*, 10.

[50] R. J. Temansky, D. W. Balogh, L. A. Paquette, *J. Am. Chem. Soc.* **1982,** *104,* 4503.

[51] J. Poater, M. Sola, C. Viñas, F. Teixidor, *Angew. Chem. Int. Ed.* **2014,** *53,* 12191.

[52] J. Poater, M. Sola, C. Viñas, F. Teixidor, *Chem. Eur. J.* **2013,** *19,* 4169.

[53] J. Poater, M. Sola, C. Viñas, F. Teixidor, *Chem. Eur. J.* **2016,** *22,* 7437.

[54] R.N. Grimes, *Carboranes,* 3rd Ed, *Elsevier*. **2016**.

[55] R. Caputo, S. Garroni, D. Olid, F. Teixidor, S. Suriñach, M.D. Baro, *Phys. Chem. Chem. Phys.* **2010,** *12,* 15093.

[56] A. M. Cioran, A. D. Musteti, F. Teixidor, Ž. Krpetić, I. A. Prior, Q. He, C. J. Kiely, M. Brust, C. Viñas, *J. Am. Chem.Soc*. **2012,** *134,* 212.

[57] C. Viñas, R. Benakki, F. Teixidor, J. Casabó, *Inorg. Chem*.,**1995**, *34,* 3844–3845.

[58] E. Oleshkevich, F. Teixidor, D. Choquesillo-Lazarte, R. Sillanpää, C. Viñas, *Chem. Eur. J.* **2016,** *11,* 3665.

[59] R. Gomes, A. Hassinen, A. Szczygiel, Q. Zhao, A. Vantomme, J. C. Martins, Z. Hens, *J. Phys. Chem. Lett.* **2011,** *2,* 145.

[60] S. Taniguchi, M. Green, S. B. Rizvi, A. Seifalian, *J. Mater. Chem.* **2011,** *21,* 2877.
[61] A. E. Raevskaya, A.L. Stroyuk, S.Y. Kuchmiy, *J. Colloid Interface Sci.* **2006,** *302,* 133.
[62] P. Frantsuzov, M. Kuno, B. Janko, R. Marcus, *Nature Phys.* **2008,** *4,* 519.
[63] A. Saha, E. Oleshkevich, C. Vinas, F. Teixidor, *Adv. Mat,* **2017,** *29,* 1704238.

3.1.2. Next Stage in Aqueous Synthesis of Quantum Dots

QDs of CdSe have been produced with high yield and showing high QY using common reagents in water at 150oC using ace pressure tubes. Their size and emission can be controlled similarly to the organometallic method of synthesizing QDs and can be stored dry very easily. The prepared QDs have shown the same intense emission for over a year after being synthesized.

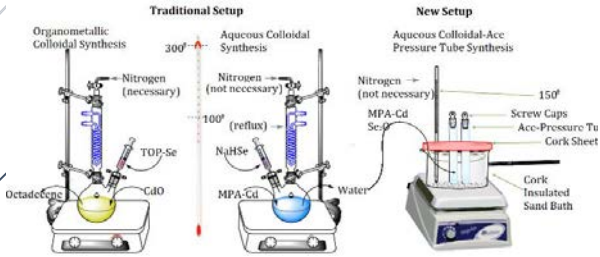

Arpita Saha
ICMAB-CSIC (UAB)

Contents

1. Introduction

Quantum Dots (QDs) have already been introduced in the thesis. It has also been previously explained that QDs differ by composition of the elements and the choice of solvent in which they are produced. As seen in the previous chapter, that we have concentrated ourselves with the aqueous method due to its numerous advantages. In-spite of the number of advantages, the aqueous method does possess a lot of disadvantages. We were successful in producing highly luminescent QDs with a new architecture using carborane ligands, but on being able to obtain that and have gained some experience in this field, we wanted to try to synthesize QDs in water using common reagents with improved properties. Carborane capped QDs, though provided us with a new architecture which could pave the way for us to obtain new properties using that architecture, are expensive for the common applications of the QDs in today's world. The recent problems of QDs in water are primarily its low quantum yield (QY) [1] and the precise tuning of its size in order to obtain different luminescence colours [2]. Though there are few examples where people have tried new methods, new precursors and size selection processes like in organometallic method of synthesising them [3], there has been less success so far and the research still demands considerable attention. This motivated us to work towards this particular problem of devising a water based synthetic route to obtain QDs with different luminescent colours and a higher QY. The next section describes what improvements we have been able to make using a new method of synthesis. The aqueous synthesis procedure used by us helps to improve certain aspects of the QD properties even though using the common reagents used for water based synthetic route.

1.1. Aqueous vs Organometallic vs Our Method

We have been able to design a new synthetic procedure for CdSe QDs in water producing a high throughput, emitting intense fluorescence and possessing a high QY of almost 80% by using simple glass pressure tubes at an easily achievable high temperature. The method uses the most common precursors needed for the synthesis of CdSe QDs in water and by changing the temperature and synthetic vessel commonly used we obtain QDs which are extremely intense when compared to other CdSe QDs synthesized in water and they also give us a higher yield. They can be easily isolated in solid form and dispersed in ethanol, toluene or remain suspended in water and they can also preserve their fluorescence for more than a year in the suspended state. This procedure leads the way for a QD synthesis in water which can match the fluorescence emission properties of those QDs which are produced in an organometallic synthesis. It is also able to synthesize QDs in water emitting different colors of emission by changing the time duration of the synthesis. The synthesis opens a new avenue in the synthesis of QDs in water with varying colors of emission, along with an enviably high quantum yield and high yield of QDs in powdered form and long durability in terms of the fluorescence emission. The Table 1 below summarizes the attributes between the standard aqueous method and our aqueous synthetic route vs the organometallic route of synthesizing QDs. It shows the advantages of the organometallic method vs the standard aqueous method and the fact that our improved synthetic method helps to produce QDs combining the advantages of both the organometallic method and the aqueous method. It imbibes the size selectivity, broad fluorescing range of colors from the organometallic synthesis while preserving the low cost, environmental-friendly and easy separability aspect of the aqueous synthetic route.

3.1.2. Next Stage in Aqueous Synthesis of Quantum Dots

Organic Synthesis	**Commonly used Aqueous Synthesis**	**Our New Method of Aqueous Synthesis**
High Quantum Yield (QY) (up-to 85% for CdSe and 65% for CdTe) [2,4,5]	Lower QY (up-to 4.1% using SeO_2 as precursor for CdSe) [1]	High QY (up-to 80%)
Wide range of colours (from blue to red)	Smaller range of colours (usually individual colours or yellow and orange emission)	Good range of colours (from green to red)
Better control over size [2,4,5]	Less control over size	Better control over size than previous aqueous syntheses
Use of extremely high temperatures (above 200°C used) [2]	Room temperature or Lower temperatures of 100°C used [6]	Moderately high temperatures used (150°C)
Longer lifetime with less decay in emissive properties	Shorter lifetime with rapid decay in emissive properties	Longer lifetime with very less degradation in emissive properties
Hard to isolate in powdered form	Easy isolation in powdered form [2]	Easy isolation in powdered form and in large quantities
Toxic solvent, difficult to dispose or remove	Green solvent and environmentally friendly	Green solvent and environmentally friendly
Difficult to use them in medical applications as it requires cumbersome ligand exchange reactions to make them water soluble [2]	Can be easily used in medical applications but lack the intense emissive properties of organically synthesized QDs [2]	Can be easily used in medical applications and possesses the intense emissive properties of the organically synthesized QDs
Quicker reaction time [2]	Sometimes the reactions are slower and longer taking up to days for the synthesis of QDs	Quicker reaction time

Table 1: Summary of the properties of QDs from different methods.

1.2. Commonly Used Ligands and Synthetic routes

The QDs can be synthesized in many ways but the colloidal synthetic route remains the primary method for this because it is the most facile and easy way to produce QDs in large quantities. [7] Among the many different combinations of elements used for the synthesis of these semiconductor nanocrystals, CdSe nanocrystals continue to be the most investigated QD till date. The continued interest in CdSe originates from its easy synthetic procedure and the allowance of an exceptional degree of control in the size and shape of the QDs to be produced. [8-10] The colloidal method is preferred for its easy reproducibility and by changing the solvent and the ligands during the synthesis, the size and the properties can be easily manipulated. There are many different types of colloidal methods used to synthesize QDs for the last two decades. It started initially with arrested precipitation synthesis process. In this, dilute solutions in water based medium with low heat or almost no heat was used. The method was highly crude and gave samples which were not crystalline and had poor properties and could not be scaled up easily either. After, this came the method of decomposing metal-organic salts or organometallic precursors in hot coordinating solvents. This method of organometallic synthesis using hot-injection method became very popular and used tri-*n*-octylphosphine (TOP) commonly for passivating the surface and also as solvent. This method typically uses high temperature (above 200^{o}C), but it has a major problem of isolating the QDs. It can be done by centrifugation and by adding non solvents like methanol or ethanol to precipitate the QDs, but the obtained quantity is less and yield is very poor. It also does not produce very biocompatible QDs. So aqueous method was explored. It tried to follow the same decomposition of metal salts in water. These used mild temperature and conditions. These QDs could not match the properties obtained with the previous organometallic synthesis. Due to this a lot of research went into obtaining new synthetic

routes using new precursors and also using microwaves or autoclaves for synthesizing QDs. This is still an ongoing field of research and improvements are still being made every day and QDs with better properties are being made. But in all of this, the requirement for finding a purely water-based method without the use of external instruments like autoclaves or microwaves remains crucial and we tried to contribute to wards this problem with the method we have designed. The tables 2 and 3 below show some examples of all the different ligands and methods which have been predominantly used to prepare CdSe QDs of different kinds.

QD Type	Synthesis method	Solvent	Capping Ligand	Reference
CdS	Arrested precipitation	Acetonitrile or water	Styrene/maleic anhydride copolymer	Rossetti et al. [3]
CdS	Arrested precipitation	Water	Thiophenol	Noglik & Pietro [11]
CdS	Arrested precipitation	Water	Uncapped/Stabilized	Ladizhansky et al. [12]
CdSe, CdSe/CdS, CdS/CdSe	Arrested precipitation	Water	$(NaPO_3)_6$	Tian et al. [13]
CdS	Organometallic Synthesis	TOPO, 1-Octadecene	TOPO, pyridines, 4-picolene, tris(2-ethylhexyl)phosphate, 4-trifluoromethyl(thiophenol)	Kuno et al. [14] Murray et al. [15] Ludolph et al. [16]
CdSe	Organometallic Synthesis	TOPO, TOP, 1-Octadecene, Hexylphosphonic acid (HPA)	TOPO, Oleic acid, n-tributylphosphine (TBP)	Murray et al. [15] Ludolph et al. [16] Ubani et al. [17] Bowen Katari et al. [18]

Table 2: QDs synthesized using different ligands and methods

3.1.2. Next Stage in Aqueous Synthesis of Quantum Dots

QD Type	Synthesis method	Solvent	Capping Ligand	Reference
CdS	Microwave	N, N, dimethylformamide	Thiourea	Wada et al. [19]
CdSe	Microwave	Water	Common thiols, ethylene glycol	Grisaru et al. [20]
CdS	Langmuir Blodgett	Aqueous solutions of precursors used	Poly (maleic anhydride)	Peng et al. [21]
CdSe	Langmuir Blodgett	Aqueous solutions of precursors used	Arachidic acid	Facci et al. [22]
CdSe	Langmuir Blodgett	Aqueous solutions of precursors used	16-8 diynoic acid	Scoberg et al. [23]
CdSe	Autoclave	Water	3-MPA	Li et al. [24]

Table 3: QDs synthesized using different ligands and methods.

As seen in the above-mentioned tables 2 and 3 that various methods have been used to synthesize QDs in water and other solvents and at different temperatures to get improved luminescent properties and higher yield. But all the processes have one or the other issues. In order to minimize the majority of the problems faced by the synthetic routes of obtaining QDs and to enhance the properties possessed by these synthesized QDs, we used ace-pressure tube synthesis which is described in the next section.

2. Ace-Pressure Tube Synthesis

The ace-pressure tube synthesis was designed by our group to synthesize QDs in water at a moderately high temperature and high pressure in glass tubes with screw caps. These glass tubes are called the ace-pressure tubes. These ace-pressure tubes were bought from Sigma Aldrich and they have o-rings and screw caps. This synthesis uses high pressure to increase the boiling temperature of water like in autoclave but takes shorter time frame than requires in usually autoclave based synthesis of QDs in water. The Figure 1 below shows the setup comparison between the traditionally used organometallic synthesis versus traditionally used water synthesis at 100°C and our synthesis using these pressure tubes.

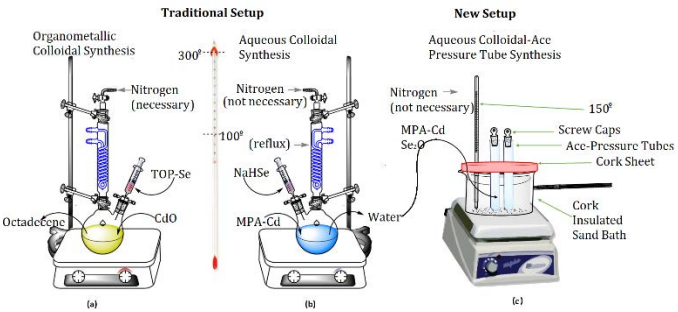

Figure 1: The traditional setup and approach used to synthesize QDs in (a) in organometallic synthesis, (b) in aqueous synthesis and the new setup and approach used by us (c) in aqueous synthesis using glass pressure tubes.

The synthesis procedure is as follows. Two separate solutions of $CdCl_2.2.5H_2O$ (Cd precursor) and SeO_2 (Se precursor) were prepared in distilled water and stirred for 10 minutes till they formed clear solutions. Everything in this procedure is done in normal conditions, N_2 atmosphere is not necessary. The Cd solution was then transferred to a Sigma Aldrich Ace pressure tube. The tube was inserted in a sand bath well insulated with cork. The sand bath had been covered with a cork sheet on the outer walls and the

top of the bath had been covered with a cork sheet with holes to insert the tubes in them. Then, when the tube with the Cd solution was started to being heated, 0.2 ml of Mercaptopropionic acid (3-MPA) was added to the Cd solution followed by the addition of NH_4OH to maintain the pH around 11. Mercaptoacetic acid (MAA) can also be used as the capping ligand and using different Cd precursors but keeping the same Se precursor. Afterwards, when the temperature had reached 80^{o}C, the Se precursor was added into the tube. Then, the tube was closed and heated up to 150^{o}C. It was maintained at this temperature for 30 minutes. The reaction was also carried out for other time durations of 60 minutes and 90 minutes. After that the tube was pulled out of the sand bath and left to cool down to room temperature. It was normally quenched at room temperature with normal cool tap water. The water solution was yellow in color after 30 minutes which is Sample 1, the one after 60 minutes was mostly orange in color which is Sample 2. The final sample was obtained after 90 minutes and it was a red colloid which is the Sample 3. The solutions were then centrifuged for 30 minutes at 6000rpm and colored precipitates were obtained. The precipitates were further washed with water twice and then they were left for drying in vacuum and dispersed in ethanol, toluene or fresh water. The suspension showed bright green fluorescence for Sample 1, yellow fluorescence for Sample 2 and orange for Sample 3 and all had QDs in them. The samples were then characterized using the various techniques. This method helped us to obtain QDs having the properties similar to the QDs produced using organic hot-injection method using a simple aqueous method. The setup is shown in Figure 1(c).

This method of synthesis was designed to use the water-based system at a high temperature and for short durations to obtain QDs of different dimensions and emitting different colors based on their dimensions.

2.1. Understanding the Synthesis

Liquid boils at that particular temperature when the vapor pressure of the liquid is equal to the pressure of the gas above it. When the pressure is lower, lower energy is required to boil the liquid, that is less heat or less temperature. On the contrary, if the pressure increases, or higher the pressure, higher temperature is required to boil the liquid, that is more heat or temperature is needed for the liquid to start boiling. Using this dependence of boiling point on pressure for solvents, this reaction was designed. That is why we used the high-pressure ace tubes for the reaction. The pressure of the reaction vessel increased autogenously inside the tubes, increasing the boiling temperature of the water inside the reaction mixture so the reaction could be done at temperature above 100ºC. The boiling point of both the solvent and the capping ligand is 100ºC but in this case they are trapped inside a high-pressure system and thus their boiling point has increased and moreover even if they did vaporise, the gaseous phase will not be able to escape the reaction vessel as it is screwed tightly. Neither gas nor volatile component of the reaction mixture can leave the reaction vessel because it is closed. The same concept applies to 3-MPA that equilibrates between the gas phase and the liquid. Thus 3-MPA can stabilize CdSe because it is in the water as well as it may be in the gas. All this explains why we mention that this synthesis technique presents a new way of synthesizing QDs in water at a higher temperature by using these high-pressure ace tubes. Also, the different reaction times yields different sizes of the QDs. This is similar to the high temperature organometallic synthesis. Following the idea from that, we removed the samples at different time intervals from the sand bath and quenched them using water. This quenched the reaction and stops the QDs from growing and thus prevents the size from increasing. By keeping the reaction vessel longer at the high-temperature the QDs were given more time to increase in size, thus the

latter samples were larger in size compared to the previous samples. There have been cases in which the sample in water done at 100°C under reflux has been removed from the heating at different time intervals but they were not quenched immediately and thus the size of the nanoparticles were not so well controlled leading to the presence of differently sized particles together.
This synthetic route helps in easy isolation process too like in most aqueous solution methods by simple centrifugation of the colloid. The precipitate is washed and re-dispersed easily in fresh new water or ethanol or toluene. The precipitate can also easily be stored in solid form in bottles and can used whenever necessary. The yield produced by this method is high and almost 90% yield is obtained. The method accounts for high-throughput in the production of QDs.

3. Characterization

The QDs synthesized were thoroughly characterized using the different techniques. Photoluminescence (PL) emission and excitation spectra were measured in Perkin Elmer LS45 fluorimeter. Transmission electron microscopy (TEM) studies were carried out using JEOL JEM 1210 at 120 kV. TEM samples were made by dropping a drop of CdSe suspension onto the carbon coated copper grids. Electron diffraction studies were done in the same machine. International Centre for Diffraction Data was used to check the electron diffraction studies (file numbers- 00-019-0191 and 04-011-9599). Dynamic Light Scattering (DLS) measurements and Zeta Potential studies were carried out in the Zetasizer Nano ZS (For DLS light source used was He-Ne Laser, 633nm, Max 4mW, back scattering angle used was 173° and for zeta potential electrophoretic light scattering principle was used to do the measurements). Infrared Spectrum (IR) studies were done using the Perkin Elmer Spectrum One FT-IR machine. Energy Dispersive X-ray Spectroscopy (EDX) analysis was done using the QUANTA

FEI 200 FEG-ESEM device and the sample was analyzed in powdered form in SEM stubs with carbon tapes. UV-vis Spectrum was carried using Cary-5000 UV-vis-NIR spectrophotometer. ImageJ software was used for measuring the particles.

3.1. TEM, DLS and Size

TEM Studies: Transmission Electron Microscopy (TEM) analysis was done on the samples to study the size and shape of the particles. They appeared agglomerated as is common with the QDs synthesized in water medium. The TEM images showed the spherical quantum dots formed (Figure 2a, b and c). The average size of the QDs was obtained by manually measuring more than 200 QDs from the TEM images using ImageJ software and plotting the histogram using Gaussian function. The average size for the sample kept at 150°C for 30 minutes is 4.18nm, the one kept at 150°C for 60 minutes is 6.7nm and the one kept at 150°C for 90 minutes is 8.6nm (Figure 3a, b and c). The size consecutively grew as the reaction time was increased. This was observed well by the change in the emission wavelength of the QDs. This growth in size for QDs with increasing reaction time is consistent with the behavior exhibited by the QDs. In general, when QDs are synthesized in high temperature hot-injection method, with increasing time of the reaction the size of the particle grows. This is because after the initial nucleation for the formation of the QDs, the size continues to grow during the entire period of the reaction time. The capping ligands are used to control the size of the QDs but with more passage of time there is more accumulation of the precursors and the capping ligands on the nucleated sites, thus giving rise to larger size of the QDs. In colloidal synthesis like this for QDs, the size is controlled kinetically. CdSe tends to aggregate as the reaction proceeds further at high temperature thus increasing the size of the final QDs obtained. By stopping the reaction at specific time periods, removes the heat and quenches the reaction mixture, thus stopping the growth of the particles further and obtaining the QDs of a particular

size. The quenching of the reaction mixture is done here by cool normal tap water after the end of 30 minutes, 60 minutes and 90 minutes.

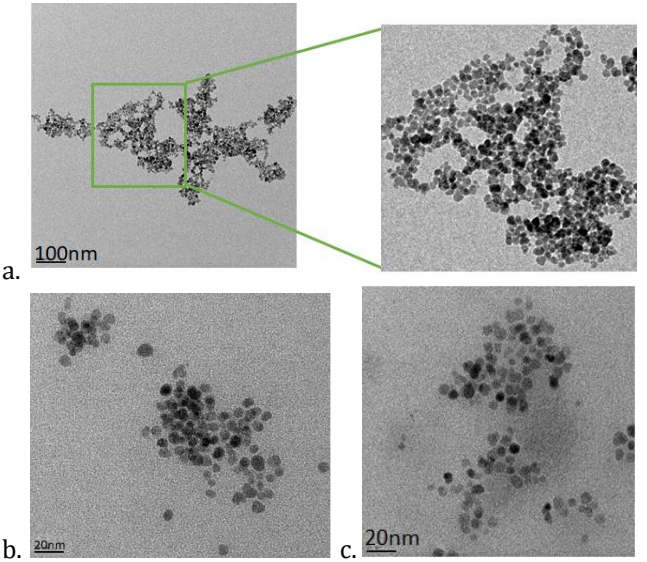

Figure 2: (a) TEM micrograph of the QDs at 100nm magnification for sample after 60 minutes of synthesis. (b) and (c) TEM micrograph of the QDs at 20nm magnification for sample after 30 minutes of synthesis.

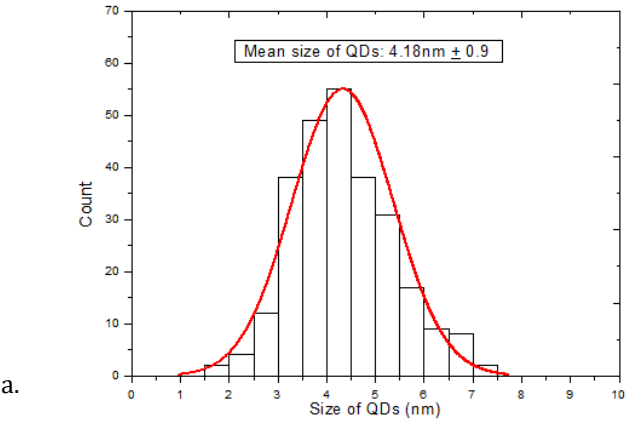

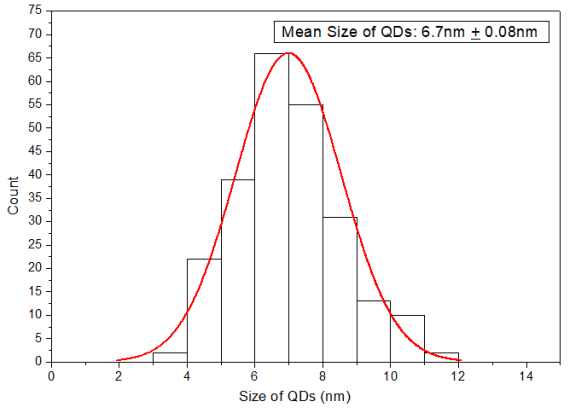

b.

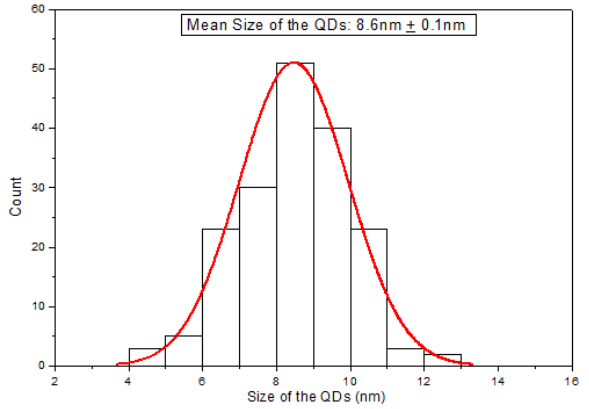

c.

Figure 3: The Gaussian histogram for the size of the QDs synthesized **(a)** after 30 minutes which is 4.18nm **(b)** after 60 minutes which is 6.7nm and **(c)** after 90 minutes which is 8.6nm.

DLS Studies: The size was further measured with Dynamic Light Scattering (DLS) studies and it mostly corroborated with the size obtained by TEM. The average size obtained by the DLS was 3.6nm, 5.6nm and 8.7nm for the time durations of 30, 60 and 90 minutes (Figure 4). The DLS

results showed a monodispersed peak thus proving that the QDs were quite homogeneously produced by this method. Generally, the size of the particles seen in TEM studies are smaller compared to the size of the particles when measured using DLS. This is because DLS gives the hydrodynamic diameter and the particles tendency to aggregate while being measured. This is contrary to what we observe. This perhaps could be because the measurement of the TEM was done by the drop-dry method. The sample was prepared on a Cu grid, by drop-dry and it could have led to minor aggregation of the particles on the grid, such that when it was measured it showed a slightly increased size. While, during the DLS measurements, the particles were in solution and well dispersed by sonication prior to measuring them. This could have made the QDs less aggregated and more well separated while being measured in the DLS and thus leading to slightly smaller dimensions.

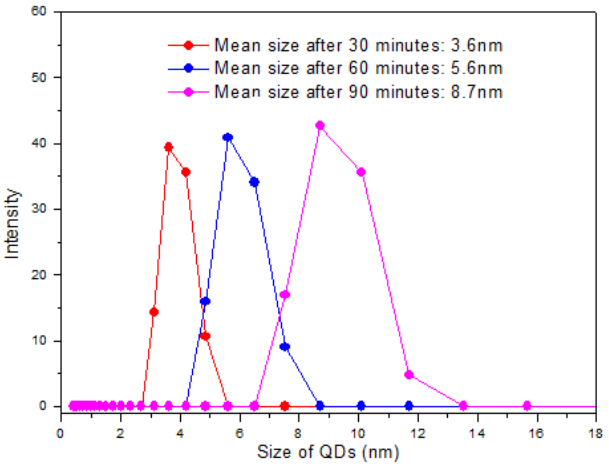

Figure 4: The DLS graphs for the size of the QDs synthesized after 30 minutes which is 3.16nm, after 60 minutes which is 5.6nm and after 90 minutes which is 8.7nm.

3.2. Fluorescence Studies

The fluorescence studies include the study of the PL emission, excitation and the UV-vis absorption. Their intensities have also been recorded over time to see the degradation of their emission properties. The quantum yield (QY) values are calculated using the relative formula in which the emission is compared to the standards. There are many ways of calculating the QY of QDs as studied thoroughly by Grabolle et al. [25] but out of all the methods mentioned by them, we followed the method of comparing luminescence with standards and calculating the yield. Though this is not the most accurate way of calculating the yield, it is the most adopted method of quantifying the QY. In order to reduce the discrepancies, the standard has to be carefully selected and must fall within the same range of excitation and emission of the QDs and preferably different excitation wavelengths and more than one standard should be selected. The exciton peak in the UV-vis should not be taken for the QY calculation.

PL Emission and Intensity Studies: Due to the changes in the size with the temperature, the emission color also changed as mentioned before. This is because of the characteristic property of QDs, where they possess a size tunable band-gap and size tunable color. As the QDs grow in size, the bang gap of the QDs changes, the energy difference between the states change, due to which the emission color changes. The wavelength of luminescence emitted varies with the change in the band gap of the QD, thus with increase in size, the band gap reduces and the emission spectrum of the QD shifts more towards the red region. This is seen with QDs we synthesize in this paper, as with growing size the emission color shifts from green to yellow to orange and this was confirmed by the PL studies done on them. The normalized emission is shown in the Figure 5 which shows that the emission peaks shift with the increase in the size of the QDs. The QDs after 30 minutes have a green emission,

while after 60 minutes they have a yellow emission and after 90 minutes they have orange emission.

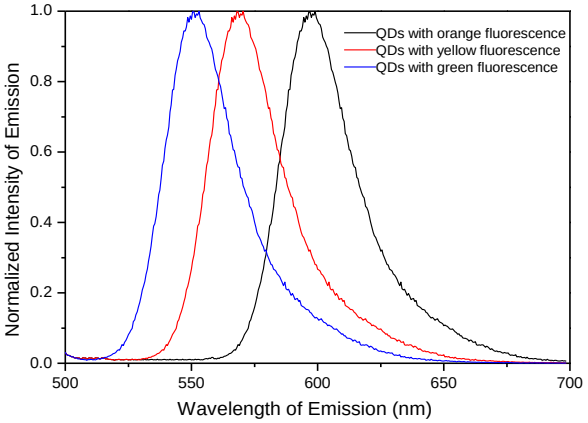

Figure 5: The emission spectrum of the QDs after 30 minutes, 60 minutes and 90 minutes.

The emission spectrum of these QDs after 30 minutes is at 550nm, after 60 minutes at 580nm and after 90 minutes at 620nm. This falls well within the spectrum of the colors green, yellow and orange respectively. They emit intensities which are almost comparable to QDs synthesized in organic solvents at a much higher temperature of 300°C. It is first time that such highly luminescent QDs purely synthesized in water with the usual precursors exhibit such luminescent properties.

These QDs showed intense emission when re-dispersed in ethanol, toluene or in fresh water solutions. They are also extremely stable and have been stable showing the same intense emission for over a year after being synthesized (Figure 6). The intensity was well preserved when it was quantified after 6 months and after almost 1 year. In Figure 6, you can see the intensity variance over a period of 1 year being documented. For 1 year, the measurements were done after the end of 1st, 3rd, 5th, 7th, 9th, 11th and 13th months. The degradation in the intensity of these stored QDs was not significantly huge and quite maintained.

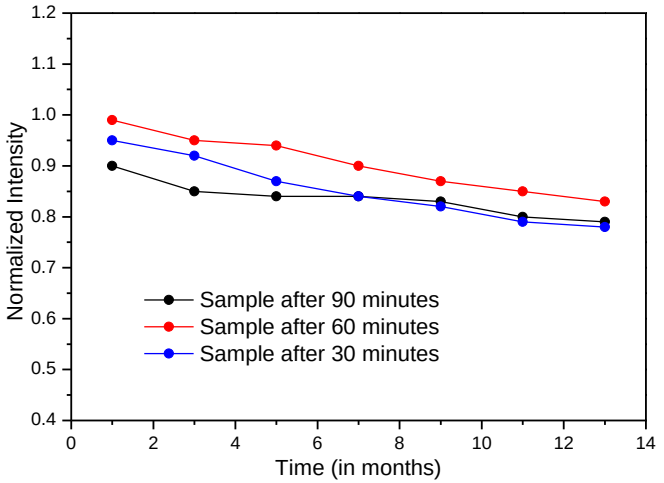

Figure 6: The intensity record over a period of 13 months for different samples. The intensity does not degrade much over the period of 1 year for these QDs. The naked eye photos of the QDs under UV irradiation at 366nm is seen below. We can clearly see the green, yellow and orange fluorescence emitted by the QDs made by our method (Figure 7).

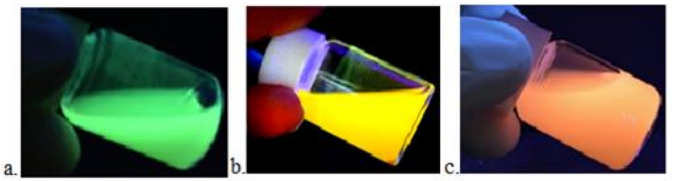

Figure 7: The image of the QDs illuminated under the UV light of 366nm. (a) After 30 minutes of synthesis, (b) after 60 minutes of synthesis and (c) after 90 minutes of synthesis.

UV-vis and Excitation Studies: The UV-vis spectrum of the QDs were also measured and they showed absorbance at 465nm, 510nm and at 546nm for 30, 60- and 90-minutes sample (Figure 8). The excitation spectrum was also studied (Figure 9) and it showed a peak at 392nm and the QDs were excited at 365nm and 392 nm for the emissive studies and both showed similar emission.

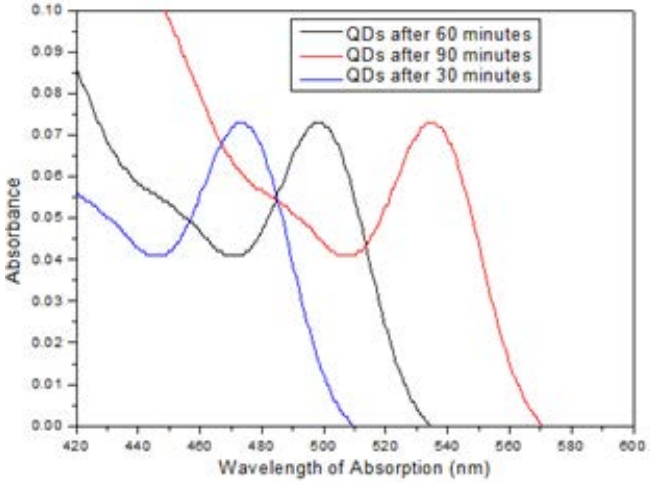

Figure 8: UV-vis spectrum of the QDs synthesized at different time periods.

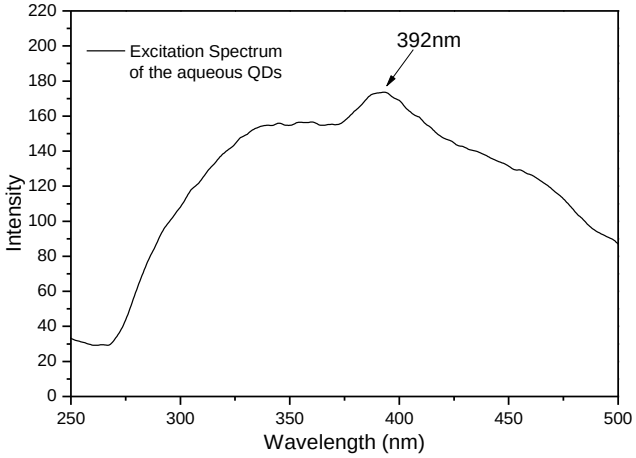

Figure 9: The excitation spectrum of the aqueous QDs. The excitation peak was obtained at 392nm wavelength.

Quantum Yield Measurement: The Quantum yield (QY) measurements were done using the formula given below:
$QY = QY_{ref} \{\eta^2 I A_{ref} (\eta_{ref} I_{ref} A)^{-1}\}$
Where QY_{ref} – Quantum Yield of the reference (Rhodamine 6G)
η- Refractive index of the solvent (Ethanol)
η_{ref}- Refractive index of the solvent of the standard (Ethanol)
I- Integrated area of emission spectrum of sample
I_{ref} – Integrated area of emission spectrum of reference
A- Absorbance value of sample
A_{ref}- Absorbance value of the reference

The reference used for the QY measurement was Rhodamine 6G and its QY in ethanol (0.95) was taken as the reference. Rhodamine 6G was used as it had the emission in the same wavelength range as the QDs produced in this paper. The excitation wavelength used for the QY studies were 392nm and 425nm for the 30 minutes sample, 392nm and 450 for 60 minutes samples and 392nm and 480 for 90 minutes samples. The two different wavelengths were used to excite the different samples and also the reference. Their emission obtained at the two different wavelengths were considered for the calculation of the QY. The sample were diluted until their absorbance values were obtained to be less than 0.1 for the QY measurements. We used the relative Quantum yield calculation formula mentioned above and the standard given and using that we obtained almost 80% for the green emission, 78% for the yellow emission and 76% for the orange emission. This is a massive improvement in the QY of the aqueous synthesized QDs that were available so far. This method helps us to achieve such luminescent QDs in water which has been very difficult in the study of QDs so far. The only known highest QY values for QDs synthesized in water using Selenium Dioxide as a reagent is 24%. So, these QDs clearly supersede the available QDs that are synthesized in water till now and present us with a new generation of water based QDs.

3.3. Chemical Composition Studies

Electron Diffraction Studies: The selected area electron diffraction (SAED) pattern was obtained for the samples (Figure 10). The rings present corresponded to the hexagonal wurtzite structure of the CdSe QDs. Though the zinc blende phase of CdSe QDs are more common at lower temperature water-based synthesis of QDs and the hexagonal wurtzite phase is more common for the higher temperature synthesis of QDs in organic samples, we could very well observe the hexagonal phase of these QDs. The unique way of synthesizing these QDs at high temperature in high pressure tubes help us obtain unique features of these QDs. Usually at high temperature with high pressure synthesis of QDs, that is the hydrothermal synthesis is done using autoclaves. In these synthesis processes, either it takes more time for the QDs to be obtained or if obtained in shorter time duration the properties are not much improved than QDs synthesized under usually used normal conditions. The unique use of glass pressure tubes along with a cork encapsulated heating system provides for an ideal condition to synthesize QDs in water with properties obtained in hot-injection synthetic conditions.

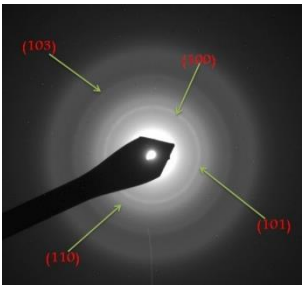

Figure 10: The Electron Diffraction pattern for the QDs synthesized in water. They all show the hexagonal wurtzite phase of CdSe.

EDX Studies: The EDX studies showed very well the presence of Cadmium, Selenium and Sulphur. This confirmed the formation of the QDs with the capping effectively done by the 3-Mercaptopropionic acid (Figure 11). The chemical composition in terms of atomic percentage for the different elements went well in accordance with the synthesized QDs. It showed that the

ratio of Cd:Se:S present is 4:1:2. It showed an excessive presence of Cd in the sample which provides for the excessive positive charge in the sample. It has been reported that usually in aqueous synthesis an excess of Cd is needed to improve the photophysical properties and the luminescent properties and this is compensated by anionic ligands of 3-MPA or MAA. [26] Though there have also been studies showing that excess Se can lead to narrower spectra but as we can see in these samples the PL spectra is quite broad owing to the presence of excess Cd ions which also help in improved QY of the QDs.

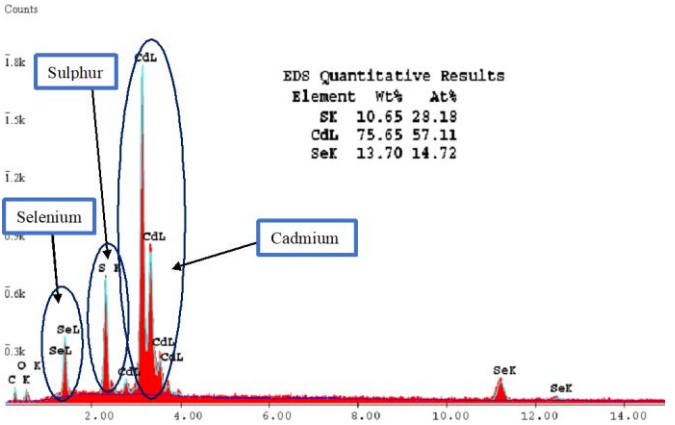

Figure 11: EDX of the QDs in water. It shows the presence of Cadmium, Selenium and Sulphur.

IR Studies: The IR study was done for all the samples and they all showed a similar spectrum (Figure 12). A broad absorption peak at around 3440 cm^{-1} is assigned to the O–H vibration. The absence of S–H stretching band around 2557 cm^{-1}clearly indicates that thiolates are connected to the Cd^{++} sites on the CdSe QD surface via Sulphur atom of organic molecule. The sharp peak at 1540 cm^{-1} can be assigned to the vibration of the carboxylate anion of MPA molecules. The band at 1420 cm^{-1} is due to the symmetric stretching vibration C–O. The blue one is for the QDs produced after 30 minutes of heating and the black one is for the sample extracted after 60 minutes of heating.

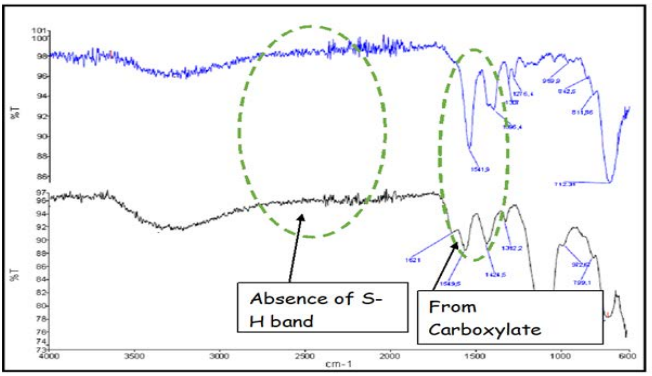

Figure 12: The Infra-Red spectrum shows the presence of the COOH group capping the QDs and the absence of S-H band, proving that the particles are effectively capped with 3-MPA. Blue spectra for QDs after 30 minutes and Black spectra for QDs after 90 minutes of heating.

3.4. Zeta Potential Studies

These quantum dots are also extremely stable for more than a year when dispersed in ethanol, toluene or water. Their stability has been tested by zeta-potential values. Zeta-Potential is a technique which helps us determine the stability of a colloidal system. Zeta-potential as defined is the potential difference between the slipping plane in the electronic double layer and the bulk potential. The values of zeta-potential when above $\pm$30 means that the particles are electrostatically stable. Although in colloidal system the stability of the particles is dependent on electrostatic and steric repulsion, zeta potential can still be considered as a good indication of the stability of the particles in the dispersing media. The values of zeta-potential obtained for the samples dispersed in ethanol was -57.9mV, in toluene was -38.6mV, and in water was -51.7mV thus confirming that the QDs are extremely stable in these solvents. (Figure 13, 14 and 15).

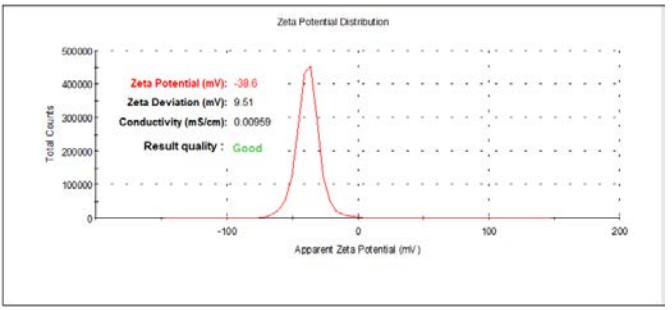

Figure 13: The zeta-potential of CdSe QDs dispersed in toluene. The suspension shows very good stability and has a zeta potential value of -38.6mV.

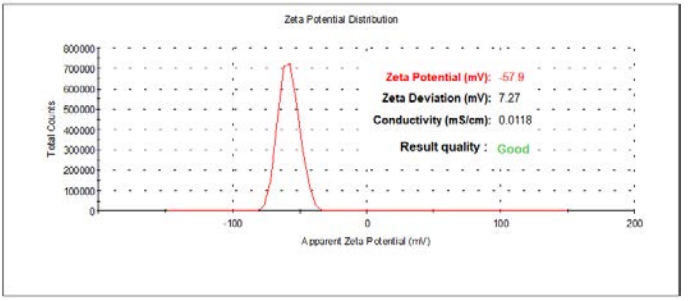

Figure 14: The zeta-potential of CdSe QDs dispersed in ethanol. The suspension shows very good stability and has a zeta potential value of -57.9mV.

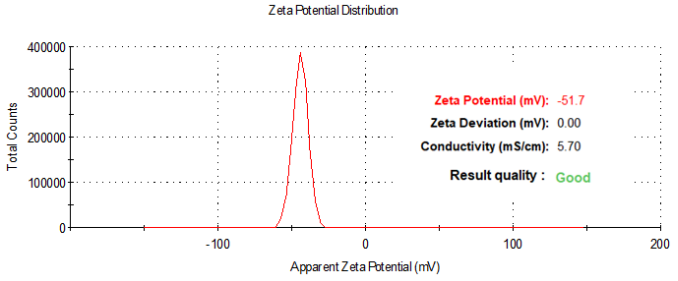

Figure 15: The zeta-potential of CdSe QDs dispersed in fresh water. The suspension shows very good stability and has a zeta potential value of -51.7mV.

4. Comparisons

The QDs thus made were also compared with the QDs traditionally made under reflux at 100°C and also at room temperature. Their intensities of emission were compared. These comparisons were necessary in order to check how these QDs fared with the QDs synthesized in the traditional method. The comparison showed us the enhanced properties obtained by this synthetic route.

4.1. Comparison with usual water-based QDs

The intensity of the emission of the QDs synthesized using the new method is extremely high and when compared with QDs synthesized normally with 3-MPA under normally used conditions, they are almost 100 times more fluorescent according to the arbitrary units of the machine (Figure 16).

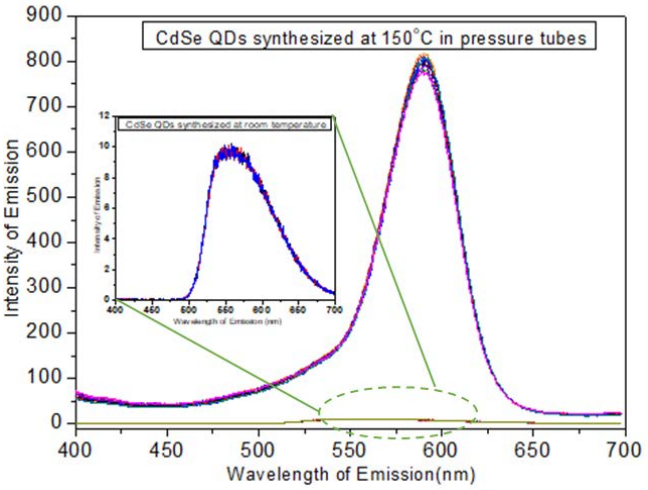

Figure 16: Comparison of the emission of the QDs produced by the new method versus the QDs synthesized using traditional method at room temperature using 3-MPA.

The emission produced by these QDs also supersede the emission produced by the QDs at 100°C in water or normally synthesized in autoclaves at other higher temperatures and pressure (Figure 17). This shows that in general these QDs have higher emission over other water synthesized QDs.

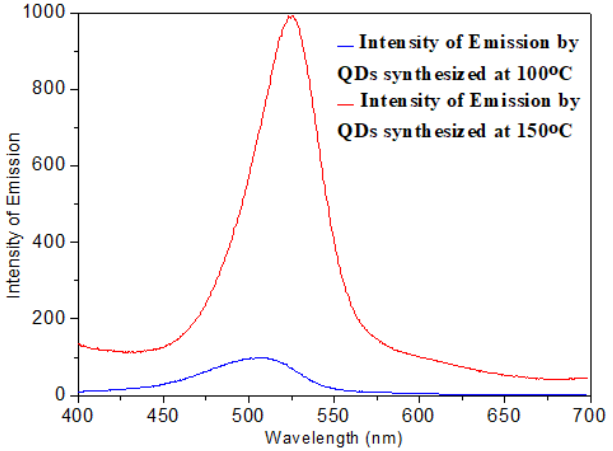

Figure 17: Comparison of the emission of the QDs produced by the new method versus the QDs synthesized using traditional method at 100°C under reflux using 3-MPA.

Not only the emission intensity was measured for a single reading but also over a period of time to see the stability of the intensity. The intensity of the fluorescence was measured over a period of time to check how stable the emission is and we could observe very well over the period of 60 minutes that all the QDs emitted with no degradation in the intensity (Figure 18). For 60 minutes, 4 samples were tested in this. The one at 150°C showed the maximum intensity for the samples prepared after 30, 60 and 90 minutes followed by the one synthesized at the same temperature for 120 minutes and 150 minutes. The least intense were the ones synthesized at 100°C for 30, 60 and 90 minutes. Though all the samples clearly maintained their

respective intensity of emission we can clearly see that the particles synthesized at 150°C in the glass tubes have superior intensities. We also have the image of the QDs made by the method used to synthesize them in water at 100°C and it can be seen that they are much less-brighter than the QDs synthesized by us as seen by their UV illuminated image before in Figure 7.

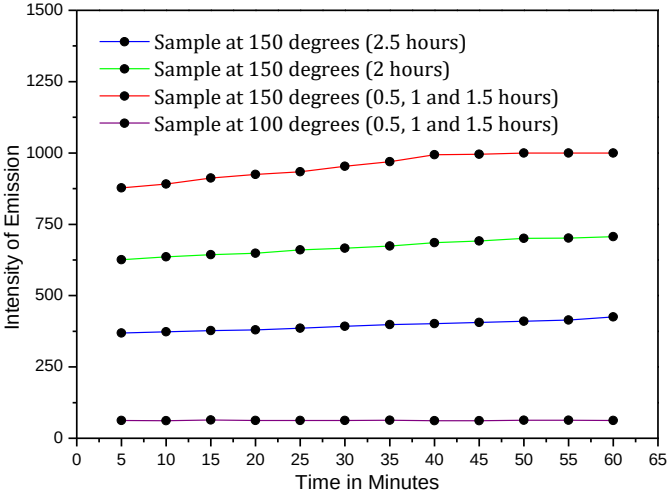

Figure 18: The intensity record for different samples over a period of 60 minutes.

The reaction was also stirred for further time frames of 120 minutes and 150 minutes but they gave poor emissive properties and hence were not pursued further. This was because the particles formed got aggregated sooner and the sizes were much larger and exceeded the quantum regime dimensions.

5. Conclusions

The high temperature boiling organic solvent method to produce Quantum Dots (QDs) offered the best procedure to control the size, thence the PL emission and the stability of the QDs. The QDs produced this way show high QYs. The problem was the isolation to get the QDs in solid, the procedure requires a non-green solvent and the QDs are not water compatible, thus the as produced QDs cannot be used in biological experiments. On the contrary the aqueous method, that is using a green solvent, is slow, cannot tune the size and neither the PL; further the materials thus produced are not very stable. In this work CdSe QDs have been produced in water at 150^{o}C following a sequence of temperature ramps. The QDs thus produced are water compatible, show intense fluorescence emission and high quantum yields (QYs). Their dimensions have been controlled keeping the temperature constant but allowing different times of growth thus with distinct fluorescence. These QDs and the QDs produced in the high boiling method show comparable QYs. These water QDs can be easily separated and stored dry. The sizes obtained by TEM for 30, 60 and 90 minutes of reaction are 4.18nm, 6.7nm and 8.6nm, respectively, corresponding to green, yellow and orange luminescence, respectively. These QDs display the hexagonal wurtzite phase, as for the higher temperature synthesis of QDs in organic samples, and not the zinc blende phase of CdSe QDs common for the lower temperature water synthesis of QDs. These QDs have shown the same intense emission for over a year after being synthesized. These results have been published in ChemNanoMat. [27]

6. References

[1] Y. Wang, H. Yang, Z. Xia, Z. Tong, L. Zhou, *Bull.Korean Chem. Soc.* **2011**, *32*, 2316.

[2] S. M. Farkhani, A. Valizadeh, *IET Nanobiotechnology*, **2014**, *8,* 59.

[3] R. Rossetti, J. L. Ellison, J. M. Gibson, L. E. Brus, *J. Chem. Phys.* **1984,** *80*, 4464.

[4] N. A. Bakar, A. A. Umar, T. H. T. Aziz, S. H. Abdullah, M. M. Salleh, M. Yahaya, B. Y. Majlis, *2008 ICSE 2008 IEEE Int. Conf.* **2008**.

[5] N. Gaponik, D. V. Talapin, A. L. Rogach, K. Hoppe, E. V. Shevchenko, A. Kornowski, A. Eychmüller, H. Weller, *J. Phys. Chem. B* **2002,** *106*, 7177.

[6] R. M. Hodlur, M. K. Rabinal, *Chem. Eng. J.* **2014**, *244*, 82.

[7] Y. Pu, F. Cai, D. Wang, J. X. Wang, J. F. Chen, *Ind. Eng. Chem. Res.* **2018**, *57*, 1790.

[8] L. Liu, Z. Zhuang, T. Xie, Y. G. Wang, J. Li, Q. Peng, Y. Li, *J. Am. Chem. Soc.* **2009**, *131*, 16423.

[9] X. Peng, L. Manna, W. Yang, J. Wickham, E. Scher, A. Kadavanich, A. P. Alivisatos, *Nature* **2000**, *404*, 59.

[10] E. M. Chan, R. A. Mathies, A. P. Alivisatos, *Nano Lett.* **2003**, *3*, 199.

[11] E. Noglik, W. J. Pietro, *Chem. Mater.* **1994**, *6*, 1593.

[12] V. Ladizhansky, G. Hodes, S. Vega, *J. Phys. Chem.* **1998,** *102,* 8505.

[13] Y. Tian, T. Newton, N. A. Kotov, D. M. Guldi, J. H. Fendler, *J. Phys. Chem.* **1996,** *100*, 8927.

[14] M. Kuno, J. K. Lee, B. O. Dabboussi, F.V. Mikulec, M. G. Bawendi, *J. Chem. Phys.* **1997,** *106,* 9896.

[15] C. B. Murray, D. J. Norris, M. G. Bawendi, *J. Am. Chem. Soc.* **1993,** *115,* 8706.

[16] B. Ludolf, M. A. Malik, P. O'Brien, N. Revaprasadu, *Chem. Commun.,* **1998,** 1849.

[17] C. A. Ubani, M. Y. Sulaiman, Z. Ibarahim, N. B. Ibrahim, M. Y. Othman, *J. Mod. Educ. Rev.* **2011**, *1*, 63.

[18] J. E. Bowen-Katari, V. L. Colvin, A. P. Alivisatos, *J. Phys. Chem.* **1994,** *98,* 4109.

[19] Y. Wada, H. Kuramoto, J. Anand, T. Kitamura, T. Sakata, H. Mori, S. Yanagida, *J. Mater. Chem.* **2001**, *11*, 1936.

[20] H. Grisaru, O. Palchik, A. Gedanken, V. Palchik, M. A. Slifkin, A. M. Weiss, Y. Rosenfeld Hacohen, *Inorg. Chem.* **2001,** *40,* 4814.

[21] X. Peng, R. Lu, Y. Zhao, L. Qu, H. Chen, T. Li, *J. Phys. Chem.* **1994,** *98*, 7052.

[22] P. Facci, V. Erokhin, A. Tronin, C. Nicolini, *J. Phys. Chem.* **1994,** *98,* 13323.

[23] D. J. Scoberg, F. Grieser, D. N. Furlong, *Chem. Commun.* **1991,** 515.

[24] Y. Li, Y. Ding, Y. Quian, Y. Zhang, L. Yang, *Inorg. Chem.* **1998,** *37*, 2844.

[25] M. Grabolle, M. Spieles, V. Lesnyak et al., *Anal Chem.* **2009,** *81,* 6285.

[26] Y. Bao, J. Li, Y. Wang, L. Yu et al. *J. Opt. Mater (Amst).* **2012,** *34,* 1588.

[27] A. Saha, A. Saini, C. Vinas, F. Teixidor, *ChemNanoMat.* **2019**, *5,* 1.

3.1.3. Quantum Rods and Rings in Water

CdSe Quantum Rods (QRods) and Quantum Rings (QRs) with high quantum yield (QY) have been synthesized in water for the first time using a novel hydrothermal method. The QNCs were encapsulated in polymers to generate photoluminescent polymeric films. The quantum nanocrystals (QNCs) hence produced, can be easily separated from the water, show remarkable photoluminescent intensity as well as electroluminescence in polymeric films.

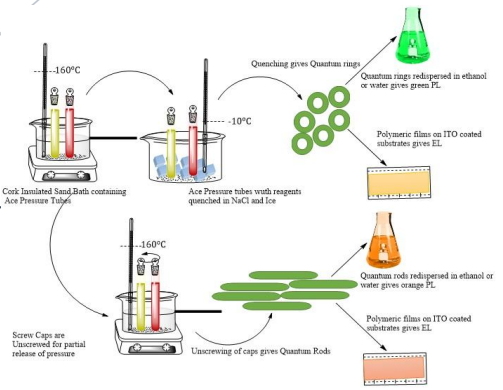

Arpita Saha
ICMAB-CSIC (UAB)

Contents

1. Introduction

Quantum Nanocrystals (QNCs) have been the core of research for material scientists over the last two decades. Among these QNCs, Quantum Dots (QDs) have been of foremost interest. QDs have already been introduced in the previous chapters and we have done most of the work with the QDs synthesized in aqueous media. After achieving considerable success in the synthesis of QDs in aqueous media and obtaining new properties in them, we shifted our focus on other QNCs like Quantum Rods (QRods) and Quantum Rings (QRs). These QNCs have been known theoretically for a long time but they have been difficult to synthesize for years. Though QRods have seen some considerable research being done on their colloidal synthesis, QRs have really never been touched at the colloidal level. QRods have been synthesized in colloidal medium, but they are mostly restricted to the organometallic medium [1]. After the success of highly luminescent QDs in organometallic synthesis, QRods were pursued and since QRods are achieved with rapid increase in temperature, the organometallic synthesis was apt to be used for it [2]. There has been considerable research involving QRods synthesis albeit none of them have been in water medium. The QRods have always been subjected to long process of ligand exchange or silanization to make them water soluble [3]. While QRods have still been explored, QRs have not been explored in colloidal synthesis routes. Barring one long cumbersome procedure, [4] they have predominantly been synthesized using physical methods of epitaxy or Stranski-Krastanov etc. Hence, we focussed out attention to achieve a simple colloidal route to obtain these QNCs in water.

1.1. Quantum Rods

QRods are semiconductor materials having long rod like structures which have their cross section within the quantum regime of 0-20nm, while their length is longer of the order of 100-200nm. [5] QDs are 0D structures while QRods are 1D structures. QRods help us to study the shape dependant optical and electronic properties of NCs, as well as quantum confinement effects in 1D and quasi-1D regime in comparison with the much studied 0D structures. They too possess a tuneable bandgap like the QDs owing to their cross-section dimensions. [5] The size and shape of the NCs have huge implications on the optical properties and electronic structures of band edge. [6] This is further supported by the measurements on CdSe QRods showing that their Stokes shift is much larger than the corresponding QDs and it increases even further with increase in the length of QRods.[7] The polarization of emission of CdSe QRods also shows a significant difference in comparison to QDs.[7] Additionally, they also demonstrate faster radiative decay rate,[8] have larger absorption cross section than QDs[9] and can be functionalized with numerous binding moieties. Due to their unique properties and morphology, QRods have found use in applications such as fluorescent labels and markers[10,11] and also as polarized emitters for light-emitting diodes.[12,13] But one of the most promising applications of QRods is their ability to track single molecules,[3] which is a powerful method to study the dynamic and kinetic behaviour of biomolecules inside living cells. Their enhanced fluorescent signal compared to QDs makes them ideal probes for single molecule tracking. They show higher resistance to degradation as compared to other optical probes such as organic dyes.[14] QRods due to their long length and intense emissive properties compared to QDs have lots of advantages over them and hence their application prospects cover a wider range. This is exactly why there is a need to synthesize QRods in solely aqueous media and yet there has been very less research in this arena and not with much success.

1.2. Quantum Rings

The term "Quantum rings" refers herein to ring like structures (toroidal topology in the quantum regime), having a diameter in the range of 5 to 20 nm. QDs, while interesting, have already been studied extensively and the focus has now shifted to structures that can be made in quantum regime without any natural analog. Quantum rings (QRs) are one such possibility in this field. They possess all the qualities of QDs with enhanced photoluminescence and conductance properties. By confining an electron to a 1D ring we fix the magnitude of its dipole moment, but not its direction. Classically an array of such rings will align in striped anti ferroelectric order (AFE). QRs such as InGaAs QRs present an outer diameter between 60 and 140 nm, a height of about 2 nm and a center hole of about 20 nm in diameter.[15] Due to the fascination that the macroscopic interaction between loops and magnetic fields exerts on scientists and engineers, there is a genuine interest to see what happens at the nano scale.[16] QRs provide the unique opportunity to study rings in the true quantum regime. According to quantum mechanics, small ring-like structures threaded by a magnetic flux bear persistent (dissipationless) circulating electron currents.[17] Other effects such as oscillation in magnetization can also be studied with QRs.[18] Another feature of such semiconductor QRs is that they provide ample opportunity to study Stark Effect[19] and Aharanov-Bohm Oscillations.[20-22] To carry on with these studies, efficient methods to produce QRs are necessary. But for one reported case of colloidal organometallic synthesis that requires etching,[4] QRs are currently made by physical methods using electron beam lithography, and ion beam milling. Presently, the most commonly used technique is the lattice-mismatched technique by the Stranski–Krastanov (S-K) model,[23-26] and the more recent droplet epitaxy (DE) from Koguchi and his co-workers. In general, physical methods of preparation, although producing highly pure materials, have a very low throughput. So, it is high time that we developed a method to obtain these in a facile green synthesis.

2. Synthesis

The process of the present work is a green chemical process performed under hydrothermal conditions where aqueous solutions of precursors are added into the high-pressure tubes while conventional processes for obtaining QNCs use pyrolysis of often hazardous organometallic precursors at high temperatures instead. The QNCs obtainable by the process presented here show high aqueous stability and biocompatibility. Furthermore, the fluorescence intensity of the obtained QNCs, both QRods and QRs, are extremely high when compared to the traditional QDs made in water. The high-pressure tube method of synthesizing these QNCs is similar to the method used in the previous chapter for the synthesis of QDs. But in that case the synthesis procedure varied slightly than the one done here. The modifications done on that method helps us to obtain these new QNCs in water for the first time. There is a pictographic depiction of the synthetic procedure given in Figure 1.

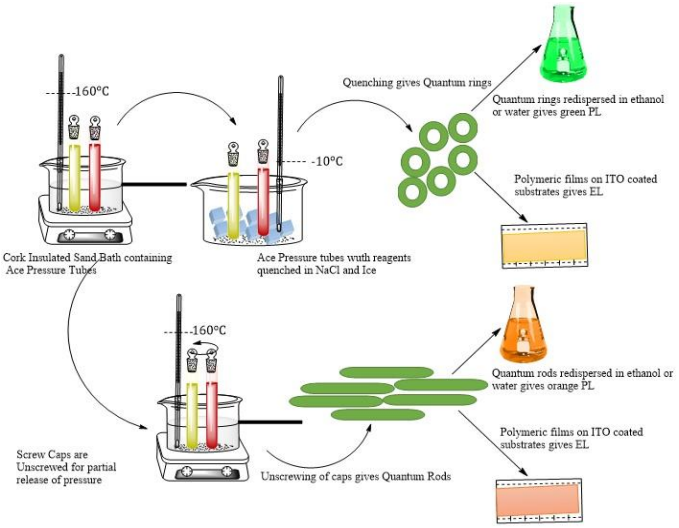

Figure 1: Synthetic route used to obtain QRs and QRods in water using ace pressure tubes.

2.1. Synthesis of Quantum Rods

456mg of $CdCl_2.2.5H_2O$ (Cadmium precursor) was dissolved in 5 ml of distilled water, 56 mg of SeO_2 (Selenium precursor) was dissolved in 5 ml of distilled water. The two solutions were prepared separately and stirred for 10 minutes till they both formed clear solutions. Everything in this procedure is done in normal conditions and not under N_2 atmosphere. The Cd solution was then transferred to a Sigma Aldrich Ace pressure tube. The tube was inserted in a sand bath well insulated with cork. The sand bath had been covered with a cork sheet on the outer walls and the top of the bath had been covered with a cork sheet with holes to insert the tubes in them. Then when the tube with the Cd solution was started to being heated, 0.2 ml of Mercaptopropionic acid (3-MPA) was added to the Cd solution followed by the addition of Ammonium Hydroxide (NH_4OH) to maintain the pH around 11. Afterwards, when the temperature had reached 90ºC, after 20 minutes of heating, the Selenium solution was added into the tube. Then, the tube was closed and heated up to 160 ºC. It took around 15 minutes to reach the temperature. It was maintained at 160°C for 5 to 10 minutes till the temperature became stable. Next the pressure tubes were opened a turn of the screw cap (7 turns in 1.5 cm) to let the pressure release and the water evaporate. These opened tubes were maintained at 160°C for 60 mins.

After that the tube was pulled out of the sand bath and left to cool to room temperature. The water had mostly evaporated and the precipitate had stuck to the walls of the tube. The obtained precipitate which was mostly orange and red in colour, was further washed with water twice and then the precipitate is left for drying in vacuum and re-dispersed in ethanol, toluene or fresh distilled water. This suspension showed bright orange fluorescence and had QRods in them.

2.2. Synthesis of Quantum Rings

456 mg of $CdCl_2.2.5H_2O$ (Cadmium precursor) was dissolved in 5 ml of distilled water, 56 mg of SeO_2 (Selenium precursor) was dissolved in 5 ml of distilled water. The two solutions were prepared separately and stirred for 10 minutes till they both formed clear solutions. Everything in this procedure is done in normal conditions and not under N_2 atmosphere. The Cd solution was then transferred to a Sigma Aldrich Ace pressure tube. The tube was inserted in a sand bath well insulated with cork. The sand bath had been covered with a cork sheet on the outer walls and the top of the bath had been covered with a cork sheet with holes to insert the tubes in them. Then, when the tube with the Cd solution was started to being heated, 0.2 ml of 3-MPA was added to the Cd solution followed by the addition of NH_4OH to maintain the pH around 11. Afterwards, when the temperature had reached 90ºC, after 20 minutes of heating, the Selenium precursor was added into the tube. Then, the tube was closed tightly and heated up to 160ºC. It took around 15 minutes to reach the temperature. It was maintained at this temperature for 60 minutes.

After that the tube was pulled out of the sand bath and left to cool to room temperature. The water colloid was mostly yellowish in color. The yellow solution was then centrifuged for 30 minutes at 6000rpm and yellow precipitate was obtained. The precipitate was further washed with water twice and then the precipitate was left for drying in vacuum and dispersed in ethanol, toluene or fresh water. This suspension showed bright green fluorescence and had QRs in them.

2.3. Synthesis of Polymeric Films

Polymeric films were made using two different polymers: Polyvinyl Alcohol (PVA) and Polydimethylsiloxane (PDMS). For the film with PVA, firstly 300mg of PVA was dissolved in 10mL of distilled water by heating for 8 to 10 hours under reflux at 80°C. It formed a viscous liquid with the PVA being fully dissolved in water. Then 25, 30, 35, 40 mg of QRs or QRods were dispersed in 3-4mL of PVA each. These films were then doctor bladed on glass slides or conductive ITO coated glass slides. The PVA films were dried over-night and then they were further dried with heat-gun at 80°C. An Al mask was made with holes punched into them, then cotton swabs were used to make the contacts using the eutectic mixture of In-Ga (24.5%-75.5%) through the holes of the mask. For PDMS films, the PDMS was used from the commercial Dow Corning Sylgard 184, the QRods or QRs were mixed in the PDMS and then it was doctor bladed on the glass slides with the curing agent of the PDMS kit and left overnight to dry. After it has dried, it was very easily peeled off from the glass slides. PDMS films were more flexible than the PVA films which were more brittle and would break down easily. The contacts on the PDMS films were also made the same way it was made for the PVA films.

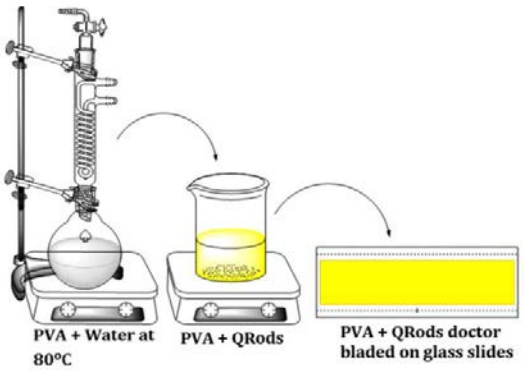

Figure 2: Pictographic representation of the formation of films.

3. Characterizations of the QNCs in Solution

The QRods or QRs were stored in dry powder form. They could easily be re-dispersed in ethanol, toluene or fresh distilled water. The solutions made showed intense luminescence properties. These solutions were characterized thoroughly using TEM, fluorescence emission, composition studies and zeta potential properties.

Photoluminescence (PL) emission and excitation spectra were measured in Perkin Elmer LS45 fluorometer. Transmission electron microscopy (TEM) studies were carried out using JEOL JEM 1210 at 120 kV. Energy Dispersive X-ray Spectroscopy (EDX) analysis was done using the QUANTA FEI 200 FEG-ESEM device and the solid sample was analyzed. Zeta Potential studies were carried out in the Zetasizer Nano ZS (For DLS light source used was He-Ne Laser, 633nm, Max 4mW, back scattering angle used was 173^{o} and for zeta potential electrophoretic light scattering principle was used to do the measurements). UV-vis Spectrum was carried using Cary-5000 UV-vis-NIR spectrophotometer. ImageJ software was used for measuring the particles.

3.1. TEM Study and Size

Quantum Rings (QRs): The TEM images show that the rings are formed. The images are taken using JEOL JEM 1210 at 120 kV. TEM samples were made by dropping a drop of CdSe QR suspension onto the carbon coated copper grids. The sample where the reaction was done for at 160^{o}C and then quenched at low temperature showed perfectly formed rings. For the sample, the reaction done at 175^{o}C or 180^{o}C, it showed that at higher temperature it causes the rings to be aggregated and the sample becomes contaminated with smaller QDs and hence we decided to keep the temperature at 160^{o}C. While at higher

temperatures the samples became contaminated, at lower temperatures of 120°C, the rings were not fully formed and had open ends, resembling the horseshoe structure. The images of each are shown in Figure 3.

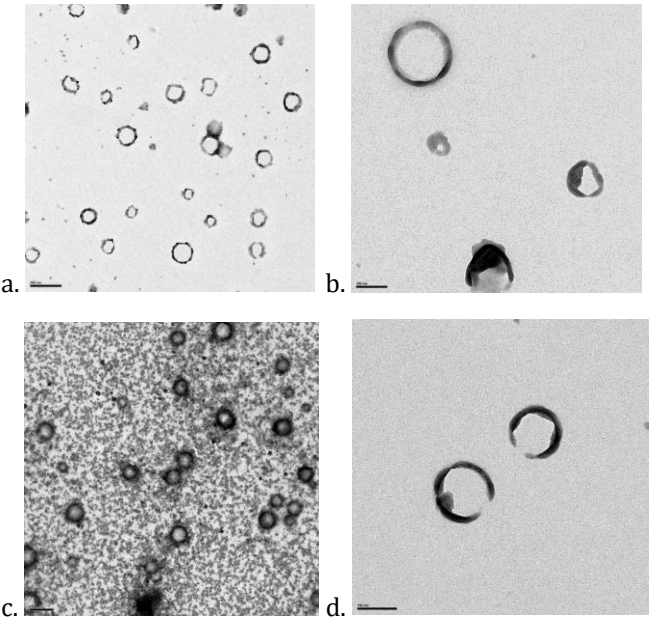

Figure 3: TEM images of (a) Rings formed at 160°C, (b) ring formed at 160°C at higher magnification, (c) rings formed with aggregation of dots at higher temperature of 175°C and (d) open ended rings or horseshoes formed at 120°C.

Gaussian Size Graph for QRs: The Gaussian size graph of the QRs at 160°C showed the size well distributed with a mean of 10.12nm, while on increasing the temperature, the rings were not formed uniformly and the distribution was less even and it had a mean of 29.3nm. The rings were much thicker with increase in temperature as seen in the mean toroidal size. This makes the rings fall outside the quantum regime when synthesized at a higher temperature than 160°C while at 160°C, it is not the case.

3.1.3. Quantum Rods and Rings in Water

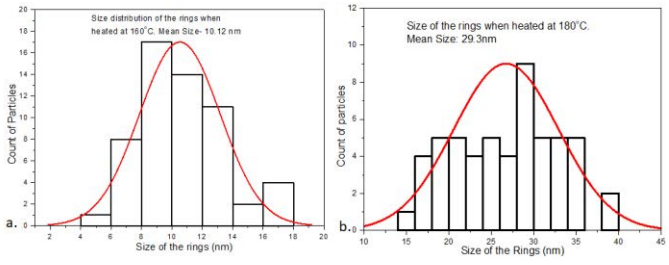

Figure 4: Gaussian Size graphs of (a) Rings formed at 160°C and (b) Rings formed at 175°C.

Quantum Rods (QRods): TEM studies were carried out using JEOL JEM 1210 at 120 kV. TEM samples were made by dropping a drop of CdSe QRod suspension onto the carbon coated copper grids. The microscopy images showed QRods being formed. The sample synthesized at 160°C with partial release of pressure shows well formed rods while the sample prepared at higher temperatures than this show aggregated rods. The sample though is not contaminated as is in the case of QRs.

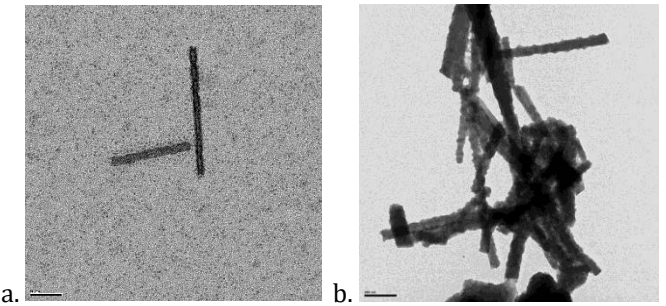

Figure 5: TEM images of (a) Rods formed at 160°C and (b) Rods formed at 175°C.

Gaussian Size Graph for QRods: The Gaussian size graph of the QRods at 160°C showed the size well distributed with a mean of 19.5nm, while on increasing the temperature, the rings were not formed uniformly and the distribution was less even and it had a mean of 39.7nm. Though at higher temperatures the size of the rods were outside the quantum

regime, they did show fluorescence which was not so in the case of the QRs. This will be shown in the fluorescence section.

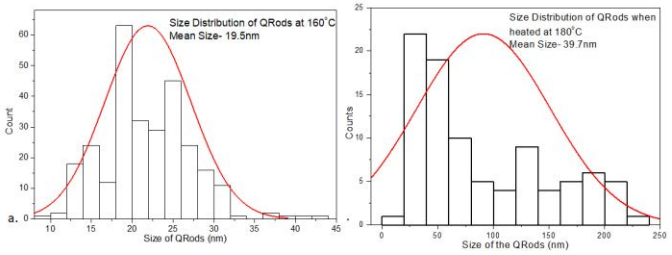

Figure 6: Gaussian Size graphs of (a) Rods formed at 160°C and (b) Rods formed at 175°C.

3.2. Composition Study

EDX Studies of QRs and QRods: The chemical composition was studied for the solid samples in HRSEM with EDX technique and the presence of Cd, Se and S was observed. In the EDX studies, we found a large amount of Cd compared to S and Se. It must be noted that these morphologies have been obtained by using a higher ratio of Cd:Se, that is three times more than what is the standard ratio. Using the standard ratio of Cd:Se as 2:1, along with the conditions used in this work does not lead to any of these morphologies hence necessitating the presence of this particular quantity of Cd and Se. The need for excess Cd was important in both the cases of QRs and QRods. The preferred ratio for the synthesis of these morphologies is 4:1 or 6:1. These ratios help us obtain the best results. At higher ratios the samples have lot of unreacted precursor salts of Cd while at lower ratios of 3:1 or 2:1 we do not obtain anything other than QDs.

3.1.3. Quantum Rods and Rings in Water

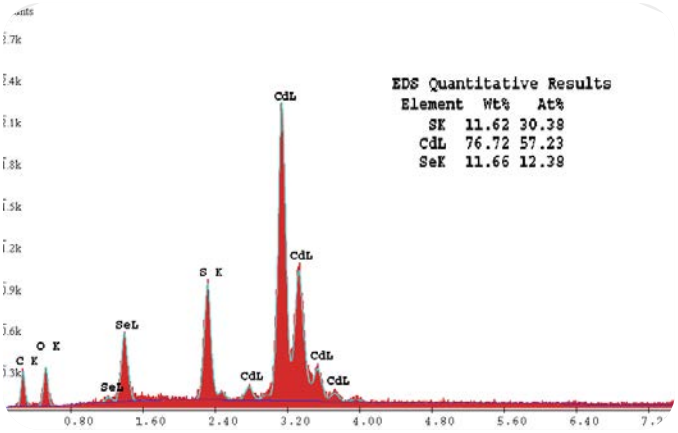

Figure 7: EDX spectrum of QRs. It shows the presence of Cd, Se and S.

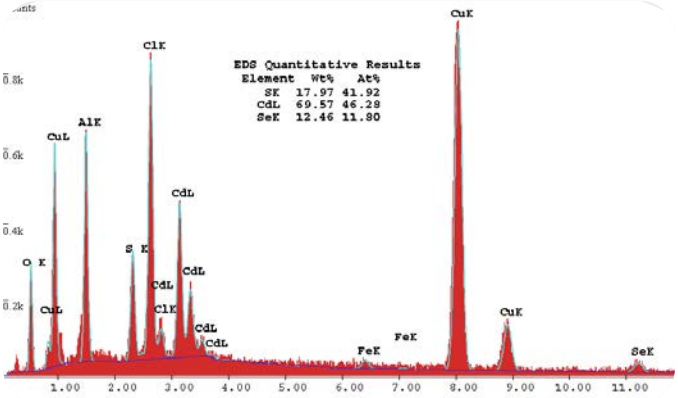

Figure 8: EDX spectrum of QRods. It shows the presence of Cd, Se and S.

Electron Diffraction of QRs and QRods: The electron diffraction studies were done on the selected area of the sample on TEM grids. For both the QRs and QRods it was confirmed that hexagonal wurtzite structure of CdSe was formed.

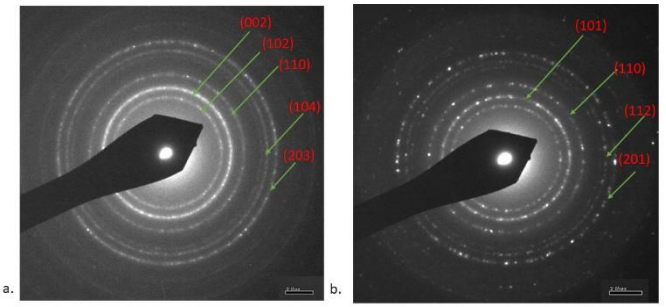

Figure 9: Electron diffraction patterns of (a) QRs and (b) QRods. It confirms the formation of CdSe in hexagonal wurtzite structure.

3.3. Fluorescence Study

Naked eye Luminescence under UV-Vis: The QRs and QRods samples were isolated and stored in powdered form. Then they were re-dispersed in ethanol, toluene or fresh water and they showed bright luminescence. The QRs upon UV illumination showed bright green luminescence and did not change the color of luminescence with time of reaction or storage. While in case of the QRods, initially they showed bright yellow luminescence but with increase in time of reaction they changed their emission to orange as larger rods grew with larger cross-sections. This changed the bandgap of the QRods thus they emitted a different color. Once the color emitted, it did not change the color with the period of storage.

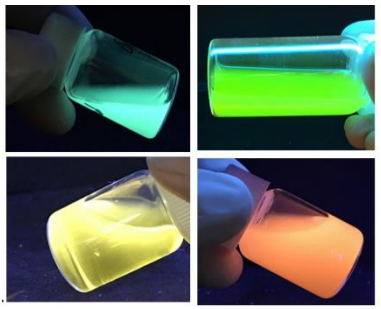

Figure 10: QRs at the top of the figure and QRods at the bottom with changes in colour of emission over time.

3.1.3. Quantum Rods and Rings in Water

PL Emission Study: The emission spectra of the QRs and QRods were recorded using the Fluorometer. The wavelength of emission for QRs is 525nm while for QRods is around 555nm. Their intensities were remarkably high. To check their brightness, their emission spectra were plotted with the emission spectrum of QDs synthesized in water at normal room temperature and also at 100°C under reflux. In both cases the intensity of emission of QRs and QRods were superior to the QDs. The intensity emitted by the QRs were superior to the intensity emitted by the QRods.

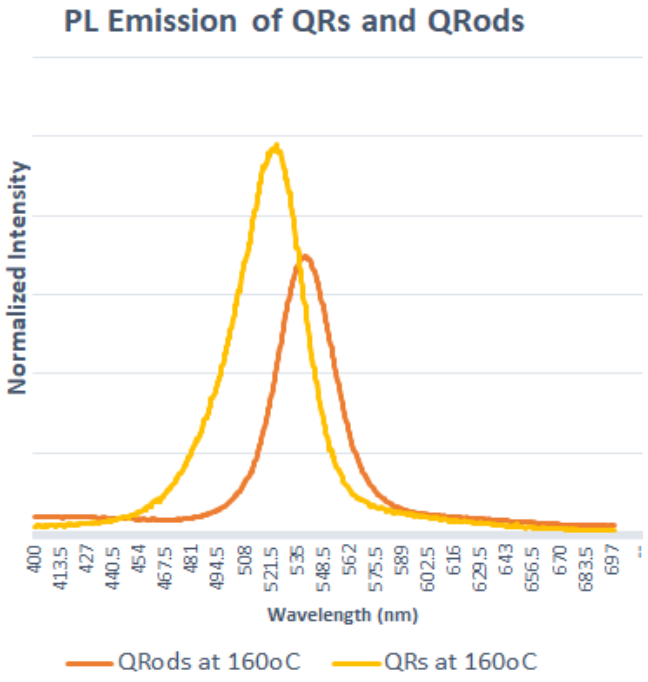

Figure 11: Emission Spectra of QRods and QRs.

3.1.3. Quantum Rods and Rings in Water

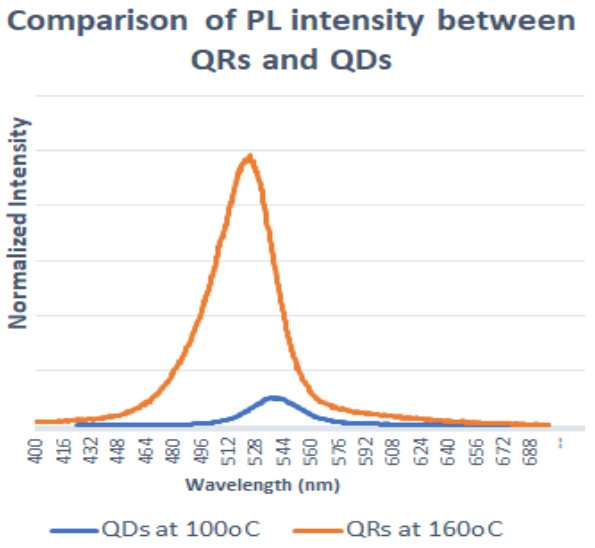

a.

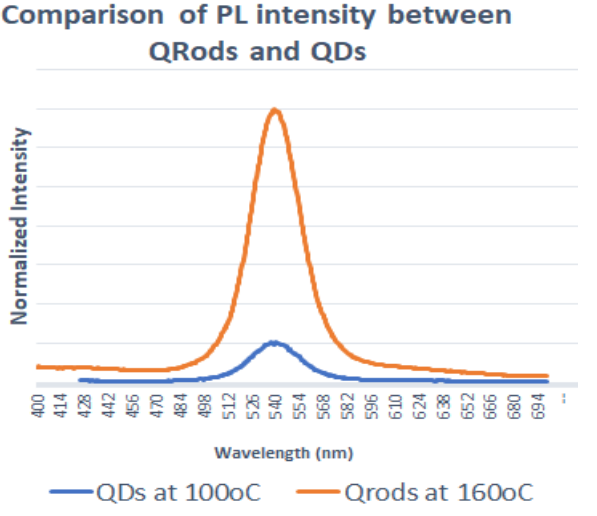

b.

Figure 12: Emission of a) QRs in comparison with QDs synthesized at 100°C and (b) QRods in comparison with QDs synthesized at 100°C.

UV-vis and Excitation Spectra: The excitation spectra were recorded using the fluorometer for the samples and the UV-vis was recorded in UV spectrometer. For the UV-vis, the sample was made of different concentration in order to obtain the absorbance value below 0.1. A 5mM and 2 mM solution of QRs and QRods in ethanol was used for obtaining the desired UV-vis spectra. The absorbance was around 480nm for QRs and around 500nm for QRods. This was consistent with the larger size of the QRs and QRods formed. The excitation spectra for both the QRs and QRods were recorded for the respective samples. The excitation spectra coincided with the range of the absorbance observed in the UV-vis. The images below show the UV-vis spectra and the excitation spectra plotted on top of the UV-vis spectra.

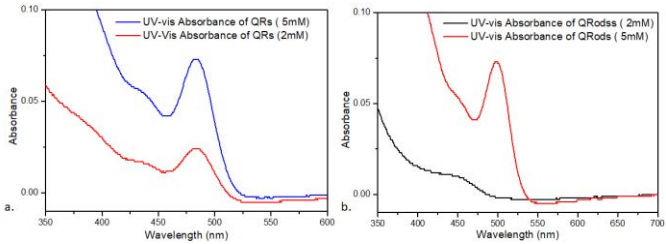

Figure 13: UV-vis absorbance spectra of (a) QRs and (b) QRods.

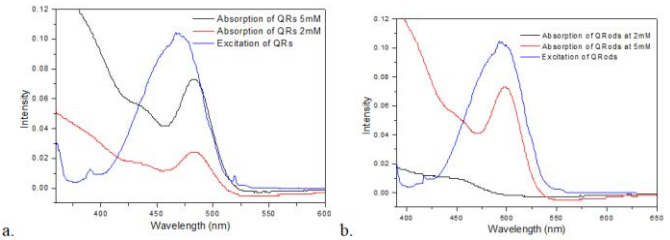

Figure 14: Excitation Spectra on top of UV-vis spectra of (a) QRs and (b) QRods.

Quantum Yield (QY) Calculation: The QY of these samples were measured with the formula given below:

$QY = QY_{ref} \{\eta^2 I A_{ref} (\eta_{ref} I_{ref} A)^{-1}\}$
Where QY_{ref} :QY of the reference (Rhodamine 6G)
η: Refractive index of the solvent (Ethanol)
η_{ref}: Refractive index of the solvent of standard (Ethanol)
I: Integrated area of emission spectrum of sample
I_{ref} : Integrated area of emission spectrum of reference
A: Absorbance value of sample
A_{ref}: Absorbance value of the reference

The reference used for the QY measurement was Rhodamine 6G and its QY in ethanol (0.95). The standard used was Rhodamine 6G as it had the absorbance and emission around the similar regions and also the solvent used was ethanol for the sample and the standard.
Two concentrations of the sample were used to measure the absorbance until the values of absorbance were less than 0.1 as mentioned above. These absorbance values were taken for the QY measurement, while the excitation wavelength used was 480nm and 465nm to record the emission peaks. The emission peaks were at around 525nm for the QRs while the ones for QRods were around 550 to 560nm. The integrated area under these emission peaks was used in the QY measurements. The quantum yields obtained for the QRods was 42% while for the QRs was around 49% which are both quite high when compared to QY of QDs in water. Since there has been no water based QRs or QRods synthesized before so we could not compare the values with them.

PL Intensity over a year: The PL emission intensities were studied over a year in suspension. Their intensities were studied over time, the first reading was taken after 1 month, then it was consecutively recorded every month for 12 months and it showed very little degradation in the intensity values of their emission when in suspended state.

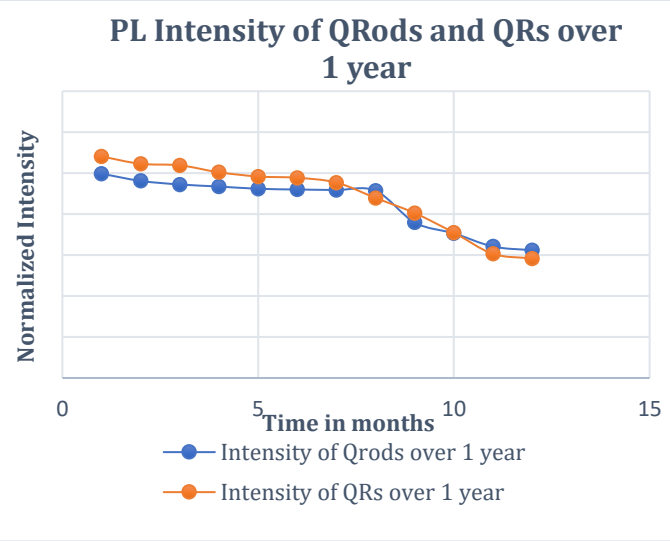

Figure 15: PL emission intensity study for a year for suspensions of QRs and QRods.

3.4. Zeta Potential Study

The CdSe QRs and QRods were studied by zeta-potential using the electrophoretic light scattering principle for their stability in ethanol and water. In both the solvents they showed a zeta-potential above ||30||mV, thus proving that the suspensions are stable.

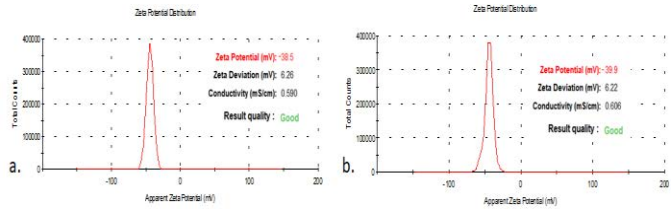

Figure 16: Zeta Potential of the QRs in (a) Ethanol (-38.5 mV) and (b) Water (-39.9 mV).

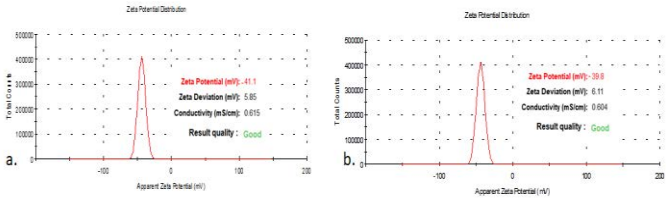

Figure 17: Zeta Potential of the QRods in (a) Ethanol (-41.1 mV) and (b) Water (-39.8 mV).

The zeta- potential remained almost constant for 12 months since being suspended in ethanol. The study of zeta potential was done for ethanol as we calculated the quantum yield in ethanol and kept them suspended in ethanol for a year to study the luminescence emission intensity too. The zeta potential was measured after every month as is the case when their luminescent properties were evaluated in the suspended state. It was important to measure both of them in parallel to study their stability in suspension and their intensity to check whether one affected the other or not. After 12 months of evaluation we could see that the degradation in their stability and luminescent properties was quite negligible.

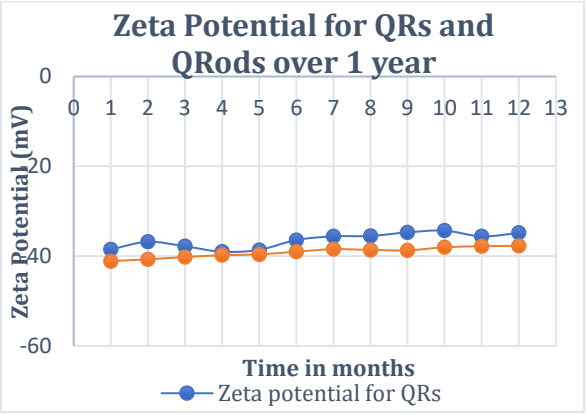

Figure 18: Zeta Potential of the QRods and QRs in ethanol over 12 months of time.

4. Characterizations of the QNCs in Films

The polymeric films were made as mentioned before in order to test these QNCs in solid form and to study their photoluminescence and electroluminescence in the polymeric films. They were thoroughly characterized using the HRTEM, HRSEM and Optical Microscopy in order to observe the structures inside the films. EDX was done using the TEM grids for compositional study. Confocal microscopy was done to see their PL while electroluminescence was studied using metal contacts and ITO substrates.
HRTEM was done using JEM-2011 at 200kV with 0.18nm resolution. Polymeric samples for HRTEM were cut using Cryo Ultramicrotome Leica FC6. HRSEM was done using Zeiss Merlin and the samples were analyzed in films on wafer holders. Au Sputtering was done using E5000 Sputter Coater, Polaroid Equipment Limited. Optical microscopy was done using Olympus DP20. Confocal microscopy was done using Olympus Fluoview 1000. Sample was analyzed in normal glass slides. Electroluminescence was done using a Cascade Microtech Summit 11000 probe station, properly screened from external electromagnetic noise by means of a Faraday cage. The $I(V)$ characteristics were performed using an Agilent B1500 semiconductor device analyzer. EL spectra were acquired via a Princeton Instruments LN_2-cooled CCD coupled to a monochromator (400–1100 nm range).

4.1. HRTEM and HRSEM Studies

HRTEM Studies: High resolution transmission electron microscopy was needed to observe the QNCs inside the polymeric films. For the HRTEM studies, the polymeric films were quite large and thick. So, they had to be cut into

smaller pieces to be placed on the grid of the TEM. They were sliced using a cryomicrotome and then placed on the holder for HRTEM. The films were studied and the QRs and QRods were seen inside the films at high magnification.

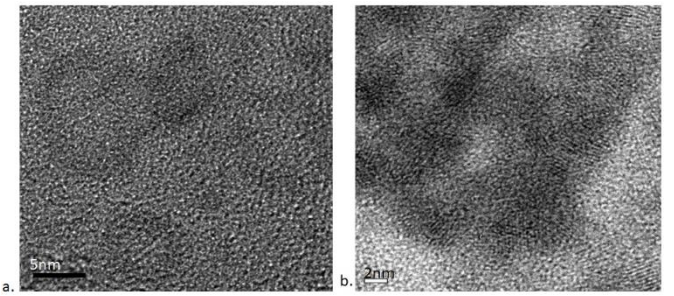

Figure 19: HRTEM images of polymeric films containing (a) QRs and (b) QRods in them.

The polymeric films were insulating and hence the images obtained from the HRTEM were not very clear as obtained by the suspensions of the QNCs but still we can clearly visualize the QNCs being present within the films.

HRSEM Studies: As we had already seen that the films were insulating and since the resolution of the SEM machine is not as high as the TEM, so, we decided to sputter the films with a layer of Au before studying them. A thin layer of 1nm of Au was sputtered onto the films and these films were then studied using the HRSEM. The rods due to their longer dimensions were more clearly visible than the rings.

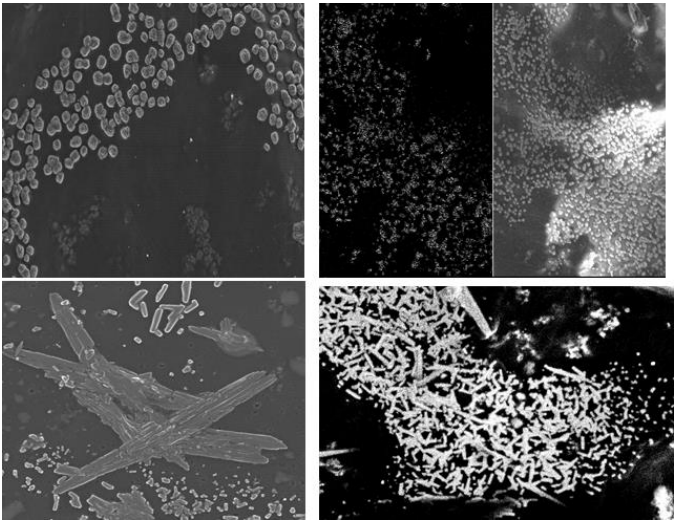

Figure 20: HRSEM images of polymeric films containing QRs (top) and QRods (bottom) in them.

The HRTEM and HRSEM both helped us to confirm the presence of the QNCs inside the films. Both the films of PVA and PDMS were studied and the results obtained were the same. After this, we wanted to study their composition and the luminescence properties so as to see if there was any change when they were used in a nanocomposite form other than in a suspended form.

4.2. Composition Study

EDX Studies: After the confirmation that we could see the QNCs inside the film we proceeded further to study the composition with the EDX. The EDX was studied on the TEM grid and we could very well observe the presence of Cd, Se and S like we saw in the powdered samples of the QNCs.

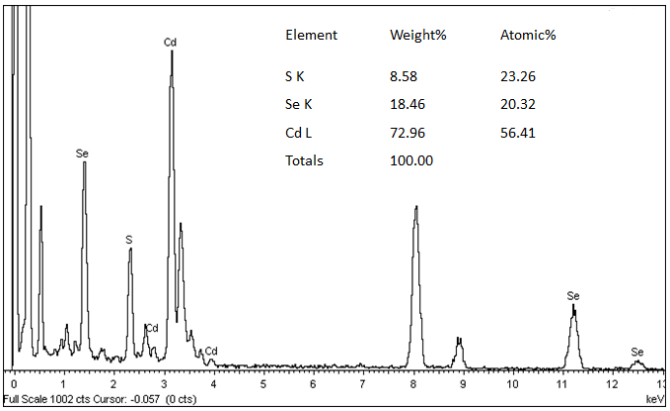

Figure 21: EDX obtained from the TEM grid containing the Polymeric film embedded with QRs. It shows the presence of Cd, Se and S.

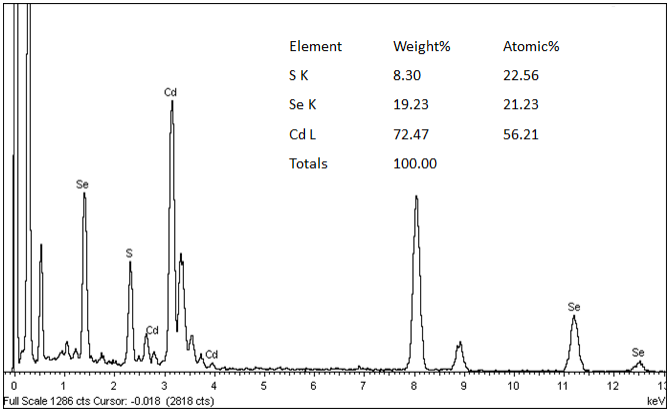

Figure 22: EDX obtained from the TEM grid containing the Polymeric film embedded with QRods. It shows the presence of Cd, Se and S.

Characteristically the amount of Cd was higher compared to the normal amount of Cd used as seen previously in the EDX of the powdered samples.

Electron Diffraction Study: Electron diffraction patterns could not be obtained clearly from the TEM grids due to the insulating nature of the polymeric film which contained the QNCs in them. Due to the insulation of the polymer, the

diffraction patterns were too diffused and the diffraction rings could be seen very faintly. Still we tried and could obtain some rings which corresponded with the hexagonal wurtzite structure of CdSe.

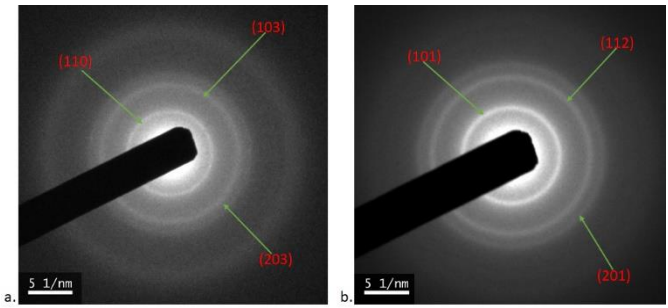

Figure 23: Electron diffraction pattern of (a) QRs and (b) QRods inside the PVA films. These patterns confirm the presence of CdSe in hexagonal wurtzite structure inside the films.

4.3. Photoluminescence Study

The PL study for the films were necessary to see whether the luminescent properties of the QNCs were preserved or not. For this, we used the confocal microscopy to check the wavelength of emission of the QNCs and UV illumination was used to see the colour emitted by them.

Naked eye luminescence under UV-vis: The films were prepared and illuminated under UV-vis lamp of 365nm wavelength and the films emitted luminescence. The films containing QRs emitted green luminescence while the film containing QRods emitted orange or yellow luminescence as was observed in the suspension of these QNCs. QDs were also made at 150oC as described in chapter 2 and these were also encapsulated in the polymer matrix to obtain films but their intensity of emission was much lower than

the QRs and QRods as seen in the figure 22. This was done to compare the intensities of all the three QNCs under UV illumination. Clearly in the image we can see that the emission produced by the QRs and QRods is much brighter when compared to the QDs. Out of the three QRs is the brightest, then the QRods and then the QDs. QRs emitted green, QRods emitted orange while QDs emitted a faint luminescence of yellowish orange.

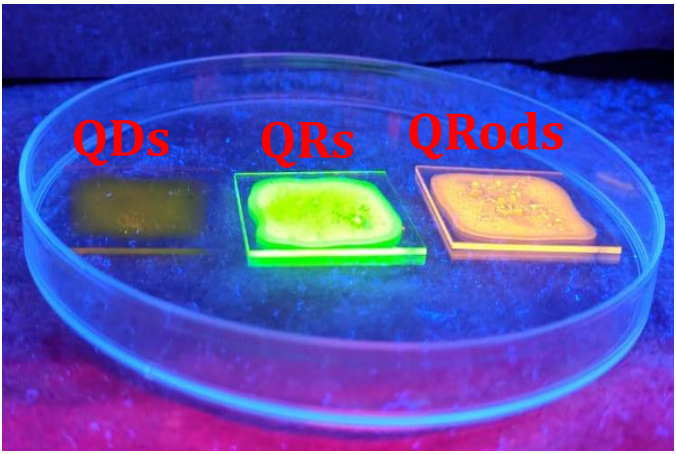

Figure 24: Polymeric films of PVA containing QDs, QRs and QRods under UV illumination at an excitation wavelength of 365nm.

These films above are made in PVA. Flexible films were made too in PDMS as mentioned before. These films could be easily peeled off and separated from the glass slides. The PVA films could also be removed from the glass slides, but in that case the films were more brittle and would break off easily compared to the PDMS ones. The PDMS films could be made of different shapes as desired.

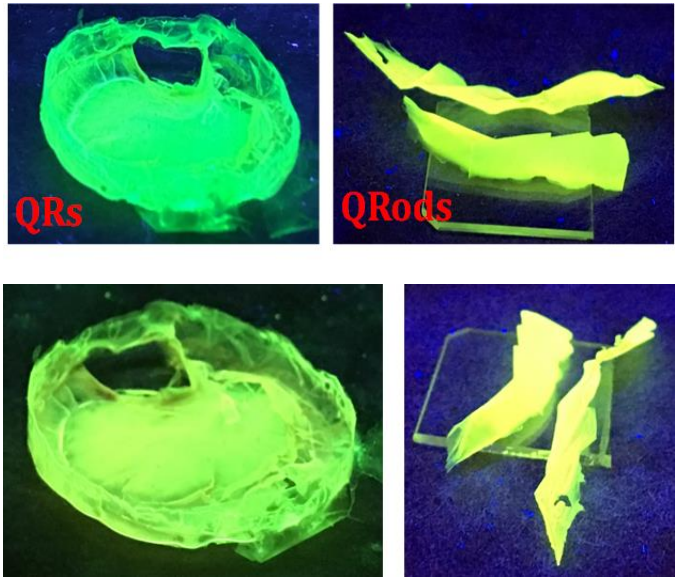

Figure 25: Polymeric films of PDMS containing QDs, QRs and QRods under UV illumination at an excitation wavelength of 365nm (top) and 405nm (bottom).

Confocal Microscopy: After observing the luminescence of the films under the UV lamp, we decided to quantify the luminescence in them. For this we used the confocal microscopy. This was because the confocal microscopy could be easily done on the glass slides and there was no need to peel off the film from them. Moreover, the laser used to excite in confocal microscopy was 405nm and 488nm which is well in accordance with the absorption wavelength of these QNCs. Also, the wavelength of 488nm corresponded with the one of the values of wavelength used for calculating the QY.

In the confocal microscopy we could obtain the emission from the QNCs embedded within the films very well. The QRs and the QRods showed the emission at the exact wavelength at which we obtained their emission when suspended in ethanol.

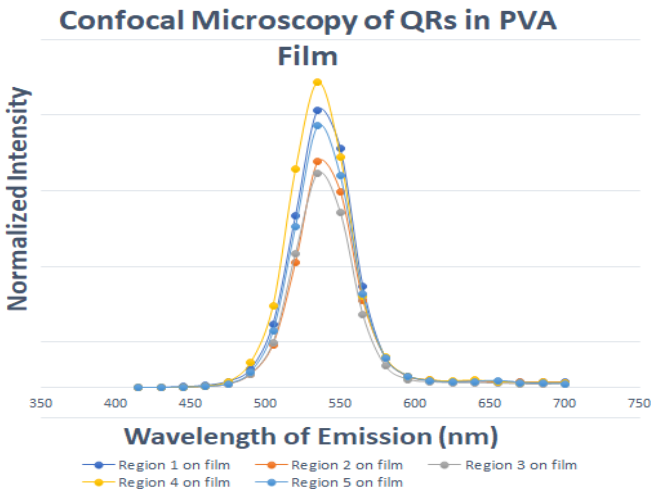

Figure 26: Confocal Microscopy of polymeric film of PVA containing QRs in them.

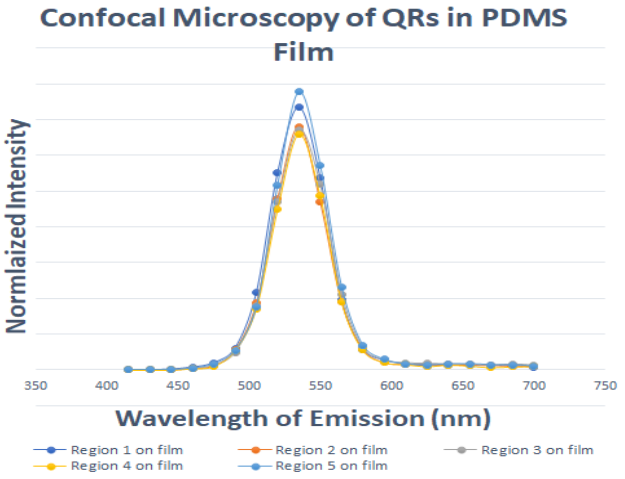

Figure 27: Confocal Microscopy of polymeric film of PDMS containing QRs in them.

Different regions on the film was illuminated using the lasers from the confocal microscope and their emissions

were checked. All of the wavelengths coincided with each other. The intensities of the emission varied a little. This was due to the non-uniform distribution of the QRs inside the films. The regions with more concentration or aggregates of the QRs showed more intense emission than the regions containing less amount of the QRs in them. The emission was also recorded for the PDMS films.

Similar confocal microscopy was done for the QRods too. Their emission wavelength also matched with their emission in suspension, Further, a comparative study was done regarding the emission of the films containing QRs, QRods and QDs in PVA. We compared the intensities obtained by each film. We plotted them together by normalizing the obtained intensity and we could clearly see the difference in the emissive properties of these QRs and QRods than to the QDs. The emission was also compared in suspension and even there the emissions of the QRs and QRods were superior and even here it was the same story. So, we could quantitatively agree that these new QNCs had superior emissive properties to the QDs used in water so far.

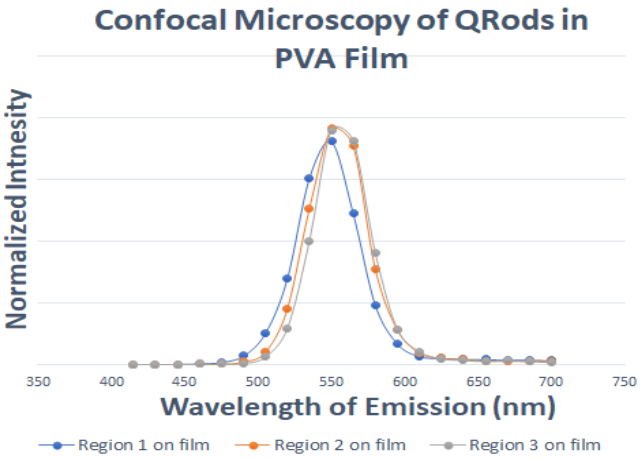

Figure 28: Confocal Microscopy of polymeric film of PVA containing QRods in them.

3.1.3. Quantum Rods and Rings in Water

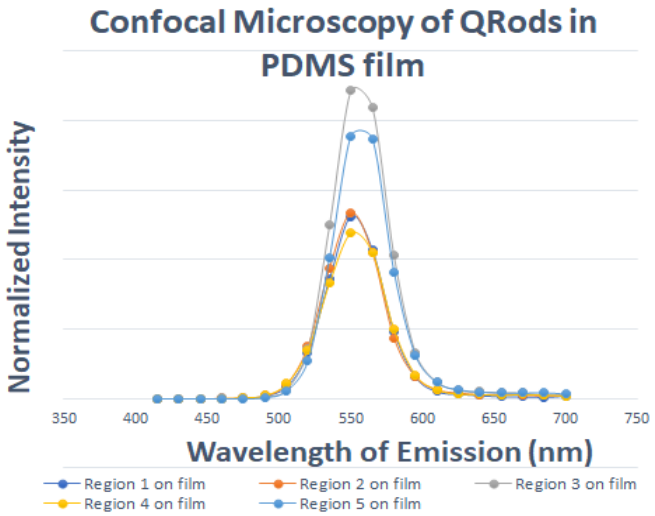

Figure 29: Confocal Microscopy of polymeric film of PDMS containing QRods in them.

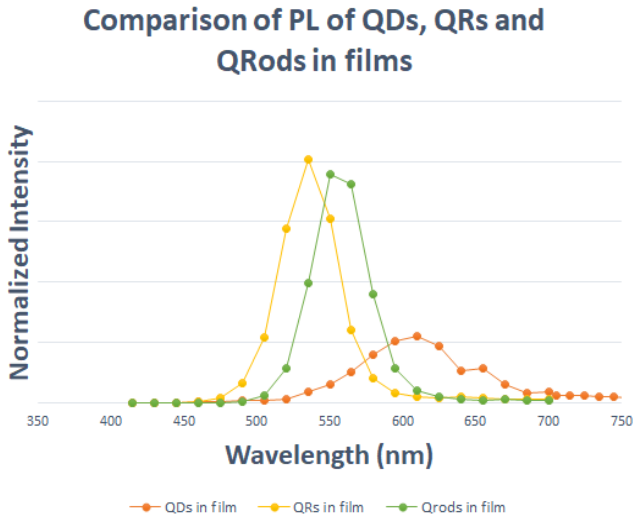

Figure 30: Confocal Microscopy of polymeric films of PVA containing QDs, QRs and QRods for comparison of their emission intensities inside the film.

4.4. Electroluminescence Studies

After succeeding with the PL studies of the QRs and QRods in the polymeric films we wanted to test their electroluminescence (EL) properties. As described earlier the films were deposited using doctor blading on the conductive surface of the ITO coated glass slides. Then on completely drying the films the contacts were made of the eutectic mixture.

Then these samples were used to test the EL using the positive contact on the ITO and the negative contact on the eutectic mixture. With this improved way of measuring the EL, we could obtain the EL emission of these QNCs. The EL properties were not as remarkable as compared to the PL properties obtained by these QNCs, but they could be easily obtained using this method of measurement. The reduction in the EL intensity may arise due to the non-conducting polymeric film surrounding the QNCs, which could have hindered the passage of current. The EL peaks were slightly redshifted than the PL peaks by around 10nm. The intensities of these peaks were low compared to standard EL emitting species and further work needs to be done to improve this aspect of these QNCs. The EL peaks were visible after 10V of current applied. The recorded spectrum is shown at 12V and 15V. The need to apply higher voltage is due to the insulating behavior of the polymer matrix in which the QNCs were embedded for the EL study. Efforts were made to increase the conductivity of the polymer matrix by adding graphite into the polymer along with the QNCs and then depositing the films. But due to the black color of the graphite, the emission was hindered, though the conductivity increased. To be able to overcome this we used NaCl as the next ingredient to obtain higher conductivity and also to get better emission as was seen in the previous samples. The NaCl did not increase the conductivity as graphite had but it did not suppress the emission as graphite either. We tried to test with these new samples, but even here the emission got diffused due to the presence of the salt inside the polymer matrix. We need to do further

work on this to improve the EL emission of these films so that they could be used for display purposes in the future.

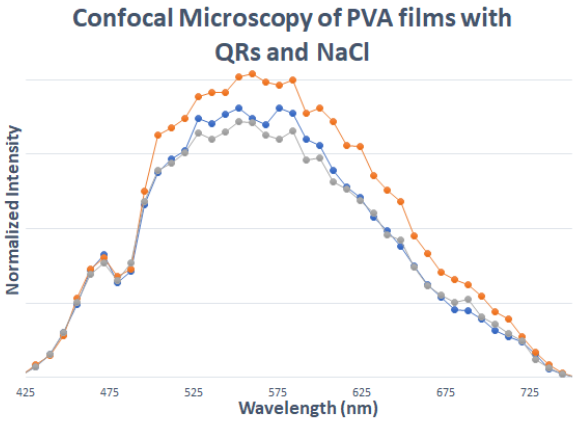

Figure 31: Confocal Microscopy of the PVA film containing QRs and NaCl. The emission does not give a particular peak as the salt diffuses the emission.

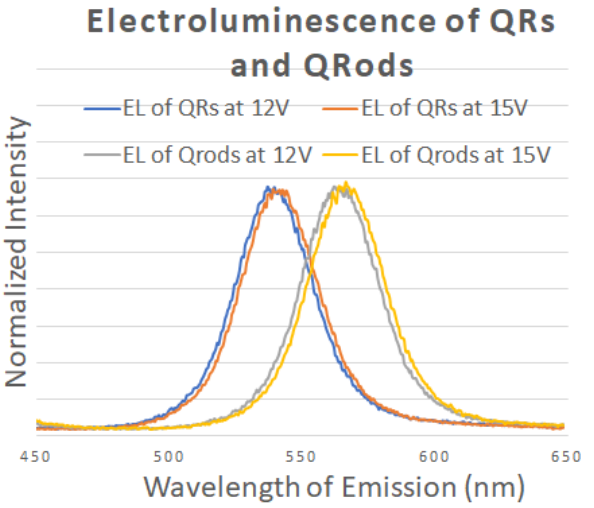

Figure 32: Electroluminescence of the QRs and QRods inside the polymeric film of PVA.

4.5. Thickness of the Films

The thickness of the films was measured using the optical techniques and not the profilometry because the films were highly photoluminescent. The confocal microscopy was used to study the thickness of these films by using z-stacking from the reflection of the films when irradiated by the laser. According to the calculations the films were around 60-80 micrometres thick. The 3D images of the pictures were obtained and each film was composed of either 21 to30 slices stacked together and showed quite an homogeneous distribution of the QNCs in them in all the slices.

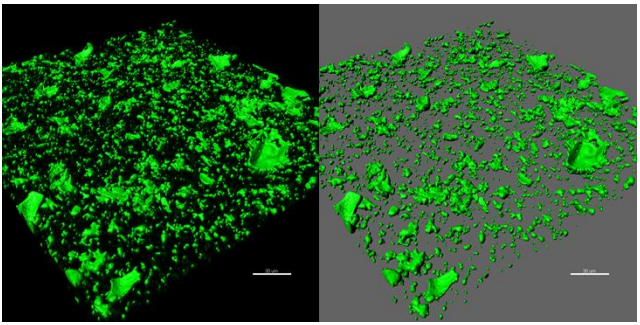

Figure 33: Confocal microscopy images of the Polymer films containing QRs. It shows an even distribution of the QRs throughout the films.

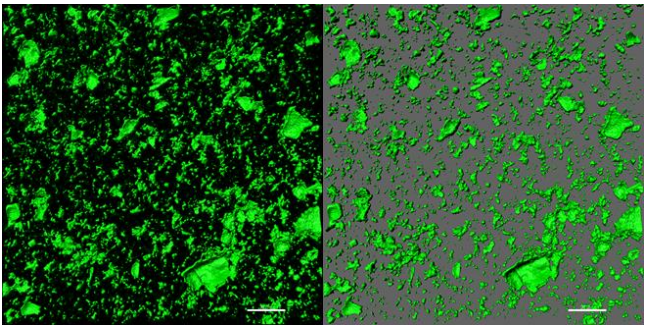

Figure 34: Confocal microscopy images of the Polymer films containing QRods. It shows an even distribution of the QRods throughout the films.

5. Conclusions

A simple hydrothermal method has been developed to produce distinct quantum morphologies: QRs, QRods and Quantum Horseshoes. The reagents utilized are those commonly mentioned in the synthesis of CdSe QDs in aqueous preparations. The key points to produce the distinct quantum morphologies are the ratio Cd:Se that is considerably leaning in favor of Cd with regard to the typical 2:1, the T near 160ºC, the fast T rise achieved with good isolation of the setup, and the play with the endogenous pressure and pressure release of the reaction vessel. The success in obtaining the distinct morphologies is due to the interplay of these parameters. Moving away from the found parameters leads to QDs or to non-luminescent materials. The materials produced are easily isolatable; display highly bright PL and high QYs. These QNCs can be stored in powdered solid form, as well as in a suspension with ethanol, toluene or water. With no exception, the QRs and the QRods are far brighter than the corresponding QDs produced in similar conditions but at lower T. The QRs and QRods have been dispersed in polymeric matrices and the PL characteristics have remained unaltered for months, as is the case in solutions. Furthermore, they do show considerable EL and this can be further improved with better conductivity achieved within the polymer matrix without hindering the emission of these materials.

6. References

[1] S. N. Raja, A. C. K. Olson, K. Thorkelsson, A. J. Luong, L. Hsueh, G. Chang, B. Gludovatz, L. Lin, T. Xu, R. O. Ritchie and A. P. Alivisatos, *Nano Lett.*, **2013**, *13*, 3915.

[2] L. Manna, E. C. Scher, L. S. Li, A. P. Alivisatos, *J. Am. Chem. Soc.* **2002,** *124*, 7136.

[3] A. Fu, W. Gu, B. Boussert, K. Koski, D. Gerion, L. Manna, M. L. Gros, C. A. Larabell, A. P. Alivisatos, *Nano. Lett.* **2007,** *7,* 179.

[4] I. Fedin and D. V Talapin, *J Am Chem Soc*, 2016, **138**, 9771–9774.

[5] L. Li, J. Hu, W. Yang and a. P. Alivisatos, *Nano Lett.*, **2001**, *1,* 349.

[6] A.L. Efros, M. Rosen, M. Kuno, M. Nirmal, M.G. Bawendi, *Phys. Rev. B*. **1996,** *54,* 4843.

[7] X. Peng, L. Manna, W. Yang, J. Wickham, E. Scher, A. Kadavanich, A.P. Alivisatos, *Nature* **2000,** *404*, 59.

[8] A. Shabaev, L. Efros, *Nano Lett.* **2004,** *4,* 1821.

[9] H. Htoon, J. A. Hollingworth, A. V. Malko, R. Dickerson, V. I. Klimov, *Appl. Phys. Lett.* **2003,** *82,* 4776.

[10] D.W. Oxtoby, *Acc. Chem. Res.* **1998,** *31*, 91.

[11] J.W. Mullin, *Crystallization*, 3rd Edition, ButterworthHeineemann, Oxford, **1997.**

[12] M. Bruchez, M. Moronne, P. Gin, S. Weiss, A.P. Alivisatos, *Science.* **1998,** *281,* 2013.

[13] W.C.W. Chan, S.M. Nie, *Science.* **1998,** *281,* 2016.

[14] U. Resch-Genger, M. Grabolle, S. Cavaliere-Jaricot, R. Nitschke, T. Nann, *Nat. Methods.* **2008,** *5*, 763.

[15] C. Tong, S. Yoon and L. Wang, *Nanoscale Res. Lett.*, 2012, **7**, 520.

[16] V. E. Demidov, S. Urazhdin, G. de Loubens, O. Klein, V. Cros, A. Anane and S. O. Demokritov, *Phys. Rep.*, **2017**, *673*, 1–31.

[17] A. Fuhrer, S. Lüscher, T. Ihn, T. Heinzel, K. Ensslin, W. Wegscheider and M. Bichler, *Nat.*, **2001**, *413*, 822–825.

[18] W. C. Tan and J. C. Inkson, *Phys. Rev. B - Condens. Matter Mater. Phys.*, **1999**, *60*, 5626–5635.

[19] V. I. Klimov, S. A. Ivanov, J. Nanda, M. Achermann, I. Bezel, J. A. McGuire and A. Pirystinski, *Nature*, **2007**, *447*, 441–446.

[20] G. O. De Sousa, D. R. Da Costa, A. Chaves, G. A. Farias and F. M. Peeters, *Phys. Rev. B*, **2017**, *95*, 20514.

[21] L. L. Li, D. Moldovan, P. Vasilopoulos and F. M. Peeters, *Phys. Rev. B*, **2017**, ***95***, 205426.

[22] D. R. Da Costa, A. Chaves, W. P. Ferreira, G. A. Farias and R. Ferreira, *J. Phys. Condens. Matter*, **2017**, *29*, 165501.

[23] A. Lorke, R. J. Luyken, M. Fricke, J. P. Kotthaus, G. Medeiros-Ribeiro, J. M. Garcia and P. M. Petroff, *Microelectron. Eng.*, **1999**, *47*, 95–99.

[24] A. Lorke, R. J. Luyken, A. O. Govorov, J. P. Kotthaus, J. M. Garcia and P. M. Petroff, *Phys. Rev. Lett.*, **2000,** *84*, 2223–2226.

[25] D. Haft, F. Bickel, A. Lorke, K. Karrai, J. M. Garcia, W. Schoenfeld and P. M. Petroff, *Nature*, **2000**, *405*, 8–11.

[26] M. Bayer, M. Korkusinski, P. Hawrylak, T. Gutbrod, M. Michel and A. Forchel, *Phys. Rev. Lett.*, **2003**, *90*, 4

Results and Discussions Part 2
(Magnetic Nanoparticles)

3.2.1. Nano-Hybrids for Cancer Therapy

The potential biomedical applications of the MNP nanohybrids coated with m-carboranylphosphinate(1-MNPs) as a theranostic biomaterial for cancer therapy was tested. The studies of colloidal stability of the 1-MNPs' suspension in different culture media and temperatures were carried out before testing 1-MNPs' in vitro toxicity. The cellular uptake and toxicity profile of meta carboranyl phosphinate-MNPs from culture media by human brain endothelial cells (hCMEC/D3) and glioblastoma multiform A172cell line was demonstrated.

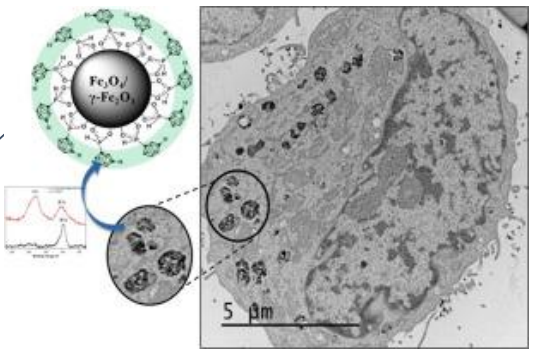

Arpita Saha
ICMAB-CSIC (UAB)

Contents

1. Introduction

Nanoparticles (NPs) are solid colloidal particles having dimensions in the range of 10 to 100 nm. [1] NPs have now become the primary materials to be used in biomedical applications as they offer many advantages over larger particles such as an increased surface to volume ratio and increased electric, optical or magnetic properties. [2] NPs are used in the form of nano-systems for biological applications. Not just NPs but combination of NPs with other materials forming hybrid nano-systems, being used for biological studies have become a new trend in the field of research. In recent years, there has been a steadily growing interest in using these nano-systems in different biomedical applications such as targeted drug delivery, hyperthermia, photoablation therapy, bioimaging and biosensors. [3,4] Out of the numerous nano-systems and NPs, much of the focus has been on iron oxide nanoparticles (SPIONs) because of their superior chemical, biological and magnetic properties including chemical stability, non-toxicity, biocompatibility, high saturation magnetisation and high magnetic susceptibility.[5-8] These properties allow for its use in many biomedical applications: bioimaging[9–12], hyperthermia [13,14], drug delivery [15-18], cell labelling [19,20] and gene delivery [21,22]. Not just SPIONs, it has also been reported that other magnetic nanomaterials such as Fe–Co, Cu–Ni, Fe–Ni, Co–Fe_2O_4 and Mn–Fe_2O_4, nanoparticles are being investigated for use in bioimaging [23-26], hyperthermia [27-29] and drug delivery [30-32] as possible alternatives to SPIONs. [4] Nanomedicine results from these NPs or nano-systems. It is one of the most promising areas in science and technology by the convergence of various disciplines with the aim of taking advantage of the original and unique properties of nanomaterials toward improved diagnostic and therapeutic strategies in medicine in today's world. The main area in which nanomedicine is currently applied is cancer therapy
where major research has been developed. Here, in this chapter we discuss about SPIONs with boron clusters

forming a new type of nano-hybrid system for use in cancer therapy. This kind of a hybrid system has not been studied before and it was specifically to be tested for a new kind of therapy called Boron Neutron Capture Therapy (BNCT).

1.1. Magnetic Nanoparticles (MNPs)

SPIONs are the most researched and commonly used materials for biomedical applications as mentioned in the start. Its popularity is due to unique chemical, biological and magnetic properties as mentioned. [5–8] The MNP is composed of a single magnetic domain if its size decreases below a critical limit. It displays superparamagnetic [33, 34] behaviour as long as the temperature is above the blocking temperature (T_B). In the superparamagnetic state, the magnetic moments of the nanoparticles fluctuate around the easy axes of magnetization. Thus, each one of the MNPs will possess a large magnetic moment whose orientation is continuously changing. When a magnetic field is applied, MNPs in the superparamagnetic state display a fast response to the changes of the magnetic field without remnant or residual magnetization and without coercivity. This plays an extremely important role in the various applications for which they are used. Iron oxide has different oxidation states including iron (II) oxide (FeO), iron (III) oxide (Fe_2O_3) and iron (II, III) oxide (Fe_3O_4). Iron (III) oxide (Fe_2O_3) has different crystalline polymorphs α-Fe_2O_3, β-Fe_2O_3, γ-Fe_2O_3 and ε-Fe_2O_3. It was found that out of all the different forms, maghemite (γ-Fe_2O_3) and magnetite (Fe_3O_4) are the most biocompatible ones. Out of these two though, magnetite (Fe_3O_4) is the most commonly used form for biomedical applications.[3] However, this form of iron oxide has a tendency to oxidise so coating with a biocompatible shell is required. Some examples of coatings include polymers [35,36], ceramics [37,38] and metals. [15] Coating with a shell offers many advantages such as it prevents agglomeration and helps with further functionalisation and conjugation to proteins, enzymes, antibodies, anticancer drugs etc. Iron oxide nanoparticles

have been investigated for use in magnetic hyperthermia treatment [13,14], targeted drug delivery [30-32] and contrast agents in magnetic resonance imaging (MRI) [39,40]. The magnetic properties of iron oxide nanoparticles can be improved by doping with magnetically susceptible elements such as manganese (Mn), cobalt (Co) and nickel (Ni). [41] MNPs used in this chapter is Fe_3O_4 and it is coated with *m*-carboranyl phosphinate and they are referred to as 1-MNPs. This is a ligand to be used in conjugation with the MNPs. In the next section, there is a short discussion on the commonly used ligands to coat MNPs and also the common synthetic routes used to synthesize MNPs having a magnetic core and an organic/inorganic shell.

1.2. Commonly used Coatings and Ligands

The main aspect to consider when designing nanomaterials for medicine is biocompatibility. This feature is achieved by the selection of biomaterials or synthetic non-toxic materials which provide a platform for *in vivo* applications. The MNPs need to be coated with a shell or ligands which can act as a barrier between the magnetic core of iron oxide and the environment in which it will be used. The shell also helps in dispersing it in different media and water at a range of pH. Plus, the surface plays an important role in effective interfacing with the biological systems. Thus, there is a huge need of surface coatings in the form of ligands or shell of different organic or inorganic materials for their use in biological systems. There are two ways the MNPs are coated, 1st during the synthesis in-situ and 2nd after the synthesis process. The most common ones used are listed below:

- *Organics*: dextran, starch, poly(ethylene glycol), (PEG), poly (d,l-lactide) (PLA), polyethylenimine (PEI), especially for hydrophilic organic materials. These organic materials are elected because of their hydrophilic properties which are mandatory for a good dispersion in aqueous media.[42]

- *Small molecules with functional groups*: Smalls molecules having functional groups such as –OH, –COOH, –NH_2 or –SH. Their role is to provide anchorage for further attachment of biomolecules or drugs to specific biomedical applications. Protection of the magnetic component has been achieved by coating with oleic acid, for example [43,44]. Oleic acid can be used even at high temperature to obtain stable iron oxide nanoparticles. This coating does not affect the magnetic behaviour of resultant nanoparticles [45]. Amino acids, citric acid, and vitamins are small molecules very useful for the synthesis of water-soluble magnetic nanoparticles. In some cases, in which the resultant formulation is stable but not aqueous soluble due to coating with hydrophobic small molecules, ligand exchange procedure is used to change polarity [46].

- *Polymers (sub part of organics)*: A large number of either natural or synthetic polymers can be employed for the coating of magnetic nanoparticles. Polysaccharides in general, gelatin, alginate, polyethylene glycol (PEG), poly(d, l-lactide) (PLA), and chitosan are being extensively studied, among others, for biomedical applications—especially, as drug targeting and contrast agents. Biocompatibility is the main feature to achieve on these systems to ensure the expected applications.[47]

- *Biomolecules*: Coating with biomolecules has emerged especially for biological separation, detection, and sensors. Enzymes, antibodies, and proteins in general are biomolecules feasible to bind to nano-iron oxides [48].

- *Inorganic materials*: Improving the stability in dispersion or solution is one of the most intended challenges to achieve by coating with inorganic materials. For biomedical applications, this kind of functionalization enables the binding of biological ligands to iron oxide cores. Metal oxides and silica are examples of inorganic coating agents.

- *Different Coatings:* Other coatings made of carbon are currently being studied due to chemical and thermal stability as well as conductivity. Metallic nanoparticles are also under investigation as coating materials. Gold (Au) and Silver (Ag) are the most common metals employed, but further research is required to improve stability of the obtained nano-systems.

1.3. Common Synthetic Routes for MNPs

The synthetic routes for core MNPs are usually divided with regards to the medium or the number of steps involved in the procedure. Aqueous routes are low cost and sustainable methods and render water dispersible nanoparticles, which are in general desired for biomedical applications considering blood and plasma features in terms of hydrophilicity. Non-aqueous routes render nanoparticles soluble in non-polar solvents. These systems are of interest for encapsulation of lipophilic drugs although they involve functionalization strategies to disperse them in physiological media. The other classification of synthesis procedures for nano-magnetic cores lies in one-step or multi-step procedures. This classification is important to consider for the preparation of MNPs depending on environment and available instruments and facilities at disposal in the laboratory. All the methods present advantages and disadvantages. The election of a specific methodology depends on the final properties of the desired product. [42]

- Co-precipitation Method
- High temperature thermal decomposition method
- Hydrothermal and Solvothermal method
- Sol-Gel reactions and Polyol method
- Microemulsion
- Sonolysis and Sonochemical method
- Microwave assisted synthesis
- Biosynthesis
- Other methods (Electrochemical method, Flow Injection method and Spray Aerosol technology)

The method used here for MNP synthesis is co-precipitation[49] method. The co-precipitation method is favoured because it is simple and easy to be done and helps to obtain MNPs in water medium. The key in this synthesis lies in controlling the pH and temperature of the reaction to obtain different sizes of the MNPs.

1.4. MNPs in biological studies and BNCT

Biological studies: There are a lot of aspects that needs to be considered before designing MNPs for biomedical applications. The typical structure of MNPs intended to be used in medicinal purposes, consists of functionalized magnetic core. The feasibility of targeting a specific site of the body by the influence of a magnetic field turns these nano-systems into promising agents for localized treatment of diverse pathologies. Size of these MNPs is of key importance in order to pass through the endothelium, which is the barrier they have to cross in blood vessels to arrive at the organs and tissues as well as to penetrate cell membranes to achieve targeted cells.
The biodistribution of SPIONs has been studied with respect to size. Size ranges from 30nm to 100nm has been studied in mice and it was noticed that the larger MNPs distributed themselves in the liver [50]. Others studies focused on nanoparticles with size around 200 nm also demonstrated the liver as the responsible organ for first uptake after administration [51,52]. Other than the size, surface coating and surface charge also determine the distribution of the MNPs within the biological medium. Surface charge is an important property which influences the biodistribution of magnetic nanoparticles. Neutral nanoparticles would be most adequate by their trend to avoid reticuloendothelial system capture. Zeta potentials near 0 mV on the surface are feasible to decrease opsonization [53]. On the other hand, positively charged MNPs have shown a rapid clearance by liver, diminishing the time of blood circulation, while negatively charged

MNPs presented an incremented blood circulating time with biodistribution profile similar to nearly neutrally charged nanoparticles [54]. Iron (III) ions are present in the human body, by this, maghemite results as one of the most suitable magnetic materials for biomedicine considered to not cause significant side effects. Anyway, the cellular accumulation of this metal is a topic of intense research to ensure safety and biocompatibility. Besides the development of much research on these materials, their application in biomedicine is limited due to the toxicity associated with the rare earth metals and transition metal clusters. Iron alloys are being widely studied as materials for targeting and image contrast for diagnosis [55]. FePt, FeAu, and FeAg are promising compositions intended for biological applications.

Boron Neutron Capture Therapy (BNCT): Boron Neutron Capture Therapy (BNCT) is based on the nuclear capture and fission reactions that occur when the stable isotope ^{10}B is irradiated with epithermal neutron beam radiation in clinical use, which become thermalized as they penetrate tissue.[56] BNCT,[57–63] is an alternative radiotherapy used for aggressive and infiltrating types of cancer that cannot be treated with surgery or standard radio or chemotherapy, and by drug delivery.[57,64] The theoretical advantage of BNCT is that it can selectively destroy tumour cells by infiltrating cancerous tissue with the requirement that sufficient amounts of ^{10}B and thermal neutrons are properly delivered to the site of the tumor. [57-64] Clinical interest in BNCT has focused primarily on high grade gliomas and on recurrent tumours of the head and neck region who have failed conventional therapy. BNCT integrates the focusing approach of chemotherapy and the gross anatomical localization advantage of traditional radiotherapy, offering the ability to deposit an immense dose gradient between the tumour cells and normal cells.[65] For this, new and better boron delivery agents targeting cancer cells are needed for the clinical use.

Due to this, we needed a boron cluster attached to some nanocarrier for them to be used in this neutron capture therapy. However, only one example of o-carborane cage attached to MNPs through a long linker for cancer treatment can be found in the literature.[66] Among different surface coating *o*-carborane cages, carboranylphosphinates,[67] have many advantages due to their good affinity towards MNPs, their highly biocompatible tri-dimensional structure and their high boron content, which can be exploited for BNCT. Particularly in this work, the carborane derivative utilized, is *m*-carboranylphosphinate and its acid form that is *m*carboranylphosphinic acid (Figure 1), which was recently reported.[67] The ligand is subjected to the properties bestowed by the m-carborane, though the most notable properties in reference to the results obtained in this work are the reduced tendency of the phosphinate coordinated group to be oxidized (a property which is uncommon among organic phosphinates), the spherical nature of the carborane (driving to space-filling efficiency) and the hydrophobicity of the carboranyl unit.

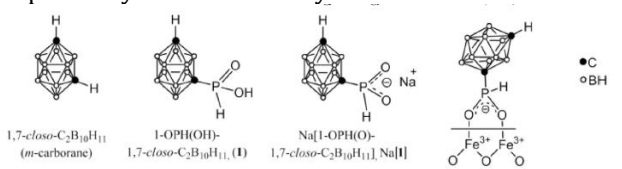

Figure 1: Schematic representation of m-carborane, m-carboranyl phosphinic acid (H[1]), its sodium salt (Na[1]) and bidentate bridging coordination mode of $[1]^-$ onto the MNPs' surface.

The next sections deal with the synthesis of the new nanohybrid system merging boron clusters and the MNPs and their characterizations and study for their potential application in BNCT.

2. New 1-MNPs

The new MNPs called 1-MNPs are synthesized and studied. The MNPs are initially synthesized using the classic co-precipitation method. Then the 1-OPH(OH)-1,7-*closo*-$C_2B_{10}H_{11}$ (H[1]) is used to cover the surface of the MNPs. 1-OPH(OH)-1,7-*closo*-$C_2B_{10}H_{11}$ (H[1]) is synthesized as reported. [67] The detailed synthesis procedure is given below.

2.1. Synthesis of the 1-MNPs

1-MNPs: The synthesis of MNPs coated with *meta*-carboranylphosphinate (1-MNPs) was performed in two steps as follows:[68]

- *Preparation of the core MNPs:* It was synthesized using the aqueous co-precipitation method using an inert atmosphere of nitrogen. This method, which is the concomitant precipitation of Ferrous and Ferric salts in alkaline aqueous solution, is the most widely applied synthesis route for the synthesis of MNPs as described above. $FeCl_2$ and $FeCl_3 \cdot 6H_2O$ salts were dissolved in a 1:2 ratio in deionized and degassed water at room temperature. After stirring for 20 minutes, $[NH_4]OH$ aqueous solution (30 wt.%) was added at once to the above mixture under vigorous stirring. Immediately a black suspension was formed, which suggested the formation of the magnetic nanoparticles. The reaction mixture was then stirred vigorously for 2 hours. The precipitate was isolated from the aqueous solution by magnetic decantation and washed with distilled water three times.
- *Functionalization of the MNPs with meta-carboranylphosphinate:* A saturated solution of 1-OPH(OH)-1,7-*closo*-$C_2B_{10}H_{11}$, H[1], in H_2O was added. Next, the mixture was sonicated for 2 hours. The 1-MNPs were separated from the aqueous solution by magnetic decantation, washed with distilled water three times and dried at 80°C for 6 hours in vacuum.

Preparation of 1-MNPs aqueous suspension at the physiological pH: A stable 1-MNPs (0.5 mg/mL) colloidal aqueous dispersion was prepared as follows. 1-MNPs (5 mg) were re-dispersed in deionized H_2O (10 mL) containing 1 μL of $[NMe_4]OH$ by using ultrasonication. The as-prepared dispersion had a pH of about 5.5-6.5, and then the pH was adjusted to 7.3-7.5 by using additional $[NMe_4]OH$ aqueous solution. The corresponding vehicle media used in control conditions consisted of equal content of *m*-carboranylphosphinic acid (H[1]) and $[NMe_4]OH$ as in a 1-MNPs colloidal suspension.

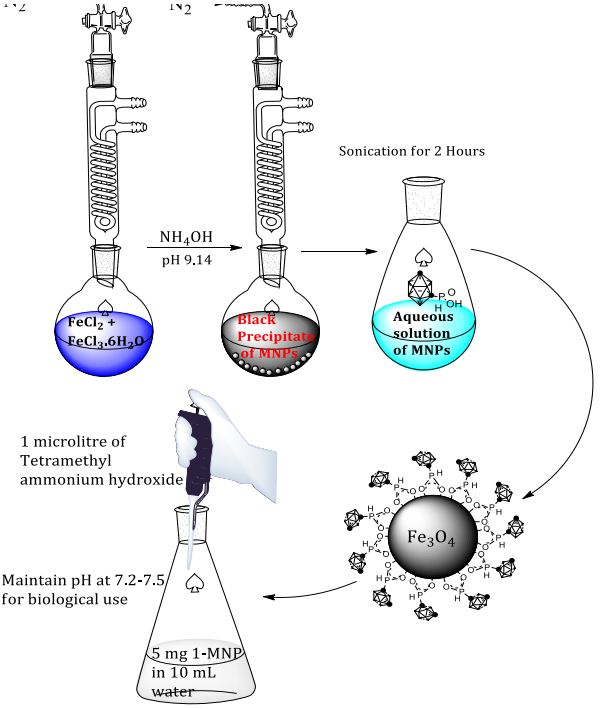

Figure 2: Schematic representation of the synthesis procedure for the m-carboranylphosphinate capped MNPs and their preparation in the physiological pH.

3. Characterizations

The prepared 1-MNPs were characterized using multiple techniques. For their morphology and size, they were studied using the Transmission electron microscopy (TEM). The gaussian size graphs were plotted from the TEM images. Their chemical composition was studied primarily using Infra-red (IR) studies, Energy Dispersive X-ray (EDX) analysis, X-ray Photoelectron spectroscopy (XPS) and Electron Diffraction.

3.1. TEM and Size

TEM Studies: The TEM studies were done in JEOL JEM 1210 at 120kV on a copper grid by drop-dry method. The 1-MNPs showed perfectly spherical structure and morphology. They were quite uniformly formed (Figure 3). The magnetic properties of nanoparticles depend upon their physical structure: the size and the shape of the particles, their microstructure and the chemical phases in which they are present. Moreover, the biological behaviour of magnetic nanoparticles also strongly depends upon their size and shape as well as their polydispersity, charge and nature of the coating.

Since the size and shape is of importance to obtain good magnetic nanoparticles and also for their further applications, their size was studied using gaussian size graphs from the TEM micrographs. Mean particle diameters (ØTEM) were statistically calculated for each sample by counting 200 particles and fitting the particle size histogram from three different batches prepared following the same way of synthesis to a Gaussian function, producing a mean particle diameter of 7.6 ± 0.6 nm (Figure 4). The 8 % polydispersity indicates the narrow particle size distribution, although *meta* carboranyl phosphinate-MNPs were prepared by the aqueous co-precipitation method. Usually the size distribution with the co-precipitation method is not so narrow, but due to the presence of the m-carboranylphosphinate coating, the 1-MNPs have a very

uniform size distribution and shape. Also, there was not much change observed in the size or the shape of the particles after the change of the pH. The co-precipitation method is heavily dependant on the pH of the reaction and needs to be strongly alkaline but when these 1-MNPs were dispersed in an aqueous solution and the pH was maintained between 7.2 to 7.5, the size and shape of the 1-MNPs did not show any change thus showing that these 1-MNPs were quite stable after they were formed.

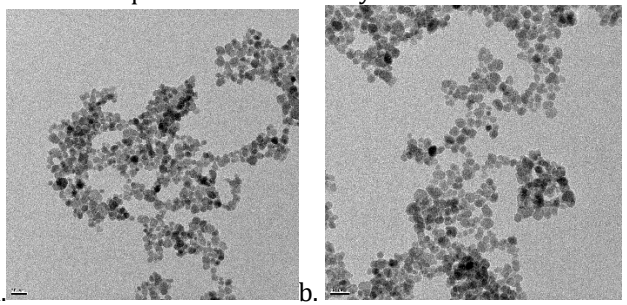

Figure 3: TEM image of the (a) 1-MNP after synthesis and coating with m-carboranyl phosphinate and (b) after the preparation of the 1-MNPs in physiological pH.

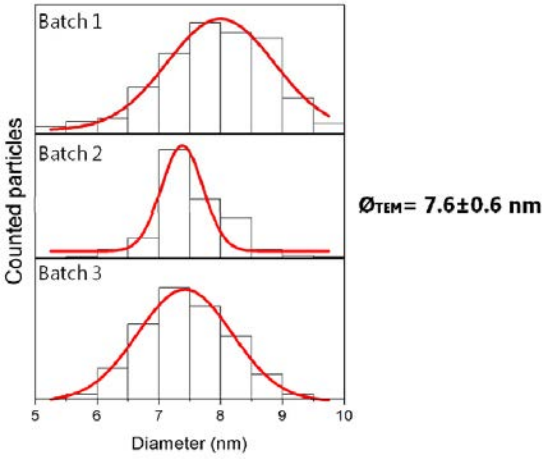

Figure 4: Gaussian size graphs for the 3 different batches of the 1-MNPs showing the average particle size distribution.

3.2. Chemical Composition Studies

The chemical composition was studied using the IR, EDX XPS and Electron diffraction.

IR Studies: The IR spectra of the ligand, 1-MNPs (functionalized), and the nonfunctionalized core of MNPs are shown in Figure 5 on a PerkinElmer Universal ATR Accessory. The presence of absorptions at 2594 cm^{-1} in both of the pure m-carboranylphosphinic ligand and 1-MNPs, due to B−H stretching, dominates the IR spectra and supports the presence of a closo-carboranyl cluster structure in the molecules as well as on the surface of 1-MNPs. It is worth noting that the P=O stretching band of the phosphinate group, which was present at 1210 cm^{-1} in the spectrum of the ligand only, is absent in the spectrum of 1-MNPs, but two new bands at 1189 and 1068 cm^{-1} appeared, which are ascribed to the asymmetric $\nu_{as(PO0-)}$ and symmetric $\nu_{s(P00-)}$ stretch of the coordinated phosphinate group (Figure 5). This result revealed that the ligand was chemisorbed onto the surface of the nanoparticles as a phosphinate bi-dentated bridging ligand coordinated to the iron atoms of the iron oxide super paramagnetic nanoparticles (Figure 1). In addition, the IR spectrum of pristine MNPs shows a peak at 1629 cm^{-1} that remains in the 1-MNP spectrum and is associated with coordinated water to the Fe centres of the core.

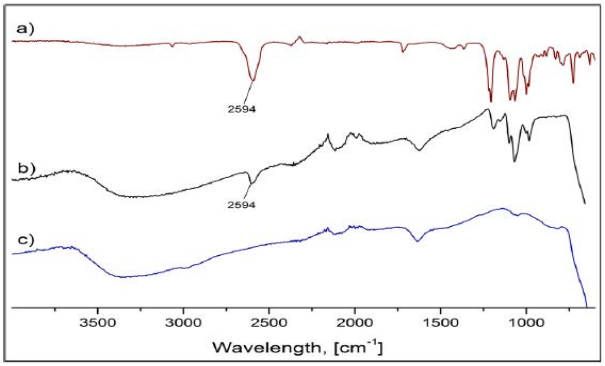

Figure 5: IR Spectra of (a) ligand (b) 1-MNPs and (c) only MNPs.

EDX Studies: EDX analysis was further performed in SEM QUANTA FEI 200 FEG-ESEM device to further find the presence of phosphorus and iron in the sample. This would prove the presence of the boron cluster surrounding the 1-MNPs. Phosphorus was detected by EDX analysis (Figure 6) proving that 1 was coating the MNP surface with an atomic composition for 1-MNPs of 92.89% and 7.11% for Fe and P, respectively. This corresponds to a ratio 13:1 (Fe/P), indicating that the composition of the 1-MNPs can be referred: (1-OPH(O)-1,7-closo-$C_2B_{10}H_{11})_8(2Fe_3O_4{\cdot}Fe_2O_3)_{13}$.

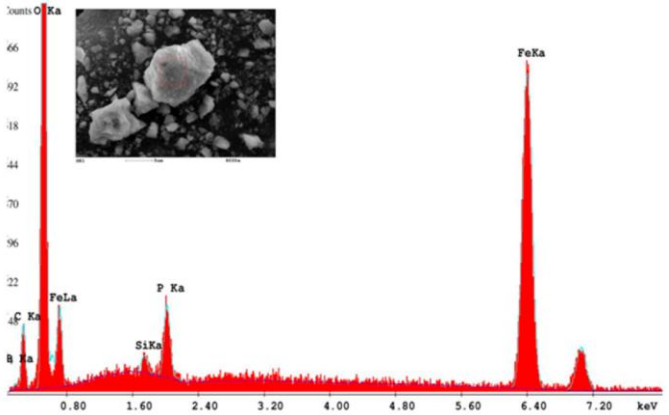

Figure 6: EDX spectrum of 1-MNPs. It clearly shows the presence of P and Fe in the samples.

We did a geometrical calculation on the surface coverage of the Carboranyl phosphinate ligands (CarbPhos) on the 1-MNPs using the EDX data and geometrical assumption of the close square packing of spherical carborane ligands on the spherical core of 1-MNPs.

Geometry calculations: At first, we did an estimation of how many carboranyl phosphinate can cover the surface of the 1-MNP core, considering the 1-MNP core and the carborane cluster as ideal spheres, and that the carborane clusters have a square packing onto the surface of 1-MNP core.
Dimensions of *meta*-carboranylphosphinate was measured from its crystal structure, and determined as 0.5 nm

($Ø_{carbphos}$) as the diameter for carborane cluster "sphere" and 0.7 nm (L) in length including the phosphinate group. The diameter of the core of 1-MNP NPs was found subtracting the two lengths of carbPhos ligand, 2L, from mean diameter of 1-MNP NPs found by TEM,

$Ø_{TEM}$ = 7.6 ± 0.6 nm, which resulted to 6.2 ± 0.6 nm. It was considered as $Ø_1$.
So $R_1 = Ø_1/2$, R_1= 3.1 ± 0.3 nm;
Now, $Ø_2 = Ø_{TEM} - 2(L - 1/2Ø_{carbSH})$ = 6.9 ± 0.6 nm, So, $R_2 = Ø_2/2$=3.45 ± 0.3 nm.

Now in order to calculate the surface area we need to use the formula for surface area of sphere which is $4\pi r^2$.
$A_2 = 4\pi R_2^2$ = 176.68 ÷ 124.66 nm^2 (150.67 $\pm$ 25.67 nm^2)
A_2 is the surface area of the core. For square packing we need to calculate the area of carboranyl phosphinate
$A_{carbPhos} = Ø_{carbPhos}^2$= 0.5 x 0.5= 0.25 nm^2
n_{max} (maximum number of CarbPhos that can cover the surface of the 1-MNP Core with a diameter of 6.2 $\pm$ 0.6nm) = $A_2/A_{carbPhos}$= 706.72 ÷ 498.64 (602.68 $\pm$ 104.04)
Now, in order to determine the surface coverage values from EDX results we do the following calculations:

Surface calculations: We already know the At % ratio of Fe:P is 13:1 from the EDX results. Using chemical titration for these as mentioned in reference 68, we know the composition of these 1-MNPs is Fe_8O_{11}. Using the composition, the At % ratio of Fe:P is now 1.625:1. Now from the geometrical calculations we know the exact diameter (d) of the 1-MNP core is 6.2 $\pm$ 0.6nm. So, the mass of the core is calculated from here (m_{MNPs})

$m_{MNPs} = (1/6)\pi d^3 \rho_{MNPs}$ (where d is the diameter of the 1-MNP core and ρ is the true density of MNPs)
m_{Au}= (1/6) x 3.141 x (6.2 $\pm$ 0.6)^3 x 5.175 g/cm^3= (66.4 $\pm$ 19)E-20g
$Mole_{MNPs} = m_{MNPs}/M_{2Fe3O4.Fe2O3} = N_{Fe8O11}/N_A$,

where $M_{2Fe3O4.Fe2O3}$ is the molecular weight of magnetite/maghemite couple which is 622.75 g/mol, N_{Fe8O11} is the number of Fe_8O_{11} units that contains one NP core with the diameter of 6.2 $\pm$ 0.6nm and N_A is the Avogadro number.

So now, $N_{Fe8O11}=m_{MNPs} \times N_A/M_{Fe8O11}= 642 \pm 182$
Now taking into account the ratio obtained in the EDX spectrum for Fe:P as 1.625:1, each nanoparticle bears $n_{carbPhos} = N_{Fe8O11}/1.625= 395 \pm 112$
Therefore, from here the saturation of the surface of the 1-MNP core with CarbPhos in terms of % can be calculated with respect to the maximum number of CarbPhos that we estimated from the geometrical calculations.
$S_{carbPhos}= n_{carbPhos}/n_{max} \times 100\%= 65.5\%$ (ignoring the error factor).

So, by these calculations we can deduce an approximate surface coverage % of the carboranyl phosphinate on the 1-MNP core of 6.2 $\pm$ 0.6 nm diameter. The coverage is approximately 65%.

XPS Studies: XPS analysis was performed in a Phoibos 150 analyzer (SPECS GmbH, Berlin, Germany) under ultrahigh vacuum conditions (base pressure 4×10^{-10} mbar) with a monochromatic aluminum K alpha X-ray source (1486.74 eV). The energy resolution as measured by the fwhm of the Ag 3d5/2 peak for a sputtered silver foil was 0.8 eV. The high resolution XPS analysis performed on 1-MNPs (Figure 7) displays peaks at 189 and 133 eV, which are characteristic of a B–B and P–O bonds (Figure 7b,c), confirming the presence of m-carboranyl and phosphinate groups as well as the peaks at 711.2 and 724.9 eV indicating Fe in the Fe_3O_4 phase at the MNP core (Figure 7d).

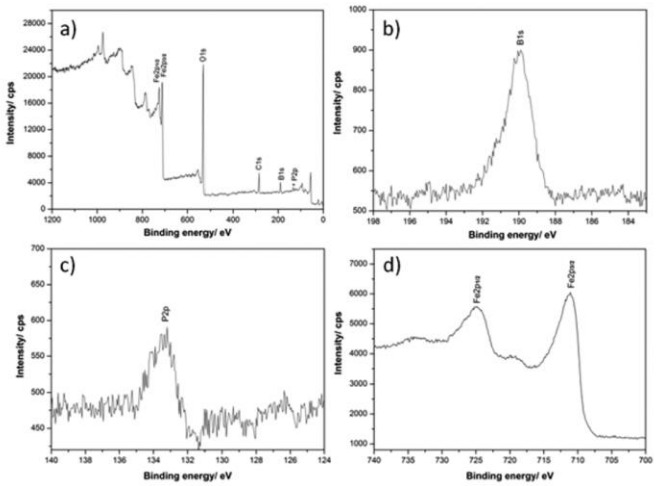

Figure 7: XPS spectra of (a) 1-MNPs, (b) zoomed portion of B 1s region, (c) zoomed portion of P 2p region and (d) zoomed portion of Fe 2p region.

Electron Diffraction Studies: The electron diffraction of 1-MNPs were done on the TEM grid and it showed well-defined diffraction rings confirming that the particle core composition is made of a magnetite/maghemite spinel structure (Figure 8). The line profile was fitted for six observed rings on the diffraction pattern with the following Miller indices: (220), (311), (400), (422), (511), and (440). The electron diffraction pattern showed quite good crystalline pattern for the 1-MNPs.

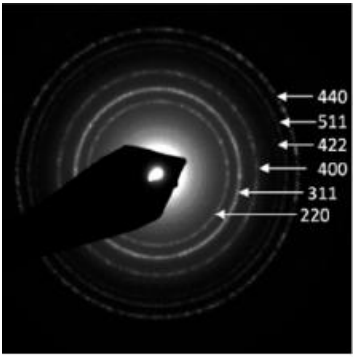

Figure 8: Electron diffraction pattern of 1-MNPs.

3.3. Hysteresis Study

Magnetic characterization of 1-MNPs was carried out in a Superconductive Quantum Interference Device (SQUID) magnetometer (Quantum Design MPMS5XL). Magnetization *vs* magnetic field measurements were performed at 300 K and 5 K in a field 6 T. Zero-field cooling (ZFC) and field cooling (FC) temperature dependent magnetization measurements were carried in a field of 50 Oe. The samples were prepared using a polycarbonate capsule filled with 1 mg of 1-MNPs and compacted cotton.

The magnetic property of iron oxide (Fe_3O_4) nanoparticles is dependant on the distribution of Fe ions in octahedral and tetrahedral sites of the spinel structure.[69] The magnetic spins of the ions in the octahedral sites are ferromagnetically coupled to each other and antiferromagnetically coupled with tetrahedral sites. Because the number of Fe^{3+} ions in the octahedral sites and the tetrahedral sites are the same, their magnetic spins cancel each other. Consequently, the magnetic spins of only Fe^{2+} ions in the octahedral sites contribute to the net magnetic moment in a spinel structure.
However, Fe^{2+} can be oxidized upon harsh conditions of temperature, moisture, and oxygen, as these that can be found in an autoclave for sterilization. Thus, one important point to be addressed in the use of MNPs for medical applications and consequently, on their autoclave sterilization for their application on cultures is to learn the fate of the MNPs and their ligands, particularly what occurs to Fe^{2+} upon the autoclave sterilization process, and to this purpose it is necessary to learn the fate of functionalized MNPs at room temperature and after the autoclave sterilization process. In order to test the viability of these 1-MNPs for use in biological applications, hysteresis measurements of freshly prepared 1-MNPs were done (Figure 9). Figure 9a and b show a typical magnetization curve at 300 K for superparamagnetic nanoparticles in which neither remnant magnetization (magnetization at

zero field, M_R) nor coercivity (hysteresis loop, H_c) were observed. The saturation magnetization value of 1-MNPs at 300 K was 65 emu/g, which indicates a high degree of crystallinity which was also seen with the distinct electron diffraction pattern.

As expected, saturation magnetization was higher at 5 K (76 emu/g 1-MNPs). Super paramagnetism was also proved by the ZFC–FC magnetization curves (Figure 9c). The ZFC increased with temperature until reaching the maximum value corresponding to the blocking temperature (TB) at 111 K. The FC curve increases as the temperature decreases and never reaches saturation at low temperature, suggesting that inter particles' interactions do not significantly affect the relaxation dynamics. These studies were done with the 1-MNPs before autoclave sterilization.

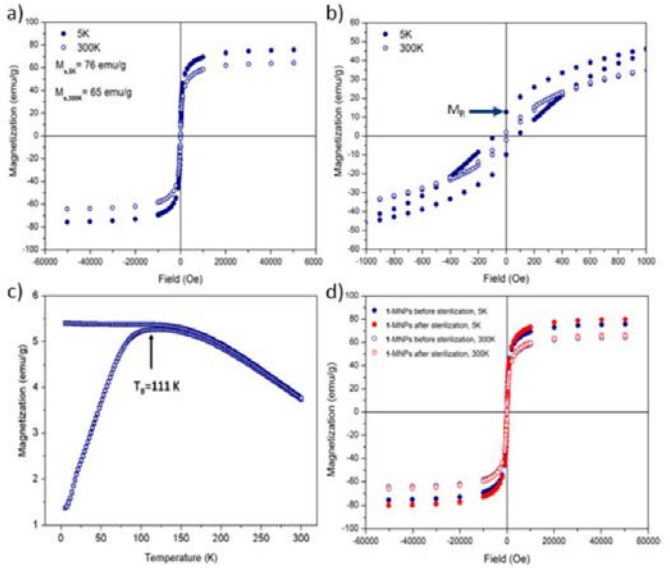

Figure 9: (a) Hysteresis cycle for *meta* carboranyl-MNPs at low temperature (5K) and at room temperature (300K), (b) Zoomed image of the hysteresis cycle of the *meta* carboranyl -MNPs, (c) ZFC and FC curves of *meta* carboranyl -MNPs at 50 Oe and (d) Hysteresis cycles of 1-MNPs at low temperature (5K) and at room temperature (300K) before (blue) and after (red) autoclave sterilization.

On the other hand, very less information is available on MNPs after sterilization in the autoclave, though it is necessary to be known for their use in medical applications. To test their viability for these applications, magnetic properties of *meta* carboranyl capped-MNPs were measured after the autoclave sterilization process. Magnetization curves of 1-MNPs before (blue) and after (red) the autoclave sterilization process at 5K and 300K as a function of the applied 6T magnetic field are displayed in Figure 9d. The graph demonstrates that the autoclave sterilization process does not produce significant changes on magnetic properties of *meta* carboranyl capped MNPs. The saturation magnetization value of *meta* carboranyl capped-MNPs at 300 K was 65 emu/g and 66 emu/g before and after autoclave sterilization, respectively. As expected, saturation magnetization was higher at 5 K (76 emu/g before and 80 emu/g after autoclave sterilization, respectively).

4. Colloidal Stability Studies

The hydrodynamic diameter ($Ø_{HYD}$) of 1-MNPs dispersed in water and in several biological media was investigated with a ZETASIZER NANO ZS (Malvern Instruments Ltd) equipped with a He-Ne 633 nm laser using 1 mL of particle dispersion in a disposable plastic cuvette. Measurements were run in triplicate at ambient temperature and at 37°C for samples in biological media. Number of scans was set up in automatic mode. Laser Doppler Micro-electrophoresis is the technique used to measure zeta potential. The zeta potential of a colloidal suspension in aqueous media was obtained by filling a disposable cell with 1 mL of the colloidal suspension. Measurements were run in triplicate at ambient temperature. Number of scans was set up in automatic mode.

Colloidal Stability at different pH and before and after Autoclave Sterilization: The use of magnetic nanoparticles in

biological systems require a strict modulation on their mono-dispersity and size. This is because their biological properties are heavily influenced by the polydispersity index of these nanoparticles along with the size, shape, charge and the coating on the surface of these particles. Using the technique of Laser doppler microelectrophoresis, zeta potential can be measured in the nanoparticles which help in determining the surface charge. The zeta potential and the size which is measured by dynamic light scattering (DLS) needs to be done at different pH in order to see how the nanoparticles are while they are adjusted in the physiological pH. The pH of the solution was adjusted using aqueous $[NMe_4]OH$ solution (25 wt.%). DLS technique also provides information on the hydrodynamic diameter and, thus, on the colloidal behaviour of the 1-MNPs in a different environment. As the mean effective diameter of the particles depends on the size of the core, the size of the shell, particle concentration as well as the type of ions in the medium, the influence of pH on the stability of colloidal aqueous dispersion of 1-MNPs was studied and their results collected in Table 1. DLS analysis reveals that the hydrodynamic diameter radius of the particle increases when decreasing the pH, which indicates the particles aggregate when pH decreases. On the other hand, when pH is basic, the electrostatic repulsion force seems to be higher (ζ= -44 ± 5 mV), therefore the dimensions of the aggregates ($Ø_{HYD}$ = 23 ± 11 nm) are closer to the size of particles determined by TEM ($Ø_{TEM}$) that is 7.6 ± 0.6 nm. At physiological pH, the size of aggregates are $Ø_{HYD}$= 45 ± 20 nm and Zeta potential value, ζ= -30 ± 4 mV, that was enough to avoid the aggregation with further precipitation of colloid. This fact can be attributed to the negatively charged surface of the core of magnetic nanoparticles and by the hydrophobicity due to the carboranyl spheres coordinated to the surface $Fe_{2+/3+}$ ions through the phosphinate binding sites.

pH	$Ø_{HYD}$, (nm)	PdI	Zeta potential, ζ (mV)	Diffusion Coefficient, (μm²/s)
5.30	> 60	0.446	+17	1.77
7.45	45 ± 20	0.454	-30 ± 4	3.77
9.21	23 ± 11	0.482	-44 ± 5	7.49

Table 1: Hydrodynamic size, polydispersity index and zeta potential of *meta* carboranyl capped-MNPs at different pH.

The colloidal behaviour of an aqueous solution at the pH range 7.4-7.6 of the 1-MNPs (0.5 mg/mL) that had been under autoclave sterilization process conditions (steam heated to 121 °C under pressure during 1 hour) were studied by DLS measurements. Figure 10 shows that the dimensions of the aggregates are the same before and after the autoclave sterilization and, as said earlier, the magnetic properties of 1-MNPs remain unaltered after the autoclave sterilization process.

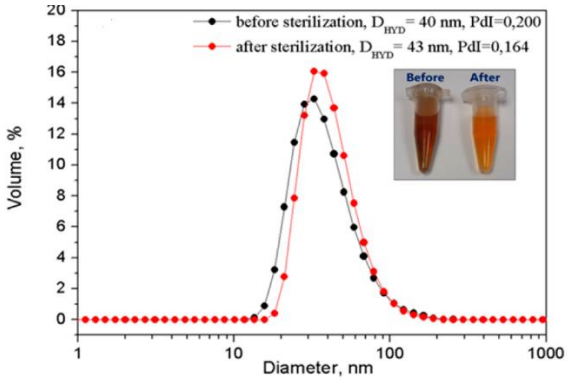

Figure 10: Hydrodynamic size by DLS before and after sterilization.

Colloidal Stability of the 1-MNPs in different culture mediums: The stability of the colloidal dispersions of 1-MNPs (50 μg 1-MNPs/mL) was studied by DLS in different culture media (DMEM-F12–1% FBS, DMEM-1% FBS, EGM2–2%FBS and RPMI) and as well as in phosphate-

buffered saline (PBS) solution that contains inorganic salts (NaCl, Na_2HPO_4, KH_2PO_4, KCl) at different time intervals (10 min. and 24 h.) and temperatures (r.t. and 37 °C). The results are on display in Table 2 and Figure 11.

In all tested culture media, no precipitation was observed either after 10 min or after incubating 24 h at r.t. or at 37°C, while in PBS 1-MNPs sediment within 24 h at r.t. In the case of DMEM F12–1% FBS, 1% non-essential amino acids and 1% antibiotics, and in RPMI the size of detected particles was close to the mean particle diameters determined by TEM, $Ø_{TEM}$ = 7.6 ± 0.6 nm. In EGM-2 medium with 2%FBS and in DMEM-1%FBS 1-MNPs rapidly formed aggregates with hydrodynamic diameters in the range of 50-140 nm and 60- 170 nm, respectively, maintaining an invariable size for 24 hours. Comparing results at r.t. and 37°C, a slight increase in hydrodynamic diameters was observed in all culture media (Table 2). To know more about the stability of 1-MNPs in PBS, DLS measurements at 10 and 30 minutes as well as at 2, 4 and 8 hours were conducted (Figure 12 and Table 3).

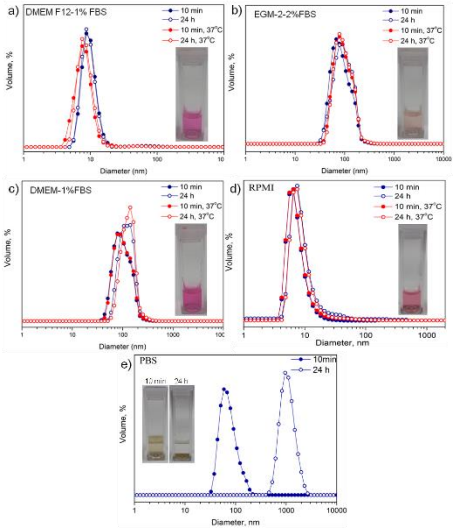

Figure 11: DLS of *meta* carboranyl -MNPs in different culture media at different times and at different temperatures.

Media	T, °C	$Ø_{HYD}$, (nm)	Diffusion Coefficient, (μ^2/s)
10 min			
DMEM F12–1% FBS	r.t	9.8 ± 2.5	3.40
	37	8.2 ± 2.6	3.63
EGM-2 medium with 2%FBS;	r.t	90.3 ± 40.7	4.43
	37	98.7 ± 41.6	5.69
DMEM-1% FBS	r.t	103.4 ± 40.7	4.14
	37	106.6 ± 42.9	5.13
RPMI	r.t	9.0 ± 2.3	4.16
	37	8.4 ± 2.0	4.19
PBS	r.t	76.1 ± 31.1	4.90
24 hours			
DMEM F12–1% FBS	r.t	9.5 ± 2.2	3.50
	37	8.5 ± 2.3	4.03
EGM-2 medium with 2%FBS;	r.t	99.5 ± 41.9	4.31
	37	101.0 ± 42.6	5.54
DMEM-1% FBS	r.t	123.6 ± 40.8	3.42
	37	133.3 ± 43.4	4.24
RPMI	r.t	10.8 ± 4.4	3.92
	37	11.0 ± 12.9	4.09
PBS	1276 ± 435 (precipitated)		

Table 2: Hydrodynamic size of *meta* carboranyl -MNPs at different temperatures and in different culture mediums.

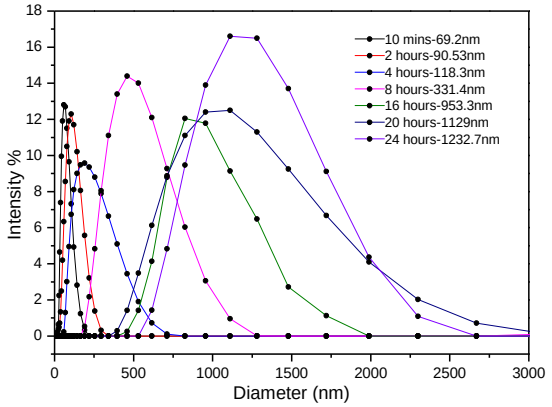

Figure 12: Hydrodynamic size of *meta* carboranyl -MNPs at different times in PBS.

Time	*Size (nm)*	*Zeta Potential*
10 mins	69.2 nm	-18.1
30 mins	71.48 nm	-19.5
1 hour	82.77 nm	-21.8
2 hours	90.53 nm	-18.3
3 hours	101.2 nm	-19.7
3.5 hours	107.8 nm	-19.6
4 hours	118.3 nm	-20.8
5 hours	158.9 nm	-19.5
6 hours	219.9nm	-21.7
6.5 hours	260.3 nm	-21.1
7 hours	291.8 nm	-17.1
8 hours	331.4 nm	-13.1
9 hours	447.4 nm	-12.7
14 hours	931.6 nm	-10.9
15 hours	948.4 nm	-10.3
16 hours	953.3 nm	-11.1
18 hours	1050.5 nm	-11.4
19 hours	1132.6 nm	-9.54
20 hours	1129 nm	-9.67
22 hours	1217.23 nm	-9.7
24 hours	1232.7 nm	-8.3

Table 3: Hydrodynamic size and Zeta potential of *meta* carboranyl -MNPs in PBS at different time.

The increase of the size of the *meta* carboranyl-MNPs in PBS was gradual and also the zeta-potential values showed that they were never really stable when compared to the stability of these *meta* carboranyl-MNPs in other culture media. After characterizing the *meta* carboranyl -MNPs, and then testing their magnetic properties and size and stability before and after sterilization in autoclave, and obtain the results to be satisfactory we can finally move on to test them in biological applications with in vitro and in vivo testing.

5. Biological Studies

The conducted study overlaps nanoscience experiments (stability studies of coated MNPs with Boron clusters) with functional in vitro and in vivo experiments (cellular uptake and imaging, BNCT irradiation in glioblastoma cells, and nanohybrid biocompatibility in mice) including: Dynamic Light Scattering (DLS) and Zeta Potential; Superconductive Quantum Interference Device (SQUID) magnetometer (Quantum Design MPMS5XL); TEM of cells; preparation of 1-MNPs aqueous suspension at the physiological pH; cellular uptake of 1-MNPs; cell viability assays; cell count; dried cells preparation for magnetization measurements, XPS, HRSTEM, EELS and EFTEM studies; cytoplasmic 1-MNPs detection by Prussian blue and 1-MNPs visualization by Transmission Electron Microscopy (TEM); Magnetic Resonance Imaging (MRI); Boron and Iron determination by Inductively Coupled Plasma Mass Spectrometry (ICP-MS) analysis; Cell irradiation and proliferation assays and "*in vivo*" 1-MNPs administration in mice.

5.1. Cellular Uptake Studies

The first step of the biological studies was to confirm the uptake of the sterilized *meta* carboranyl-MNPs colloidal suspension by the cultured cells (hCMEC/D3 or endothelial cells and A172 or glioblastoma cells). 1-MNPs (first sonicated for 10 minutes) were tested at concentrations varying from 0 to 100 μg/mL of total iron $Fe^{2+/3+}$ or with vehicle solution ((equal content of m-carboranylphosphinic acid (H[1]) and $[NMe_4]OH$ as in a 1-MNPs colloidal suspension), and incubated at 37°C in a CO_2 incubator and as follows: Brain endothelial cells (hCMEC/D3, $1x10^4$ cells) were cultured in 24-well plates, and after 48 hours, cells were washed with PBS twice and treated with *meta* carboranyl-MNPs or vehicle at the concentrations described above. Finally, glioblastoma A172 cells were seeded in 24-well plates ($15x10^4$ cells/well) and grown for 24 hours.

Afterwards cells were washed with PBS twice and treated with the indicated concentrations of 1-MNPs in DMEM-1% FBS. A172 and hCMEC/D3 cells were also treated with m-carboranyl phosphinate from 0 to 7.5 mM in each corresponding basal media. All cells were incubated for 24 hours with corresponding medium containing 1-MNPs or the m-carboranyl phosphinate in duplicate. Afterwards, cells were used to assess cell viability or to determine the intracellular uptake of the 1-MNPs

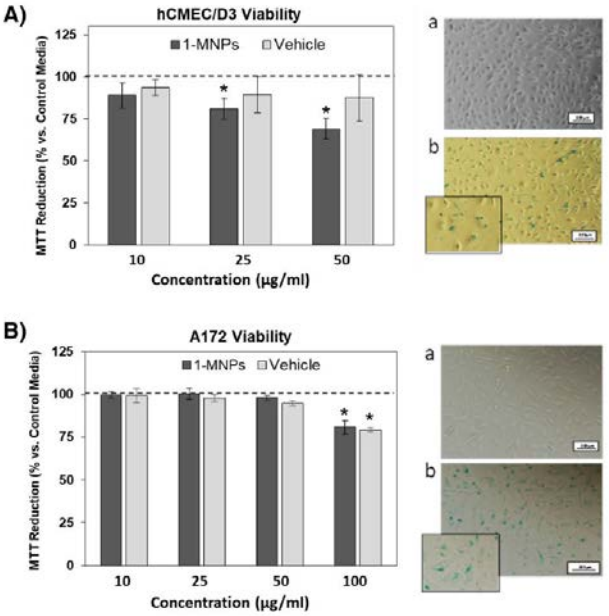

Figure 13: Cell viability was tested after exposing brain endothelial cells (A), and Glioblastoma cells (B) to increasing doses of 1-MNPs and corresponding vehicle solutions for 24 h. Data are expressed as mean ±SD of n = 3/4 per condition; * $P < 0.05$ indicates differences vs. control media (dashed line). Right panels correspond to images of each cell line (a) and to iron deposits observed after Prussian Blue Stain (b, treatment dose 10 µg/mL).

As shown in the right panels of Figure 13, the Prussian blue stain enables us to identify the presence of intracellular iron after 24 h treatment with 1-MNPs. Cell viability assay also

shows that brain endothelial (hCMEC/D3) cells were more sensitive to *meta* carboranyl-MNP toxicity than glioblastoma A172 cells (Figure 13, A and B) since doses of 25 μg $Fe^{2+/3+}$/mL significantly reduced endothelial cell viability. The reduction in hCMEC/D3 viability could be only partially explained by the vehicle solution consisting in equal content of m-carboranylphosphinic acid (H[1]) and [NMe_4]OH as in a 1- MNPs colloidal suspension, but certainly the 1-MNPs nanohybrid induced cell toxicity starting at 25 μg/mL. Under the same administered doses of 1-MNPs, glioblastoma A172 cells presented full viability as observed in Figure 13, B. However, higher doses induced cell toxicity to the cancer cells, maybe due to the acidity of m-carboranylphosphinic acid present in the vehicle solution. These results provide a proof of dose dependent effects of the 1-MNPs compound in normal tissue (endothelial) and tumour cells (glioblastoma) which are considered for further 1-MNPs loading experiments.

Quantification of the cellular 1-MNPs uptake: To confirm the uptake of MNPs core by the A172 and hCMEC/D3 cells after 6 or 24 h of incubation in the presence of 1-MNPs, the washed cells were dried, as described below and the magnetism measurements were run. Total cells collected from the cell count cultures were centrifuged at 1500 rpm for 5 minutes, then the cell pellet was suspended in 50 μL of each cell culture media, and transferred into a polycarbonate capsule to be dried at 60 °C using a speed vacuum centrifuge (1500 rpm for 1 hour).

The results determine the amount of iron per cell and show a clear time and dose-dependent relationship with both endothelial and glioblastoma cell lines as shown in Figure 14, A. Moreover, with the same dose of 1-MNPs (25 μg/ml) A172 cells presented larger cellular iron content than endothelial cells (6-fold and 4-fold increase after 6 and 24 h, respectively) as shown in Figure 14, B, indicating a higher capacity of cellular load with iron oxides without toxic effects (Figure 14). These are interesting results suggesting

that by using low doses of 1-MNPs, glioblastoma cancer cells may be largely loaded with the 1-MNPs compound compared to other healthy neighbouring cells in the tissue such as endothelial cells.

A

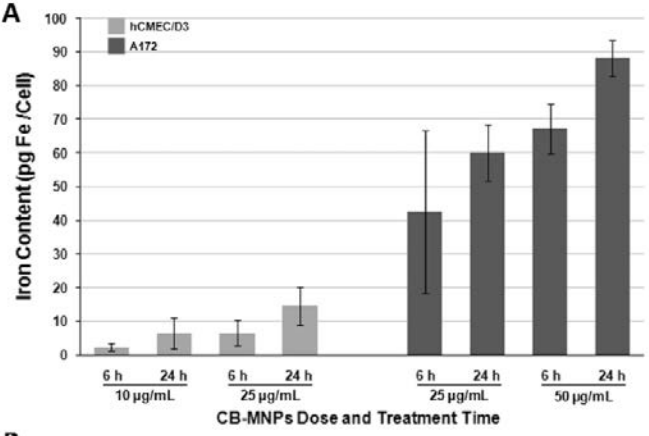

B

	hCMEC/D3				A172			
	10µg/mL		25µg/mL		25µg/mL		50µg/mL	
	6h	24h	6h	24h	6h	24h	6h	24h
MEAN	2.32	6.56	6.61	14.66	42.49	60.07	67.38	88.26
SD	1.16	4.52	3.73	5.69	24.14	8.27	7.33	5.37

Figure 14: The amount of $Fe^{2+/3+}$ per viable cell was determined after treating cells with increasing doses of 1-MNPs for 6 or 24 h. Bar graph (A) shows that the amount of Fe/cell was time- and dose-dependent in both cell lines. The tested glioblastoma cells (A172) were capable to uptake the largest amounts of iron at all sub-toxic tested doses (B). Data are expressed as mean ± SD pg $Fe^{2+/3+}$/Cell of n = 3 independent experiments per condition.

Cell visualization of meta carboranyl-*MNPs uptake:* The presence of cytoplasmic 1-MNPs core and its intracellular localization into hCMEC/D3 and A172 cells were visualized by TEM analysis in membrane-bound compartments matching with endosomal or lysosomal organelles (Figure 15) at least 24 h after labeling, as described for other iron oxide compounds.[70-72] This result confirms the cellular load with the 1-MNP compound and confirms the cell dependent *meta* carboranyl-MNP load, being higher in A172 glioblastoma cells.

For verifying the presence of cytoplasmatic MNPs core by TEM, cells were prepared as follows: cells were seeded in 25 cm^2 flasks, grown, treated with **1**-MNPs for 24 h (for the hCMEC/D3 cells, [Fe] = 25 µg/mL; for the A172 cells, [Fe] = 50 µg/mL), trypsinized, and collected by standard centrifugation. Then 1.5 mL of 2% glutaraldehyde in cacodylate buffer was added to the remaining pellets and cells were quickly incubated in the fixation solution at 4 ºC for 1 h, post-fixed in 1% OsO_4, dehydrated in 12 steps by using 50-100% acetone (Dehydration with acetone in 12 steps: 50% acetone, 5 min, x1; 70% acetone, 5 min, x2; 90% acetone, 5 min, x3; 95% acetone, 5 min, x3; 100% acetone, 15 min, x3) and embedded in Epon resin. Finally, ultrathin sections (70 nm) were transferred onto copper grids and analyzed by TEM at 120 kV.

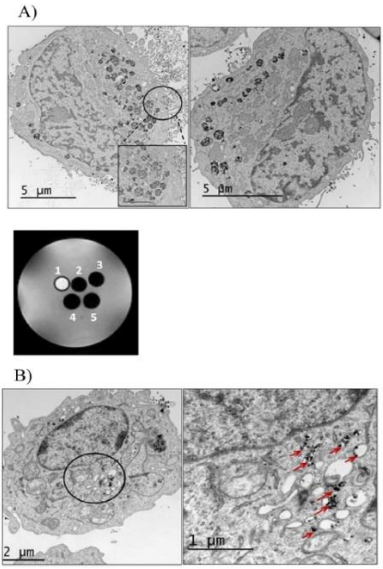

Figure 15: Transmission electron microscope (TEM) image of (A) glioblastoma cells (A172) and (B) endothelial hCMEC/D3 cells showing the presence of 1- MNPs into the cytoplasm with a larger load in A172cells. Glioblastoma cells (A) were also imaged by T2-weighted MRI at 7 T in glass capillaries containing cell pellets of untreated A172 cells (1) or A172 cells incubated for 6 h with 25 or 50 µg Fe/mL 1-MNPs (2 and 3, respectively) or for 24 h with 25 or 50 µg Fe/mL NPs (4 and 5, respectively).

5.2. Magnetic Resonance Imaging (MRI) Study

Additionally, to assess whether the amount of Fe internalized in A172 cells was enough to allow MRI visualization on a T2- weighted image, cells were incubated in the presence of 1 MNPs (25 and 50 μg/mL Fe) for 6 or 24 h and prepared for MRI as described. 5×10^5 A172 cells were seeded in 6 cm diameter dishes. After 24h, cells were incubated for 6 and 24 h with 25 and 50 μg/mL Fe of 1-MNPs (determined by ICP-MS, explained later) in DMEM-1% FBS. At the end of the incubation, cells were washed three times with PBS and detached with trypsin/EDTA (ethylenediaminetetraacetic acid). A172 cells were then transferred into glass capillaries inside an agar phantom and a T_2-weighted MRI image was acquired using a RARE sequence protocol (TR/TE/NEX=5000:13.5:12 FOV=1.13 cm). The MRI scanner used for this study was a Bruker Avance300 spectrometer (7T) provided with a Micro 2.5 micro imaging probe (Bruker BioSpin, Ettlingen, Germany).

As shown in Figure 15 the acquired signal intensity is dramatically lower (hypointense) in all the treated samples with respect to non-treated control cells. This opens the opportunity to use MRI to carry out a non-invasive quantification of Fe and consequently Boron taken up by target cells, respectively. However, the presence of the *m*-carboranyl cluster surrounding the observed MNPs core present in the glioblastoma A172 cytoplasm could not be confirmed by EELS and EFTEM elemental maps, probably because of the low levels of boron, thus only Fe was clearly detected (Figure 16). To overcome this drawback and to unambiguously prove the presence of the *m*-carboranyl cluster coordinated at the MNPs core, high resolution XPS and EELS spectra on the A172 dried-cells sample were done. EELS analysis on the A172 dried-cells sample showed the B-K and PL2,3 edges present in the sample proving that the *m*-carboranylphosphinate coordinates to MNPs surface (Figure 17 and 18).

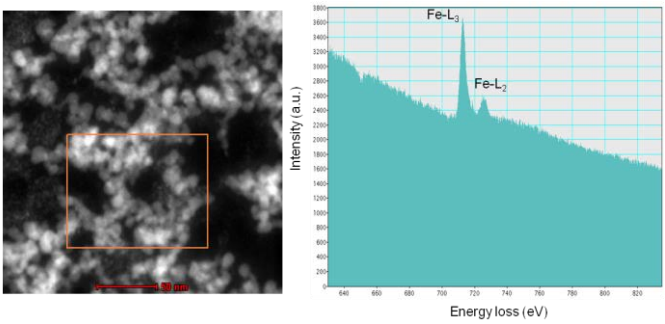

Figure 16: EELS analysis spectra on the square area showing the characteristic peaks for Fe.

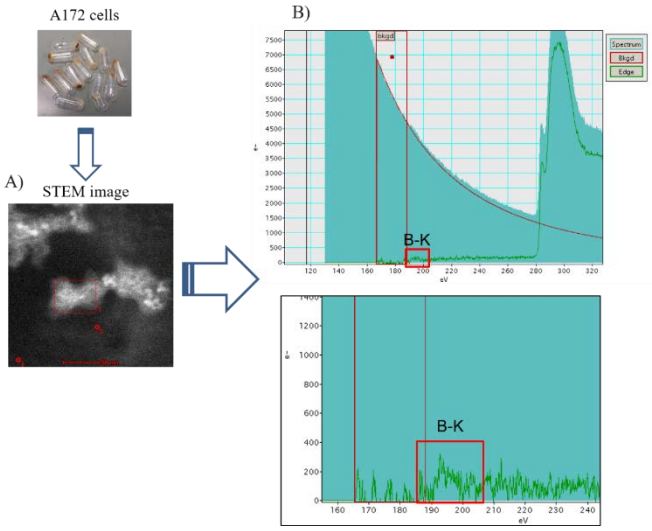

Figure 17: A) HAADF STEM image of A172 cells and B) EELS spectra on the square area. Energy loss peaks with onsets at 188 eV correspond to B containing in the sample.

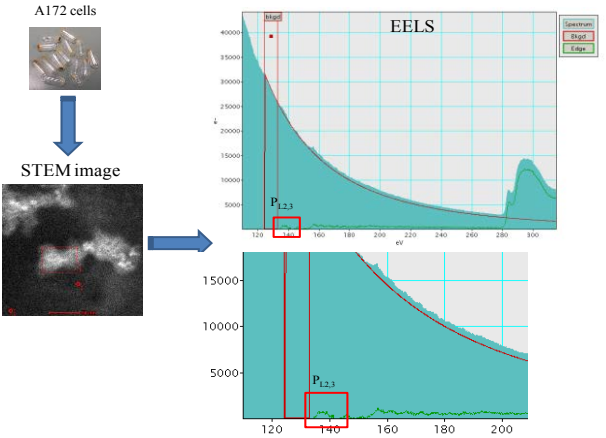

Figure 18: HAADF STEM image of A172 cells and EELS spectra on the square area. Energy loss peaks with onsets at 133 eV correspond to $P_{L2,3}$ containing in the sample.

Peaks at 189 and 133 eV in the XPS analysis, which are characteristic of B-B and P-O bonding, were observed and that clearly confirmed the presence of m-carboranyl phosphinate coordinated to the MNP core (Figure 19).

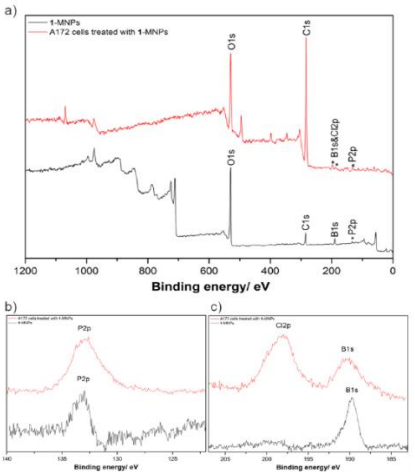

Figure 19: High resolution spectra XPS of 1-MNPs and A172 cells treated with 1-MNPs (A) in the B 1 s and P 2p regions, (B) and (C), respectively.

5.3. BNCT Studies

BNCT studies were carried out incubating A172 cells for 24 h with 1-MNPs (20 μg/mL Boron). The amount of internalized Boron measured by ICP-MS was of 133 ± 25 μg/g corresponding to a ^{10}B concentration of 26 ± 5 μg/g. Using the above-mentioned condition, two groups of A172 cells were irradiated for 15 min in the thermal column of the TRIGA Mark II reactor at the University of Pavia (Reactor Power 30 kW): untreated control cells and 1-MNPs-treated cells. These were further compared with the respective non-irradiated controls. The proliferation rate (Figure 20) of irradiated and 1-MNPs treated cells re-plated the day after BNCT is considerably lower than both control cells, thus demonstrating the efficacy of 1-MNPs as boron carriers for this cancer therapy. On day 6, BNCT irradiation reduced by 2.5 the number of cancer cells treated with 1-MNP when compared to non-treated cells (Table 4).

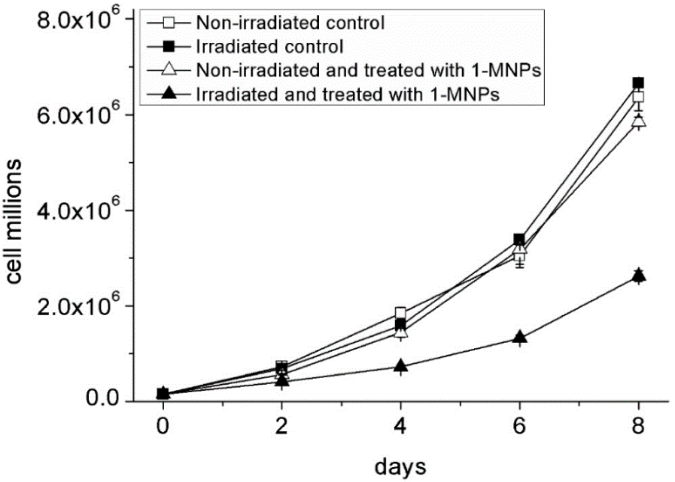

Figure 20: Proliferation curves of A172 cells re-plated one day after BNCT treatment. Data are the mean ± SD of two different experiments.

Cell number (media)	Non irradiated control	Irradiated control	Non-irradiated and treated with *meta* carboranyl-MNPs	Irradiated and treated with *meta* carboranyl - MNPs	Decrease in cell number
Day 2	726000	684000	566000	410500	1.67
Day 4	1.847E6	1.587E6	1.439E6	721000	2.20
Day 6	3.052E6	3.382E6	3.186E6	1.321E6	2.56
Day 8	6.362E6	6.66E6	5.85E6	2.623E6	2.54

Table 4: The A172 cell number of the BNCT irradiation study.

5.4. Toxicity Studies (*in-vitro* and *in-vivo*)

Cell Toxicity to the ligand shell coating of 1-MNPs: Finally, the toxicity of the ligand shell coating the MNPs core (Na[1] salt of *m*-carboranyl phosphinic acid) was determined in both A172 and hCMEC/D3 cells in a dose–response cell viability assay. As observed for the whole 1-MNPs compound, endothelial cells were more sensitive to the Na[1] salt of *m*-carboranyl phosphinic acid than the glioblastoma cells since Lethal Dose 50 was around 1 mM compared to the 7.5 mM observed in A172 cells; see Figure 21, A and B. Those doses correspond to 230 μgNa[1] of *m*-carboranyl phosphinic acid /mL and 1725 μgNa[1] of *m*-carboranyl phosphinic acid/mL of Na[1] of *m*-carboranyl phosphinic acid, respectively.

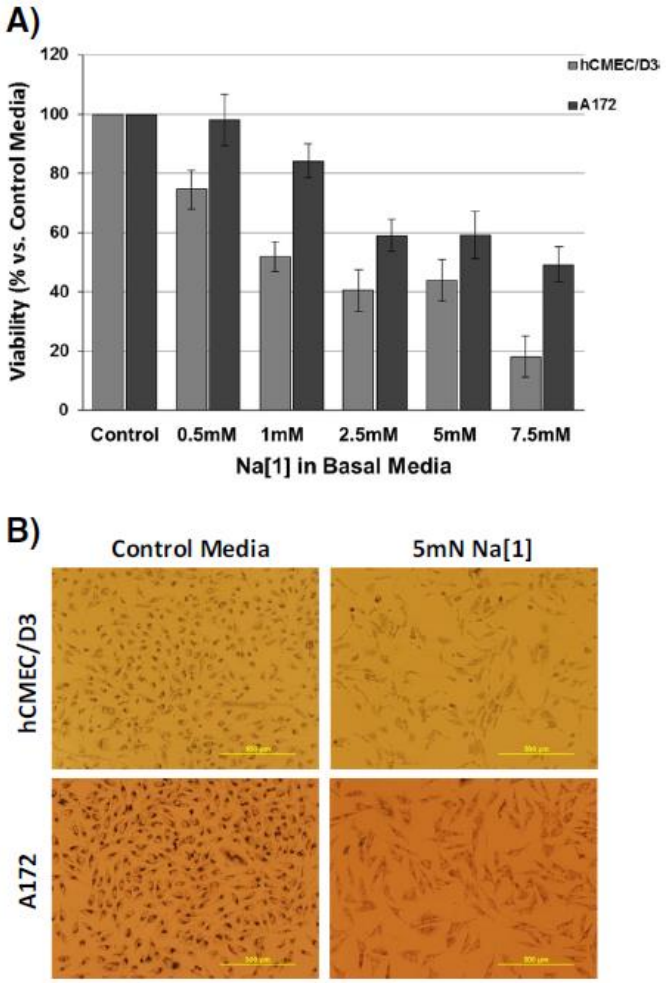

Figure 21: Cell viability after exposing brain endothelial cells (hCMEC/D3) and glioblastoma cells (A172) to increasing concentrations of the Na[1] salt compared to control treatment (vehicle). (A) Bar graph representing cell viability after 24 h treatment (mean ± SD). (B) Representative images of cells after MTT assay.

Evaluation of in-vivo toxicity of the 1-MNP Compound in mice: We aimed at proving for the first time that the 1-MNPs were well-tolerated and did not induce major acute toxicity signs such as death, seizures or convulsions but also acute pain, distress, decreased/increased motor activity or dehydration by monitoring body weight before and after treatment.

To explore potential "*in vivo*" toxicity of the new 1-MNP nanohybrids, adult C57BL/6 mice (males, 11-12 weeks-old) received one intravenous administration of 80 µL of 1-MNPs at 218 µg/mL iron concentration or corresponding vehicle solution used along the study (equal content of m-carboranylphosphinic acid (H[1]) and $[NMe_4]OH$ as in a 1-MNPs colloidal suspension). 80 µL of 1-MNPs intravenously corresponds to 0.58 ± 0.03 mg/kg of body weight, very close to the approved dose for Feridex® in humans (0.56 mg/kg of body weight) and previously tested in other "in vivo" studies.[73] The mice were briefly anesthetized with 5 % isoflurane in Medicinal Air (from Air Liquide), weighed and treated with 1-MNPs or vehicle solution by retro-orbital injection as described. After recovery from anaesthesia, the mice were returned to their housing boxes and supervised daily looking for sudden death, seizures, dystonia, dehydration or restrictions in mobility. Additionally, body weight was registered before administration (baseline), at day 1, 2, 3 and 10 in both the treated and the naïve mice. Importantly, all mice survived the study period (10 days) with no major signs of toxicity. In particular, we found that the individual body weight of the 2 treated groups were comparable with the control group (naïve mice) with day to day fluctuations but without showing significant differences between groups in the body weight ($p = 0.9$; Figure 22, A-B).

Differences in weight between groups were subjected to analyses of variance and statistical significance was considered when $p < 0.05$.

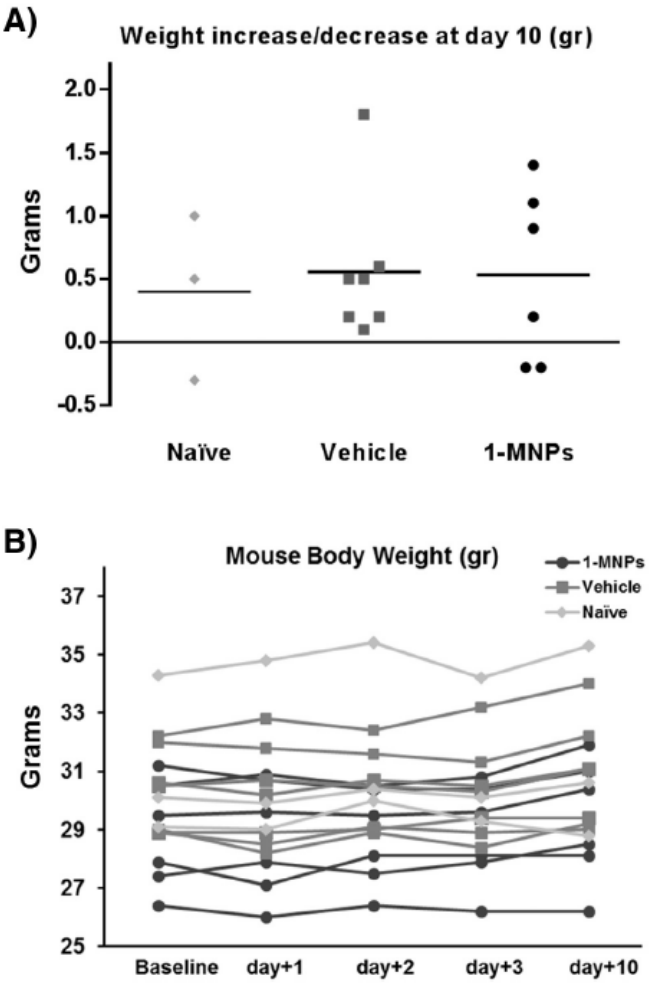

Figure 22: Mouse weight after *in vivo* administration of 1-MNPs or vehicle in mice: mice were weighted before 1-MNPs (n = 6) or Vehicle (n = 7) intravenous administration, and followed up at 1, 2, 3 and 10 days of injection. A group of naïve mice who did not receive any treatment was also weighed at the same days (n = 3). (A) The Individual weight increase or decrease at day 10 was calculated for each mouse and represented, showing no differences between treatment groups (p = 0.9). (B) Graph showing the individual time course of the body weight during the study period.

6. Conclusions

The development of multifunctional hybrid nanomaterials which could be applied in multi-modal treatments to obtain more efficient drugs with diminishing secondary effects is of great interest nowadays. Thus, based on the biofunctional properties of the multifunctional hybrid nanomaterials, our aim in the present study was to prepare MNPs coated with m-carboranylphosphinate ([1]⁻)) to be applied as a theranostic biomaterial for cancer therapy: biocompatible agents for cell labelling used for both tracking purposes and BNCT treatments.

The study shows that the newly synthesized nanohybrid 1-MNPs could be used to target cancer cells for tumour imaging and treatment with BNCT therapy. This technique is a highly selective type of radiation therapy that can target tumour cells without causing radiation damage to the adjacent normal cells. Specifically, the 1-MNPs compound is taken up from culture media by glioblastoma multiform cell line A172 in a higher amount than in the endothelial cells with cell-tracking properties due to the magnetic core of 1-MNPs by showing a reduced signal on T2 weighted Magnetic Resonance Imaging (MRI). This characteristic could allow the indirect quantitative determination of boron at the target site before and during neutron irradiation becoming an advantage during cancer treatment since it allows the determination of the optimal neutron irradiation time and a precise calculation of the delivered dose. [74,75]

Moreover, BNCT was performed on A172 cells treated with 1-MNPs, demonstrating the eligibility of 1- MNPs as boron vectors for an efficient BNCT. Finally, it was assessed that the systemic administration of these 1-MNPs in adult mice are well tolerated at mid-term with no major signs of toxicity. It has been recently reported that pH produces an effect on the hydrodynamic radius of aqueous 1-MNPs suspensions and many studies have revealed that MNPs behave differently in biological media than in water at physiological pH (7.45)[76] because of the presence of

inorganic salts, proteins, amino acids or polysaccharides in biological media. Our newly synthesized boron nanohybrids 1-MNPs showed colloidal stability and a nanometric size in different culture media and at temperatures (room temperature and 37°C), supporting their use in biological studies. The hybrid nature of MNPs is conceptually divided into the inorganic core, the engineered surface coating comprising the ligand shell and the corona of adsorbed biological molecules. Empirical evidence shows that all three components may degrade individually *in vivo* and can drastically modify the life cycle and biodistribution of the whole heterostructure. Thus, MNPs may be decomposed into different parts, whose biodistribution and fate would need to be analysed individually. In this regard, functional studies confirmed the uptake of 1-MNPs by the cultured cells by Prussian blue staining identifying the presence of intracellular iron after 24 h treatment with 1-MNPs. These experiments suggest that there has been cytoplasmic endocytosis of the iron core of the 1-MNPs, as previously described for other iron oxide nanoparticles by other authors.[77,78] These findings were further confirmed by electron microscopy on both endothelial and glioblastoma cells treated with 1-MNPs showing internalized iron particles in membrane vesicles (endosomes/lysosomes).

On the other hand, high resolution XPS and EELS spectra on the A172 dried-cells sample unambiguously proved the presence of the *m*-carboranylphosphinate; peaks at 189 and 133 eV, which are characteristic of B-B and P-O bonding, thus, confirming the presence of boron cluster ligands in the treated cells. Quantification of 1-MNPs uptake by cells displayed that glioblastoma A172 cells presented larger cellular iron contents than brain endothelial (hCMEC/D3) cells when treated at similar conditions of the 1-MNPs compound, suggesting that by using low doses of MNPs, glioblastoma cancer cells might be largely labelled with the 1-MNPs compound compared to other neighbouring cells more sensitive to the compound such as

endothelial cells. These newly synthesized boron nanohybrids have significant biocompatible properties at certain administered doses allowing cell labelling with potential applications to penetrate into malignant tumour cells as drug carriers or for Boron Neutron Capture Therapy. The amount of both Fe and Boron internalized by A172 tumour cells in our study is sufficient to allow a successful MRI guided BNCT since it exceeds the minimum amount of ^{10}B necessary to perform BNCT[79].

Moreover, nanoparticles could also be prepared using ^{10}B enriched carboranes to improve the toxic effect of neutrons. Importantly, in terms of drug safety we have shown that the systemic administration of the 1-MNPs nanohybrids does not show major signs of toxicity in mice, supporting its potential translation into the biomedical setting. This is a preliminary but relevant result before moving to the efficacy studies in the preclinical setting using tumour models in rodents.

In conclusion, we believe that these new boron cluster-MNPs nanohybrids, 1-MNPs, might offer a broad scope for exciting research and future biomedical applications, including cancer therapy. These results have been published in Nanomedicine:NBM journal.[80]

7. References

[1] J. Kreuter, *Int. J. Pharm.* **2007,** *331*, 1.
[2] B. Issa, I.M. Obaidat, B.A. Albiss, Y. Haik, *Int. J. Mol. Sci.* **2013,** *14*, 21266.
[3] K. McNamara, S.A.M. Tofail, Biomedical applications of nanoalloys, in *Nanoalloys: From Fundamentals to Emergent Applications*, C. Florent, ed., Elsevier, Oxford, **2013**, 345.
[4] K. McNamara, S.A.M. Tofail, *Phys. Chem. Chem. Phys.* **2015,** *17*, 27981.
[5] C. Sun, J.S. Lee, M. Zhang, *Adv. Drug Delivery Rev.* **2008,** *60,* 1252.
[6] Z. Karimi, L. Karimi, H. Shokrollahi, *Mater. Sci. Eng., C.* **2013,** *33,* 2465.
[7] B. Tural, N. Ozkan, M. Volkan, *J. Phys. Chem. Solids.* **2009,** *70,* 860.
[8] Z.P. Chen, Y. Zhang, S. Zhang, et. al., *Colloids Surf., A.* **2008,** *316,* 210.
[9] R.Y. Hong, B. Feng, L.L. Chen, et. al., *Biochem.Eng. J.* **2008,** *42,* 290.
[10] Y. Zhang, J.Y. Liu, S. Ma, et. al., *J. Mater. Sci. Mater. Med.* **2010,** *21*,1205.
[11] N. Arsalani, H. Fattahi, M. Nazarpoor, *Express Polym. Lett.* **2010,** *4*, 329.
[12] J.H. Maeng, D.H. Lee, K.H. Jung, et. al., *Biomaterials* **2010,** *31*, 4995.
[13] K.C. Barick, S. Singh, D. Bahadur, M.A. Lawande, et. al., *J. Colloid Interface Sci.* **2014,** *418,* 120.
[14] Q.L. Jiang, S.W. Zheng, R.Y. Hong, et. al., *Appl. Surf. Sci.* **2014,** *307*, 224.
[15] Y. Jia, M. Yuan, H. Yuan, et. al., *Int. J. Nanomedicine* **2012,** *7*,1697.
[16] A. Akbarzadeh, M. Samiei, S.W. Joo, et. al., *J. Nanobiotechnol.***2012,***10*,1.
[17] S. Mohammadi-Samani, R. Miri, M. Salmanpour, et. al., *Res. Pharm. Sci.* **2013,** *8,* 25.
[18] W. Ding and L. Guo, *Int. J. Nanomedicine* **2013,** *8*, 4631.
[19] M. Barrow, A. Taylor, P. Murray, et. al. *Chem. Soc. Rev.* **2015,** *44,* 6733.
[20] B.J. Tefft, S. Uthamaraj, J.J. Harburn, et. al., *JoVE.* **2015,***104*, e53099.
[21] X. Peng, J. Chen, T. Cheng, et. al., *Mater. Lett.* **2012,** *81*, 102.
[22] S.W. Zheng, G. Liu, R.Y. Hong, et. al., *Appl. Surf. Sci.* **2012,** *259*, 201.
[23] W.S. Seo, J.H. Lee, X. Sun, et. al., *Nat. Mater.* **2006,***5*, 971.
[24] S.J. Lee, J.H. Cho, C. Lee, et. al., *J Nanotechnology.* **2011,** *22,* 375603.
[25] L. An, Y. Yu, X. Li, et. al., *Mater. Res. Bull.* **2014,** *49*, 285.
[26] S.P. Sherlock, H. Dai, *Nano Res.* **2011,** *4,* 1248.
[27] S.A. Shah, M.H. Asdi, M.U. Hashmi, et. al., *Mater. Chem. Phys.* **2012,***137*, 365.
[28] B. Sahoo, K.S.P. Devi, S. Dutta, et. al., *J. Colloid Interface Sci.* **2014,** *431*, 31.
[29] F.Y. Chen, Z.J. Gu, H.P. Wan, et. al., *Rev. Nanosci. Nanotechnol.* **2015,***4*, 81.
[30] H. Wu, G. Liu, X. Wang, et. al., *Acta Biomater.* **2011,***7*, 3496.
[31] S. Amiri, H. Shokrollahi, *Mater. Sci. Eng., C.* **2013,***33,* 1.
[32] D.H. Kim, D.E. Nikles, D.T. Johnson, C.S. Brazel, J. *Magn. Magn. Mater.* **2008,** *320*, 2390.
[33] C. P. Bean, J. D. Livingston, *Journal of Applied Physics,* **1959,***30*, 120S–129S.
[34] S. Bedanta, W. Kleemann, *Journal of Physics D,* **2009,** *42*, 013001.
[35] Y. Ding, S.Z. Shen, H. Sun, et. al., *Mater. Sci. Eng. C*, **2015,** *44,* 487.
[36] Y. Arum, H.W. Kang, J.H. Oh, *Fish. Aquat. Sci.* **2015,** *18*, 89.
[37] C.W. Zhang, C.C. Zeng, Y. Xu, *Nano* **2014,** *9*,1450042.
[38] M.Z. Iqbal, X. Ma and T. Chen, *J. Mater. Chem. B* **2015,** *3*, 5172.

[39] G. Zhao, J. Wang, X. Peng, et. al., *Chem. Asian J.* **2014,** *9*, 546.
[40] W. Chen, X. Wen, G. Zhen, X. Zheng, *RSC Adv.* **2015,** *5*, 69307.
[41] S. Sabale, V. Jadhav, V. Khot, et. al., *J. Mater. Sci. Mater. Med.* **2015,** *26*,1.
[42] M. A. Agotegaray, V. L. Lassalle, *Silica-coated magnetic nanoparticles*, Springer Publications, 1st edition, Cham, Switzerland, **2017.**
[43] P. Nicolás, M. Saleta, H. Troiani, et. al., *Acta Biomaterialia,* **2013,** *9*, 4754–4762.
[44] W. Wu, Q. G. He, C. Z. Jiang, et. al., *Nanoscale Research Letters,* **2008,** *3*, 397.
[45] V. B. Barbeta, R. F. Jardim, P. K. Kiyohara, *Journal of Applied Physics,* **2010,** *107*, 073913.
[46] M. Song, Y. Zhang, S. Hu, et. al., *Colloids and Surfaces A: Physicochemical and Engineering Aspects,* **2012,** *408*, 114.
[47] M. Agotegaray, A. Campelo, R. Zysler, et al. *Journal of Biomaterials Science*. **2016,** doi:10.1080/09205063.2016.1170417.
[48] M. Okuda, J. Eloi, S. E. Jones, et al., *Nanotechnology,* **2012,** *23*, 415601.
[49] R. Massart, *IEEE Transactions on Magnetics,* **1981,** *17*, 1247.
[50] C. Chouly, D. Pouliquen, I. Lucet, et al., *Journal of Microencapsulation,* **1996,** *13*, 245–255.
[51] T. K. Jain, M. K. Reddy, M. A. Morales, et al., *Molecular Pharmaceutics,* **2008,** *5*, 316–327.
[52] M. L. Mojica Pisciotti, E. Lima, E., M. M. Vasquez Mansilla, et al. *Journal of Biomedical Materials Research Part B: Applied Biomaterials,* **2014,***102*, 860–868.
[53] P. Aggarwal, J. B. Hall, C. B. McLeland, et al. *Advanced Drug Delivery Reviews,* **2009,** *61*, 428–437.
[54] M. I. Papisov, A. Bogdanov, B. Schaffer, B., et al. *Journal of Magnetism and Magnetic Materials,* **1993,** *122*, 383–386.
[55] T. Niendorf, F. Brenne, P. Hoyer, et al. *Metallurgical and Materials Transactions A,* **2015,** *46*, 2829–2833.
[56] R. F. Barth RF, P. Mi, W. Yang, et al., *Cancer Commun.,* **2018,** *38,* 35.
[57] T. Sun, Y. Y. Li, Y. L. Huang, et al. *Oncotarget* **2016,** *7,* 43095–08.
[58] Z. Y. Gao, Y. Horiguchi, K. Nakai, et al. *Biomaterials* **2016**,*104*,201.
[59] E. M. Heber, M. F. Hawthorne, P. J. Kueffer, et al. *S A* **2014**,*111*,16077.
[60] S. Xuan, N. Zhao, Z. H. Zhou, et al., *J Med Chem.* **2016,** *59,* 2109.
[61] A. M. Cioran, A. D. Musteti, F. Teixidor F, et al., *J Am Chem Soc* **2012**, *134*, 212.
[62] Neutron capture therapy. principles and applications. (Eds: Sauerwein WAG, Wittig A, Moss R, Nakagawa Y), Springer Science & Business Media **2012**.
[63] M. Bialek-Pietras, A. B. Oejniczak, S. Tachikawa, et al., *Bioorg Med Chem* **2013,** *21*, 1136.
[64] G. Calabrese, A. Daou, A. Rova, et al., *Med Chem Commun* **2017**, *8,* 67.
[65] K. Nedunchezhian, N. Aswath, M. Thiruppathy, S. Thirugnanamurthy *J Clin Diagn Res* **2016**,*10*, ZE01-4.
[66] Y. Zhu, Y. Lin, Y. Z. Zhu et al., *J Nanomater* **2010,** 409320.
[67] E. Oleshkevich, F. Teixidor, D. Choquesillo-Lazarte, et al., *Chem Eur J* **2016**, *11*,3665.

[68] E. Oleshkevich, F. Teixidor, A. Rosell, C. Viñas, *Inorg Chem* **2018,** *57*, 462.
[69] R. C. O'Handley, Modern Magnetic Materials: Principles and Applications; Wiley: New York, **1999**.
[70] E. Carenza, V. Barceló, A. Morancho, et al., *Nanomedicine:NBM* **2014***10*, 225.
[71] J. Matuszak, J. Zaloga, R. P. Friedrich, et al. *J Magn Mater* **2015**, *380*, 20.
[72] T. Sundstrøm, I. Daphu, I. Wendelbo, et al. *Cancer Res* **2013**, 73, 2445.
[73]M Wang Y-XJ. *Quant Imaging Med Surg* **2011**,*1*,35-40.
[74] S. Geninatti-Crich, D. Alberti, I. Szabo, et al. *Chemistry* **2011**, *17*, 8479.
[75] A. Deagostino, N. Protti, D. Alberti, et al. *Future Med Chem* **2016**, *8,* 899.
[76] A. Aires, S. M. Ocampo, D. Cabrera, et al. *J Mater Chem B* **2015**, *3*, 6239.
[77] I. Angelopoulos, P. Southern, Q. A. Pankhurst, R. M. Day, *J Biomed Mater Res A* **2016**,*104*, 2412.
[78] C. Wilhelm, F. Gazeau, *Biomaterials* **2008**, *29*, 3161.
[79] R. F. Barth, G. M. H. Vicente, O. K. Harling et al., *Radiat Oncol*. **2012**, *7*,146.
[80] E. Oleshkevich, A. Morancho, A. Saha et al., *Nanomedicine : NBM,* **2019,** *20,* 101986.

3.2.2. Magnetic Nanoparticles and Nanocomposites with H[COSAN]

Magnetic Nanoparticles (MNPs) were synthesized using colloidal co-precipitation method and coated with Silica layer and functionalized with different moieties. These different functionalized MNPs were studied and amine functionalized MNPs were further used. Their colloidal stability with different surfactants was studied.

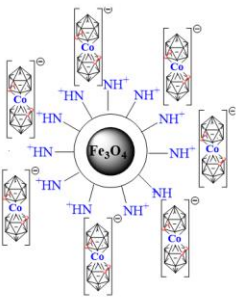

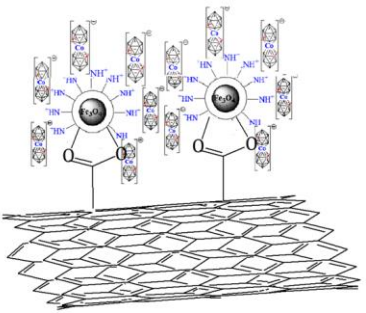

Arpita Saha
ICMAB-CSIC (UAB)

Contents

1. Introduction

Magnetic nanoparticles (MNPs) have already been introduced in the previous chapter. There we had synthesized MNPs covered with m-carboranylphosphinate to obtain nanohybrids for biological applications. In this chapter, we are going to discuss about the MNPs formed by co-precipitation method too but rather coated with an inorganic shell of silicon dioxide (SiO_2), and then further their surfaces are functionalized with carboxylic groups (-COOH) or amines (-NH_2) so that they can be further used for immobilization of antibodies or attachment of H[COSAN]. Here, nanocomposites of multiwalled carbon nanotubes (MWCNTs) along with functionalized MNPs are also discussed. All the nanoparticles and nanocomposites have been thoroughly studied and characterized using the necessary techniques. The use of novel H[COSAN] in conjugation with the MNPs and magnetic nanocomposites (MNCs) has been studied here for the first time. Also, the colloidal stability of the MNPs in water has been studied using 5 different surfactants. The colloidal stability of the MNPs is a huge issue in regards to their use in applicative purposes and is important to be addressed. There exists a conflicting nature of MNPs at present with regards to their stability and the magnetic attraction. The more stable the MNPs, the longer time they take to be attracted by the magnet and vice versa. The implemented synthetic routes are modified versions of the synthetic procedures used by Hassani et. al., Arvand et. al. and Lu et. al. [1-3] Most of the MNCs have MWCNTs or SWCNTs as the base on which the MNPs are anchored and then coated with a layer of SiO_2 or have MNPs filled inside a CNT and functionalize the surface of CNT for other bindings. But in neither case these MNPs anchored on the CNTs are further functionalized with different moieties for further binding. This has been attempted and studied by us.

1.1. MNPs with SiO_2 Coating

MNPs as described in the previous chapter are very attractive nanoparticles because of the ease with which they can be controlled with the help of an external magnet. Further their use in biological studies requires them to be coated with different other shells as mentioned in previous chapter 4. One such coating used for MNPs for many years is the silica coating. This is because of the inert properties of the silica along with the fact that it helps in improving the stability and the physicochemical properties of the MNPs. [4] The formation of a silica coating on the surface of MNPs could help prevent the aggregation of the MNPs in the solution state and improve their chemical stability. The uncoated MNPs aggregate quite quickly while the silica coating enhances the surface potential with respect to the solvent and the stability improves. [4] Another important aspect about the coating is that it makes the surface of the MNPs suited to the biological systems and biological applications.[4] Though the most important aspect of MNP coated with silica is that the silanol-terminated surface groups may be modified with various coupling agents to covalently bind to specific ligands. [5-7] This helps to tune the surface of these MNPs with different functional groups to obtain differently functionalized MNPs which can be further used for other purposes. The surface modification is needed to get useful MNPs and utilize their magnetically controlled properties in different situations. These functionalized MNPs can be used for different applications like catalysis, bio-separation, water purification, biosensing, nanomedicine and more. [9-12] Silica coated MNPs have opened a new avenue for using these MNPs in different applications by tuning their surface with various ligands and functional moieties which the naked MNP could not be used in directly as functionalizing the naked MNPs is not easy.

1.2. Cobaltabis(dicarbollide): H[COSAN]

Cobaltabis(dicarbollide) or $[Co(C_2B_9H_{11})_2]^-$ is a metallacarborane (Mcb), which belongs to the family of boranes and carboranes and is one of the first to be reported.[14] It is extremely stable and has an established chemistry. The cobaltabis(dicarbollide) anion consists of two $(C_2B_9H_{11})^{2-}$ (dicarbollide) units sandwiched around a Co^{3+} having a dihedral angle of 3.7°. The distances from cobalt to C_2B_9 faces are almost identical (1.466 and 1.476 Å respectively) and the metal is approximately at equidistant from the facial boron and carbon atoms. Cobaltabis(dicarbollide) anion can be functionalized at both the carbon and boron atoms of the cluster. This is also called H[COSAN] and is known to form ion-pair complex as H[COSAN] produces an acidic pH which favours the formation of the complex. The H[COSAN] has been used in previous studies in our group to produce ion-pair complexes for potentiometric ion-selective sensors.[15-18] The stability of H[COSAN] is exceptionally good in water. It has a zeta potential value of ||60|| mV which shows that it is extremely stable in water and it has a negative potential. This is the first time they have been used in conjugation with MNPs.

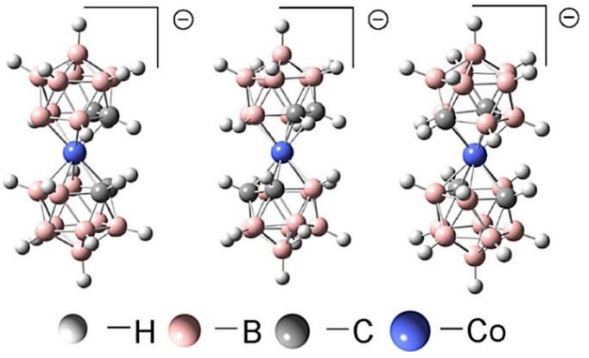

Figure 1: Chemical structure of H[COSAN].

1.3. Carbon Nanotubes (CNTs)

Carbon Nanotubes (CNTs) are cylindrical large molecules consisting of a hexagonal arrangement of hybridised carbon atoms. They may be formed by rolling up graphene. After the discovery of CNTs by Iijima in 1991[19], CNTs have attracted significant attention in a variety of scientific fields due to their unique properties such as high surface area, excellent electrical conductivity, significant mechanical strength, potential applications and high chemical stability. [20-22] CNTs are of two types: Single walled carbon nanotubes (SWCNTs) where a single sheet of graphene is rolled up and Multi walled carbon nanotubes (MWCNTs) in which case multiple sheets are rolled up into tubes. The SWCNTs have smaller diameter compared to the MWCNTs. The CNTs are long tubes and their length can be extended upto 1.3mm long. The CNTs are one of the best candidates for the preparation of the electrocatalytic nanocomposite materials. [23] Among the applications of CNTs in various fields, magnetic CNTs produced by functionalizing CNTs with magnetic nanomaterials are one of the most useful nanocomposites, which incorporate the features of both CNTs and magnetic nanomaterials. The magnetic CNTs have applications as magnetic data storage,[22] microwave absorbing materials and magnetic composites for drug delivery. [24,25]

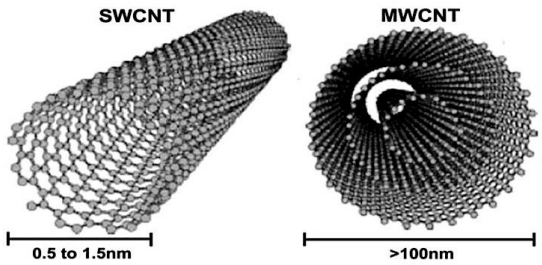

Figure 2: SWCNT and MWCNT.

2. Synthesis of MNPs

The synthesis of MNPs were done using the classic co-precipitation method which was also used in the previous chapter. In this case the co-precipitation method was used to generate the Fe_3O_4 magnetite core. This core was then further encapsulated in a silica shell using Stober process. After having the MNPs coated with SiO_2, they were further functionalised by carboxylic group or amino groups. The synthetic procedure is given below.

2.1. Fe_3O_4@SiO_2 (Small and Large)

The synthesis procedure for obtaining the Fe_3O_4@SiO_2 was the common procedure followed by everyone.

Synthesis of Fe_3O_4 Core: First, sodium hydroxide (NaOH, 15g) was dissolved into 25 mL of double distilled water. Then, a mixture of $FeCl_2.4H_2O$ (2g), $FeCl_3.6H_2O$ (5.2g), 25 mL of double distilled water and 0.85 mL of HCl (12M) was added dropwise with vigorous stirring to make a black solid product. The resultant mixture was heated using an oil bath for 4 hours at 80°C. The black magnetite solid MNPs were isolated using an external magnet and washed three times with deionized water and finally once with ethanol, and then dried at 80°C for 10 hours.

Synthesis of Fe_3O_4@SiO_2 core–shells: Fe_3O_4 (500mg, 2.1 mmol) was dispersed in a mixture of ethanol (100 mL) and deionized water (25 mL) for 30-40 minutes using an ultra sound bath. Then, 2.5 mL of NH_3 (30% for analysis) was added followed by the dropwise addition of tetraethoxysilane (TEOS) (1.5 mL). This solution was stirred mechanically for 6 hours at room temperature. Then, the product Fe_3O_4@SiO_2 was separated using an external magnet and was washed three times with deionized water and finally with ethanol, and then dried at 80°C for 10 hours. For this reaction we designed a new

teflon covered system with a crystal mechanical stirring rod.

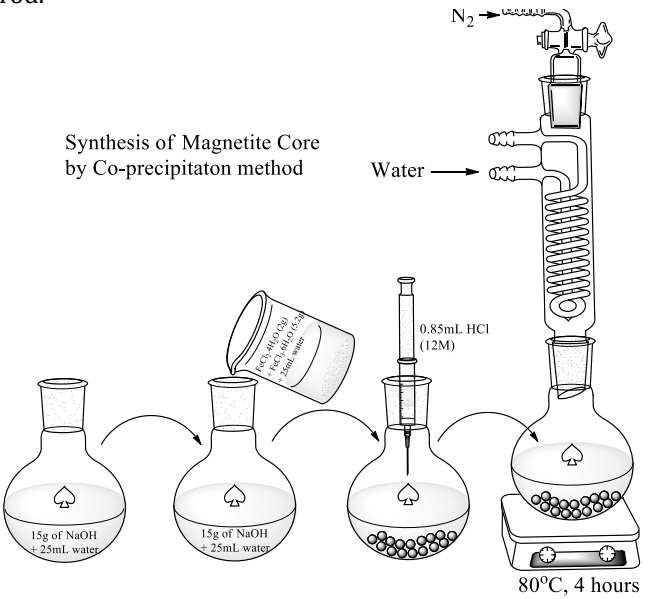

Figure 3: Synthesis of Fe_3O_4 core using co-precipitation method.

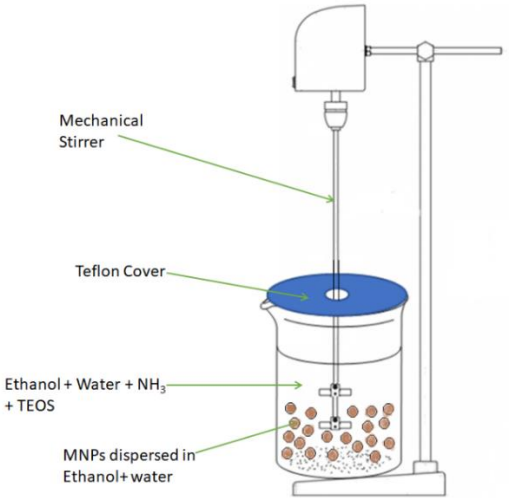

Figure 4: Synthesis of Fe_3O_4@SiO_2 core using co-precipitation method.

Small and Large particles: The smaller silica coated particles are synthesized using the standard silica coating procedure reported above. In case of larger particles, the magnetite core reaction is stirred for 6 hours and the silica reaction is stirred for 12 or 18 hours depending on the size needed to be produced. The quantity of TEOS to be added can also be controlled on the necessity of thickness of the shell. The biggest advantage of this method lies in the fact that it helps to change the size of the particles by modifying the time and temperature of the reaction. The silica coating using Stober process can also be done at a mild temperature of 40°C in need for thicker coatings over the magnetite core. This flexibility in the process makes it attractive but the disadvantage of this procedure lies in less control of the mono-dispersity of the particles.

2.2. Amine and Carboxylic Functionalized MNPs

The silica coated MNPs (Fe_3O_4@SiO_2), were further functionalized with amine groups or carboxylic groups. For carboxylic functionalization three different procedures were followed while for amine functionalization only one procedure was followed. First, the amine functionalization is discussed and then the carboxylic functionalization.

Amine functionalization: A mixture of Fe_3O_4@SiO_2 (200mg) was dispersed in ethanol (45 mL). Then 5ml of 3-(2-aminoethylamino)propylmethyldimethoxy silane (APMS) was dissolved in 20ml of ethanol and added to the suspension of Fe_3O_4@SiO_2 in ethanol. The pH value of the reaction mixture was set to 11 using tetramethyl ammonium hydroxide (TMAH). The reaction mixture was then heated to 50°C and stirred for 5 hours. After ageing for a night, the suspension of functionalized nanoparticles was completely stable. It was then precipitated using NaCl

solution. Then the nanoparticles were thoroughly washed with distilled water using magnetic separation and finally dried at 80°C in vacuum.

For this amine functionalization instead of APMS other reagents like (3-aminopropyl)triethoxy silane (APTES) or (3-aminopropyl)trimethoxy silane (APTMS) can also be used which give the same result.

Carboxylic functionalization method 1: This method is used as an extension of the method of the amine functionalized MNPs. The Fe_3O_4@SiO_2-NH_2 are used in this reaction to make them COOH functionalized. The Fe_3O_4@SiO_2-NH_2 (100mg) was suspended in 45ml of dry DMF. Then 60 mg of succinic anhydride was dissolved in 5 ml of dry DMF and added to the suspended nanoparticles. The reaction mixture was then stirred for 20 hours at room temperature. The nanoparticles were then washed repeatedly with acetone using magnetic separation and then dried under vacuum. This helped us to obtain Fe_3O_4@SiO_2-NH_2-COOH MNPs.

Carboxylic functionalization method 2: The Fe_3O_4@SiO_2 magnetic nanoparticles were functionalized with malic acid in this method. Briefly, 2g of dried Fe_3O_4@SiO_2 MNPs was dispersed in 100mL of water, followed by addition of 2 g of malic acid under vigorous stirring at 90°C for 90 min. the resulting functionalized nanoparticles were then washed with distilled water three times to remove any unreacted chemicals and dried in vacuum at 80°C to obtain Fe_3O_4@SiO_2 -COOH MNPs.

Carboxylic functionalization method 3: A mixture of Fe_3O_4@SiO_2 (200 mg) and maleic anhydride (200 mg) in $CHCl_3$ (10 mL) was magnetically stirred at 50°C for 5 h. The Fe_3O_4@SiO_2-COOH MNPs were isolated using an external magnet, washed with ethanol and dichloromethane each and then dried at 80°C to obtain the Fe_3O_4@SiO_2-COOH.

Out of the above three methods for the synthesis of Fe_3O_4@SiO_2-COOH, the method 3 has been the most productive method in obtaining the Fe_3O_4@SiO_2-COOH MNPs. The 3rd method is the most reproducible and produces MNPs of uniform size distribution. The 1st method was though used too to generate carboxylic coated MNPs but in that case the purpose was to not saturate all the amines with COOH groups but leave a few NH_2 groups free to bond with other moieties especially like H[COSAN] which favours the NH_2 group to form an ion pair complex. It is described later.

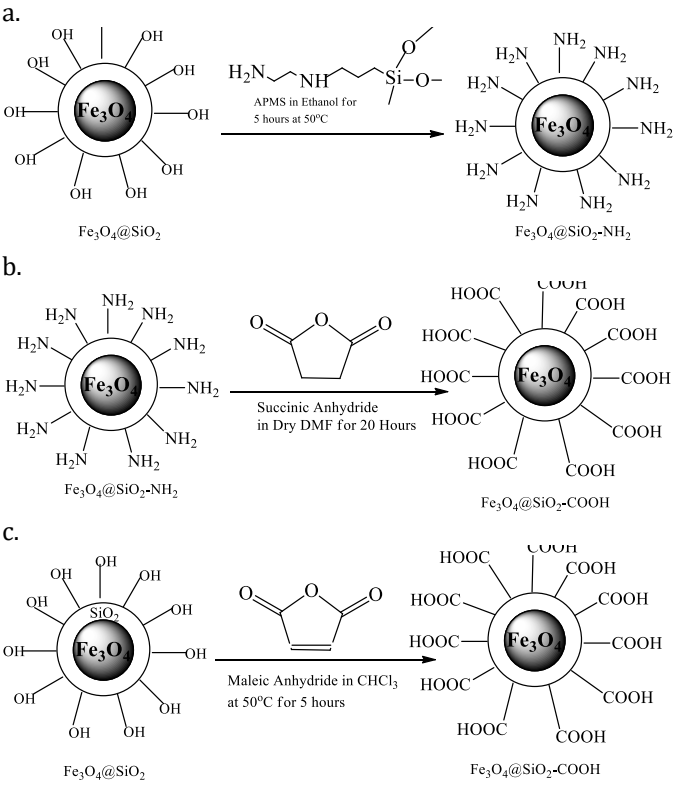

Figure 5: Synthesis of (a) Fe_3O_4@SiO_2-NH_2 (b) Fe_3O_4@SiO_2-COOH using method 1 and (c) Fe_3O_4@SiO_2-COOH using method 3.

2.3. H[COSAN] attached to MNPs

The attachment of H[COSAN] to MNPs has never been explored before and it has been done and studied by us for the first time. The H[COSAN] as mentioned before, is extremely stable in water and can form an ion pair complex. It has been demonstrated earlier that the Mcb has the capacity to produce Cc-H···H-B, B-H···H-N dihydrogen bonds. Moreover, the Mcb forms ion-pair complexes with protonated amino groups ([cation-NH]$^+$[Mcb]$^-$) with an ionic interaction. So, to facilitate this formation of the ion pair complex it was necessary to have the NH_2 functionality. Due to this, the MNPs functionalized with NH_2 and also the one with NH_2 and COOH was used for attaching H[COSAN] to them in a non-covalently bonded way. We did try at first to attach the H[COSAN] to the COOH functionalized MNPs but with no success. They did not show any interaction and could not be obtained.

Fe_3O_4@SiO_2-NH_2-H[COSAN] and Fe_3O_4@SiO_2-NH_2-COOH-H[COSAN]: 50 mg of Fe_3O_4@SiO_2-NH_2 or Fe_3O_4@SiO_2-NH_2-COOH was suspended in 10 mL of water and with 5 mM of $H[Co(C_2B_9H_{11})_2]$. The mixture was sonicated in an ultrasound bath for 30 minutes and then washed 10 times with water using magnetic separation. Finally, the sample was dried under vacuum at 80°C.

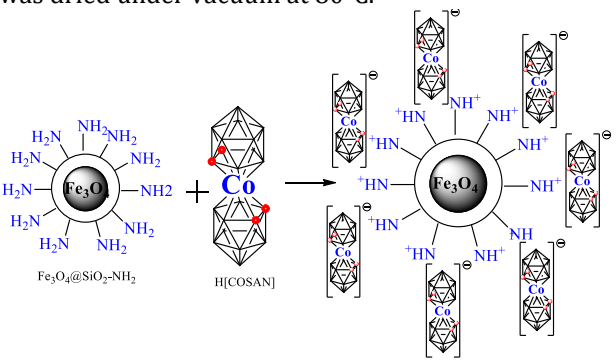

Figure 6: Synthesis of Fe_3O_4@SiO_2-NH_2-H[COSAN]

3. Characterization

The MNPs were thoroughly characterized using various characterization techniques in order to study their size, shape, magnetic hysteresis cycle, stability etc.

Transmission electron microscopy (TEM) studies were carried out using JEOL JEM 1210 at 120 kV. Scanning electron microscopy (SEM) and Energy Dispersive X-ray Spectroscopy (EDX) analysis was done using the QUANTA FEI 200 FEG-ESEM device. The solid sample was analysed for this. HRTEM was done using JEM-2011 at 200kV with 0.18nm resolution. HRSEM was done using Zeiss Merlin. ImageJ software was used for measuring the particles. Zeta Potential studies were carried out in the Zetasizer Nano ZS (For DLS light source used was He-Ne Laser, 633nm, Max 4mW, back scattering angle used was 173^{o} and for zeta potential electrophoretic light scattering principle was used to do the measurements). UV-vis Spectrum was carried using Cary-5000 UV-vis-NIR spectrophotometer. Infra-red spectroscopy (IR) was done using JASCO FTIR-4600 spectrometer. Magnetization hysteresis cycle was measured using Quantum Design MPMS-XL system at 300K with a maximum of 60kOe. Scanning transmission microscopy (STEM) and EELS measurement was done using FEI Technai F20 S/TEM HRTEM device at 200kV.

3.1. TEM, STEM and SEM studies and Size

The TEM studies were done to see the particles shape and obtain their size. SEM was done to check their morphology too, while STEM was mostly done with MNPs attached with H[COSAN].

TEM Studies: Fe_3O_4@SiO_2 MNPs are seen in TEM images with a spherical shape characteristic of these nanoparticles with a mean size of 9.34 ± 1.6 nm. The size was calculated by measuring the particles manually using ImageJ software and plotting the Gaussian graph. When the Fe_3O_4@SiO_2 MNPs are coated with carboxylic acid, the spherical shape is

maintained as seen in the images and the size increases till 12.63 ± 2.67 nm.

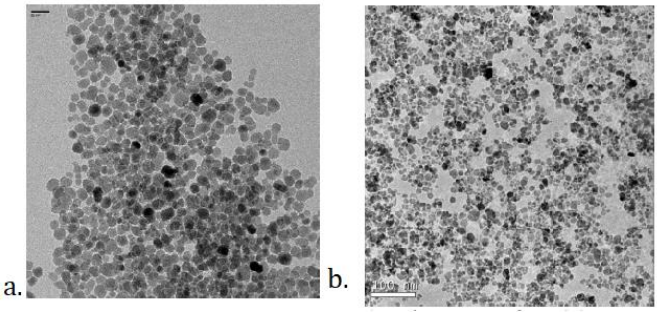

Figure 7: TEM image of (a) Fe_3O_4@SiO_2 and (b) Fe_3O_4@SiO_2-COOH.

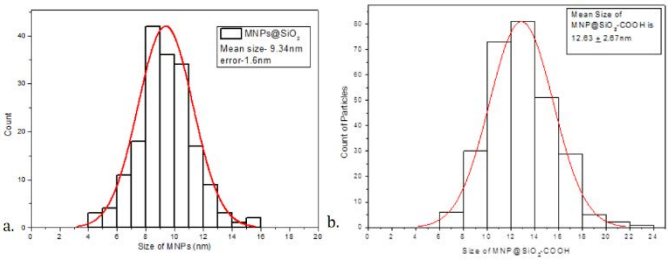

Figure 8: Gaussian Size graphs of (a) Fe_3O_4@SiO_2 (9.34nm) and (b) Fe_3O_4@SiO_2-COOH (12.63nm).

TEM image of Fe_3O_4@SiO_2-NH_2 showed aggregated particles when compared to the MNPs with COOH. They had a mean diameter size of 11.22 ± 2.13 nm. The TEM image of Fe_3O_4@SiO_2-NH_2-Mcb showed a mean diameter size of 14.17 ± 1.03 nm. The complex Fe_3O_4@SiO_2-NH_2-Mcb produces nanoparticles 3 nm bigger in diameter and if we observe the extension image, we can notice that the H[COSAN] is preferentially located between the NPs and tends to aggregate the complex. The size increase is due to the presence of the H[COSAN] with the MNPs. While the size of Fe_3O_4@SiO_2-NH_2 is almost comparable to the size obtained for the Fe_3O_4@SiO_2-COOH MNPs.

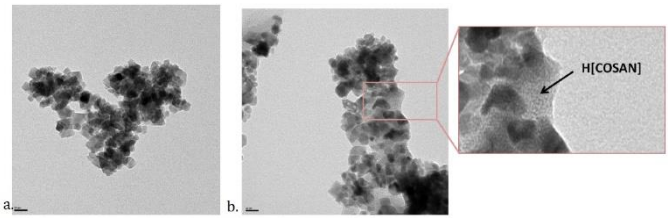

Figure 9: TEM images of (a) Fe_3O_4@SiO_2-NH_2 (11.22nm) and (b) Fe_3O_4@SiO_2-NH_2-Mcb (14.17nm).

The Fe_3O_4@SiO_2-NH_2-COOH was also characterized using TEM. It showed aggregated particles with thick silica coating. The aggregation in these particles was too much to measure individual particles and obtain the size. So, the size could not be determined. Moreover, the attachment of H[COSAN] could not be determined as clearly as seen in the amine functionalized ones. Only little presence of H[COSAN] could be seen.

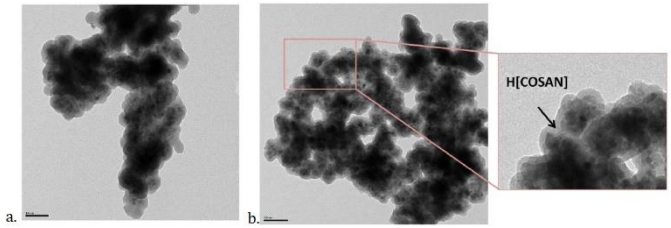

Figure 10: TEM images of (a) Fe_3O_4@SiO_2-NH_2-COOH and (b) Fe_3O_4@SiO_2-NH_2-COOH-Mcb.

SEM Studies: The SEM studies were done on the Fe_3O_4@SiO_2 nanoparticles. Solid samples were used for this and they showed the spherical nanoparticles but the resolution of the image was not good as the MNPs were less than 10nm and the SEM resolution showed them as an aggregated mass of particles. Due to this, other MNPs were not characterized using SEM. Though the SEM did confirm their spherical morphology.

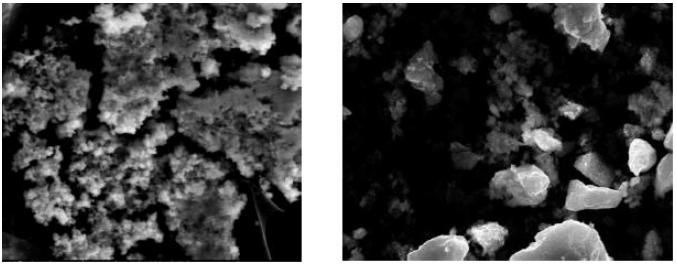

Figure 11: SEM images of $Fe_3O_4@SiO_2$

STEM Studies: The scanning transmission electron microscopy (STEM) was done on the samples containing Mcb. This was because in STEM mode we have certain advantages over the traditional TEM and SEM modes. It combines the advantages of the TEM and SEM both and helps to obtain both the dark field and bright field images and hence it helps to visualize the Mcb attachment to the MNPs better than in the TEM.

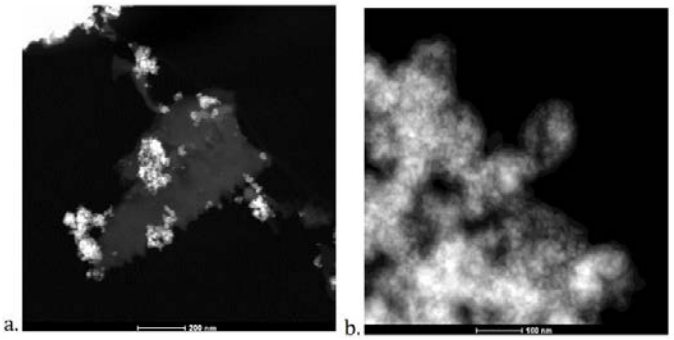

Figure 12: STEM images of (a) $Fe_3O_4@SiO_2$-NH_2-Mcb and (b) $Fe_3O_4@SiO_2$-NH_2-COOH-Mcb.

The STEM image of the $Fe_3O_4@SiO_2$-NH_2-Mcb clearly showed the H[COSAN] but the $Fe_3O_4@SiO_2$-NH_2-COOH-Mcb did not show the presence of H[COSAN]. This could be because in this all the NH_2 groups had already been saturated with the COOH groups so it cannot be used to attach the H[COSAN]. Thus, the best one to attach the H[COSAN] was the $Fe_3O_4@SiO_2$-NH_2 MNPs.

3.2. Chemical Composition Studies

The chemical composition of the different MNPs were studied using the IR, EDX, Electron Diffraction and EELS.

IR Studies: The IR spectrum was recorded for the samples of Fe_3O_4@SiO_2-COOH, Fe_3O_4@SiO_2-NH_2 and Fe_3O_4@SiO_2-NH_2-Mcb. For the Fe_3O_4@SiO_2-COOH sample we can see the bond stretching of C=O at 1739cm^{-1} and the Si-O stretching was observed at 1058cm^{-1} (Figure 13). Also we can observe the band of Fe-O at 546 cm^{-1} in the MNPs.
Figure 14 shows the IR spectrum Fe_3O_4@SiO_2-NH_2 and Fe_3O_4@SiO_2-NH_2-Mcb. We can observe in both samples the band of Fe-O at 546 cm^{-1} in the MNPs and at 542 cm^{-1} in the complex, the band of Si-O at 1074 cm^{-1} in the MNPs and at 1071 cm^{-1} in the complex and the bending band of N-H at 1638 cm^{-1} in the MNPs and at 1632 cm^{-1} in the complex. And in the case of the complex Fe_3O_4@SiO_2-NH_2-Mcb we can see the B-H band at 2563 and 2526 cm^{-1} characteristic of the metallacarborane.

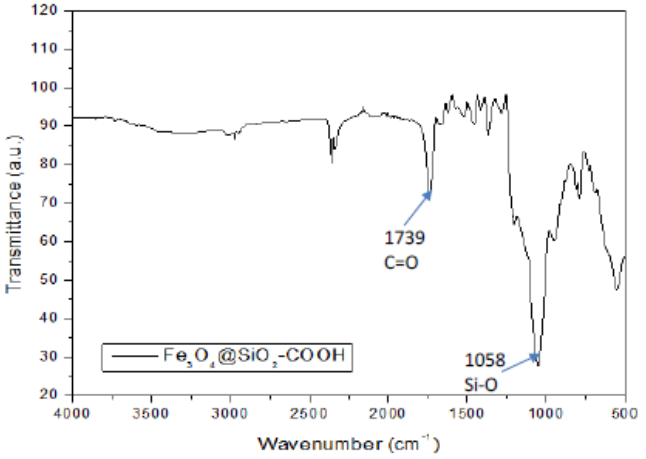

Figure 13: IR spectrum of Fe_3O_4@SiO_2-COOH.

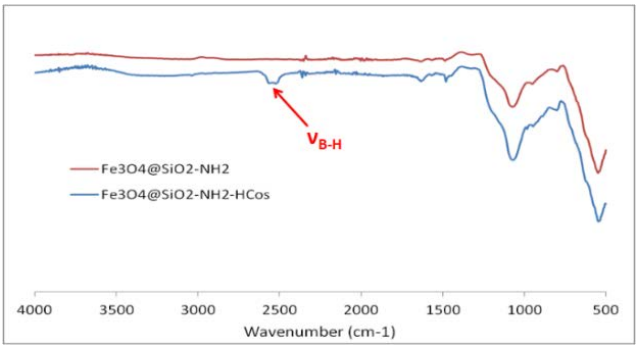

Figure 14: IR spectrum of Fe_3O_4@SiO_2-NH_2 and Fe_3O_4@SiO_2-NH_2-Mcb.

EDX Studies: EDX studies were done for the sample of Fe_3O_4@SiO_2 to check the presence of Fe and Si mostly. This was because the EDX is more efficient to check heavier metals and not the light metal like Boron. We could very well observe the presence of Fe and Si in the sample (Figure 15).

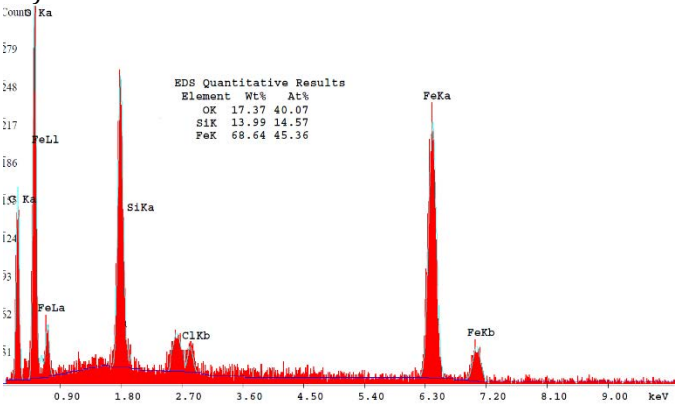

Figure 15: EDX spectrum of Fe_3O_4@SiO_2.

EELS Study: It is not possible to observe the Boron in the EDX due to its lower atomic weight and atomic number. Different treatment is required for light elements because measuring the X-rays generated by them reliably is difficult, if at all they have been detected. Ionizing an atom will be difficult when the atomic number is reduced and the ionized atom generated is less likely to emit an X-ray. The result is

a weaker signal from the light elements. Longer wavelength X-rays are generated by light element atoms and are easily absorbable within the sample when compared to shorter wavelength X-rays. Most of the weak signals generated will be absorbed within the sample itself. This means that much of the X-rays from light elements received by the detector are from near the surface of the sample. As a result, sample contamination or coatings used to avoid charging strongly affect the light element analysis. These effects make light element measurement impossible and the X-ray intensity measurements from light elements more often encounter systematic errors when compared to the X-ray intensity measurements from heavier elements. The dominance of these effects is more when the atomic number is lower. In order to check the presence of Boron we used the Electron Energy Loss Spectroscopy (EELS). This shows clearly the Boron peak in the samples Fe_3O_4@SiO_2-NH_2-Mcb, thus confirming the presence of Boron and also that the MNPs synthesized contains the Mcb. But for the Fe_3O_4@SiO_2-NH_2-COOH-Mcb, we could not observe the Boron peak thus confirming that the interaction had not taken place.

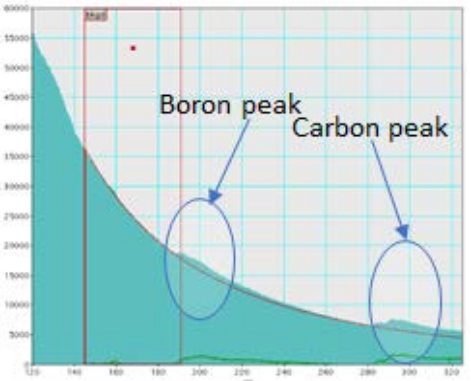

Figure 16: EELS spectrum of Fe_3O_4@SiO_2-NH_2-Mcb.

The attachment of H[COSAN] to the MNPs is important as the Mcb is a redox specie and has a tuneable HOMO-LUMO. This enables the MNP complex to be used in sensors like ISFET (Ion selective Field effect transistor). The tuneable HOMO-LUMO enables the complex to tune the energy levels

in order to improve the conductivity. The advantage of H[COSAN] with respect to ferrocene is that Mcb has 3 redox potentials compared to ferrocene and therefore the advantage to tune it. The energy levels between each Mcb attached to the MNPs can be tuned too, and if these Mcbs are aligned within close range, then it opens up the possibility of the electrons to tunnel from one Mcb to the other Mcb attached to the MNPs surface thus improving the conductivity of the complex. This would enhance the sensing layer of the sensors in which they will be used. Also, the advantage of the Mcb lies in the fact that they can self - assemble themselves. This self-assembly property enables the Mcb to form layers on the surface of the MNPs easily. This is the reason to form this magnetic complex, in order to further their use in sensing layers. The unique properties of Mcb was the reason they were incorporated in the MNP.

Electron Diffraction Studies: All the samples were tested using selected area electron diffraction pattern for confirmation of the magnetite. And the diffraction patterns for all showed that Fe_3O_4 was synthesized in its cubic spinel structure.

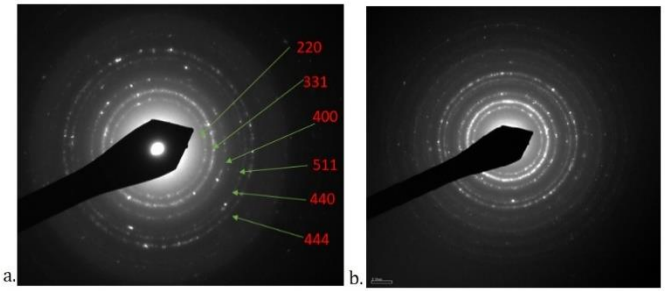

Figure 17: Electron diffraction pattern of (a)Fe_3O_4@SiO_2-COOH and (b) Fe_3O_4@SiO_2-NH_2. It confirmed the cubic spinel structure of Fe_3O_4.

3.3. UV-vis Studies and Zeta-Potential

The UV-vis studies were done to demonstrate the attaching of the H[COSAN] to the MNPs with NH_2. Also, the zeta potential provides us with proof of the presence of H[COSAN] on the surface of the MNPs.

UV-vis Studies: The chosen Mcb as we know is $H[Co(C_2B_9H_{11})_2]$, also named H[COSAN], because it was used to form the ion-pair complexes in previous studies and also H[COSAN] produces an acidic pH that favours the formation of the complex. Figure 18 shows the UV-Visible spectra of free 1 mM H[COSAN] (blue line) in water at 446 nm. The sample for this experiment was prepared by mixing 5 mg of Fe_3O_4@SiO_2-NH_2 in the H[COSAN] solution, sonicating for 15 minutes, and then collecting the MNPs with the help of a magnet for about 10 minutes; the MNPs are concentrated at the bottom of the flask and the clear liquid at the top is measured in the UV-Visible (see Figure 18). This procedure was done for 5, 10, 15, 20, 25 and 30 mg of Fe_3O_4@SiO_2-NH_2 keeping constant the amount of H[COSAN]. The idea was that if H[COSAN] interacts with the Fe_3O_4@SiO_2-NH_2 MNPs, the UV-Visible absorbance will decrease and the difference between the two absorbance peaks will be the quantity of H[COSAN] that takes part in the formation of the complex, so this way we would know about the interaction of H[COSAN] with the MNPs. Figure 18 shows that H[COSAN] interacts with Fe_3O_4@SiO_2-NH_2 MNPs because the absorbance decreases with increasing amounts of MNPs and for every 5 mg of Fe_3O_4@SiO_2-NH_2 MNPs, 0.14 ± 0.03 mM H[COSAN] is used to form the complex. The UV-vis studies were a confirmation of the interaction of H[COSAN] with the MNPs. Another experiment was done to check related to the time required for the extraction of the MNPs with the magnet and studying it in UV-vis. It was seen that 10 minutes was sufficient to attract all the MNPs with the magnet and further time was not required for this procedure (Figure 19).

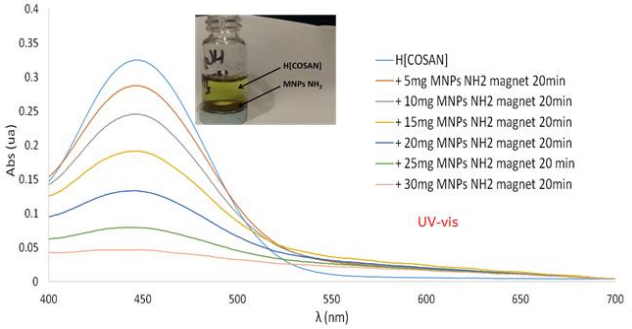

Figure 18: UV-vis of Fe_3O_4@SiO_2-NH_2 with Mcb. It confirmed interaction between the Mcb and the MNPs. The inset photo shows the liquid which was measured while the MNPs at the bottom extracted using an external magnet.

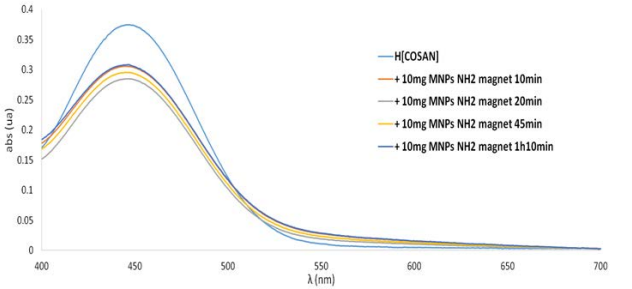

Figure 19: UV-vis with different time of extraction of the MNPs. It shows that 10 minutes is sufficient for the extraction of all the MNPs by an external magnet.

The same procedure to make Fe_3O_4@SiO_2-NH_2-Mcb is used to form the complex Fe_3O_4@SiO_2-NH_2-COOH-Mcb but in this case, the amino groups accessible at the surface of the MNPs are reduced and as a consequence the quantity retained of H[COSAN] is not enough to be measured and to be detectable in IR and EELS. Moreover, the UV-Visible measurements (see Figure 20) doesn't show any evidence that confirms the formation of the complex. However, the absorption bands of increasing amounts of MNPs are higher than free H[COSAN] because a colloid is formed and the turbidity of the solution produces an increase in the absorption.

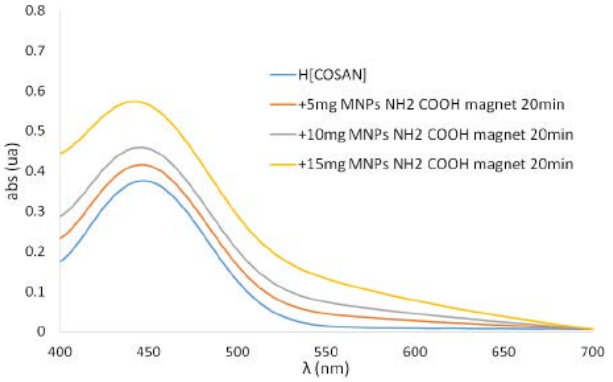

Figure 20: UV-vis of Fe_3O_4@SiO_2-NH_2-COOH with Mcb. The interaction between the MNPs and the Mcb could not be confirmed here.

Zeta-Potential Studies: Figure 21 shows the zeta potential (ζ-potential) value of Fe_3O_4@SiO_2-NH_2 MNPs: 13.7 mV, that means, the MNPs have a positive value because the amine groups are on the surface of the nanoparticles and the ζ-potential is between 10 / 30 mV, so consequently, the MNPs tend to aggregate. When the MNPs form the complex Fe_3O_4@SiO_2-NH_2-Mcb the ζ-potential becomes negative -15.2 mV (see Figure 22) and confirms that H[COSAN] is on the surface of the nanoparticles because [COSAN] is an anion. The ζ-potential is between -10 / -30 mV again indicating that the complex tends to aggregate. This clear shift in the polarity of the MNPs before and after the interaction with the Mcb confirms the presence of H[COSAN] on the surface of the MNPs.

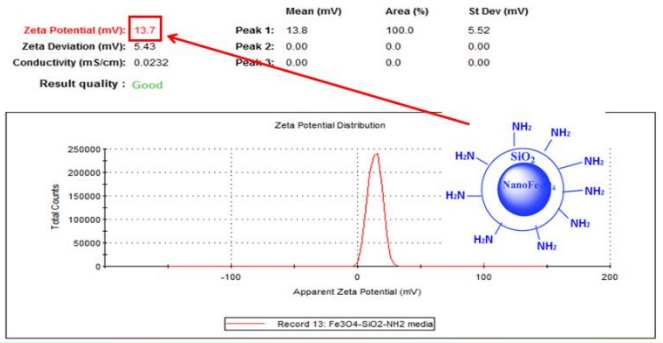

Figure 21: Zeta-potential of Fe_3O_4@SiO_2-NH_2. The zeta-potential is positive here.

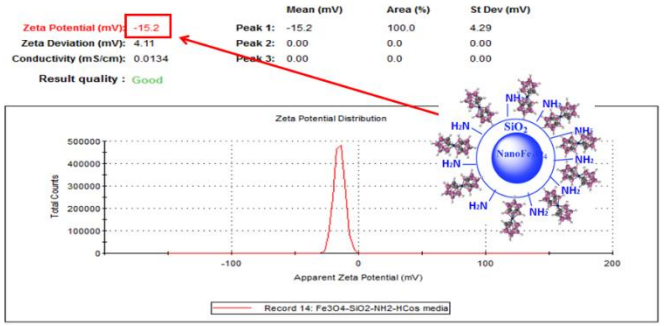

Figure 22: Zeta-potential of Fe_3O_4@SiO_2-NH_2-Mcb. The zeta-potential is negative here proving the formation of the complex.

Figure 23 shows the zeta potential of Fe_3O_4@SiO_2-NH_2-COOH: -29.4 mV, that confirms that the methodology used to decorate the MNPs with –COOH works well and the value is between -10/-30 mV that means the MNPs tend to aggregate. Figure 24 shows that the zeta potential for Fe_3O_4@SiO_2-NH_2-COOH-Mcb is -34.8 mV. The slight difference with its precursor prevents from being sure that the complex is formed; these MNPs also tend to aggregate too. The value is above 30mV because of the presence of both -COOH and the Mcb, as they are both negative ions.

		Mean (mV)	Area (%)	St Dev (mV)
Zeta Potential (mV): -29.4	Peak 1:	-29.4	100.0	4.43
Zeta Deviation (mV): 4.21	Peak 2:	0.00	0.0	0.00
Conductivity (mS/cm): 0.00990	Peak 3:	0.00	0.0	0.00

Result quality : Good

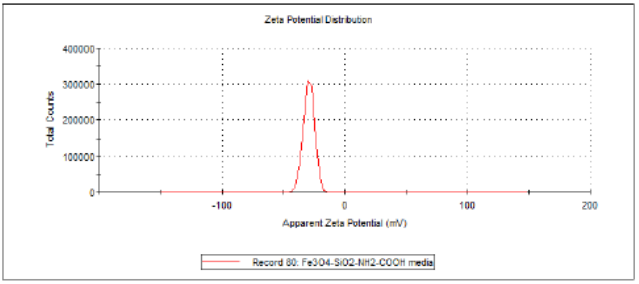

Figure 23: Zeta-potential of Fe_3O_4@SiO_2-NH_2-COOH.

		Mean (mV)	Area (%)	St Dev (mV)
Zeta Potential (mV): -34.8	Peak 1:	-34.8	100.0	4.45
Zeta Deviation (mV): 4.21	Peak 2:	0.00	0.0	0.00
Conductivity (mS/cm): 0.0204	Peak 3:	0.00	0.0	0.00

Result quality : Good

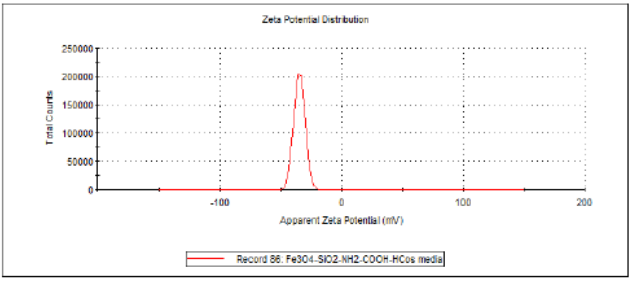

Figure 24: Zeta-potential of Fe_3O_4@SiO_2-NH_2-COOH-Mcb.

3.4. Elemental Mapping

The elemental mapping was done on the STEM image to check the distribution of the elements of Boron, Iron and Silicon. The three elements were represented in three different colours which enabled us to visualize the position of the three elements within the sample.
Figure 25 shows the mapping of Fe (red), Si (green) and B (blue) of the STEM image and we can confirm that the

majority of H[COSAN] is located in the layer that connects the MNPs and the Fe and Si are in the MNPs with a small quantity of SiO_2.

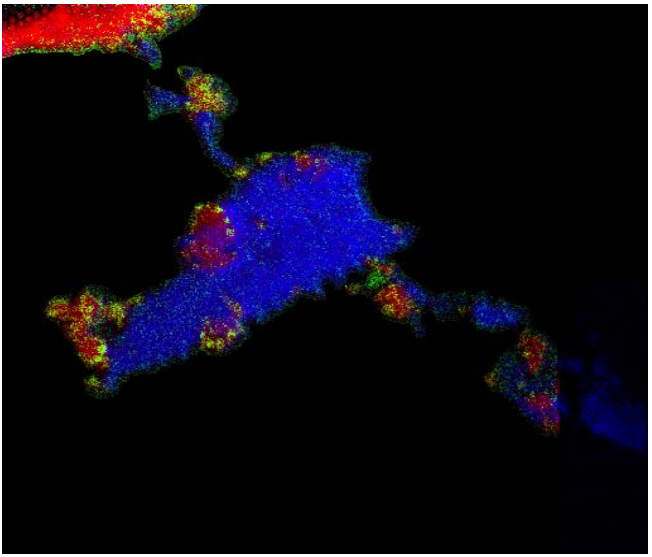

Figure 25: Elemental Mapping of Fe_3O_4@SiO_2-NH_2-Mcb. It shows **Boron-Iron-Silicon**.

3.5. Magnetic Hysteresis Study

The magnetic hysteresis study was done for all the samples at 300K temperature and not at lower temperature. The hysteresis study for MNPs with COOH was done after 1 week and after 1 month to check their magnetisation value and this showed no decrease in their magnetic properties. The samples were prepared using a polycarbonate capsule filled with 1 mg of MNPs and compacted cotton.

For the sample of MNPs with amino groups the hysteresis was studied and the magnetisation value was lower than the MNPs with COOH functionalization. Moreover, the magnetisation value reduced further upon the formation of the complex with the Mcb. This showed us that with

addition of more layers and components to the MNP core the value of magnetisation changed and reduced considerably. So, in order to obtain higher magnetisation, we need to have a larger core as it enhances the magnetisation value. Though with loading of other components there will be a reduction in the final MNP but with a larger core the reduction is mitigated. The saturated magnetisation (M_s) for Fe_3O_4@SiO_2-NH_2 is 0.0708 emu/g while for Fe_3O_4@SiO_2-COOH is 0.382 emu/g after 1 month. There is a drop of almost 5.5 times in the value for amine functionalized MNPs when compared to the COOH MNPs. But in case of the amine functionalized ones the formation of complex with Mcb is easier so we have to make a compromise in this situation.

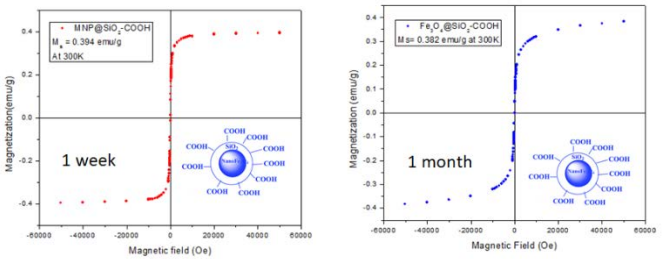

Figure 26: Magnetic Hysteresis of Fe_3O_4@SiO_2-COOH at 300K. It shows the hysteresis curves after 1 week (M_s: 0.394 emu/g) and after 1 month (M_s: 0.382 emu/g).

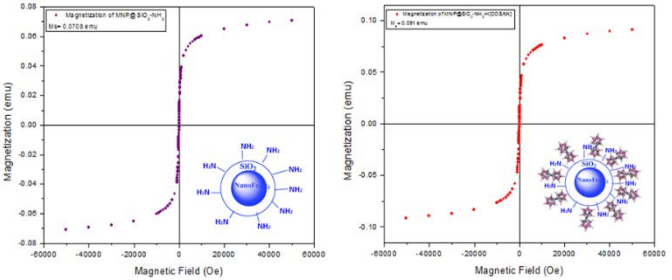

Figure 27: Magnetic Hysteresis of Fe_3O_4@SiO_2-NH_2 (Ms: 0.0708 emu/g) and Fe_3O_4@SiO_2-NH_2-Mcb (Ms: 0.09 emu/g) at 300K.

4. Synthesis of Nanocomposite

After synthesizing the MNPs and the MNP complex with the H[COSAN] we moved onto the synthesis of the nanocomposite material which includes the MWCNTs.

In this the MWCNTs formed the base, which were oxidized using the standard acid mixture of H_2SO_4 and HNO_3, to form the COOH groups on the walls of the MWCNTs. These COOH groups acted as anchors upon which the MNPs were attached by using co-precipitation method. These MNPs were then coated with silica using the Stober process. But in this case, not only the MNPs, but a layer of SiO_2 was formed on top of the CNTs too and the layer of silica covered everything. Then this nanocomposite was functionalized with amino groups as we had already seen previously with the MNPs, that only the amine functionalized could be further used to attach H[COSAN] or the Mcb. This is why only amine functionalization was done on this nanocomposite using the same method used previously for the MNPs and then H[COSAN] was used to form a complex with this nanocomposite. For the first time such a nanocomposite was made. The functionalization of the MWCNTs@Fe_3O_4@SiO_2 is not common and we not only functionalized it, we also made a complex with the H[COSAN]. The detailed synthetic route is described below.

4.1. Nanocomposite of CNT with functionalized MNPs

Oxidizing and functionalizing MWCNT: The carboxylated MWCNTs (MWCNTs–COOH) were prepared by refluxing the MWCNTs (500mg) in a mixture of concentrated sulfuric acid and nitric acid (3:1 v/v ratio) at 70°C for 6 hours. The total volume of acid used was 80ml. After 6 hours at 70°C, the mixture of acid along with the MWCNT was left for next 15 hours in the same flask at room temperature. After 15 hours at the room temperature, the mixture was filtered

using 0.2μ PTFE hydrophobic filter membrane and washed with double distilled water until the pH of the filtrate became ~7 and finally dried at 60 °C overnight.

Synthesis of Fe_3O_4 nanoparticles onto the MWCNT walls: About 100 mg of MWCNTs–COOH was dissolved in 70 mL of water by ultrasonic irradiation for 20 min. The mixture was further stirred vigorously magnetically for 30 min at 60°C. Then 177 mg of $FeCl_3 \cdot 6H_2O$ was added under stirring. After the mixture was stirred vigorously for 30 min under N_2 atmosphere, 95 mg of $FeSO_4 \cdot 7H_2O$ was added and keeping it stirred under N_2 atmosphere for 30 min. At last 30 mL of 6% NH_4OH aqueous solution was added into the mixture drop by drop at 60°C during 1h and reacted for another 2h. N_2 atmosphere was used during the reaction to prevent critical oxidation. The reaction mixture was then centrifuged, washed with double distilled water and dried. The obtained black precipitate was Fe_3O_4/MWCNT nanoparticles and was ready for use.[1]

Coating of the Fe_3O_4 nanoparticles attached to MWCNT with SiO_2: Core–shell Fe_3O_4@SiO_2/MWCNT nanocomposites were prepared by growing silica layers onto the surface of the Fe_3O_4/MWCNTs. 50 mL of ethanol, 2 mL water, 1.7 mL NH_4OH and 300 μL of TEOS were added in a 100 mL beaker in a 40°C water bath. Fe_3O_4/MWCNTs (100mg) were added to the above solution under mechanical stirring. The solution was stirred for 12 hours and then extracted with external magnet and washed with double distilled water and vacuum-dried at 60°C over-night.[2]

Preparation of amine supported on Fe_3O_4@SiO_2 nanoparticles [Fe_3O_4@SiO_2-NH_2] on MWCNT: A mixture of MWCNT@Fe_3O_4@SiO_2 (200mg) was dispersed in ethanol (45mL). Then 5ml of 3-(2-aminoethylamino) propylmethyl dimethoxy silane (APMS) was dissolved in 20ml of ethanol and added to the suspension of MWCNT@Fe_3O_4@SiO_2 in ethanol. The pH value of the reaction mixture was set to 11 using Tetramethyl ammonium hydroxide (TMAH). The

reaction mixture was then heated to 50°C and stirred for 5 hours. After ageing overnight, the suspension of functionalized nanocomposite was completely stable. Then the nanocomposite was thoroughly washed with distilled water using magnetic separation.[3]

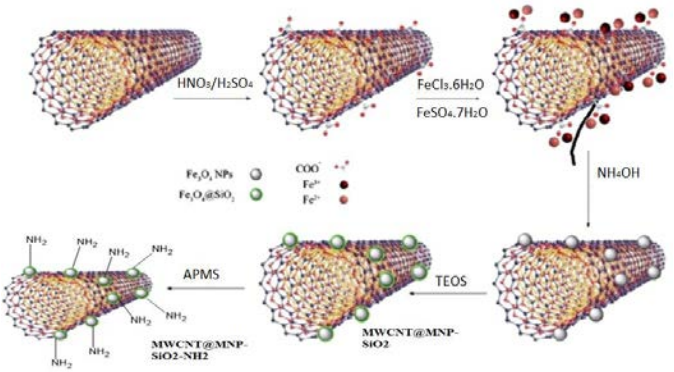

Figure 28: Synthesis of MWCNT@Fe_3O_4@SiO_2-NH_2 Nanocomposite.

4.2. H[COSAN] attached Nanocomposite

The H[COSAN] was attached the same way it had been done for the MNPs to form the complex.

Preparation of MWCNT@Fe_3O_4@SiO_2-NH_2 with Metallacarborane [MWCNT@Fe_3O_4@SiO_2-NH_2-Mcb]: 50 mg of MWCNTs@Fe_3O_4@SiO_2-NH_2 was suspended in 10 mL of water and with 5mM of H[Co($C_2B_9H_{11}$)$_2$]. The mixture was sonicated for 15 min and cleaned 10 times with distilled water using magnetic separation. Finally, the sample was dried under vacuum at 80°C.

The pictographic representation of this process is shown here which shows that the yellow solution of H[COSAN] turns colourless once all the H[COSAN] forms the complex with amine functionality on the nanocomposite.

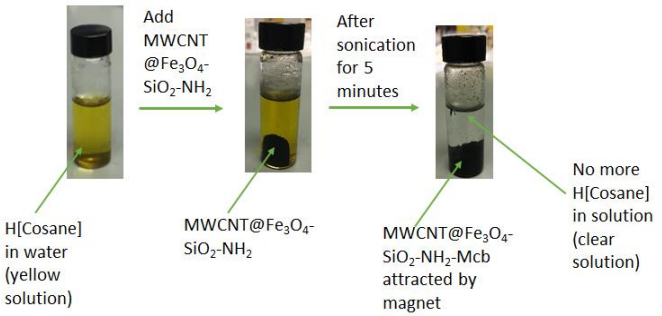

Figure 29: Synthesis of MWCNT@Fe_3O_4@SiO_2-NH_2-Mcb Nanocomposite.

5. Characterizations

The nanocomposite was similarly characterized like the MNPs and the presence of the Mcb was confirmed by various techniques. The results of the characterizations are as follows.

5.1. TEM, STEM and SEM studies

TEM and HRTEM studies: There were two samples of MWCNT@Fe_3O_4 prepared. This one below is of the sample in which the CNT has been oxidized only for 6 hours using the acid mixture procedure. In this case the carboxylated MWCNTs (MWCNTs–COOH) were prepared by refluxing the MWCNTs (500mg) in a mixture of concentrated sulfuric acid and nitric acid (3:1 v/v ratio) at 70°C for 4 hours. The total volume of acid used was 80ml. After 4 hours at 70°C, the mixture of acid along with the MWCNT was left for next 2 hours in the same flask at room temperature. After 2 hours at room temperature, the mixture was filtered using 0.2µm PTFE hydrophobic filter membrane and washed with double distilled water until the pH of the filtrate became ~7 and finally dried at 60 °C overnight. This was done and then further the Fe_3O_4 nanoparticles were attached onto the walls of the MWCNT as stated in the synthetic procedure

before. But we found during the TEM analysis that very few nanoparticles were attached to the MWCNTs. This is probably because of the partial oxidation of the CNTs occurring. This produced less COO^- groups to attach the Fe_3O_4 nanoparticles further onto the walls of the CNTs. So, we increased the time for oxidation procedure to 21 hours and got better results regarding the attachment of the MNPs. Once we saw that the MNPs were more readily attached to the CNT which had undergone 21 hours of acid treatment, we further proceeded with that sample to coat the MNPs with silica and amine functional groups.

The silica coated nanocomposites were studied in HRTEM as it showed a thick coating of SiO_2 on top of both the MWCNTs and the MNPs attached to the MWCNTs, so a better resolution was needed to visualize them. HRTEM was also used for Mcb loaded nanocomposite.

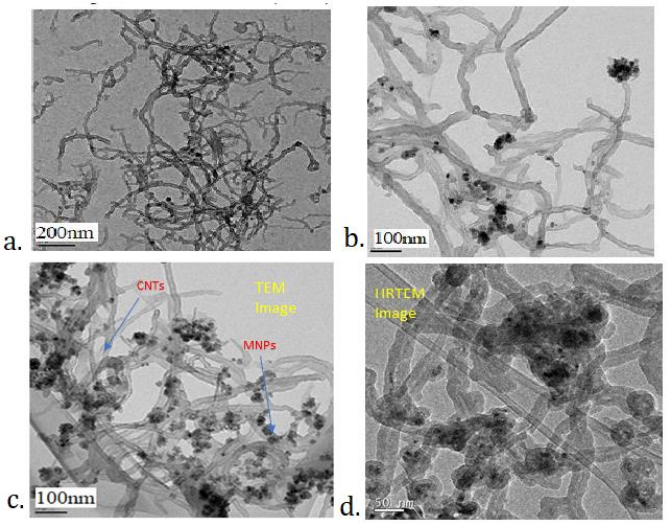

Figure 30: TEM images of (a) naked MWCNT, (b) MWCNT@Fe_3O_4 after 6 hours of oxidation, (c) MWCNT@Fe_3O_4 after 21 hours of oxidation and (d) HRTEM of MWCNT@Fe_3O_4@SiO_2-NH_2.

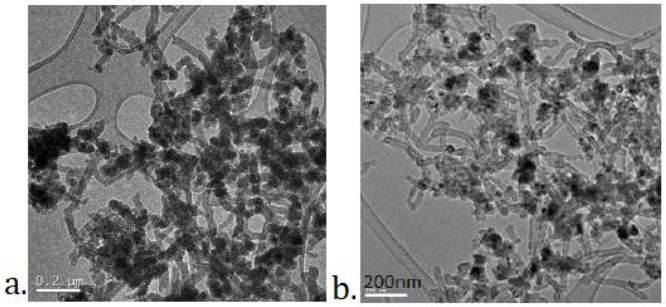

Figure 31: HRTEM images of (a) MWCNT@Fe_3O_4@SiO_2-NH_2-Mcb at 0.2µm and (b) MWCNT@Fe_3O_4@SiO_2-NH_2-Mcb at 200nm.

SEM and HRSEM studies: SEM and HRSEM were done for the nanocomposites without Mcb and with Mcb respectively. The SEM/HRSEM studies showed a 3D view of the nanocomposite. It showed the tubular structures of the MWCNTs and aggregated spherical structures of the MNPs. The Mcb was not clearly visible though in the SEM or HRSEM, but the formation of nanocomposite was clearly observed.

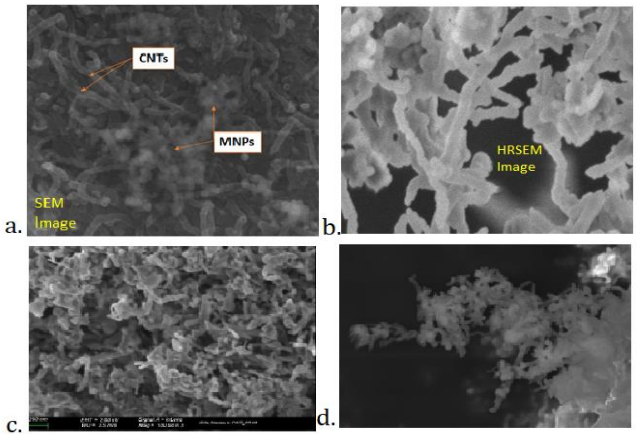

Figure 32: SEM images of (a) MWCNT@Fe_3O_4@SiO_2-NH_2, (b) HRSEM of MWCNT@Fe_3O_4@SiO_2-NH_2, (c) HRSEM of MWCNT@Fe_3O_4@SiO_2-NH_2-Mcb and (d) SEM of MWCNT@Fe_3O_4@SiO_2-NH_2-Mcb.

STEM Studies: The STEM studies were done in order to visualize the Mcb in the nanocomposite as STEM allows to capture the bright field and dark field images. The contrast helps in separating the MWCNTs from the MNPs and the Mcb from the other two. In this case the STEM studies were done not only in an HRTEM machine but also in an Extreme high-resolution scanning electron microscopy (XHRSEM) with high angle annular dark field STEM images for the nanocomposite. In these images we could visualize the Mcb clearly which we could not observe in the HRTEM or HRSEM.

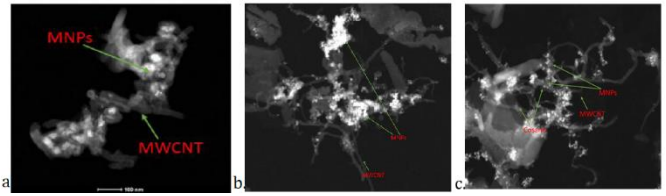

Figure 33: STEM images of (a) MWCNT@Fe_3O_4@SiO_2-NH_2-Mcb from HRTEM, (b)MWCNT@Fe_3O_4@SiO_2-NH_2-Mcb from HRTEM and (c) MWCNT@Fe_3O_4@SiO_2-NH_2-Mcb from the HAADF-STEM of XHRSEM. The HAADF-STEM of XHRSEM gives a clearer visual of the cosane than the STEM of HRTEM.

5.2. Chemical Composition Studies

The chemical composition of the nanocomposites was studied with EDX, Electron diffraction and EELS.

EDX Studies: 3 EDX studies were done. The MWCNT@Fe_3O_4@SiO_2-NH_2 was studied in both HRSEM with EDX and HRTEM with EDX, while MWCNT@Fe_3O_4@SiO_2-NH_2-Mcb was done in HRTEM too.

The EDX for the MWCNT@Fe_3O_4@SiO_2-NH_2 in both HRSEM and HRTEM show the presence of Iron and silicon as seen in Figures 34 a and b.

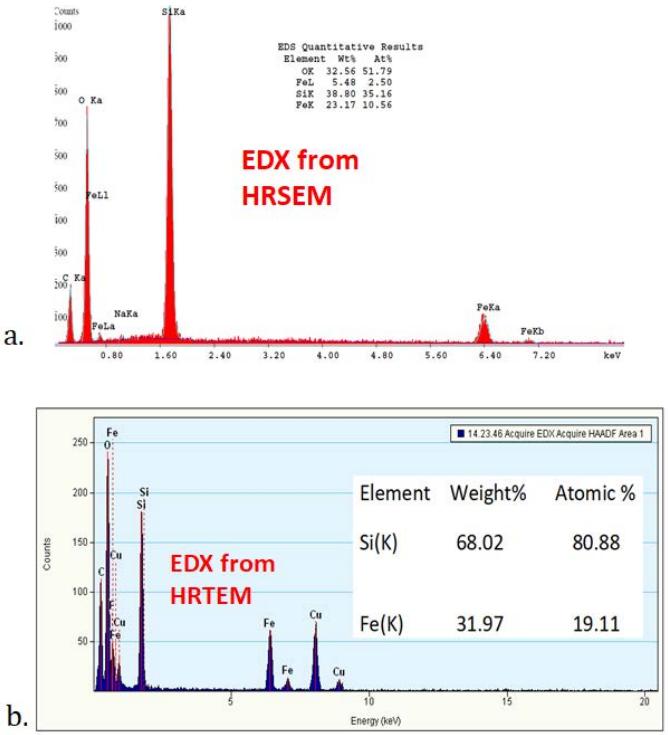

Figure 34: EDX spectra of (a) MWCNT@Fe_3O_4@SiO_2-NH_2 from HRSEM, and (b)MWCNT@Fe_3O_4@SiO_2-NH_2 from HRTEM. The presence of Iron and Silicon is observed.

The EDX for the MWCNT@Fe_3O_4@SiO_2-NH_2-Mcb was done in HRTEM. It is difficult to observe Boron in EDX as is explained before for the complex formed with MNPs. Still the EDX was done here in an attempt to observe the cobalt present in the Mcb. Due to the longer dimension of the MWCNTs, the amount of H[COSAN] present would be more than the amount of H[COSAN] present for the MNPs, so it would be possible to obtain even a minor peak of Co and it would confirm the formation of the complex on the nanocomposite of MWCNTs and the MNPs supported on it.

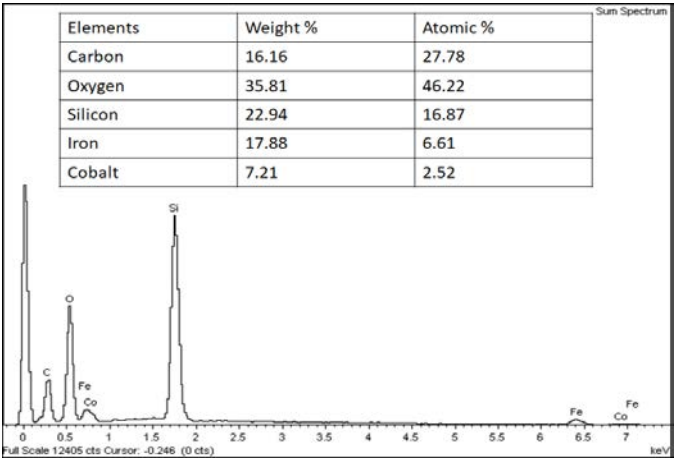

Elements	Weight %	Atomic %
Carbon	16.16	27.78
Oxygen	35.81	46.22
Silicon	22.94	16.87
Iron	17.88	6.61
Cobalt	7.21	2.52

Figure 35: EDX spectra of MWCNT@Fe_3O_4@SiO_2-NH_2-Mcb from HRTEM. The presence of Cobalt of Mcb was detected which confirmed the presence of H[COSAN] in the nanocomposite.

Electron Diffraction Studies: The selected area diffraction pattern was done on the nanocomposite MWCNT@Fe_3O_4@SiO_2-NH_2 and MWCNT@Fe_3O_4@SiO_2-NH_2-Mcb. The diffraction pattern of the latter was more crystalline compared to the former, because of the presence of the Mcb. Due to its presence, the sample was more conductive.

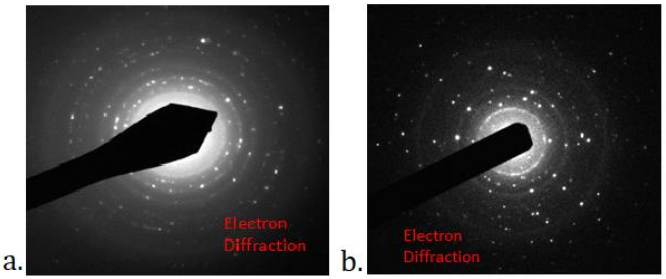

Figure 36: Electron diffraction pattern of (a) MWCNT@Fe_3O_4@SiO_2-NH_2 from HRTEM and (b) MWCNT@Fe_3O_4@SiO_2-NH_2-Mcb. The second one is more crystalline as the sample is more conductive due to the presence of Mcb.

EELS Spectroscopy: In order to check the presence of Boron we used the Electron Energy Loss Spectroscopy (EELS). This shows clearly the Boron peak in the samples, thus confirming the presence of Boron and also that the nanocomposite synthesized contains the Mcb. The EELS spectrum showed the boron peak quite prominently and also the carbon peak in the sample was quite prominent. The carbon peak was prominent in the nanocomposite due to the MWCNTs being present in them.

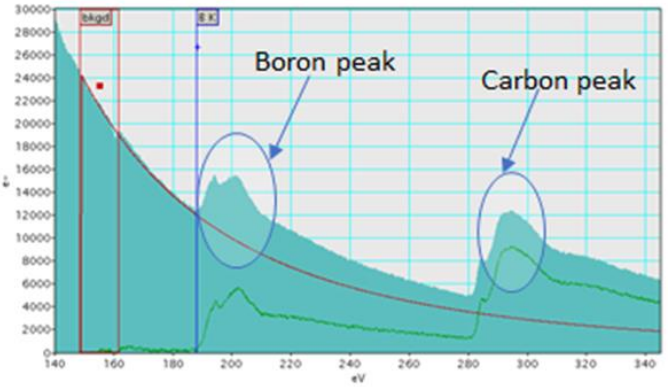

Figure 37: EELS spectrum of MWCNT@Fe_3O_4@SiO_2-NH_2-Mcb from HRTEM. The presence of Boron of Mcb was detected which confirmed the presence of H[COSAN] in the nanocomposite and also carbon peak was observed too from the MWCNTs.

5.3. UV-vis Studies and Zeta Potential

UV-vis Studies: The UV-vis studies were done to see how the absorbance of naked H[COSAN] changes with the addition of the MWCNT@Fe_3O_4-SiO_2-NH_2. The H[COSAN] normally shows an absorbance at 446nm and forms a yellow colour solution in water. So, 1mM solution of H[COSAN] was made in 5mL of water and the UV-vis was measured and it showed an absorbance around 446nm. Then, 2mg of MWCNT@Fe_3O_4-SiO_2-NH_2 was added to the solution of H[COSAN] and the solution was sonicated for 5 minutes.

Then, the nanocomposites were attracted by the magnet for around 10 minutes and the remaining solution was used to take the UV-vis measurement. It showed a considerable decrease in the intensity of absorbance. Then, the same thing was done again, more 2mg of MWCNT@Fe_3O_4-SiO_2-NH_2 was added and sonicated for 5 minutes. Then magnetic extraction was performed and the remaining solution was measured and it showed almost negligible absorbance in the UV-vis. After the addition of 6mg of MWCNT@Fe_3O_4-SiO_2-NH_2 there was no H[COSAN] remaining in the solution and the solution had turned clear.

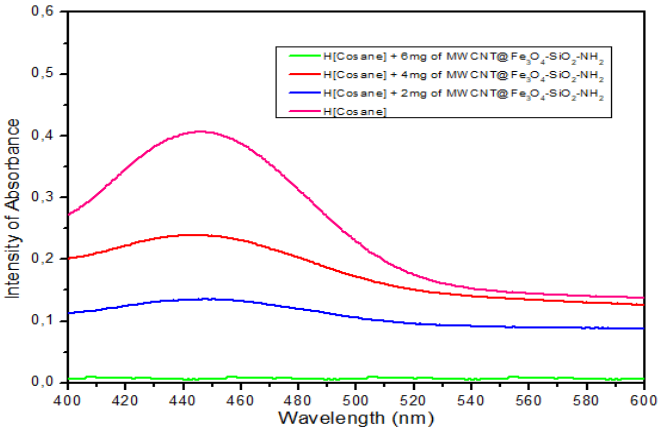

Figure 38: UV-vis spectrum of Mcb upon addition of MWCNT@Fe_3O_4@SiO_2-NH_2. The intensity of absorbance of Mcb reduces with increasing amounts of MWCNT@Fe_3O_4@SiO_2-NH_2 confirming an interaction between them.

There was another set of experiments done with the UV-vis in which different amounts of time was used to extract the MWCNT@Fe_3O_4-SiO_2-NH_2-Mcb. It was seen that 8 minutes was sufficient to extract all the MWCNT@Fe_3O_4-SiO_2-NH_2-Mcb. The solution of H[Cosane] prepared was the same as the previous study with UV-vis and the amount of MWCNT@Fe_3O_4-SiO_2-NH_2 added was 5mg. 5mg was used as the quantity because we earlier saw that with 6 mg of

MWCNT@Fe_3O_4-SiO_2-NH_2, almost no absorbance was seen, so with 5 mg we could see a similar thing here. Keeping the quantity constant, the extraction was done for 2 minutes, then 4, 6 and 8 minutes. By 8 minutes we could extract almost all of the nanocomposite and get no absorbance from the remaining solution.

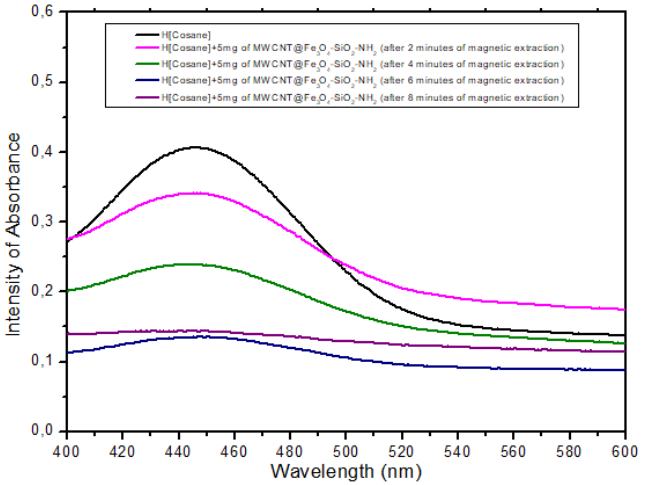

Figure 39: UV-vis spectrum of Mcb upon addition of MWCNT@Fe_3O_4@SiO_2-NH_2 with different times of magnetic extraction.

Zeta-Potential Studies: The zeta potential was measured for the nanocomposite of MWCNT@Fe_3O_4-SiO_2-NH_2-Mcb and the MWCNT@Fe_3O_4-SiO_2-NH_2. The one without the Mcb has a positive zeta potential due to the presence of the NH_2 groups at the surface while on attaching the Mcb the polarity changes swiftly to negative potential due to the Mcb being present on the surfaces. The change in polarity gives conclusive proof of the presence of Mcb in the nanocomposite and its attachment to the MWCNT@Fe_3O_4-SiO_2-NH_2. The zeta potential values lie between 0 to 30mV, thus making the suspension not very stable. The particles have the tendency to aggregate and precipitate after some time.

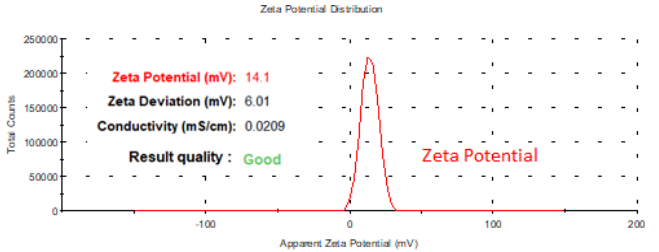

Figure 40: Zeta Potential of MWCNT@Fe_3O_4-SiO_2-NH_2. The value is +14.1mV

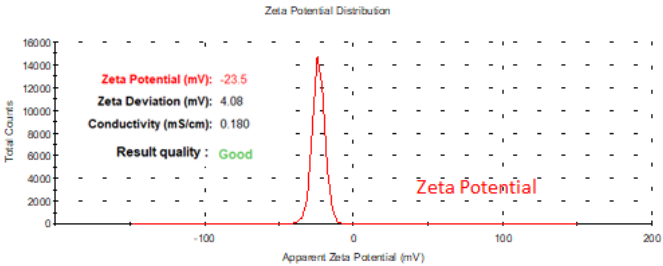

Figure 41: Zeta Potential of MWCNT@Fe_3O_4-SiO_2-NH_2-Mcb. The value is -23.5mV

5.4. Elemental mapping

Elemental mapping in HRTEM: The elemental colour mapping was done. The mapping shows the different elements in different colours spread across the sample. The mapping was done in order to see the distribution of boron, iron, carbon and silicon. In the mapping the Boron in red is very clearly visible and the MNPs in green colour. The silicon is visible all throughout the sample as it has coated everything from the MNPs to the MWCNTs and it is visible in blue all through-out the sample. The carbon is visible in the bottom left in green, the background showing green colour is coming from the sample holder and the highlighted greenish regions showing the MWCNTs.

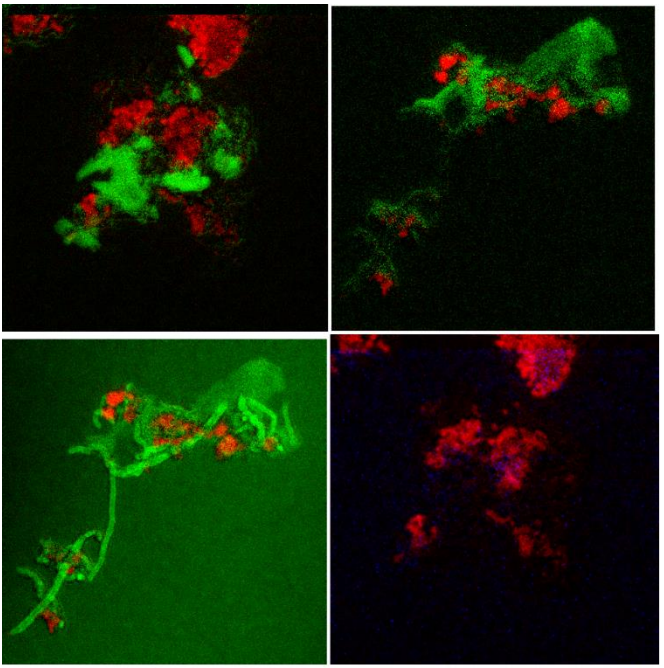

Figure 42: Elemental mapping of MWCNT@Fe_3O_4-SiO_2-NH_2-Mcb. The top images show Iron (green) and Boron (red). The bottom left image shows Carbon (green) and Iron (red) and the bottom right image shows Iron (red) and Silicon (Blue).

Elemental mapping in XHRSEM: The colour mapping was done in an XHRSEM machine. In higher resolution the SEM micrograph images were taken and mapped by different colours to show the presence of three different elements. It shows the presence of carbon, iron and the oxygen. The distribution is given in different colours. It is Iron in yellow, Oxygen in green and Carbon in red. It is difficult to detect Boron with SEM elemental map. Boron can only be mapped if it is present in great excess throughout the sample. Silicon is not mapped in these SEM elemental mapping because the silicon is present in the detector and that is why the mapping is not correct for Silicon in these maps.

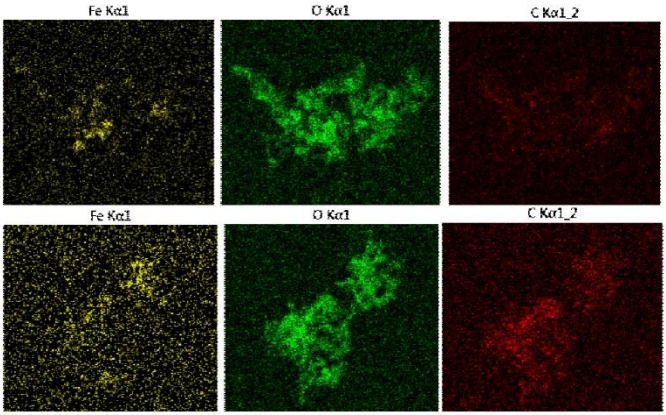

Figure 43: Elemental Colour Mapping of MWCNT@Fe_3O_4-SiO_2-NH_2-Mcb with Iron (yellow), Oxygen (green) and Carbon (red).

5.5. Magnetic Hysteresis Study

Magnetic Hysteresis: The hysteresis loop was studied on a Superconducting quantum interference device (SQUID) at room temperature (300K). It shows the superparamagnetic property of the MWCNT@Fe_3O_4-SiO_2 nanocomposite prepared. The saturated magnetisation is of around 0.03 emu/g while the saturated magnetisation is around 0.06 emu/g for MWCNT@Fe_3O_4-SiO_2-NH_2. It is higher than the magnetisation achieved with only silica coated MNPs attached to the walls of MWCNT.

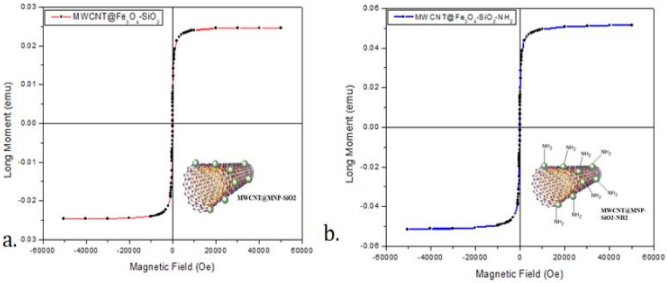

Figure 44: Magnetic Hysteresis of (a) MWCNT@Fe_3O_4-SiO_2 (M_s: 0.03 emu/g) and (b) MWCNT@Fe_3O_4-SiO_2-NH_2 (M_s: 0.06 emu/g).

There is a slight reduction in the magnetization value further though when the Mcb is attached to the nanocomposite. The one with Mcb has 0.024 emu/g compared to the 0.06 emu/g of MWCNT@Fe_3O_4-SiO_2-NH_2. All the samples preserved their superparamagnetic properties.

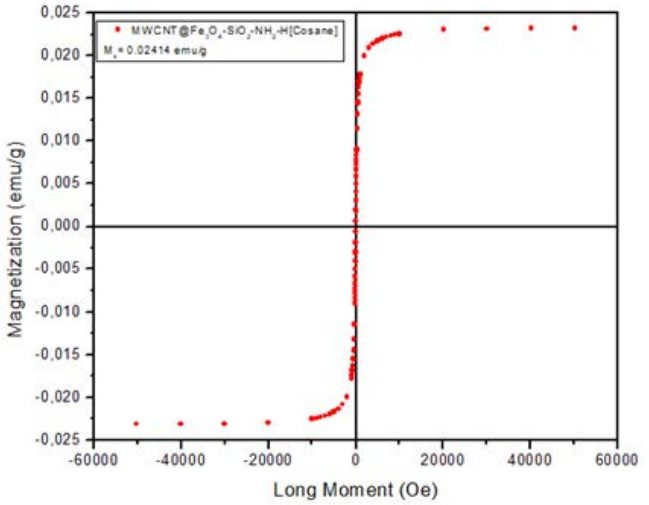

Figure 45: Magnetic Hysteresis of MWCNT@Fe_3O_4-SiO_2-NH_2-Mcb (M_S: 0.024 emu/g).

6. Colloidal Stability

The colloidal stability is a big issue with the MNPs or magnetic nanocomposites. Since their advent there remains a big issue surrounding the stability of the MNPs in colloids. The more stable they are in a colloidal state, the less easy it is to use them for magnetic separation. While on the other hand if they are less stable then they are easier to isolate by external magnetic field application. So, for this a compromise has to be made regarding them and based on their application they are synthesized as needed. In order to

improve magnetisation, larger particles can be synthesized as we have discussed in this chapter. These show higher magnetisation but much less stability in colloidal state as due to their large sizes they have a greater tendency to aggregate.

3 reasons why the MNPs are more prone to aggregation are listed below:

- Compared to other nanoparticles, agglomeration is even more significant for MNPs as there exist magnetic dipole-dipole attraction among themselves (Golas et al. 2010).
- In particular, the magnitude of this magnetic dipole-dipole attraction is directly proportional to power 2 of the particle saturation magnetization and power 3 of the particle size.
- Sedimentation of the agglomerates from its suspension is a challenge (Yu and Xie 2012) which could limit mobility and applicability of MNPs (Matlochová et al. 2013).

In order to improve stability and also preserve the magnetic properties few things can be done which are listed below:

- Sonication: this is a mechanical way and very effective in disaggregating the particles and dispersing them in colloidal state.
- One of the other methods is using inorganic shell coating like Silica or carbon coating to improve the stability.
- Also, surface coating with macromolecules like polymers or surfactants can be used for improving stability.
- Increasing viscosity of the medium can also prevent aggregation as the particles cannot get dispersed easily and travel through the viscous medium thus preventing aggregation. This can be done by gum gelation or by emulsion formation.

We have already tried sonication for their stability improvement. The MNPs and nanocomposites synthesized in these have already been sonicated to improve their stability but it does not make the MNPs last in suspended state for more than a few hours. We have also coated them with silica and H[COSAN] to increase their stability in suspension. They have improved their stability but does not make them stable enough for applications in long term purposes. These MNPs and nanocomposites that we made can be used for faster applications which can be done within a few hours. So, in order to further work on this, we tried 5 different surfactants.

6.1. Stability with different Surfactants

The 5 different surfactants were used for this purpose. They are:

- Citric Acid
- Tricaprylylmethyl ammonium chloride
- Cetyl trimethyl ammonium chloride (CTAC)
- Tetrabutyl ammonium chloride
- Dimethyl di-octadecyl ammonium chloride

Out of these 5 the last one was successful in providing long term stability. This was so because, it increased the viscosity of the medium and hence stopped the MNPs from aggregating. But this came with a major drawback, that these MNPs were harder to extract using an external magnet. Different concentrations of the surfactant were studied but the trend was same, the more stable they became the harder it was to extract them. The zeta-potential values obtained for each surfactant is given in the table and also the different zeta-potential obtained for different concentrations of dimethyl di-n-octadecyl ammonium chloride.

Surfactant	Zeta-Potential
Citric acid	15.6mV
Tricaprylyl methyl ammonium chloride	26.8mV
CTAC	22.6mV
Tetrabutyl ammonium chloride	36.9mV
Dimethyl di-n-octadecyl ammonium chloride	54.2mV

Table 1: Stability of Fe_3O_4@SiO_2-NH_2 with different surfactants.

The stability was checked for amine functionalized MNPs as they gave the best results with H[COSAN] so we wanted to stabilize them for further use.

MNPs (wt)	Dimethyl di-n-octadecyl ammonium chloride (wt)	Zeta-Potential
5mg/10mL	2.5mg	15.4mV
5mg/10mL	5mg	18.9mV
5mg/10mL	10mg	28.4mV
5mg/10mL	15mg	30.2mV
5mg/10mL	20mg	38.7mV
5mg/10mL	25mg	44.65mV
5mg/10mL	30mg	50.2mV

Table 2: Stability of Fe_3O_4@SiO_2-NH_2 with different amounts of dimethyl di-n-octadecyl ammonium chloride.

Till 15 mg of the surfactant the dispersion was stable and with lots of time small amount of MNPs could be extracted by the magnet. But to obtain them completely dry and free of the surfactant is difficult as it makes the suspension extremely viscous.

More work needs to be done in improving the stability of these magnetic nanoparticles and nanocomposites to be utilised in all sorts of applications and not just of one kind.

7. Conclusions

We have successfully synthesized magnetic nanoparticles (MNPs) and magnetic nanocomposites (MNCs) using colloidal chemistry. These nanoparticles have been functionalized with both NH_2 groups and COOH groups. They have been used to form a non-bonded complex for the first time with H[COSAN] and thoroughly characterized. Also, for the first time functionalized magnetic nanocomposites have been formed and also, they have been used to form complexes with the H[COSAN] and tested. The synthetic procedure uses mechanical stirring for the MNPs to be coated with SiO_2 layer. This is important for the reaction as magnetic stirring will hinder the MNPs from being stirred in the reaction mixture as all the MNPs get attached to the stirring bead. Hence for the inorganic shell coating it is imperative to use a mechanical stirrer.

Their attachment to the H[COSAN] was done in order to use the MNPs and the MNCs for sensing applications. This is because the H[COSAN] is a redox specie and has a tuneable HOMO-LUMO which enhances the possibility of using it in sensing applications. Attempts have been made to improve the colloidal stability of these MNPs and nanocomposites using various methods like surface coating with inorganic materials or surfactants, increasing viscosity or by sonication. Moreover, the presence of H[COSAN] opens up avenues for these MNPs or nanocomposites to be utilised in catalytic or other applications in the future. Also, the functionalization with COOH and NH_2 has been done on these MNPs and magnetic nanocomposites because they can be used to be attached to antibodies in the future and help in detection of varied antigens. All this work has been done as part of a European Project KARDIATOOL for designing a new Point of Care Device (POC) for heart failure patients.

8. References

[1] H. Hassani, B. Zakerinasab, M.A. Nasseri, M. Shavakandi, *RSC Adv*. **2016**, *6*, 17560-17566.

[2] M. Arvand and M. Hassannezhad, *Materials Science and Engineering C,* **2014**, *36***,** 160-167.

[3] Z. Lu, J. Dai, X. Song, G. Wang, W. Yang, *Colloids Surf. A*, **2008**, *317***,** 450-456.

[4] M. A. Agotegaray, V. L. Lassalle, *Silica-coated magnetic nanoparticles*, Springer Publications, 1st edition, Cham, Switzerland, **2017.**

[5] M. Varna, P. Ratajczak, I. Ferreira, et al. *J. of Biomat. & Nanobiotech.,* **2012**,*03*, 269.

[6] M. Li, K. T. Al-Jamal, K. Kostarelos, et al. *ACS Nano,* **2010**, *4*, 6303–6317.

[7] S. Chono, T. Tanino, T. Seki, K. Morimoto, *J. of Pharmacy and Pharmacology,* **2007**,*59*,75–80.

[8] C.T. Yavuz, A. Prakash, J. T. Mayo, V. L. Colvin, *Chem Eng. Sci,* **2009**, *64*, 2510–2521.

[9] J. Gómez-Pastora, E. Bringas, I. Ortiz, *Chem Eng J.,* **2014**, *256*,187–204.

[10] W. Liu, S. Tian, X. Zhao, W. Xie et al. *Curr. Pollut. Rep.* 2015, *1*, 280–291.

[11] L. Mohammed, H. G. Gomaa, D. Ragab, J. Zhu, *Particuology.,* **2017**, *30*, 1–14.

[12] Q. H. Ng, J. K. Lim, A. L. Ahmad, et al., *J Membr Sci.,* **2015**, *493*, 134–146.

[13] B. P. Dash, R. Satapathy, B. R. Swain, et. al., *J. Org. Chem.,* **2017**, *849,* 170-194.

[14] M.F. Hawthorne, D.C. Young, P.A. Wegner, *J. Am. Chem. Soc.*, **1965,** *87*, 7035.

[15] C. Masalles, S. Borros, C. Vinas, F. Teixidor, *Adv. Mater*, **2002**, *14*, 449.

[16] A.I. Stoica, C. Viñas and F. Teixidor, *Chem. Commun*., **2008**, *48*, 6492-6494.

[17] A.I. Stoica, C. Viñas and F. Teixidor, *Chem. Commun*., **2009**, *33*, 4988-4990.

[18] A. Saini, J. Gallardo, A. Baraket, et. al., *Sensors and Actuators B: Chemical,* **2018**, *268,* 164-169.

[19] S. Iijima, *Nature*, **1991,** *354*, 56-58.

[20] R.N. Goyal, V.K. Gupta, S. Chatterjee, *Talanta*, **2008,** *76*, 663-669.

[21] M. Arvand, T.M. Gholizadeh, *Colloids Surf., B*, **2013,** *103*, 84-93

[22]T. Hayashi, S. Hirono, M. Tomita, S. Umemura, *Nature*, **1996,** *381*, 772-774.

[23] J. Wan, W. Cai, J. Feng, X. Meng, E. Liu, *J. Mater. Chem*., **2007**, *17*, 1188-1192.

[24]Z.F. Deng, E. Yenilmez, J. Leu, J.E. Hoffman, E.W.J. Straver, H.J. Dai, K.A. Moler, *Appl. Phys. Lett*., **2004,** *85*,6263-6265

[25] J. Wu, L. Kong, *Appl. Phys. Lett*., **2004,** *84*, 4956-4958.

Conclusions

The major conclusions of this thesis are listed here. It gives individual conclusions for the studies done in each chapter and also a general conclusion at the end.

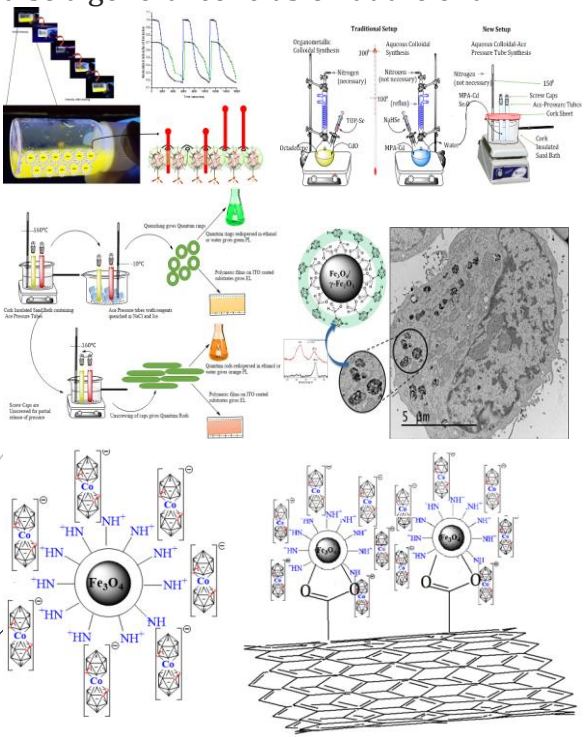

Arpita Saha
ICMAB-CSIC (UAB)

The results in this thesis has been divided into two main parts. The first part of results and discussions deals with the quantum nanocrystals and the second part with magnetic nanoparticles and magnetic nanocomposites. The first part consists of three chapters dealing with the aqueous quantum nanocrystals and their composite, the second part consists of two chapters dealing with the magnetic nanoparticles and their composites. The conclusions for the individual chapters are listed below followed by the general conclusion of the thesis.

- The first chapter deals with aqueous quantum dots being capped with *meta*-carboranyl phosphinate. The major conclusions of this chapter are:
  - ✓ It was demonstrated for the first time the ability of spherical carboranyl ligands to be appended to quantum dots. The use of spherical ligands to quantum dots is rare and has hardly ever been done before.
  - ✓ This kind of capping of a spherical core with a spherical ligand has helped us to obtain a new architecture for quantum dots named core-canopy quantum dots by us.
  - ✓ The architecture has helped us to obtain a never before luminescence phenomenon which we named as kinetic fluorescence switching (KFS). It was observed that these quantum dots showed intense luminescence, then faded and upon application of kinetic energy, showed the original intensity of luminescence again.
  - ✓ This unique luminescence phenomenon has been demonstrated as a synergy between the spherical capping ligand and the surfactants which has been used.
  - ✓ Studies have been done regarding the different surfactants and the need to use the one which is

tricaprylyl methyl ammonium chloride has been explained.

- ✓ A hypothesis has been given forward with respect to the architecture, for the reason to obtain such a luminescence phenomenon.
- ✓ The capping of the spherical core with a spherical ligand has been compared to the capping of the spherical core with long carbon chain ligands and their luminescence properties.
- ✓ Further comparison with 2D Phenyl phosphinate ligand has also been done and the necessity of 3D spherical ligands has been demonstrated.

The second chapter deals with aqueous quantum dots being synthesized using a new set up. The major conclusions are:

- ✓ A new set up has been designed using ace pressure tubes and a cork insulated bath to obtain quantum dots in water with intense luminescence properties.
- ✓ We have demonstrated a method which combines the advantages of the cheap and easy synthetic route of the aqueous synthesis and the high luminescence intensity and quantum yield obtained by the quantum dots produced in hot-injection synthesis.
- ✓ The quantum dots have been compared with the traditionally synthesized quantum dots in water and their luminescence properties have been compared.
- ✓ Time dependant luminescence colour and sizes were obtained as is common for organometallic synthesized quantum dots, but this was shown here by us in an aqueous synthesis using the new set up.

The third chapter deals with quantum nanocrystals in aqueous medium. The major conclusions are:

- ✓ The new set up was used along with a new composition of Cd:Se which is thrice the traditional composition to obtain for the first time quantum rods and quantum rings in an aqueous synthesis.

- ✓ The synthesis of these quantum nanocrystals has never been reported before in an aqueous medium, and they have been synthesized and characterized by us for the first time using common reagents.
- ✓ These quantum nanocrystals can be stored in powdered form, suspended form in different solvents for more than 18 months without degradation in colloidal stability or luminescence property.
- ✓ They showed intense luminescence compared to the traditional quantum dots in water.
- ✓ These quantum nanocrystals were used to form films using polymers like PVA and PDMS. These films or nanocomposites showed good luminescence properties and could retain their luminescence for more than a year.
- ✓ These composites were also tested for electroluminescence and showed considerable luminescence on electrical stimulation, thus making them good candidates for QLED applications

The fourth chapter deals with magnetic nanoparticles coated with *meta*-carboranyl phosphinate. The major conclusions are:

- ✓ MNPs coated with m-carboranylphosphinate was successfully synthesized and characterized.
- ✓ Our newly synthesized boron nanohybrids 1-MNPs showed colloidal stability in different culture media and at temperatures (room temperature and 37°C) and a nanometric size, supporting their use in biological studies.
- ✓ The study shows that the newly synthesized nanohybrid 1-MNPs could be used to target cancer cells for tumour imaging and treatment with BNCT therapy.
- ✓ Specifically, the 1-MNPs compound is taken up from culture media by glioblastoma multiform cell line A172 in a higher amount than in the

endothelial cells with cell-tracking properties due to the magnetic core of 1-MNPs by showing a reduced signal on T2 weighted Magnetic Resonance Imaging (MRI).

- ✓ Moreover, BNCT was performed on A172 cells treated with 1-MNPs, demonstrating the eligibility of 1- MNPs as boron vectors for an efficient BNCT.
- ✓ The amount of both Fe and Boron internalized by A172 tumour cells in our study is sufficient to allow a successful MRI guided BNCT since it exceeds the minimum amount of ^{10}B necessary to perform BNCT.
- ✓ Finally, it was assessed that the systemic administration of these 1-MNPs in adult mice are well tolerated at mid-term with no major signs of toxicity.

The last chapter deals with magnetic nanoparticles and magnetic nanocomposites with carbon nanotubes, both forming complexes with H[COSAN]. The major conclusions are:

- ✓ Magnetic nanoparticles were synthesized and coated with silica using mechanical stirrer and functionalized with amino groups, carboxylic groups and characterized.
- ✓ The magnetic nanoparticles were used to form a non-bonded complex with metallacarborane, cobaltabis(dicarbollide) or H[COSAN].
- ✓ Magnetic nanoparticles are used to form composites with multi walled carbon nanotubes. These nanocomposites are functionalized to be used for biological applications which is uncommon.
- ✓ Also, these nanocomposites have been used to form a complex with H[COSAN]. The attachment of H[COSAN] to these magnetic species is to add a redox specie to them to tune the HOMO-LUMO and use them as sensing layer in sensors.

ANNEX I:

Articles approved by the Committee of Department of Chemistry of Universitat de Autonoma de Barcelona (UAB) on 3rd June, 2019 to present the thesis as a compendium of articles are listed below:

Chapter 1(results and discussions part 1):

- Biomimetic Inspired Core-Canopy Quantum Dots: Ions Trapped in Voids Induce Kinetic Fluorescence Switching, Arpita Saha, Elena Oleshkevich, Clara Vinas and Francesc Teixidor, *Advanced Materials*, **2017**, *29*, 1704238.
  DOI: 10.1002/adma.201704238.

Chapter 2 (results and discussions part 1):

- The Next Stage in Colloidal Synthesis of Aqueous CdSe QDs: High Throughput and Intense Emissive Properties, Arpita Saha, Abhishek Saini, Clara Vinas and Francesc Teixidor, *ChemNanoMat,* **2019,** *5.* DOI: 10.1002/cnma.201900247.

Chapter 4 (results and discussions part 2):

- Combining Magnetic Nanoparticles and Icosahedral Boron Clusters in Biocompatible Inorganic Nanohybrids For Cancer Therapy, Elena Oleshkevich, Anna Morancho, Arpita Saha, Koen M. O. Galenkamp, Alba Grayston, Simonetta Geninatti Crich, Diego Alberti, Nicoletta Protti, Joan X. Comella, Francesc Teixidor, Anna Rosell and Clara Vinas *Nanomedicine : Nanotechnology, Biology and Medicine*, **2019**, 20, 101986.
  DOI: 10.1016/j.nano.2019.03.008